A Biomaterial-based Stem Cell Therapy for Retinal Regeneration

by

Pierre Colombe Dromel

B.S., M.S., Ponts et Chaussees (2013, 2015)
M.S., Imperial College London (2017)

Submitted to the Department of Material Science and Engineering
in partial fulfillment of the requirements for the degree of

Doctor of Philosophy

at the

MASSACHUSETTS INSTITUTE OF TECHNOLOGY

February 2022

Author . . . .
Department of Material Science and Engineering
September 15, 2021

Certified by . . . .
Myron Spector
Professor of Orthopedic Surgery (Biomaterials), HMS
Thesis Supervisor

Certified by . . . .
Alfredo Alexander-Katz
Associate Professor of Material Science and Engineering, MIT
Thesis Supervisor

Accepted by . . . .
Frances M. Ross
Chair, Departmental Committee on Graduate Studies
DCGS Chair

A Biomaterial-based Stem Cell Therapy for Retinal Regeneration

by

Pierre Colombe Dromel

Submitted to the Department of Material Science and Engineering
on September 15, 2021, in partial fulfillment of the
requirements for the degree of
Doctor of Philosophy

Abstract

Retinal diseases such as age-related macular degeneration and diabetic retinopathy are the leading cause of blindness worldwide with prevalence and resulting costs projected to increase. There are few available treatments, and their applicability is limited to slowing down the degeneration of the retina resulting from these diseases. New treatments are needed to either stop the degeneration or regenerate the retina with healthy cells to improve vision. Emerging therapies, in clinical trials, are investigating stem cell-derived photoreceptors injected, in a saline solution, into the subretinal space to replace dying cells caused by retinal degeneration.

The principal objectives of this thesis were to engineer a bio-inspired injectable matrix to incorporate stem cell-derived retinal cells and growth factors (viz., epidermal growth factor) for injection into the subretinal space or vitreous, in place of saline, and to evaluate the ability of the gel therapy to increase the viability, engraftment, and functionality of the exogeneous cells in the retina. To achieve this goal, we employed conjugates of gelatin with hydroxyphenyl propionic acid, an amino acid-like molecule (Gtn-HPA), and hyaluronic acid with tyramine (HA-Tyr). We also investigated an interpenetrating network (IPN) comprising a combination of Gtn-HPA and HA-Tyr, which can be tuned to obtain the optimal mechanical, chemical, and injectable characteristics tailored to improve retinal regeneration. The effects of these hydrogels on various retinal cells (human ganglion cells, human retinal progenitors, and human cones photoreceptors) were analyzed in the in vitro setting and showed positive results: high viability, controlled differentiation, and low apoptosis.

In the first of 3 application-based in vivo experiments, we investigated select hydrogels incorporating specific cell types to treat problems associated with retinal ganglion cells (RGCs) in vitreous injections. Transplanted RGCs showed significantly higher engraftment and process extension when encapsulated in our IPN compared to saline injections.

In a second in vivo experiment, we transplanted retinal progenitor cells (hRPCs) in the subretinal space environment to address problems associated with photoreceptors in the retina. Transplantations were quantified and compared to injections in saline at 1- and 3-weeks post-transplantation. At both time points, a 5-fold increase in engrafted hRPCs in the outer nuclear layer (ONL) was observed when the cells were injected in our biomaterial compared to injection in saline.

In a third vivo experiment, a novel human cone progenitor (hCP) cell line was created and studied in retinal degenerative animal models (such as RCS rats and RD1 mice). hCPs were found to engraft in high numbers and showed a significant 2-fold increase in retinal functionality, which was measured with optokinetic (OKN) and electroretinogram (ERG) assays. The results of this thesis motivate and guide further translational study in a large animal model to validate Gtn-HPA/HA-Tyr hydrogels incorporating retinal stem cells and growth factors for the promotion of retinal regeneration in a larger eyeball size with the attendant improvement in visual function.

Thesis Committee:

Myron Spector (Thesis Advisor), Ph.D.
Professor of Orhtopedic Surgery (Biomaterials), **HMS**
Department of orthopedic Surgery, **BWH**
Director, Tissue Engineering/Regenerative Medicine Laboratory, **VABHS**
Mechanical Engineering and HST, **MIT**

Alfredo Alexander-Katz (Thesis Advisor), Ph.D.
Associate Professor of Materials Science and Engineering, **MIT**

Michael young, Ph.D.
Associate Professor of ophthalmology, **HMS**
Co-Director, Ocular Regenerative Medicine Insitute, **MEEI**
Director, Minda de Gunzburg Center for Retinal Regeneration

Krystyn Van Vliet, Ph.D.
Michael (1949) and Sonja Koerner Professor of Materials Science and Engineering
Associate Vice President for Research, **MIT**
Associate Provost

Acknowledgments

I am grateful to my thesis advisor, Professor Myron Spector, for his support and mentorship during my entire doctoral research. He offered me an amazing opportunity to be involved in translational project which could one day be applied in clinic and give back sight to blind patients. I admire his responsiveness, availability, mentorship, attention to details and immense understanding of biomedical research topics.

I am thankful to my thesis co-advisor, Professor Alfredo Alexander-Katz, for his mentorship and all the support he gave over these years. I started as a visiting student in his group before performing my thesis work at MIT and, thanks to his impressive quality as a teacher, advisor, and guide, he pushed me toward research. During these difficult times of pandemic his personal guidance greatly helped me focus and live my life away from home.

I would like to give many thanks to Professor Michael Young, for his great leadership and mentorship during the time I worked in his laboratory, making it a second home to me. He has been an amazing mentor and teacher throughout my thesis, giving me the keys to perform my work and showing me how a great work-life balance can make the difference. I have been inspired by his caring attitude and humility which make him an amazing role model for my career.

I offer many thanks to my committee member-Professor Van Vliet-for her questions and guidance that helped me focus the aims of this thesis and develop my critical thinking towards my research topics.

Thank you, lab members, at the VA for creating a supportive environment and offering useful suggestions. For the helpful discussions and guidance, I would like to thank specifically Dr. Wanting Niu, Dr. Adhvait Shah, and Dr. Chris Love VA and Dr. Motoichi Kurisawa from the A*STAR Singapore for providing the polymers for hydrogels and his insight.

Thank you to my collaborators and to the Schepens Eye Research Institute for creating a welcoming environment to work. I would like to thank specifically Dr. Petr Baranov, Dr. Julia Oswald and Dr. Tatiana Perepelkina for their guidance and their

tutoring at the start of my doctoral work.

Thank you to the Laboratory for Soft Matter and the Program for Polymer and Soft matter for all the amazing teaching and learning program which greatly help me achieve my goals in the different projects. I would like to thank specifically, Dr. Karim Gadelrhab, Dr. Mukarram Tahir, Dr. Emiko Zumbro and Shayna Hilburg for their help during the qualification exams and their personal guidance.

I would like to give a special thanks to the Gilbert family foundation and the Gunzburg fund for funding different aspects of this research. A special thanks to Dr. Don Zack for his input and the human retinal ganglion cells he provided which led to great results.

I am grateful for the support and help from my friends and colleague in the PPSM program. During the difficult first year, with the qualification exams, they helped me enhance my curiosity and enjoyment towards different topics. I would like to specifically thank Katherine Mizrahi, Jake Song, Elad Deiss-Yehiely and Sachin Bhagchandani for their help and access to their laboratory facility for my project on IPN. Finally, a special thanks to Ty Christoff-Tempesta, my friend and roommate, for giving me advices throughout my thesis work and putting up with me 24/7 during the shelter in place in 2020.

Thank you to my friends in Boston for the encouragement and support over the years of the Ph.D. I am really grateful to Arun Prakash, Anne Colin and Cedric Viry, Sophie Elias and Alex Borras, and to my volleyball team.

Thank you to my long-time friends Ulysse, Eliot, Oscar, Leonie, Antoine, Victor, Laurane, Marie, Domitille, Gabriel for making the moments outside my work extremely enjoyable, together with my family, my cousins, and my grandparents for their support from the other side of the ocean.

I would like to give a special thanks to my ‘not so related’ colleague and dear friend Dr. Deepti Singh without whom none of this promising work would have been possible. She has been an amazing mentor and her example showed me, every day, what it means to be an amazing scientist, researcher, and human being. I deeply admire her courage, intelligence, and kindness which makes her the best possible partner I could have hoped for in my career.

I am thankful for the unwavering support, encouragement, and love from my fiancée Safia Dziri whose strength and kindness inspires me every day. Over the years of the Ph.D., she has been behind me at each and every step, pushing me to be the best even in difficult times. Thank you for being there in my life, for giving me the strength to reach my goals and helping me become a better person. I can't wait to see what future brings for us.

Manon, my sister, you lit up my life ever since you came into it. I promise to love you, protect and be the best brother you could ever hope for.

There are no words to describe the unconditional love I receive from my dad, Guillaume Dromel, who has protected me and encouraged me to be the best version of myself and what a powerful influence he continues to be. Thank you for believing in me and supporting my dream of becoming a biomedical scientist on the other side of the ocean.

Finally, I would like to dedicate this thesis to the person who shaped my life and personality. Whose love and generosity guided me through thick and thins of life: my mom, Adeline Dromel. She is the person who taught me the importance of helping people, not only in my daily life, but also through my work. Her kindness, intelligence, fearless attitude, rigor, and love makes her the best ally I needed to meet every challenge in my life.

Table of Contents

List of Figures

List of Tables

Chapter 1

Clinical problem and proposed therapeutic approach

1.1 Retinal Diseases background

The leading causes of blindness are primarily retinal diseases such as age-related macular degeneration or diabetic retinopathy [1], [2]. In 2021, there was an estimated of 20 million patients affected by a retinal disease. In the U.S., the total estimated number of patients legally blind over 40 years in 2019 was 4.2 million. This number is predicted to more than double by 2050 to 8.96 million due to the increasing epidemics of diabetes and the impact of ageing population. Along with AMD, many other retinal diseases (such as inherited retinal diseases [3] or retinal detachment) affect more than 1 million individuals (Figure 1.1).

Retinal diseases are either caused by a genetic mutation (IRDs), diabetes, or a disruption of the architecture of the retina via extracellular deposits (AMD). Due to the retina's vital role in vision, damage to it causes permanent blindness. Conditions such as retinal detachment [4], where the retina abnormally detaches from its usual position, can prevent the retina from receiving or processing light. That, in turn, stops the brain from receiving this information, thus leading to blindness. Using back of the eye imaging with different apparatus [5], many symptoms and sign of retinal diseases can be monitored and observed (Figure 1.2) such as: drusen (present during

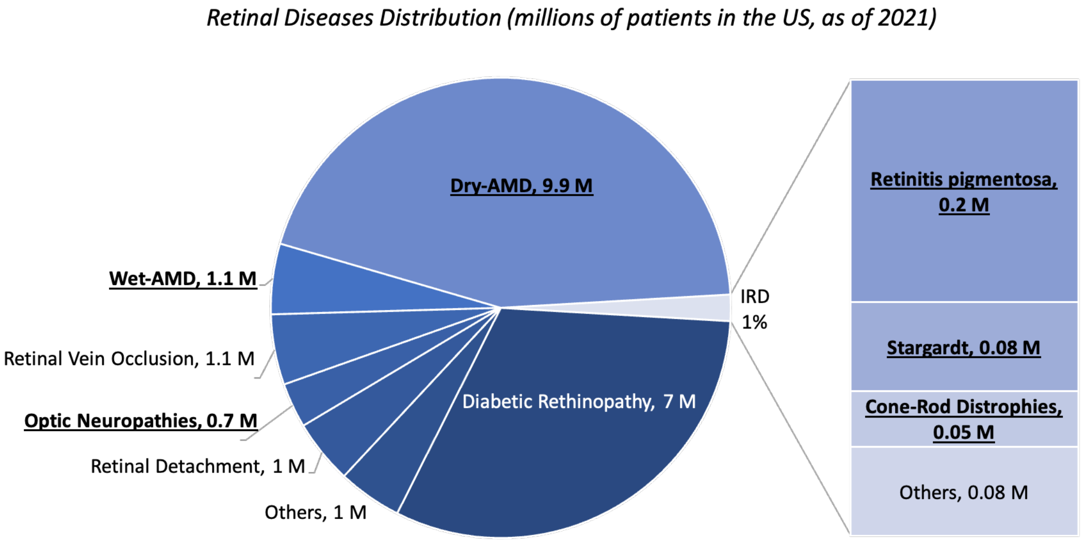

Figure 1.1: Retinal diseases distribution in the US as of 2021. Distribution of patients suffering from retinal diseases in the US. The main diseases are AMD (dry or wet) and diabetic retinopathy. 1% of patients are affected by inherited retinal diseases (IRD).

AMD), black spots (present in RP), retinal detachment, diabetes impact, hemorrhage etc.. . .

There is presently no cure for most of these retinal diseases but some treatments have emerged which might slow down the degeneration created by the disease in certain cases. These treatments include surgery [7], injection of neuroprotective factors [8], cell injection, or optogenetics.

1.2 Degeneration mechanism due to retinal diseases

1.2.1 Anatomy and architecture of the retina

The retina is a nervous membrane which is the inner lining of the eyeball, upon which the light coming from external objects is received. It is located on between the choroid (blood vessels bringing nutrients) and the hyaloid membrane (or inner limiting membrane ILM) of the vitreous body near the optic nerve. Its thickness diminishes from behind to forward and it extends as far as the ciliary body [9]. In the center

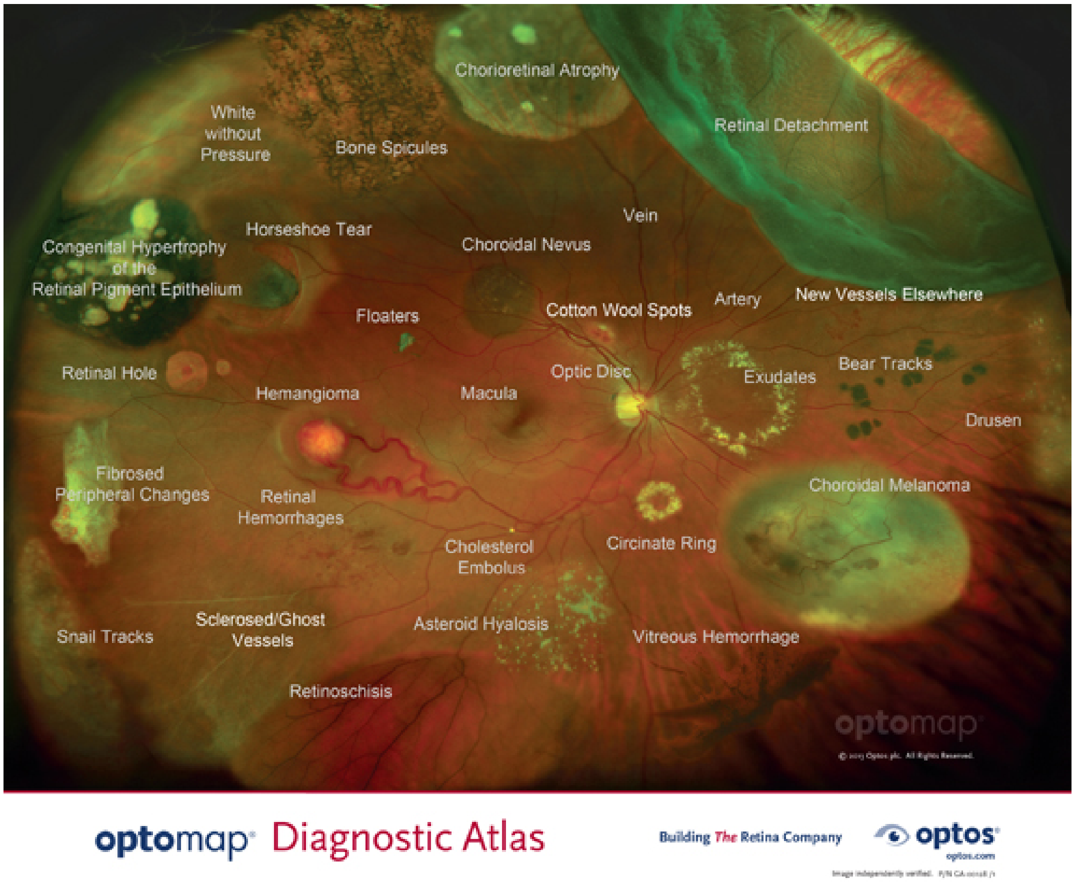

Figure 1.2: Map of the back of the eye with specific symptoms.
Map of the back of the eye constructed with the imaging of a subset of diseased retina with the Optos® Optomap®. Symptoms can be observed and monitored such as: bear tracks, drusen, hemorrhages, cholesterol embolus, holes, detachment, or tears. The architecture of the back of the eye is also observable (optic disc, vein, artery, macula). Image reprinted with permission from Optos® PLC (https://www.optos.com/providers/diagnostics–educational-tools/) [6].

of the posterior part of the retina, point at which the sense of vision is most perfect, is located an oval yellow area called the macula; in its center a central depression is called the fovea centralis. About 3 mm to the nasal side of the macula is the entrance of the optic nerve (or optic disk) which doesn't contain any photoreceptor: also called the blind spot as it is the only part of the retina which is insensitive to light. Finally, the arteria centralis pierces the center of this optic disk.

As seen in Figure 1.3, the first layer of the retina (close to the choroid) is composed of retinal pigment epithelial (RPE) cells which sit on top of the Bruch's membrane

(BM). Sitting on top of RPE is a layer of photoreceptors (rods and cones). Photoreceptors permit the transcription of light input (coming from the external object) into a neural signal which is transmitted to the rest of the retina towards the visual cortex of the brain. The density of rods vs cones is dependent on the location in the retina: the macula is mainly composed of a compact layer of cones while the rest of the retina is composed of mainly rods with cones forming a mosaic pattern. These photoreceptors are connected to bipolar, horizontal and amacrine cells via a synaptic connection: enabling the transfer of information. Finally, bipolar cells are connected to the last cell layer of the retina: ganglion cells (RGC) which extend their processes towards the center of the eye, merging and forming the optic nerve. The optic nerve flows into the brain and ends in the visual cortex, where the image is analyzed. Muller cells (in grey) possess a structure and protective role by forming the inner limiting membrane, blocking the entrance of the retina to exogeneous factors on top of the RGC layer.

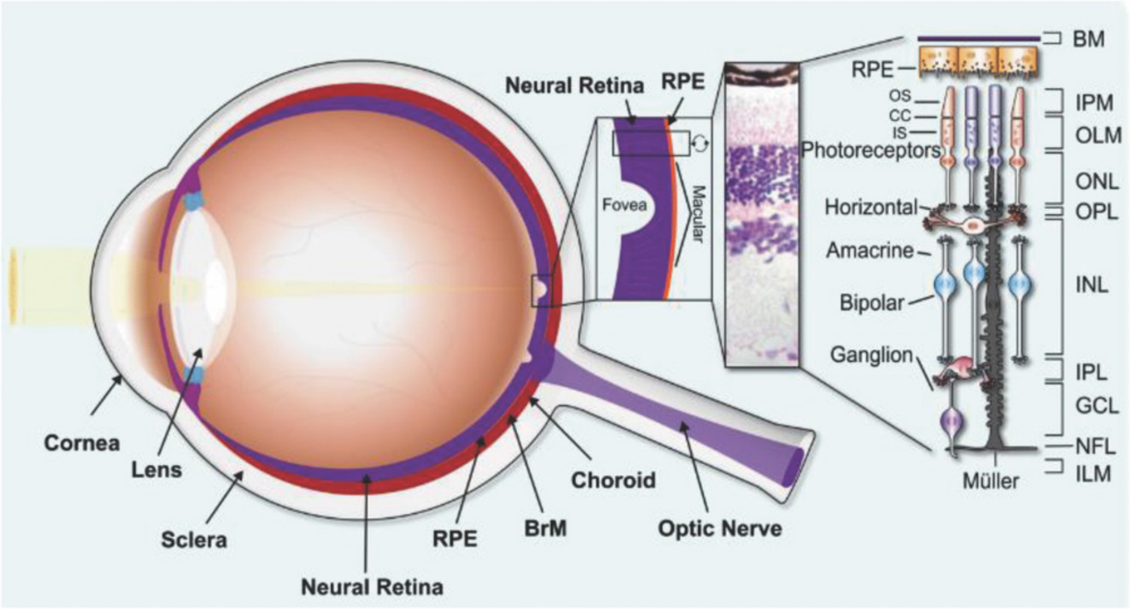

Figure 1.3: Structure of the eye and architecture of the retina.
Schematic of a section of the eye showing the cornea, lens, sclera, choroid and optic nerve; with zoom on the neural retina. H&E staining is shown and all retinal layers are observable and marked (including cell type). Image reprinted with permission from Hunt et al. [10]

Another way of labeling the retina is to differentiate it into the neural retina and the non-nervous retina (or sustentacular fibers). When examined under microscopy with H&E staining by means of sections made perpendicularly to the surface, the retina consists of 10 layers [11]:

1. Bruch's membrane (BM)
2. RPE layer
3. Layer of rods and cones
4. Outer nuclear layer (ONL)
5. Outer plexiform layer (OPL)
6. Inner nuclear layer (INL)
7. Inner plexiform layer (IPL)
8. Gemglionic layer (RGC)
9. Nerve fabier layer (NFL)
10. Inner limiting membrane (ILM)

The purpose of the retina is to receive a light input which goes through all the layers of the retina and is stopped by the RPE layer. Photoreceptors are essentially light-sensitive cells, responsible for detecting qualities such as color and light-intensity. They capture this light input and process it into a neural signal (with the use of chemical components called opsin) which is sent towards bipolar cells and then ganglion cells. This signal navigates into the processes of RGC and goes directly into the optic nerve and towards the visual cortex of the brain for visual recognition. Therefore, the delicate architecture of the retina plays a major role in visual function. Any change or disruption in one cell layer can create a cascade which can lead to vision loss: retinal disease.

1.2.2 Age-related macular degeneration (AMD)

Age-related macular degeneration (AMD), is a medical condition which may result in blurred or no vision in the center of the visual field [12]. Over time, patients experience a gradual worsening of vision that may affect one or both eyes. This disease does not result in complete blindness but in the loss of central vision that can make it hard to recognize faces, drive, read, or perform other activities of daily life. Visual hallucinations may also occur but these do not represent a mental illness.

As the disease progresses, extracellular deposits, called drusen, form beneath the retinal pigment epithelium (RPE). This deposit disrupts the overlying photoreceptor cells creating the loss of vision. Clinically, drusen represent one of the earliest biomarkers of AMD, and progression of the disease is categorized primarily based on the size, shape, and location of this cellular debris within the macula. Abnormalities in the RPE may also accompany drusen [13]. The advanced stage of dry AMD is characterized by the progressive loss of the RPE cells, the outer neurosensory retina and the choriocapillaris. Degeneration of photoreceptor cells throughout the macula results in functional deficits leading to severe loss of central vision [14]. The pathogenesis of AMD and its causes are still relatively unknown but due to the increase of research and laboratories working on curing AMD new clinical trials have appeared in the past few years.

1.2.3 Inherited retinal diseases (IRDs)

Inherited retinal diseases—or IRDs—are diseases that can cause severe vision loss or even blindness [15]. Each IRD is caused by the mutation of at least one gene which creates a cascade mechanism and disrupt one specific layer of the retina (in most cases the photoreceptors). IRDs progress at different rates are rare (orphan diseases). However, most are degenerative and symptoms get worse over time. There are many types of IRDs but the most common ones are:

- Retinitis pigmentosa [16]: is a group of disease caused by more than 100 mutations in 60 genes which affect the retina and especially the photoreceptors. RP leads to progressive and non-reversible vision loss as well as retinal dystrophy. Usually rods are the first photoreceptor to die, which then triggers a cascade killing the cones too. The first sign of RP is usually loss of night vision, called night blindness. The apparition blind spots which develop in the peripheral retina over time, reduce the patient's vision. There is presently no effective treatment to treat retinitis pigmentosa.

- Stargardt's disease [17]: is caused by damage to the macular and especially cones and rods. It is caused by the mutation of two specific genes: ABCA4 and ELOVL4. The ABCA4 and ELOVL4 genes provide instructions for making proteins that are found in photoreceptors in the retina. A fatty yellow pigment (lipofuscin) builds to cells underlying the macula which then disrupts the architecture of the retina leading to vision loss. The disease typically causes central vision loss during childhood or adolescence. Only rarely do people with the disease lose all vision.

- Cone-rod dystrophy (CRD) [18]: is a group of more than that affect the cones and rods. It is caused by the mutation of more than 30 genes, 20 of which are inherited in an autosomal recessive pattern. With the progressive deterioration of the cones and rods, people with this condition experience vision loss over time. The first symptoms usually occur in childhood, and may include blurred vision and an intense sensitivity to light (called photophobia). Most individuals with this condition lose a significant amount of vision by mid-adulthood.

1.2.4 Neurofibromatosis type 1 - Optic pathway gliomas (NF1-OPG)

A specific disease which will be discussed in this thesis is Neurofibromatosis type 1 - Optic pathway gliomas (NF1-OPG) [19]. Neurofibromatosis type 1 (NF1) is a genetic condition that causes tumors to grow along nerves throughout the entire body. The tumors are usually benign but may cause a range of symptoms. NF1 is caused by the mutation of the NF1 gene on chromosome 17. This gene produces a protein called neurofibromin that helps regulate cell growth. When mutated, the loss of neurofibromin allows cells to grow uncontrolled. In the case of NF1-OPG it is the presence and formation of optic nerve gliomas (OPG) which are benign brain tumors that grow on the optic nerves which leads to loss of vision. OPGs are found in approximately one in five children with NF1.

In NF1-OPG, mutant RGCs (forming the optic nerve) are observed and have an impaired neurofibromin function. This reduces the cAMP levels, thereby lowering the threshold for RGC death and replacement. Therefore, this triggers a cascade in which mutant and non-functional RGCs are not replaced leading to subsequent vision loss. Specifically, NF1-mutant microglia secrete chemokines (e.g., CCL5, CXCL12), which promote the proliferation and survival of NF1-deficient tumor cells. In addition, estrogen receptor β (ERβ)-mediated microglial priming leads to the production of neurotoxins (e.g., IL-1β) that increase NF1-mutant RGC axonal dysfunction and death, causing vision loss in a sex-dependent manner [20]. Nearly 75 percent of optic nerve gliomas occur in children younger than ten years old and total blindness occurs in 5% of cases.

The vision of patients affected by the listed diseases is shown is Figure 1.4.

1.3 Gold standard of therapy

1.3.1 Therapies available and their potential

As explained previously, most retinal diseases create a toxic cascade which promotes the death of photoreceptors and other cells in the retina and finally damages the structure of the tissue. The goal of a retinal therapies is not only to stop the progression of degenerating diseases but also to perform regeneration of the diseased tissue. Different types of therapies are being studied, each having its potential to cure part of a retinal disease cascade: gene therapy, neuroprotection, optogenetics and cell replacement therapy (see Table 1.1).

Several gene therapy approaches, including replacement gene therapy, addition

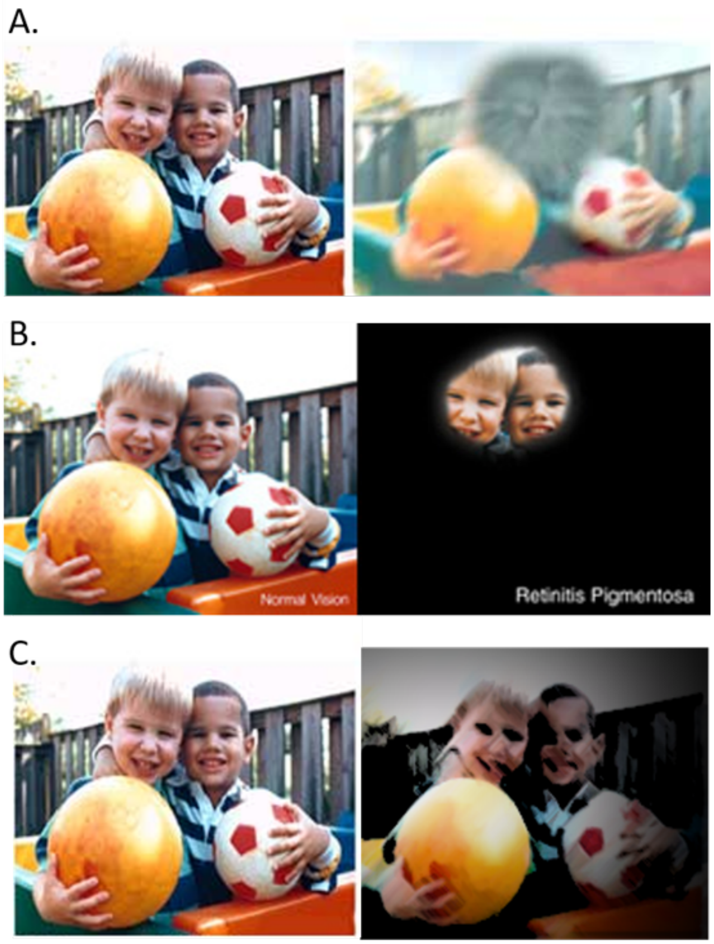

Figure 1.4: Vision of patients affected by retinal diseases.
Left panel: healthy vision, **right panel:** vision of patient affected by **A.** Age-related macular degeneration (AMD) **B.** Retinitis pigmentosa (RP) and **C.** Neurofibromatosis type 1-optic pathway gliomas (NF1-OPG). AMD induces symptoms such as blurred vision and reduced vision in the center of the visual field. RP creates a loss of peripheral and scotopic (light) vision. NF1-OPG provokes blurry and distorted vision as well as hormonal problems.

of a growth factor, suppression gene therapy, and gene editing, have been proposed in attempts to treat various ophthalmologic conditions [25]. Only one therapy has passed clinical trial and has been approved by the FDA [26]. This therapy consists in repairing a specific gene (RPE65) which, when mutated, leads to loss of vision and especially Leber congenital amaurosis which is an early onset of retinitis pigmentosa. This reparation is performed by injecting a normal copy of the gene RPE65 with a surgical incision in the subretinal space next to the photoreceptors. The results of

Table 1.1: Main therapies involved in retinal regeneration.

Therapy	Advantages	Downfalls
Gene therapy	- Only way to cure the underlying inherited disease - Can stop the degeneration of cells [21]	- Necessary to cure the disease but no sufficient - Need for healthy cells to restore vision
Neuroprotection	- Neuroprotective factors can slow retinal degeneration - Several animal models have been tested [22]	- Best for treating secondary degenerative diseases. - Need for healthy cells to restore vision
Optogenetics	- Combines genetic and optical stimulation strategies - Activates selective proteins to repair the retina [23]	- Best for slowing down degeneration - Need for healthy cells to restore vision
Cell replacement	- Could enable total sight regeneration - Many diseases type can be targeted (with different cell types) [24]	- Stem cell culture is a challenge with unwanted cells leading to tumor formation - Cannot stop the degeneration mechanism

the clinical trial and the treated patients suggest a great opportunity to stop the degeneration of certain inherited retinal disease (IRD).

Optogenetics focuses on creating artificial photoreceptors to restore photosensitivity. This is accomplished by gene delivery of light-activated optogenetic tools (channels or pumps) to surviving cells, such as ganglion cells, that remain intact in the retinal circuit in various diseases [27]. A recently approved clinical trial [28] has showed that by combining intraocular injection of an adeno-associated viral vector encoding ChrimsonR with the addition of engineered googles, patients were able to restore partially their lost vision due to retinitis pigmentosa.

Due to the drastic vision lost caused by the neurodegeneration of the retina, many studies and a couple of clinical trials have focused on the use of neuroprotective factors which have the potential to slow down or even stop the degeneration. A number of neuroprotectants, which can be injected in the vitreous or subretinal space, with defined mechanisms of action (such as saffron and coQ10 [29]) show anti-apoptotic effects.

The most promising therapy to regenerate fully sight to blind people is cell replacement. While other therapies focus on slowing down or stopping the disease, the cell replacement therapy goals are to regenerate the retina by injecting viable, live and functional cells into the retina. These cells must have the ability to engraft in the retina and attach to the right cell layer, forming a healthy retinal architecture with specific cell-cell interaction and synapses connections. The injected cells must also have the ability to proliferate and be protected from the immune system. For these goals, many studies have been performed and have shown that the use of human derived stem cells is the perfect fit to accomplish those goals [30], [31]. Stem cells have the ability to differentiate into several cell types but they are also capable of indefinite proliferation in their undifferentiated state [32]. Stem cells used for retinal regeneration can be classified in either their potency (omnipotent, pluripotent and multipotent) or origin. Omnipotent stem cells can differentiate into embryonic or create organism, pluripotent cells also known as master cells have the ability to form all 3 germ layers, and multipotent stem cells are able to differentiate into a limited number of cell types. The following list shows the different types of retinal stem cells, their properties and their origin:

- Embryonic stem cells [33]: ESCs are pluripotent, have the ability to self-renew and are derived from embryos. ESCs can differentiate into neurons, cardiomyocytes, hepatocytes, pancreatic beta cells, lung epithelium, but also photoreceptors and RPE. Several concerns rise with the use of ESCs. Indeed, they may need immunosuppression in order to remove any unwanted cells which could lead to tumor formation and immune reaction post-transplantation; they also have an ethical concern due to the fact that they are derived from blastocysts 5 days after fertilization.

- Mesenchymal stem cells [34]: MSCs can be derived from bone marrow and human umbilical cord blood. They can differentiate into mesodermal cells such as osteoblasts and adipocytes. Depending on the stiffness of the substrate they are cultured on they can differentiate in neurons (RGC or horizontal cells in the retina), muscle or bone cells.

- Induced pluripotent stem cells [35]: iPSCs have similar morphology and growth properties as ESCs. They can differentiate into tissues with a specific protocol and are derived from human adult fibroblast by applying the Yamanaka factor to them [36]. One major improvement with iPSCs is the tolerance of the immune system when transplanting those cells; no need for immunosuppression. One issue with iPSCs is the risk of tumor formation when transplanting.
- Progenitor cells [37]: PCs are isolated from tissue of developing fetuses. These cells have a high potential of proliferation (expandable) and can be maintained in an undifferentiated state. In case of retina, fetal eye tissue from early gestation week can be used to isolate retinal progenitor cells (RPCs). RPCs are multipotent and can differentiate in any cells of the retina (ganglions, RPE, photoreceptor, bipolar cells, Muller cells ...) with little to no unwanted differentiation which removes the problem of tumor formation.
- Neural stem cells [38]: NSCs are isolated from the adult subventricular zone and dentate gyrus of the hippocampus in the central nervous system (CNS). They have a high potential of proliferation however their differentiation is limited: neurons, astrocytes and oligodendrocytes. NSCs are found in the retina, the ciliary body epithelium, ciliary marginal zone, and iris.

The success of using these stem cells for treatment is based on finding an appropriate source, efficiently deriving the desired cell population, and then establishing a safe and effective method of delivery. Many studies have shown the potential of ESC derived retinal pigmental epithelial cells (RPE) to replace and regeneration the RPE layer of the diseased retina [39], [40]. Some recent clinical trials have been approved for the first in human trials of retinal progenitor cells derived photoreceptors to potential restore sight in patients possessing retinitis pigmentosa.

1.3.2 Stem cell replacement therapy

As of today, many clinical trials have been approved for the injection of stem cell derived retinal cells to induce regeneration and possible vision restoration (Table 1.2).

Table 1.2: List of ongoing clinical trials using stem cell therapy for retinal regeneration.

Type of stem cell therapy	**Injection Method**	**Pathology**	**Phase**	**Ref**
Bone marrow-derived stem cells	Intravitreal	nAMD, Stargardt	Phase I and II	[41]
Bone marrow-derived stem cells	Intravitreal	Glaucoma	Phase I and II	[41]
Central nervous system cells	Subretinal	Atrophic AMD	Phase I and III	[42]
iPSCs derived RPE cells	Subretinal	Atrophic AMD	Phase I	[43]
iPSCs derived RPE cells	Subretinal	nAMD	Phase II	[44]
hESC-derived RPE cells	Subretinal	AMD	Phase I	[45]
hESC-derived RPE cells	Subretinal	nAMD	Phase I	[46]
hESC-derived RPE cells	Subretinal	AMD, Stargardt	Phase I	[47]
hESC-derived RPE cells	Subretinal	Atrophic AMD	Phase I	[48]
hESC-derived RPE cells	Subretinal	AMD	Phase I and II	[49]
hESC-derived RPE on membrane	Subretinal	AMD	Phase I and II	[50]
human retinal progenitor cells	Subretinal	Retinitis pigmentosa	Phase I	[51]
human retinal progenitor cells	Subretinal	Retinitis pigmentosa	Phase II	[52]
human retinal progenitor cells	Subretinal	Retinitis pigmentosa	Phase I and II	[53]

Of those ongoing clinical trials, two different injection location have been used: the vitreous and the subretinal space. Cells are usually injected in a 31-gauge needle in a saline solution. In the vitreous cells are floating and tend to migrate towards the retina to attach the inner limiting membrane or RGC layer before migrating towards the right layer (RPE, photoreceptors. . .). The subretinal space is a fictive space which is created by forming a bleb between the RPE and photoreceptor layer and injecting cells in that space [54]. As seen in Figure 1.5, this bleb creates a small pocket (retinal detachment) which allow for the cells to migrate directly towards either the RPE or photoreceptor layer. With this injection mechanism a higher percentage of cells can be found engrafting in the right layer and assembling to form the architecture of the previously diseased retina.

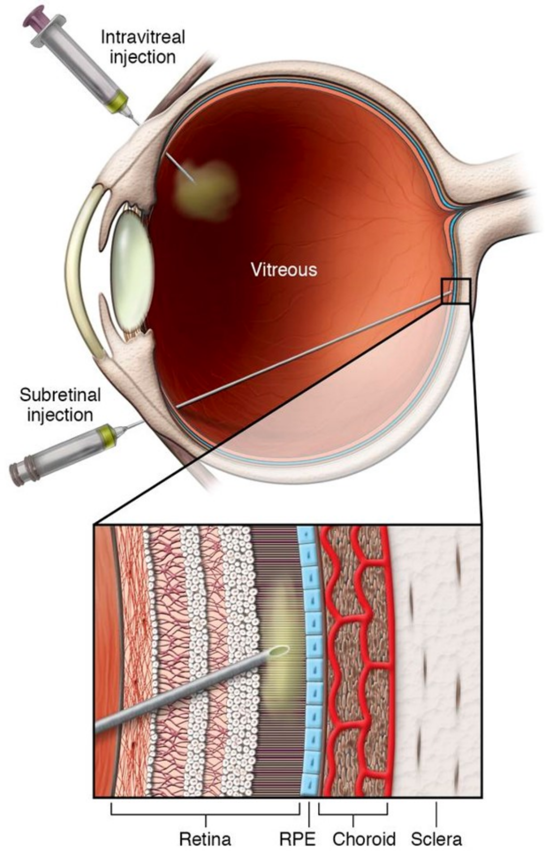

Figure 1.5: Schematic of invitreal vs subretinal injection of stem cells. Invitreal injection consist in transplanting cells through the sclera and directly into the vitreous body of the eye. Subretinal injection are performed by injecting inside the retina between the RPE and outer nuclear layer (ONL) of photoreceptors. A bleb, incorporating the therapeutic, is created at this location. Reprinted with permission from DiCarlo et al. [55].

The main downfall of stem cell replacement is that it is necessary to restore vision but not sufficient. Indeed, even if healthy and viable cells are injected and able to engraft and replace dead cells, the IRD mechanism would keep on degenerating the new cells. The final and optimal approach to fully treat IRD would ideally be a combination of gene therapy in order to stop the degeneration and stem cell therapy to replace the dead cells and promote regeneration of the retina with healthy exogeneous cells. Another option would be to create a protective envelope around cells until they migrate and form connections with the host tissue and secrete neuroprotective factors that can negates the hostile environment presented by the IRD tissue.

1.4 Biomaterials for treating retinal diseases

The environment in which cells grow and differentiate can critically influence their survival post-transplantation. The rationale behind using biomaterials for treating retinal diseases is that the transplantation of stem cell derived retinal cells needs to be injected in a hostile microenvironment as an intact layer/sheet rather than injected as a suspension [56], [57]. As mentioned in the previous section, subretinal and vitreous injection were previously performed with a bolus injection of cells in saline. One example for the need of such biomaterials is the mechanics of degeneration of AMD. As mentioned previously AMD is characterized by the complete loss of RPE but also an abnormal Bruch's membrane (BM). This membrane is a thick ECM composed of collages type I and IV, HA, laminin, fibronectin, chondroitin sulfate and elastin [58]. As such the successful injection and replacement of healthy RPE is impossible due to the degraded nature of BM during AMD. Studies have shown that by resurfacing BM with either natural of synthetic biomaterials can facilitate and improve significantly RPE engraftment and retinal regeneration [59].

Other studies have used injectable biomaterials (e.g., hydrogels) to encapsulate various stem cell derived photoreceptor progenitors with a goal to treat diseases such as RP, AMD or RD [60]. As seen in a previous section, photoreceptors have a specific layout in the architecture of the retina. Transplanting photoreceptor by a bolus injection in saline is a first step to prove their functionality in vivo however it is not optimal. By using different type of hydrogels and encapsulating biomaterial the engraftment, viability and phenotype of those injected cells can be enhanced thus improving their potential effect in the diseased retina. One emerging research concept is the injection, in the subretinal space, of a biomaterial-encapsulating cells hydrogel to replace dead photoreceptor in the diseased retina (Figure 1.6). The resulting bleb formation is filled with a solid material encapsulating the targeted stem cells. Direct injection of this biomaterial incorporating stem cells could: 1) reduce immune response and rejection; 2) facilitate the migration of stem cells into the tissue; 3) enhance stem cell viability; 4) enhance the final engraftment and replenish the retina with healthy cells that in turn improve its architecture and functionality. Moreover, the addition of therapeutic agents directly into the biomaterial, before injection, might be able to overcome the problems of low viability and unwanted differentiation.

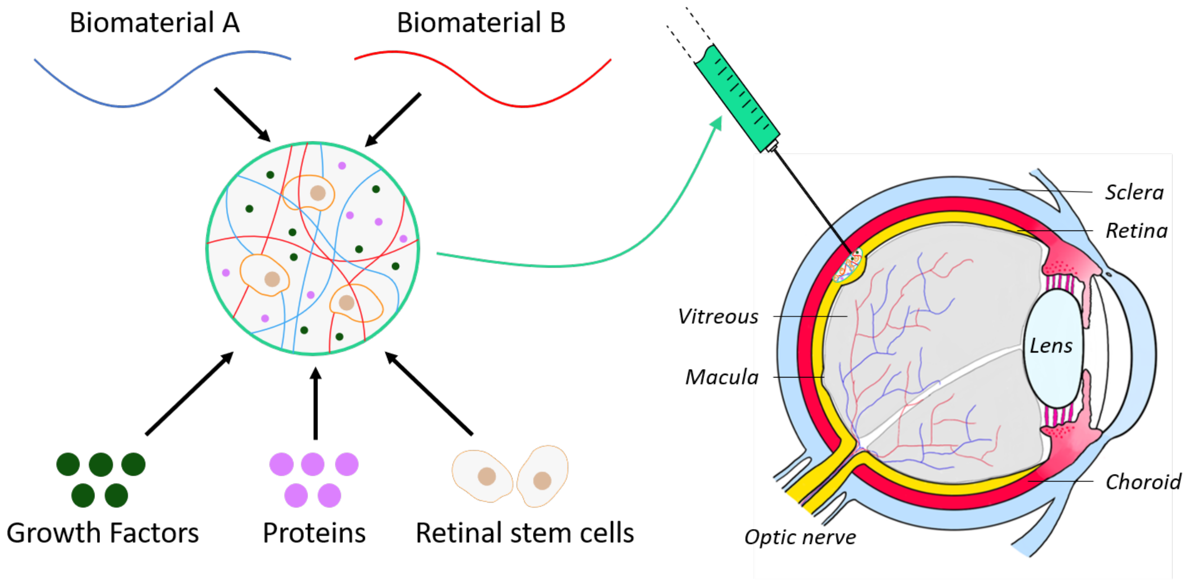

Figure 1.6: Schematic of biomaterial-encapsulating hydrogel injection into the subretinal space.
Biomaterials (synthetic, natural or hybrid) are formed in tube and mixed with the therapeutics (retinal stem cells, proteins or growth factors) and injected through a 31-gauge needle in the subretinal space. The hydrogel can either be pre-formed or possess an in-situ crosslinking mechanism. Image has been modified from Dromel et al. [61].

Biomaterials used for treating retinal diseases include naturally derived polymers, synthetic polymers, and biohybrid scaffolds. Natural biomaterials mainly include ECM proteins already found in the retina such as gelatin I, II and IV, alginates, laminin, fibronectin, Matrigel or vitronectin. These biomaterials are formed into high water-content hydrogels which are crosslinked networks of hydrophilic polymers [62]. These hydrophilic polymer chains can be crosslinked chemically, physically, or ionically. Generally, the hydrophilicity and softness of hydrogels make them biocompatible and biodegradable materials having the potential to mimic tissue where they are implanted. These hydrogels have the advantage of possessing the ligands necessary for cell-integrin adhesion, migration, and degradation. The byproduct of their degradation is usually biocompatible even if they can trigger a higher immune response from the body due to their similar chemical structure as the already present ECM.

Synthetic polymers have better mechanical properties and can resist the transplantation procedure and the hostile microenvironment there are implanted in [63]. Suitable mechanical properties can be obtained by modifying the porosity, polymer fibers density, and topographical parameters. Synthetic scaffolds are more advantageous than natural scaffold because they elicit little to no immune response when injected as they are not recognized by the immune system. Biocompatible and biodegradable synthetic scaffolds can be modified and derived from a high number of different polymers: poly(lactic-co-glycolic acid) (PLGA), poly(l-lactic acid) (PLLA), polydimethylsiloxane (PDMS), poly(methyl methacrylate) (PMMA), poly(ethylene glycol) (PEG), and polycaprolactone (PCL) [64]. The most significant downfall of these synthetic polymers is their degradation byproducts which can elicit a high immune response a long-term times.

Biohybrid scaffolds have the advantages of both synthetic and natural scaffolds by incorporating both materials to make composite scaffolds [65]. Part of the scaffold (natural polymers) could bring the adhesion ligands necessary for high cell viability when encapsulating while the synthetic polymers would bring the mechanical and tunable desirable properties. Some studies have used the blend of Silk and PCL to transplant sheets of RPE in the diseased retina showing promising result in terms of regeneration [66]. Other types of scaffolds such as scaffold free cell sheets and decellularized matrix have been studied showing their potential for regeneration part of the neural retina. Examples of scaffolds used with the cells encapsulated and animal model is shown in Table 1.3. Predominantly RPE have been transplanted in different scaffolds due to their need of BM for engraftment and viability.

Table 1.3: Example of scaffolds used for cell encapsulation and their advantages.

Biomaterial	**Type**	**Cells**	**Animal**	**Advantages**	**Refs**
Gelatin	Natural	RPCs, RPE	Rabbits	- Low immunogenicity - in-situ crosslinking	[67]
Silk Fibroin	Natural	RPE	Rodents	- Great Mechanical strenght - biocompatiblity	[68]
PLGA	Synthetic	RPCs, RPE	Rodents	- Remarkable tunability	[69]
PCL	Synthetic	Rods/cones	Rodents	- Permeable - slow degradation	[64]
SF & PCL	Hybrid	RPCs	Rodents	- Quick RPC differentiation towards cones	[66]
PNIPAAm	Thermo-responsive	RPE	Rodents	- Low immunogenicity - auto-removal	[70]
Decellularized matrix	ECM	rods/cons	Rodents	- micro- and macro-structures - functional ECM proteins	[71]

The choice of biomaterials in the case of subretinal injection of photoreceptors in narrowed by the functional and optimal requirement of the tissue. To make a therapy with little to no trauma and immune reaction, the material must be an injectable liquid formulation which solidifies post-injection (in-situ crosslinking mechanism).

Therefore, natural materials that aren't shear thinning may require some synthetic chemical modification to enable gelation in vivo. These modifications can be based on enzyme-mediated covalent crosslinking or environmental modifications (pH, temperature). In addition, the biomaterial needs to be biocompatible (minimal inflammatory response) and biodegradable over a period necessary for short- and long-term delivery of the cells with possible therapeutics. After initial design in vitro testing of an injectable formulation, degradation rate, adhesion ligands presence, cell viability and encapsulation, the effectiveness of a prospective biomaterial needs to be determined in vivo.

1.5 Gelatin-hydroxyphenyl propionic acid and HA-tyramine

1.5.1 Introduction

Gtn-HPA and HA-Tyr are injectable hydrogels biomaterial with easily tunable mechanical properties that meets the retinal disease therapies-specific requirements. Their in situ-crosslinking process offer a minimally invasive application through a needle. Multiple in vitro studies support the use of Gtn-HPA/HA-Tyr by demonstrating key properties: biocompatibility; biodegradation; cell encapsulation, high viability, maintained phenotype, migration, proliferation and differentiation [72]. In vivo studies have shown its multi-week persistence after retinal injection and easy incorporation of therapeutic agents. A few of these properties are highlighted in the sections below.

1.5.2 Synthesis and characterization

For Gtn-HPA, bovine gelatin is collected (Mw=80-140 kDa, pI=5) and HPA is covalently conjugated to the polymer's strands via a general carbodiimide/active ester-mediated (EDC/NHS) coupling reaction (Figure 1.7a). The degree of HPA conjugated to gelatin amine groups has been analyzed with the TNBS method to be

90%. The final conjugation was confirmed by HNMR chemical shift peaks of 6.8ppm and 7.1ppm. This indicated the presence of the aromatic protons of HPA. Details of the full synthesis of Gtn-HPA have been previously described [73] and are copied here: "3,4-Hydroxyphenylpropionic acid (HPA) was used to synthesize Gtn-HPA conjugates by a general carbodiimide/active ester-mediated coupling reaction in distilled water HPA (3.32 g, 20 mmol) was dissolved in 250 ml of mixture of distilled water and N,N-dimethylformamide (DMF) (3:2). To this N-hydroxy succinimide (3.20 g, 27.8 mmol) and 1-ethyl-3-(3-dimethylaminopropyl)-carbodiimide hydrochloride (3.82 g, 20 mmol) were added. The reaction was stirred at room temperature for 5 h, and the pH of the mixture was maintained at 4.7. Then, 150 ml of Gtn aqueous solution (6.25 wt.%) was added to the reaction mixture and stirred overnight at room temperature at pH 4.7. The solution was transferred to dialysis tubes with molecular cut-off of 1000 Da. The tubes were dialyzed against 100 mM sodium chloride solution for 2 days, a mixture of distilled water and ethanol (3:1) for 1 day and distilled water for 1 day, successively. The purified solution was lyophilized to obtain the Gtn-HPA."

Sodium hyaluronate was obtained from Wako Biotec (Mw=180-150 kDa, pI=1.4) and tyramine was covalently conjugated to the HA strands via the same carbodiimide/active ester-mediated coupling reaction (Figure 1.7b). HA-Tyr was synthesized similarly as Gtn-HPA by mixing HA (1 eq.) and tyramine hydrochloride (21.6 eq.) dissolved in distilled water with a tenfold-lower volume solution of 1-Ethyl-3-[3-(dimethylamino)propyl]carbodiimide (EDC, 4 eq.) and 1-hydroxybenzotriazole (HOBt, 4 eq.) dissolved in a 1:1 mixture of dimethylsulfoxide:distilled water [74]. The reaction pH was adjusted to 6.8 using 0.1 M sodium hydroxide and mixed for 48 h before purification by dialysis (MWCO = 3500 Da). The degree of Tyr conjugated to HA repeating units was found to be 92%. A 6.25 wt.% Gtn aqueous solution was then added to the reaction mixture, which was stirred overnight at pH 4.7, and the final product was purified by dialysis. Based on these studies, Gtn is coupled to HPA approximately 1 out of every 100 amino acids and HA is coupled to Tyr approximately 6 out of every 100 repeat units. Consequently, HA expresses approximately two times as many phenolic hydroxyl groups from synthetic modification as Gtn on a molar basis.

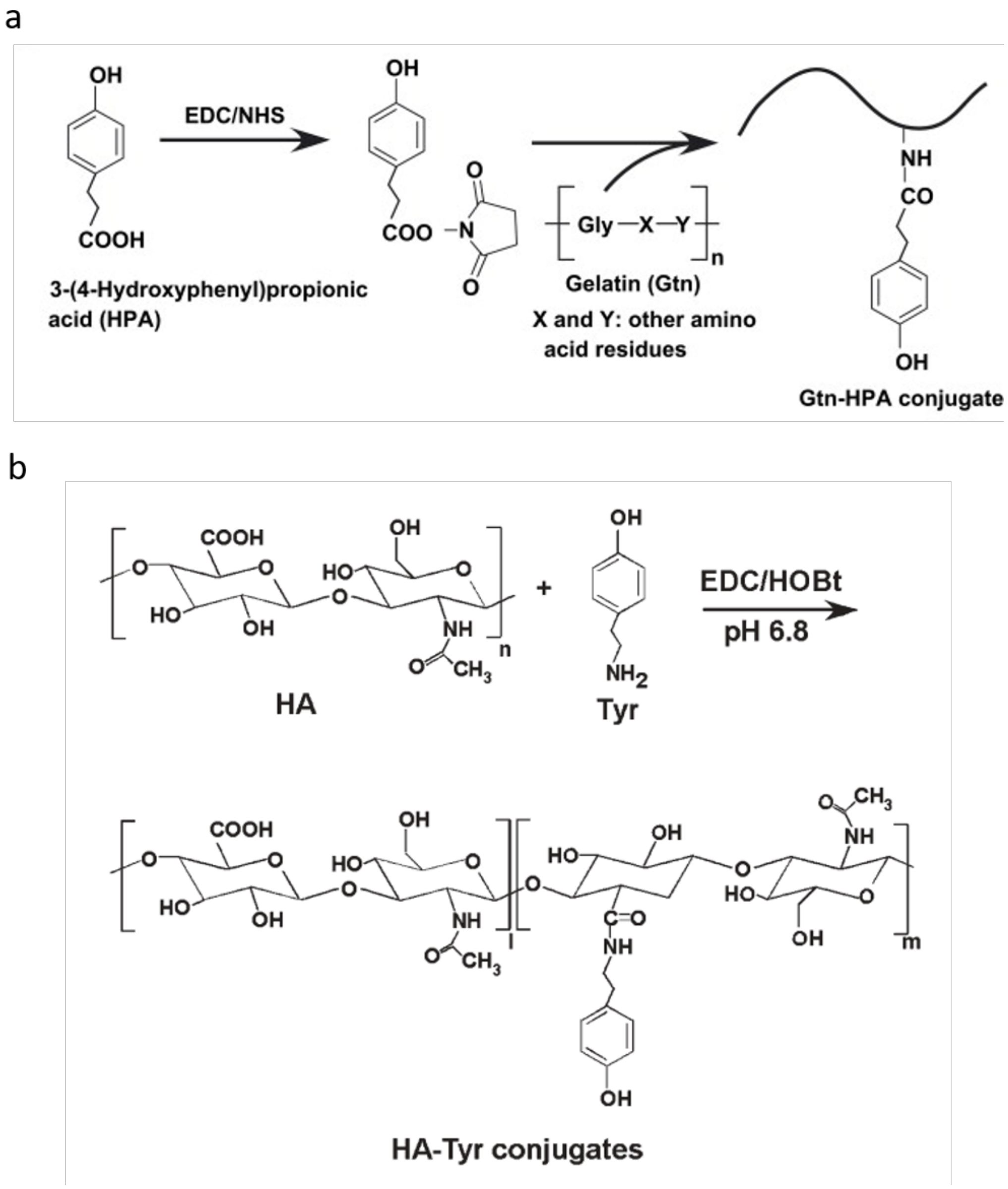

Figure 1.7: Schematic of the synthetic pathway to conjugate HPA to gelatin and Tyr to HA.
Image reprinted with permission from **(a)** Wang et al. [73] and **(b)** Kurisawa et al. [74].

Complete characterization of solid polymers (Gtn-HPA and HA-Tyr), hydrogels and copolymeric networks was performed as seen in Table 1.4. Number (Mn) and weight (Mw) averaged molecular weight, glass transition temperature (Tg) and melt-

Table 1.4: Full characterization of Gtn-HPA/HA-Tyr polymers and hydrogels.

Gels	**wt%**	**G' (Pa)**	**E (Pa)**	**Gel Point (s)**	**Time to plateau (s)**
Gtn-HPA	2	578 ± 32	2532 ± 20	42.5	220 ± 18
IPN75	2	835 ± 26	3101 ± 24	151	479 ± 10
IPN50	2	1072 ± 29	4316 ± 39	167	888 ± 9
HA-Tyr	2	1438 ± 13	6818 ± 76	273	1463 ± 5
Polymers	**wt%**	**Mn (kg/mol)**	**Mw (kg/mol)**	**Tg (C)**	**Tm (C)**
Gtn-HPA	Solid	18,000 ± 40	64,500 ± 75	140 ± 1	167 ± 2
HA-Tyr	Solid	68,000 ± 55	153,700 ± 20	148 ± 2	188 ±1

ing temperature (Tm) were measured with respectively gel permeation chromatography (GPC) and differential scanning calorimetry (DSC). As seen in Figure 1.8a, a clear glass transition and melting transition were observed. However, differing from usual DSC experiments, both samples were destructured post melting and could not be brought back to its initial shapes. Molecular weights measures were fitted with a normalized gaussian curve showing higher molecular weight for HA-Tyr than Gtn-HPA. Some peaks were seen at really low weight (<5,000 g/mol) for both samples resulting from the presence of both HPA and Tyramine groups.

1.5.3 Injectable properties

The HPA and tyramine moieties can undergo peroxidase-mediated covalent crosslinking to transform an initially liquid formulation into a solid biomaterial: the in-situ crosslinking mechanism (Figure 1.9). The specific peroxidase employed for this process is horseradish peroxidase (HRP), and the catalyst is hydrogen peroxide (H_2O_2); both reagents are used in small amounts that have not been shown to be toxic in vitro or in vivo [75].

This in-situ crosslinking mechanism offers the possibility to inject encapsulated cells in the retina with as little trauma as possible. Many studies have shown that transplanted sheet of cells in pre-formed scaffolds has great regenerating potential

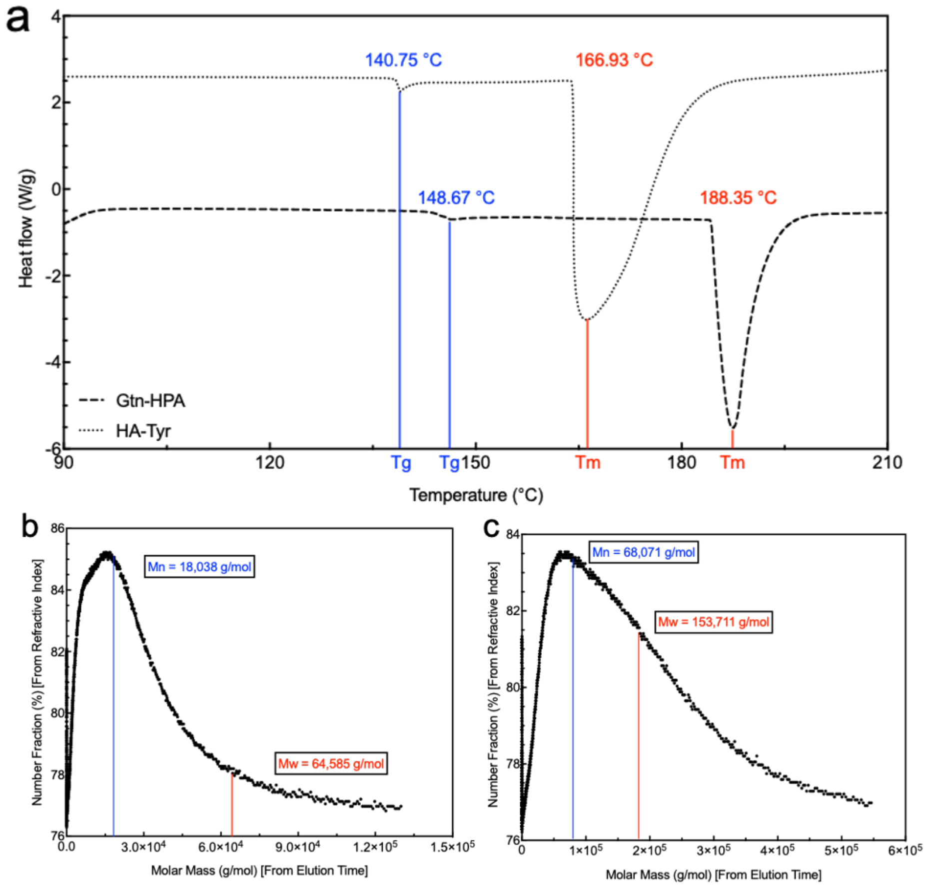

Figure 1.8: Transition temperatures and molecular weight characterizations of dry polymers.
(a) Differential scanning calorimetry measurements of solid Gtn-HPA (dashed line) and HA-Tyr (dotted line) polymers. Glass temperature (Tg in blue) and melting temperature (Tm in red) are represented with vertical lines with their values for both polymers. **(b, c)** Gel permeation chromatography measurements of solid Gtn-HPA and HA-Tyr polymers. Number average (Mn in blue) and weight average (Mw) molecular weight were calculated (see methods) and represented on both graphs.

however the trauma of injection could potentially be a factor for the non-optimal results found [76]. While HRP is derived from horseradish root, it is noteworthy that the enzyme shares a very similar active site with hemoglobin, catalase, and human peroxidases. Regarding the use of hydrogen peroxide, which is known to cause cell apoptosis, prior in vitro studies [77] have demonstrated that the low concentration of hydrogen peroxide used to initiate crosslinking doesn't affect cell viability. The effect will be analyzed in more depth in this thesis.

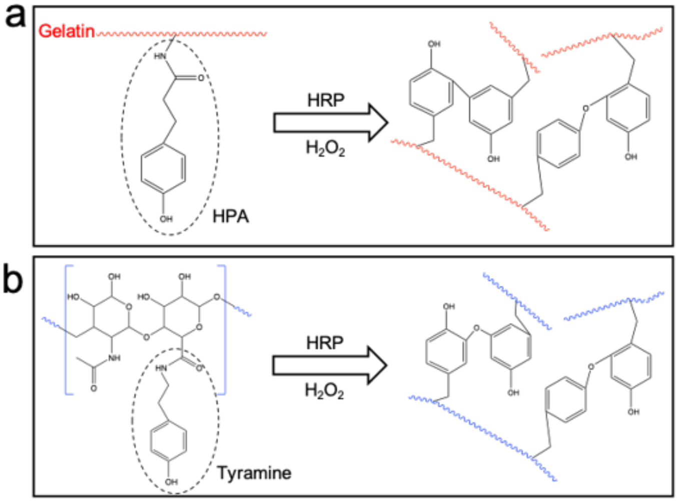

Figure 1.9: Schematic of the covalent crosslinking of Gtn-HPA and HA-Tyr.
The phenol moieties of **(a)** HPA and **(b)** Tyr upon addition of the HRP catalyst and H_2O_2 crosslink Gtn-HPA and HA-Tyr into hydrogels.

1.5.4 Mechanism of degradation in the eye

Studies have found the total degradation of Gtn-HPA by collagenase (MMP-1) and HA-Tyr by hyaluronidase [78]. Since MMPs, collagenase and hyaluronidase are found not only in the vitreous but also in the ECM of the retina to degrade extracellular matrix in normal physiological processes, Gtn-HPA/HA-Tyr can be degraded in the eye without further modification. Most of the biproducts of Gtn-HPA and HA-Tyr, after degradation by enzymes, are collagen, HA or amino acid (HPA and tyramine) based. These byproducts are non-toxic giving the ability for our biomaterials to be biocompatible.

1.6 The proposed therapeutic approach

During the early or late stage of retinal diseases (e.g., AMD or RP) the key problematic area is: the death of photoreceptor cells in a cascade which leads to partial or total loss of vision. Given the previous studies performed with different types of retinal stem cells and their results in terms of engraftment of these cells in either the outer nuclear layer (ONL) or in the retinal ganglion cells layer (RGC), the therapeutic strategy (Figure 1.10) is to inject Gtn-HPA/HA-Tyr encapsulating retinal progenitor cells (either photoreceptor progenitors or ganglion cells progenitors) and growth factors (e.g., EGF or FGF) into the subretinal space (for photoreceptors) or the vitreous (for RGC) to promote the viability, release, engraftment and correct architecture of injected exogeneous cells offering the possibility of regenerating the entire photoreceptor (or RGC) layer. This would lead to the advancement of new compensatory connections between the intact, surviving host tissue and the exogenous cells.

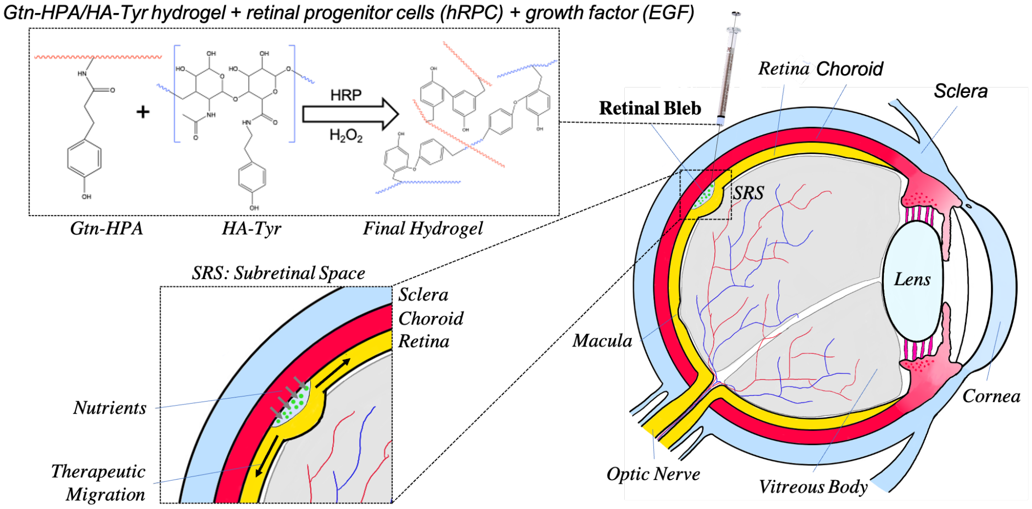

Figure 1.10: Schematic of the proposed therapeutic approach.
Retinal progenitor cells (hRPCs) and growth factor (EGF) are mixed with liquid solutions of Gtn-HPA and HA-Tyr. As soon as the catalyst (HRP) and crosslinker(H_2O_2) are added, the final therapeutic is injected into the subretinal space of patients through the sclera and the retina with a 31-gauge needle. This create a retinal bleb which contains the final solid hydrogel encapsulating cells and growth factors. This therapeutic then migrates along the retina, releasing cells to engraft in the host tissue.

Many cell types have been isolated and injected in the retina to promote cell replacement [79], however, only a few have been able to either show functionality or even be in clinical trial. In our work we have focused on two different cell line: human retinal progenitor cells (hRPC from ReNeuron) which are in clinical trial phase 2 and have been shown to be able to replace dead photoreceptor cells in the retina of RP patients [53]; and human retinal ganglion cells (isolated and purified in Dr. Don Zack laboratory at John Hopkins) which have been shown to fully attach and replace an entire layer of RGC in the disease retina [80].

EGF and FGF are selected as growth factors to be encapsulated based not only on their presence in high concentration in most retinal progenitor cells media [81] but also based on prior in vitro study in which the use of these factors enabled a higher viability, proliferation and functionality of many different retinal progenitor cell lines. In one study [82], the effect of the EGF receptor (EGFR) was analyzed to prove its function of maintenance of normal levels of progenitor cells in the retina. Mice with homozygous deletion of the EGFR gene were found to have a reduced proliferation. Moreover, following retinal damage from continuous light exposure, the EGFR expression was upregulated resulting in a renewed mitotic response to EGF. This study suggests that the use and encapsulation of EGF could enable exogeneous cells to thrive and increase their proliferation in vivo even after retinal damage.

Many studies have shown the potential of a pre-formed cell seeded scaffold on the enhancement of cell migration, viability, engraftment and final architecture in certain types of retinal diseases. One problem which could be solved with the injection of Gtn-HPA/HA-Tyr encapsulating cells is the trauma of insertion of pre-formed scaffold by the fact that our biomaterial is an injectable in-situ crosslinking hydrogel. Studies using pre-formed scaffold have shown retinal damage and a high immune response due to the trauma of insertion and the presence of those scaffolds for long time in the retina. To counteract this effect, Gtn-HPA/HA-Tyr will be tuned to be injectable with a degradation constant relatively fast to provoke as little immune response as possible while enhancing cell replacement.

Using naturally derived polymers has advantages and downfall. For the most part, all the degradation components are biocompatible and can be fully degraded by the body enzymes [83]; in our case the eye or vitreous which already contains gelatin and hyaluronic acid [84]. However, due to the close chemistry of our biomaterials to the polymers already present in the eye, naturally derived polymers could induce a higher immune response compared to synthetic polymers which would not be targeted by the immune system. These data support the strategy of incorporating cells and EGF in natural-synthetic derived polymeric combination to enhance retinal regeneration. The approach for testing the therapeutic strategy of Gtn-HPA/HA-Tyr incorporating EGF and retinal progenitor cells is summarized in Figure 1.11.

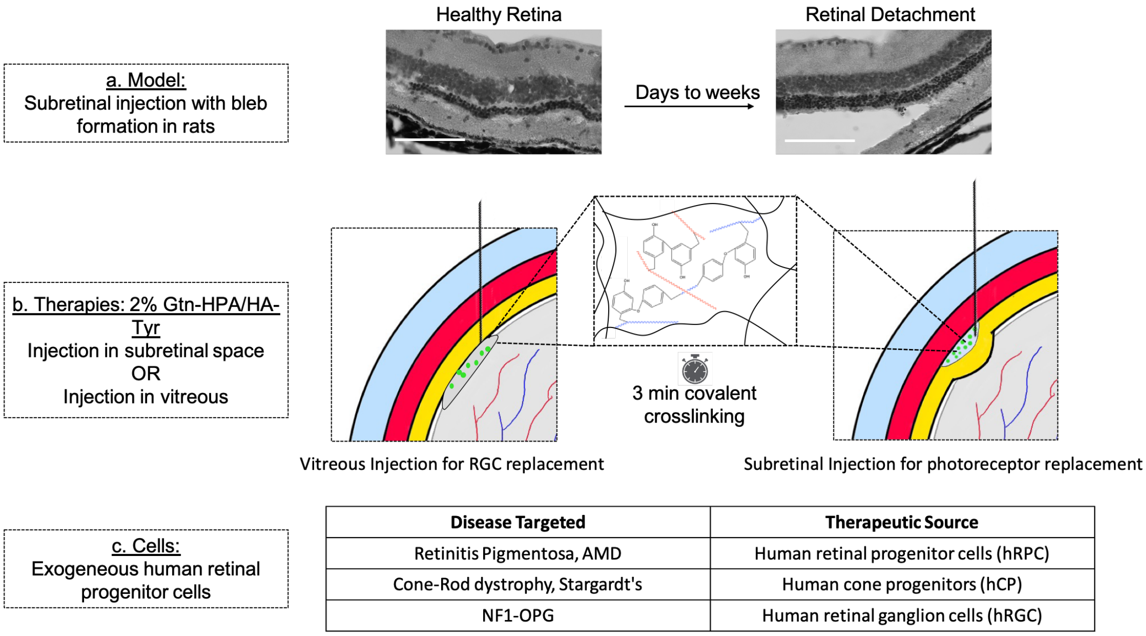

Disease Targeted	Therapeutic Source
Retinitis Pigmentosa, AMD	Human retinal progenitor cells (hRPC)
Cone-Rod dystrophy, Stargardt's	Human cone progenitors (hCP)
NF1-OPG	Human retinal ganglion cells (hRGC)

Figure 1.11: Approach to test the therapeutic strategy of Gtn-HPA/HA-Tyr.
(a) The animal model used is a subretinal injection with bleb formation in rats which creates a model a retinal detachment (RD) days to weeks post-transplantation. **(b)** Therapeutics include 2 wt% Gtn-HPA and HA-Tyr (or their mix) encapsulating hRPC (in the subretinal space) or hRGC (invitreal) with an approximate 3 min in-situ covalent crosslinking. **(c)** Different cell types (exogeneous human retinal progenitor cells) are used to target specific diseases.

.

1.7 Thesis Aims

1.7.1 Engineering a bio-inspired matrix for retinal regeneration

The principal objective of this thesis was to create evaluate the ability of an injectable, gelatin and hyaluronic acid-based biomaterial (gelatin-hydroxyphenyl propionic acid, Gtn-HPA, hyaluronic acid-tyramine, HA-Tyr, or the mix of both) incorporating different growth factor (EGF, FGF) to enhance the viability, attachment, release and engraftment of encapsulated and injected stem cells (human retinal progenitor cells, hRPC, human retinal ganglion cells, hRGC) in order to enable retinal regeneration in the case of different retinal diseases (Retinitis pigmentosa, RP, cone-rod dystrophy, or neurofibromatosis type 1 optic pathway glioma, NF1-OPG).

1.7.2 Analyzing and measuring the effect of gels on retinal stem cells

In a second objective, the mechanical and chemical effect of our biomaterials in vitro on different retinal cells was analyzed and measured. We analyzed the effect of the covalent crosslinking of our hydrogels, its stiffness, mechanical effect and chemical effect on the viability, phenotype, diffusion, release and protection of human retinal progenitor cells.

1.7.3 Optimizing retinal cell culture and animal model (NF1-OPG)

Enhancing retinal regeneration by the addition of a biomaterials is necessary but not sufficient. The third objective was to successfully optimize retinal cell culture and create novel animal models which could be faster than traditionally used for NF1-OPG.

1.7.4 Creating new clinical therapies for treating retinal diseases

Despite years of research, a pure population of cone photoreceptors has not been achieved. The fourth objective, towards clinical translation and novel therapies, was to capture this rare cell population and identify the conditions in which it can be cultured and remain functional to treat various retinal diseases.

Chapter 2

Materials testing and first results

2.1 Materials and Methods

2.1.1 Transition temperatures and molecular weights testing

All materials were analyzed using a differential scanning calorimeter (DSC 250) (TA Instruments, New Castle, USA). Polymer powders (Gtn-HPA and HA-Tyr) were analyzed from 20 to 250 °C at a heating speed of 10 °C/min. Glass transition was observed by measuring the derivative of heat flow and melting temperature was a peak above the glass temperature.

Gel permeation chromatography was performed at 35°C with a Malvern Viscotek VE 2001 GPC max UV 2501 detector, a TDA 301 chromatography system and a PL aquagel-OH MIXED-M column (Agilent). Samples were run at 1 mg/ml through a mobile phase comprised of 10mM sodium phosphate monobasic (Macron Chemicals), 100mM sodium nitrate (Sigma Aldrich), 20%wt/ml methanol (Sigma Aldrich), adjusted to pH 7.4. HA-Tyr and Gtn-HPA were dissolved in 2 ml of the mobile phase, at a concentration of 10%wt/ml, by thoroughly mixing and incubating samples for 1h at 37 C. Molecular weights were then referenced against polyethylene glycol standards (Waters). Molecular weight parameters (Mw, Mn, P, and MWD) were calculated for standards and samples using the respective GPC calibration equation: $\mathrm{Log(Mn)} = \mathrm{Ao} + \mathrm{A1}^{*}\mathrm{Vp}$, where Mn is the molecular weight, Vp is the eluded volume, Ao=10.2086 and A1=-0.7604. Chromatogram heights were measured at retention times of interval 0.5 minutes.

2.1.2 Compression test study

Unconfined compression tests were performed using a Zwick/Roell Z2.5 static materials tester (Zwick GmbH & Co., Ulm, Germany) with integrated testing software (testXpert, Zwick). 1 ml of Gtn-HPA, IPN50, IPN75 and HA-Tyr were prepared into 24-well plates to create samples 16 mm in diameter and 3-4 mm in thickness. All hydrogels were left to fully crosslink and stabilize for 2 hours at 37C before performing compression testing. All gels were swelled in PBS for 1 hour before compression testing. Mechanical tests were performed at a constant strain rate of 0.5%/s to a maximum strain of 10% using a 20 N load cell (Part No. BTC-LC0020N.P01, Zwick) sampling at a frequency of 2 Hz. The diameter of the samples at the start of the testing was measured using digital calipers. The compressive modulus was determined by the slope of the true stress-strain curve within the linear regime of the material (0-7%).

2.1.3 Fourier transform infrared (FTIR) spectroscopy analysis

Fourier transform infrared (FTIR) spectrum was recorded to detect the chemical and structural nature of Gtn-HPA powder, HA-Tyr powder and dried hydrogels (Gtn-HPA, IPN75, IPN50, HA-Tyr), using a Thermo Fisher FTIR6700 spectrometer. Samples were characterized using attenuated total reflection (ATR) mode for a total of 32 scans in the range of 500-4000 cm^{-1}. FTIR baseline was applied and normalization was performed with respect to the characteristic backbone peak (around 1600 cm-1 for Gtn-HPA and 1000 cm-1 for HA-Tyr). For dried hydrogels spectra, 10 ml of each sample was prepared at a concentration of 10wt%/ml, casted into a 5cm petri dish. Samples were left to dry overnight in a low oxygen incubator (37 °C, 5% O_2 and 5% CO_2).

2.1.4 In vitro degradation assays for hydrogels

200 µl gels (Gtn-HPA, IPN75, IPN50, IPN25 and HA-Tyr) were prepared as previously described and incubated for 30 min at 37 °C to reach stability. Samples were then combined with 200 µl of phosphate-buffered saline (PBS) containing 1000 U/ml type IV collagenase (Invitrogen) or containing 500 U/ml hyaluronidase type I-S (Sigma-Aldrich) and incubated at 37 °C on an orbital shaker at 150 rpm. Samples were collected every 5 or 10 minutes for 1 or 2 hours, for collagenase or hyaluronidase treatments respectively, and analyzed for degradation products using the bicinchoninic assay (Thermo Fisher Scientific). In order to model and replicate the in vivo conditions, slow degradation assays were also performed. 200 µl of the injected hydrogels (Gtn-HPA, IPN75 and IPN50) were prepared and incubated for 1h at 37 °C to reach stability. As suggested and explained in [85], [86], the actual concentration of collagenase (coming from MMPs) and hyaluronidase (intrinsic in the vitreous) are respectively 0.5 U/ml and 0.3 U/ml in vivo. 5 ml of the enzymes with these concentrations were used, mixed and added to the hydrogel samples. Samples were kept in incubators, collected every day for 9 days and analyzed for degradation products using the bicinchoninic assay. Degradation rate constants were derived by fitting the data for mass loss into an inverse exponential model.

2.2 Broad testing of materials

One critically important feature of Gtn-HPA and HA-Tyr hydrogels -specific to its use in retinal therapies- is the possible encapsulation of retinal progenitor cells to enhance their viability, phenotype, proliferation, and differentiation in vitro and in vivo. Many studies have shown the cell encapsulation potential of Gtn-HPA and HA-Tyr with many other cell types. Adult neural stem cells (NSCs) isolated from adult rat hippocampus were shown to differentiate into both types of the neural elements (neurons and glia) [87]. Gtn-HPA hydrogel has been shown to protect adult neural stem cells embedded in it from oxidative stress by the addition of increasing amounts of H_2O_2. Gtn-HPA and HA-Tyr have also been shown to maintain high cell viability of a variety of cell types including MSCs, ESCs, hRPCs [73], [74].

To analyze in more depth the effect of Gtn-HPA and HA-Tyr on cell encapsulation different biomaterials and potential candidates for the enhancement of retinal stem cell injections have been tested on human retinal progenitor cells. Gtn-HPA and HA-Tyr were used at the same 2%wt for all experiments: first dissolved polymers were catalyzed with horseradish peroxidase (HRP) then crosslinked with hydrogen peroxide (H_2O_2). Both form a stable hydrogel within 20 mins at 37 °C. Due to its high tunability, high molecular weight (around 10^6Da) hyaluronic acid was also tested at various weight percentages. Dissolved polymer was mixed with cells at room temperature and physical crosslinking (chain entanglement) occurred after a few minutes. Because the composition of the retina is partly collagen, a hydrogel of 2%wt collagen crosslinked with different concentrations of genipin was also prepared (Figure 2.1a). Finally, a mix of Gtn-HPA and HA-Tyr was also used with different content of gelatin in the mix (Figure 2.1b).

To determine the degree to which cell viability was maintained through the covalent crosslinking process, human retinal progenitor cells (hRPC) were incorporated into the candidate gel formulations without media and cultured for 2 days. A live and dead cell assay was then performed and the number of live/dead cells (hence viability percentage) was measured for each sample and compared to cells in 2D control culture with (media) and without (phosphate buffer saline: PBS) nutrients. Figure 2.1c summarizes this viability data (mean+/- standard error of the mean) with our negative monolayer control in PBS having only 26.5% viable cells and our positive monolayer control with medium having 91.5% viability (being significantly higher than all candidates deprived from nutrients). A threshold of 55% viability was applied to consider any sample biocompatible. Collagen-genipin (CG) hydrogel samples (averaged for all genipin concentrations) showed the lowest viability of incorporated cells, due to the fragility of retinal cells and the relatively high cytotoxicity of genipin needed to produce a stable hydrogel. Due to its high molecular weight and high stiffness, HA alone showed really low viability after 2 days, even lower than PBS. By reducing the percentage of HA and using the chemically induced crosslinking HA-Tyr viability

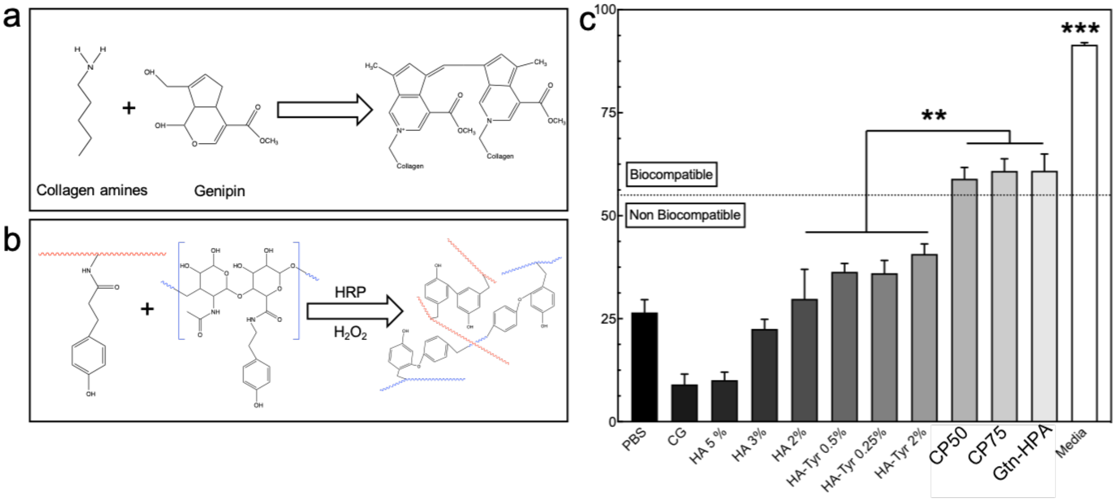

Figure 2.1: Chemical structures and biocompatibility assay of potential bioinspired hydrogels.
Chemical structure and crosslinking reaction for Collagen-genipin **(a)** and copolymeric network of Gtn-HPA and HA-Tyr **(b)**. Gelatin chemical structure is approximated with red-lines and hyaluronic acid backbone with blue lines. **(c)** Viability assay of human retinal progenitor cells in potential hydrogels to enable biocompatibility measurement. Biocompatibility threshold was placed at 55% (dotted line). Data shown as mean ± SEM of triplicate wells with 15 different fields for each well. One-way ANOVA, followed by Tukey's test, was performed and shows a statistically high significant difference between media and all other groups (***p=0.0001), being our positive control. Significant increase of viability can be seen biocompatible hydrogels (CP50, CP75 and Gtn-HPA) compared to all others (**p=0.001).

reached 37-39%. By mixing HA-Tyr and Gtn-HPA at different quantities (CP50 with 50% of each and CP75 with 75% of Gtn-HPA and 25% of HA-Tyr), viability was higher than the other groups: reaching respectively 59% and 61%. Finally, Gtn-HPA alone showed the highest viability result, being the most biocompatible polymer, with 61.2%. There was no statistical difference found between the three highest candidates (CP50, CP75 and Gtn-HPA), however they were significantly higher than all other hydrogels and PBS. The hydrogel candidates showing high biocompatibility within a first short-term viability test were Gtn-HPA and copolymeric networks made of various content of Gtn-HPA and HA-Tyr.

2.3 First results: Creation of an interpenetrating network (IPN)

The development of a bioinspired gel with suitable characteristics for encapsulating cells and intravitreal and subretinal injection (Figure 2.2) was initiated by an evaluation of the make-up of the vitreous and ECM of the retina. As explained previously, the ECM of the retina is made of:

- 1/2 fibers (collagen, elastin)
- 1/4 non-proteoglycans polysaccharides (Hyaluronic acid)
- 1/4 proteoglycans (chondroitin sulfate)
- Other proteins (fibronectin, fibrillin, laminins, and fibulins)
- Growth factors, proteases (MMPs), and regulators

The physical and mechanical properties needed for such a biomaterial are as follow:

- Biocompatibility and Biodegradability for transplant.
- Injectable/implantable polymers.
- Enable cell attachment/migration
- Can mimic the tissue they are implanted.
- Stiffness needs to be studied (Retina E=20kPa, Vitreous E=50 Pa).

In our hydrogel mix, HA-Tyr brings most optimal mechanical properties, stiffness, surgical tunability and retinal attachment while Gtn-HPA brings the biocompatibility, cell survival, attachment and biodegradability constants. To better understand the chemical and functional structure of our hydrogels we first analyzed the basic mechanism of crosslinking process of Gtn-HPA/HA-Tyr. For our system, both the Gtn-HPA and HA-Tyr networks are in-situ enzymatically crosslinked with horseradish peroxidase (HRP) and H_2O_2 [88]. Our first goal was to explore if there was any observable

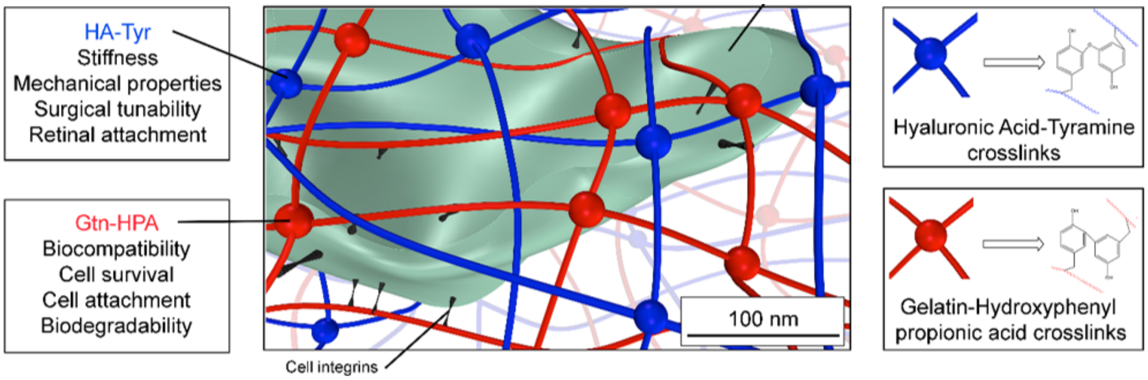

Figure 2.2: The Gelatin and Hyaluronic Acid network system and its crosslinks.
Schematic and 3D model of a human cell encapsulated in the network made of Gelatin-HPA (red) and HA-Tyr (blue) with integrins bonding to Gtn-HPA only (black). Legends shows the two different crosslinks with their respective chemical structures.

selectivity in the crosslinking. If there was, we expected to obtain a hybrid interpenetrating network (IPN) [89] instead of a random heteropolymer network. Our results showed that the crosslinking is very specific to the respective polymer. As seen in Figure 2.2, Gtn-HPA mostly crosslinks with itself (red crosslinks) and HA-Tyr with itself (blue crosslinks). To prove this, we prepared networks with varying percentages of Gtn-HPA and HA-Tyr (from 100% Gtn-HPA to 100% HA-Tyr) and enzymatically degraded them with collagenase and hyaluronidase [90]. As seen in Figure 2.3, applying either collagenase or hyaluronidase treatment degrades the exact proportion of Gtn-HPA or HA-Tyr, respectively, that was used in the preparation of network: e.g. IPN75 (containing 75% of Gtn-HPA and 25% of HA-Tyr) demonstrated a mass loss of 75% when mixed with collagenase and a mass loss of 25% when mixed with hyaluronidase. Complete degradation was observed on homopolymeric networks combined with their respective enzymes.

To confirm these findings, we performed Fourier transform infrared spectroscopy (FTIR) on all samples. The FTIR spectrum of the Gtn-HPA and HA-Tyr non-crosslinked solid polymers are shown in Figure 2.4a.

A number of bands around 1390 cm^{-1} are attributed to the presence of type-I Gelatin [91], proving the provenance of our material. Hyaluronic acid presence is

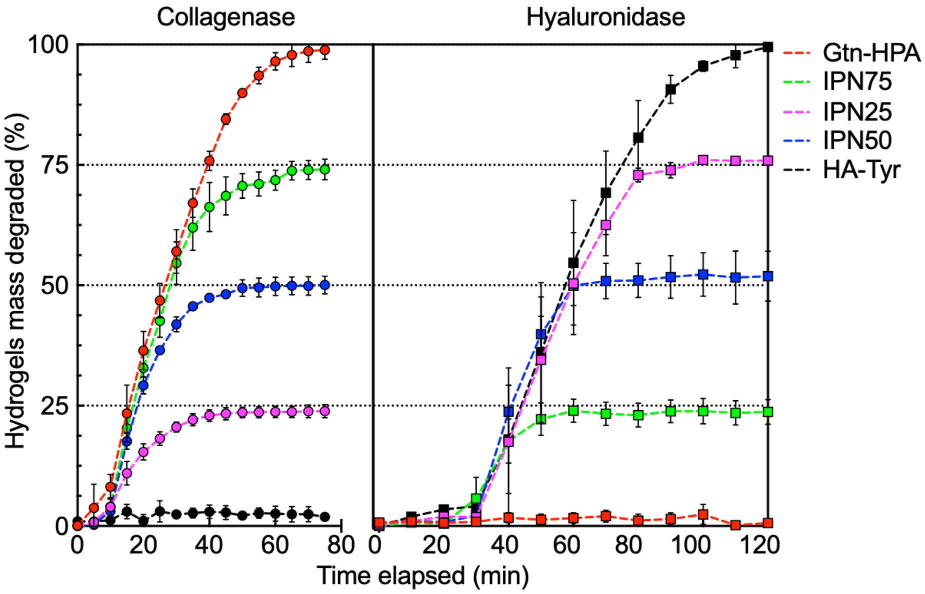

Figure 2.3: Degradation assay of Gtn-HPA and HA-Tyr IPNs.
Hydrogels' degradation assays performed with Collagenase and Hyaluronidase treatment for Gtn-HPA (red), IPN75 (green), IPN50 (blue), IPN25 (pink) and HA-Tyr (black). Degradation assay, comprising n=15 replicates, was measured every 5 min with collagenase and every 10 min with Hyaluronidase.

observed in the band at 1409 cm^{-1} which can be attributed to the stretching of COO^{-}, referring to the acid group in the HA molecule [92]. The absorption band at 1036 cm^{-1} is attributed to the linkage stretching of C-OH and finally, the stretching region of the protonated group COOH is observed at 1078 cm^{-1}. The amide A band arising from N-H stretching was distributed at 3308 and 3277 cm^{-1}, C-H stretching at 2945 and 2912 cm^{-1} for the amide B, N-H deformation at 1539 and 1574 cm^{-1} for the amide II respectively for Gtn-HPA and HA-Tyr. C $=$ O stretching at 1609 cm^{-1} for the amide I can be observed in HA-Tyr while the amide III can be seen at 1237 cm^{-1} for Gtn-HPA. The presence of HPA side group can be seen by the peaks at 1452, 1633 and 3085 cm^{-1} while Tyramine is visible at 1378 and 3085 cm^{-1}.

To quantify crosslinking reactions between HPA and Tyramine groups in both homopolymeric networks and IPN we measured the FTIR spectra of dry gels (Figure 2.4b). The appearance of a difference in transmission around 1000 cm^{-1} indicates the stretching of COO- groups and therefore the presence of hyaluronic acid, which is

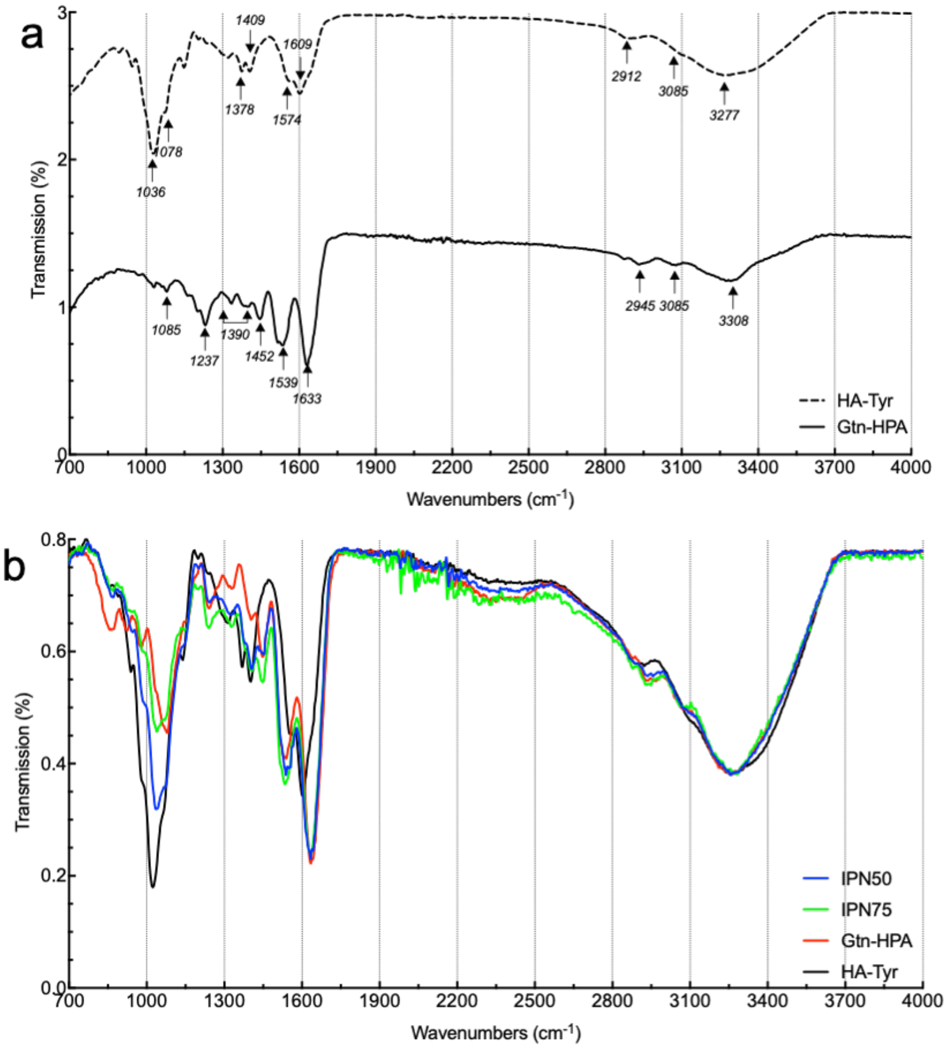

Figure 2.4: Fourier-transform infrared spectroscopy (FTIR) analysis of hydrogels and polymers.
FTIR data of solid Gtn-HPA and HA-Tyr polymers **(a)**, and dry hydrogels (Gtn-HPA, HA-Tyr, IPN75 and IPN50) **(b)** shown as baseline corrected and normalized transmission percentage in function of wavenumbers. For more visibility, polymer samples were spaced in the graph. Specific wavenumbers are marked with arrows and their value and normalized transmission percentage in function of wavenumbers.

shown to be increasing from IPN75 to IPN50 to HA-Tyr. Both side groups HPA and Tyramine have specific peaks respectively around 1600 and 1300 cm^{-1} in the non-crosslinked polymers. In IPN and hydrogels, an increase in transmission percentage can be seen for the HPA peak while a decrease is observed for the Tyramine peak from HA-Tyr to Gtn-HPA. Gtn-HPA doesn't show any transmission around Tyramine peak but IPN transmission is relatively close to HA-Tyr. At HPA peak, HA-Tyr is significantly lower than all others while both IPN are close to Gtn-HPA. The similar transmission seen in homopolymeric networks side groups and IPN suggest a strong selectivity in crosslinks and the formation of a hybrid IPN.

Proving the formation of either a hybrid interpenetrating network (IPN) or random copolymer network was critical in terms of in vivo degradation kinetics and cell encapsulation. The result presented here suggests a strong crosslinks selectivity producing a hybrid IPN hydrogel.

Chapter 3

In vitro effect of Gtn-HPA & HA-Tyr on human retinal stem cells

3.1 Introduction

One of the first objective of this thesis was to evaluate the fate of human retinal stem cells encapsulated in gelatin- (Gtn-Hydroxyphenyl propionic acid) and hyaluronic acid-based (HA-Tyramine) biomaterials and investigate their potential use as biodegradable delivery vehicle for retinal regeneration therapies. The aim of this study is to explore the use of a hydrogel as a “protective envelope” for cells that experience high stress. To achieve this goal, we cultured and encapsulated human retinal progenitor cells (hRPCs), which have demonstrated the ability to survive, differentiate and, engraft into the host retina, inside Gtn-HPA and Ha-Tyr based hydrogels. We analyzed, throughout time, their viability and phenotype, while subjecting them the different stresses [93], [94] (pressure exposure, shear stress, oxidative stress, deprivation of nutrients). One of the highest stress that can potentially affect the cells viability inside the syringe is the shear stress due to the flow of liquid through the small bore needle during injection [93]. Human retinal progenitor cells (hRPCs) are in clinical trials and well characterized cells hence any change in the cell phenotype can be easily documented.

Moreover, we analyzed the diffusion properties of Gtn-HPA and HA-Tyr, and their mix, by measuring and analytically calculating the release of growth factors (Human Fibroblast growth factor-hFGF, Human Epidermal growth factor-hEGF) from the biomaterials. hEGF is a known factor promoting and regulating proliferation and differentiation of retinal stem cells [82], [95]. Understanding the effect that the water content of injectable hydrogels has on the diffusion of molecules and cell communications is of utmost importance to improve possible treatments involving drug delivery in regenerative medicine, especially as it relates to retinal disease therapeutics [96].

Only hRPCs encapsulated in hydrogels with high content of Gtn-HPA showed high viability, controlled phenotype (with the addition of hEGF in the mix) and critical resistance to oxidative and shear stress. The analysis of growth factor diffusion enabled for a better understanding of the hydrogels' water content properties and their possible use as drug delivery vehicles.

3.2 Experimental design and theory

3.2.1 Experimental groups

The effect of Gtn-HPA, HA-Tyr and IPN hydrogels on hRPCs was observed by designing multiple experiments with different culture conditions, as seen in Figure 3.1. UC depict just the base Ultraculture medium. SS stands for shear stress which was applied with a 31-gauge needle.

To further analyze the impact and effect of our hydrogels (Gtn-HPA, HA-Tyr and IPNs) on hRPCs we designed an experiment by encapsulating hRPCs in different hydrogels (modulating the content of Gelatin in the mix) and adding different growth factor to promote cell growth and viability. For this purpose, as seen in Figure 16b, we cultured hRPCs for 14 days, adding different growth factor (base media deprived from growth factors, adding EGF, FGF or both), either in 2D culture on T75 flasks or encapsulated in hydrogels (Gtn-HPA, IPN25, IPN50, IPN75 and HA-Tyr). We analyzed hRPCs viability, proliferation, and phenotype throughout the experiment at day 1, 4, 7, 11 and 14.

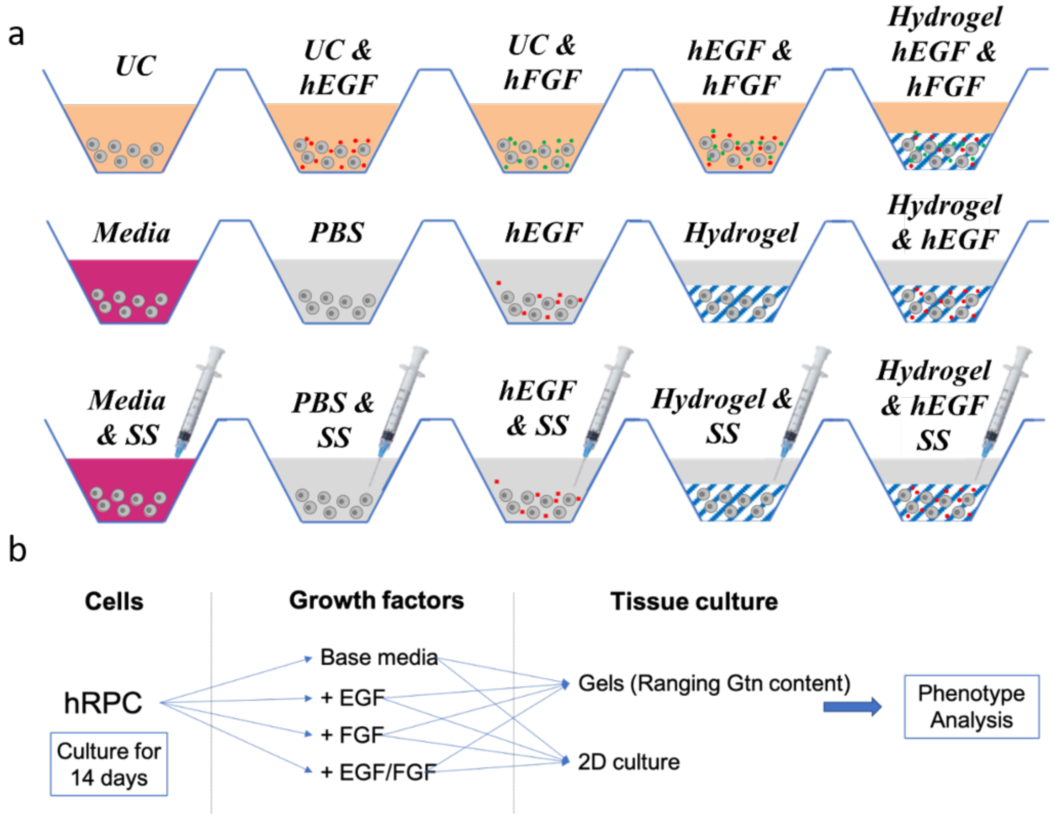

Figure 3.1: Experiment setup to test the effect of Gtn-HPA on hRPCs. **(a)** hRPCs were cultured for 14 days in different conditions: in PBS, Ultraculture base media (UC), in media including growth factors, with hEGF, with hFGF, in hydrogels, or with shear stress (SS) applied using a 31-gauge needle. **(b)** hRPCs cultured for 14 days in different media and tissue culture were then analyzed for their phenotype with flow cytometry and immunocytochemistry.

3.2.2 Shear stress measurement and calculation

Human retinal progenitor cells (hRPCs) were seeded onto fibronectin coated 6-well plate at 10^5/ml with 500 µl of culture medium (Ultraculture, hEGF, hFGF, Primocin, L-Glutamine), PBS, 20 ng/ml recombinant human epidermal growth factor (hEGF) diluted in PBS, 2wt% Gtn-HPA (crosslinked at 1 mM of H_2O_2) or 2wt% Gtn-HPA with 20 ng/ml hEGF. To mimic the shear stress exerted during transplantation, two different types of seeding techniques were applied to all these samples: a 200 µl pipette seeding (diameter 1.2 mm, sterile, filtered, polypropylene tips, volume 10-200 µl, length 5 cm, VWR) and a 31-gauge syringe seeding (diameter 0.15 mm, sterile, volume 1cc, length 1.2 cm, BD Biosciences) corresponding to the stressed samples. Gtn-HPA having 30 seconds to 1 min gelation time, HRP and H_2O_2 were added 10 seconds apart to avoid needle clogging. hRPCs in culture medium is used as a control as it represents the ideal culture conditions for these cells. The second control chosen was cells in PBS with shear stress as it mimics the in vivo transplantation in a pre-clinical trial. The number of replicate (including controls) for this experiment was n=4. After 1 day, 3 days and 6 days of incubation at 37 °C and low oxygen (5 % O_2, 5% CO_2) samples were washed and fixed (as described in next sections) to perform Live/Dead, immunohistochemistry and flow cytometry assays.

To further evaluate the protective aspect of Gtn-HPA, a modeling of the shear stress has been performed. Shear stress of a liquid (PBS) in a cylinder (needle) can be modeled by applying the Poiseuille flow equations [97], [98]. This method gives the maximum velocity which is applied to the cells in PBS (or any Newtonian fluid) in the center of the needle. The following equations (eq 3.1) relate the velocity and its maximum to all the others experimental parameters: where ΔP is the pressure applied to the needle, R (=75 µm) is the inner radius of the needle, µl (=1.05mPa.s) is the viscosity of PBS, L (=5cm) is the length of the needle, r (µm) is the distance from the center of the needle and v_l (m/s) is the velocity of the liquid.

$$v_l(r) = \frac{\Delta P * R^2}{4\mu_l L}\left[1 - \left(\frac{r}{R}\right)^2\right], \qquad v_{l,max} = \frac{\Delta P * R^2}{4\mu_l L} \tag{3.1}$$

The maximum velocity is located at the center of the needle (where r=0). To model the shear stress applied to hRPCs, that were embedded in a 2% Gtn-HPA pre-gel solution with a gelation time of 30s to 1min, the previous model had to be slightly modified. Indeed, the hydrogel in the needle is now a non-Newtonian fluid in the process of gelation (its shear modulus and viscosity are increasing throughout the gelation process). To take account of this special property of in-situ hydrogels, the cell-free marginal layer model is the best way to accurately calculate the shear stress applied to hRPCs [99]. This method consists in modeling the pre-gel as a high viscous fluid (located in the center of the needle) and a liquid-like fluid on the borders (similar to PBS). The high viscous fluid part represents the bulk of Gtn-HPA in the process of gelation. This model (eq 3.2 and 3.3) predicts a different velocity profile (in the viscous part of the needle) which is as follow: where δ (= 1-5 µm) is the liquid layer on the border of the needle, µg (mPa.s) is the viscosity of the 2% Gtn-HPA hydrogel and v_g (m/s) is the velocity of the gel.

$$v_g(r) = \frac{\Delta P * R^2}{4\mu_l L}\left[1 - \left(\frac{R-\delta}{R}\right)^2 - \frac{\mu_l}{\mu_g}\left(\frac{r}{R}\right)^2 + \frac{\mu_l}{\mu_g}\left(\frac{R-\delta}{R}\right)^2\right] \tag{3.2}$$

$$v_{g,max} = \frac{\Delta P * R^2}{4\mu_l L}\left[1 - (1 - \frac{\mu_l}{\mu_g})\left(\frac{R-\delta}{R}\right)^2\right] \tag{3.3}$$

The maximum velocity is still located at the center of the needle but is reduced by a factor. The shear rate, shear stress, and strain applied to hRPCs can be calculated by applying certain constitutive laws onto this system [100]. In order to convert the shear stress into the strain applied to the cells, the Young's modulus of the gel (E_g=600 kPa) and the Young's modulus of hRPCs (E_c=1000 kPa) were used [101] (3.4): where $\dot{\gamma}$ (s^{-1}) is the shear rate, τ (mPa) is the shear stress, and ϵ (%) is the strain.

$$\dot{\gamma} = \frac{v_{max}}{R}, \qquad \tau = \mu * \dot{\gamma}, \qquad \epsilon = \frac{\tau}{E} \tag{3.4}$$

These models demonstrate that the final shear stress applied to hRPCs is directly related to the maximum velocity in the needle (located in the center). Therefore, all seeding experiments in vitro and in vivo injections were performed with a constant 10 seconds injection time. This allow for a similar velocity to be applied to all samples (including Gtn-HPA and PBS samples) and enable us to directly compare the shear stress in both PBS and Gtn-HPA samples.

3.2.3 Diffusion theory of small particles through hydrogels

Free Volume theory

To enable the study of diffusion through hydrogels, it is necessary to include the free volume interaction and theory [102]. This theory states that solute diffuses by jumping into voids (in the case of hydrogels, this can be the porous channels) formed in the solvent space by redistributing free volume within the liquid. At any given temperature, the rate of diffusion can be calculated based on the probability of void formation with enough volume to accommodate the solute molecules. In this case, the diffusion coefficient of the solute in liquid at infinite dilution D_0 is expressed as:

$$D_0 = \nu \lambda exp\left(\frac{-\gamma V^*}{V_f}\right) \tag{3.5}$$

where ν is average thermal velocity, λ represents jump length which is approximately equivalent to the solute diameter, V^* is the critical local hole free volume needed for a solute molecule to make the jump into the new void, γ indicates the numerical factor used to correct the overlap of free volume that is available for more than one molecule, and V_f is the average hole free volume in the liquid for per molecule. This theory can be applied to gels by assuming only a small amount of solute might be present so the free volume per molecule could be represented as the free volume per molecule of water within the gel [103]. V_f was changed to $V_{f,w}$, and a free volume fraction of the polymer $V_{f,p}$ is defined, such that within a 3D gel,

$$V_f = (1-\theta)V_{f,w} + \theta V_{f,p} \tag{3.6}$$

where θ denotes the volume fraction of polymer within the gel. In other words, the free volume available for solute diffusion within the gel arises not only from random redistribution of water molecules. However, this unit is small so the free volume available to the solute is simplified to

$$V_f = (1-\theta)V_{f,w} \tag{3.7}$$

Furthermore, the degree of cross-linking also contributes to the diffusion coefficient by modifying the equation further, and if all parameters are considered, there is functional dependency of one parameter on the others. A more complete theory was previously described in [104] and includes all previous modifications and gives a free volume theory for diffusion in the gel (D_g) as

$$\frac{D_g}{D_0} = (1 - k_1 r_s \theta^{0.75}) exp\left(-k_2 r_s^2 \left(\frac{\theta}{1-\theta}\right)\right) \tag{3.8}$$

where k_1 and k_2 are structural constants and r_s is the solute radius. We will be using this free volume theory as a regression and comparison for our experiments.

Hydrodynamic theory

There are two different hydrodynamic theories for diffusion of small molecules in hydrogels: one each for homogeneous hydrogels and heterogeneous hydrogels. Homogeneous hydrogels are made of flexible fibers and usually possess a high-water content, while heterogeneous hydrogels are made of more rigid polymer fibers. However, both theories are based on the Stokes-Einstein equation for solute diffusion [105]. In that case, the diffusion coefficient is given by

$$D_0 = \frac{k_B T}{f} \tag{3.9}$$

where k_B is Boltzmann's constant, T is the temperature, and f is the frictional drag coefficient. As stated above, the theory to measure and calculate the frictional coefficient will be different whether the hydrogel studies are homogeneous or heterogeneous. For homogeneous hydrogels, an equation based on a scaling concept was previously presented that matches well with previous experiments, and which we will use in the next section to compare to our experimental soft hydrogels, [106] which gives solute diffusion in the gel as

$$\frac{D_g}{D_0} = -exp(-k_c r_s \theta^{0.75}) \tag{3.10}$$

where k_c is a constant function of the solvent and polymer. For heterogeneous hydrogels, a more complex mathematical model was obtained by calculating the frictional coefficient of each chain of polymer in the hydrogel and summing them to an effective frictional effect on the movement of the solute [107]. This gives a first order expression of diffusion as

$$\frac{D_e}{D_0} = 1 - \alpha_1\theta^{0.5} - \alpha_2\theta ... \quad with \quad \alpha_1 = r_s\sqrt{r_f} \tag{3.11}$$

in which α_2 is a constant and r_f is the diameter of the polymer fiber. For very rigid chains, this model was previously calculated and will be used for future regression:

$$\frac{D_e}{D_0} = exp\left[-\left(\frac{a\pi L_c N_A}{M_f ln\left(\frac{L_c}{2r_f}\right)}\right) r_s\theta^{0.5}\right] \tag{3.12}$$

where L_c is the length of the polymer, M_f its molecular weight, and N_A is Avogadro's number.

Obstruction theory

The obstruction theory supposes that because of the presence of polymer chains in the hydrogel, there is an increase in the path for solute diffusion transport which lowers the diffusion coefficient in hydrogels with longer or stiffer chains. One of the first theories to be applied in this context was performed by [108] where gels were viewed as a number of cylindrical cells. The average diffusion can be found in each cell by solving Fick's law, $J = -D(\frac{dc}{dx})$ [109]. This model gives, with E_1 being the exponential integral,

$$\frac{D_g}{D_0} = e^{-\alpha} + \alpha^2 e^{\alpha} E_1(2\alpha) \quad where \quad \alpha = \theta\left(\frac{r_s + r_f}{r_f}\right)^2 \tag{3.13}$$

Even when this model provides satisfactory results to explain simulations or experiments, the lack of a Brownian motion variable provides pause for hydrogels with a high-volume fraction of water. By using Brownian motion simulations and regression of the data, this model can be modified to find:

$$\frac{D_g}{D_0} = exp(-0.84\alpha^{1.09}) \tag{3.14}$$

A second, more recent obstruction model was developed where the solute diffusion is considered as a stochastic process [110]. This model, which will also be used to compare our experiments, is expressed as

$$\frac{D_g}{D_0} = exp\left[-\pi\left(\frac{r_s + r_f}{k_s\alpha^{0.5} + r_f}\right)^2\right] \tag{3.15}$$

where k_s is a constant for a given polymer-solvent system.

3.3 Materials and Methods

3.3.1 hRPCs culture

All human material work was performed with the approval of the Institutional Review Board of Harvard Medical School. hRPCs were isolated from human fetal neural retina at 16 weeks' gestation as previously described [111]. Cells were cultured onto fibronectin (Akron)-coated flask (surface 75 cm^2, vented cap, sterile, Nunclon Delta) in Ultraculture medium (Lonza), supplemented with 10 ng/ml recombinant human basic FGF (Peprotech), 2 mM L-glutamine (Invitrogen), 20 ng/ml recombinant human EGF (Peprotech), and 0.4 mM Primocin (Invitrogen) in a low oxygen condition incubator (37 °C, 5% O_2, 5% CO_2, 100% humidity) as a monolayer culture to achieve high density. Upon reaching 80% confluence cells were passaged using 10X TrypZean (Sigma-Aldrich) and HBSS (Hank's Balanced Salt Solution, no calcium, no magnesium, ThermoFisher). Cell number and viability were estimated, after each passage, using Trypan blue (Sigma-Aldrich) and a hemocytometer (Countess™ II FL Automated Cell Counter, Thermo Fischer scientific). Cells were then re-plated onto a fibronectin coated T75 surface at a density of 15,000 cells/cm^2 in the same medium. All work was performed with GMP-expanded hRPCs at passage 10.

3.3.2 Materials - hydrogel preparation and degradation

In-situ crosslinking of Gtn-HPA and HA-Tyr hydrogels were performed by an enzyme-catalyzed oxidation, as previously described [87], [112], with horseradish peroxidase as a catalyzer and hydrogen peroxide as crosslinker. For the homopolymer hydrogels, horseradish peroxidase HRP (Wako USA) and hydrogen peroxide (H_2O_2) (Sigma-Aldrich) were added to solutions containing 2 wt% Gtn-HPA or HA-Tyr hydrogels to form final concentrations of 0.1 U/ml (HRP) and 1 mM (H_2O_2), respectively.

The concentrations of catalyst (HRP), crosslinker (H_2O_2), and polymer (Gtn-HPA and HA-Tyr) were chosen based on previous studies which demonstrated their feasibility as a biocompatible and injectable hydrogel for subretinal and vitreous injection to enhance retinal regeneration [75]. Random copolymer networks (IPN10, 25, 50, 75 and IPN90) were prepared by mixing the corresponding amounts of Gtn-HPA and HA-Tyr in a 2 wt% solution (e.g. where CP75 corresponds to 75% of Gtn-HPA and 25% of HA-Tyr, both at 2 wt% solution). To create the random copolymer hydrogels, 0.1 U/ml of HRP and 1mM of H_2O_2 were mixed into the solution. Hydrogels were formed after less than 5 minutes and incubated at 37 °C to reach stability. As both Gtn-HPA and HA-Tyr are catalyzed and crosslinked with the same molecules, a random copolymer network will be formed if no preferential crosslinking is observed. Gelation time ranges from 30 seconds to 1 min and stability of the gels were obtained by incubation in low oxygen condition (37 C, 5% O_2, 5% CO_2) after 20 min.

Hydrogels (Gtn-HPA, IPN75, IPN50, IPN25 and HA-Tyr) were prepared (150 µl) as previously described, pipetted in different wells, weighed, and incubated for 30 min at 37 °C to reach stability. 200 µlo f phosphate-buffered saline (PBS) containing 1000 U/ml type IV collagenase (Invitrogen) was added to each sample before incubation at 37 °C on an orbital shaker at 150 rpm. Samples were collected 2 hours later and analyzed for mass and volume after collagenase treatment.

3.3.3 Viability and proliferation assays

hRPCs at 5 x 10^5/ml in PBS (Phosphate Buffer Saline, pH 7.4, ThermoFisher) or Ultraculture, with hEGF, with hFGF, defined media, or within 1 ml of hydrogels on top of fibronectin coated round cover slips glass (thickness 5mm, diameter 1 cm, VWR) were incubated with 2.5 µM calcein AM and 10 µM ethidium homodimer-1 in PBS for 15 min at 37 °C, 5% CO_2. Cells were then washed with PBS for 10 min three times at room temperature. Cover slips with cells were mounted on poly-l-lysine microscope slides (thickness 1mm, L x W 75 x 25 mm, Thermo Scientific Shandon) with low viscosity slide mounting medium (Fisher Scientific) before imaging with an epifluorescence microscope (Nikon's Eclipse E800, Japan). Cells in 7 randomly selected fields of view were counted under 20x objective lens magnification. hRPCs cultured in Gtn-HPA adopts a 3D configuration. Due to this special environment, epifluorescence imaging shows in focus and out of focus cells (live and dead cells not located on the focal plane). To make sure that these are not artefacts of the Gtn-HPA, the scale bar (200 µm) has been kept constant in all field of view. Gtn-HPA is a well-defined nanostructure hydrogel [113] and hRPCs size have been studied (3 order of magnitude larger than the Gtn-HPA structure) [114], we can assume that the images of the live/dead assay are indeed representing cells and not artefacts.

Proliferation assay was performed on the same samples by incubating cells in PBS, media or hydrogels with 10 µM alamarBlue (Bio-Rad) in PBS for 3 hours at 37 ℃, 5% CO_2. Cells were then washed with PBS for 10 min three times at room temperature. Cytotoxicity and proliferation were measured with spectrophotometry (ThermoFisher). Absorbance at wavelengths of 570 nm and 600 nm after required incubation were measured. The curve of relative fluorescence units vs. drug concentration was generated with a 3-point correlation method.

3.3.4 Cell morphology analysis vie image processing

All stained samples were analyzed, and images were taken using Leica SP8 confocal microscope. Images were taken with sequential scanning at 1024x1024 or 2042x2042 resolution with the following lasers intensity and characteristics: VioBlue-PMT at 5.4% with line average of 3 and gain of 875 V, FITC-HyD at 2.3% with line average of 3 and gain of 77%, PE-HyD or APC-HyD at 3.7% with line average of 3 and gain of 85%.

hRPCs viability images were taken at 20x magnification with a z-stack of 300 µm and 22 steps. A 3D projection was used for qualitative analysis while maximum projection was applied as quantification. Cells in 15 randomly-selected maximum-projected fields of view were counted under 20x objective lens magnification with a cell counting and analyzing image processing algorithm [115] (Appendix A.2). Cells number (green for live and red for dead), size (area of positive pixels) and shape factor (e.g., round versus elongated morphology) were measured for each field of view. After 1, 3, 5 and 7 days of culture, the percentage of viable cells was calculated by dividing the number of live cells (FITC) by the total number of cells in the given area (live and dead cells added).

3.3.5 Phenotype assay - flow cytometry

hRPCs at 5 x 10^5/ml in PBS or within 1 ml of hydrogels in 6-well plate (3.5 cm diameter, polystyrene, flat bottom, sterile, fisher scientific)] were maintained in PBS (replicating the in vivo conditions). At 3 days post-plating hydrogels were degraded using Collagenase IV and Hyaluronidase as explained previously. hRPCs (previously cultured in gel) were harvested and their phenotype was analyzed using Flow Cytometry with the MACSQuant flow cytometer (Miltenyi, San Diego). hRPCs, from different conditions (in PBS, in hydrogels, with or without shear stress applied, with or without hEGF/hFGF added) were collected and fixed with Perm/Fix buffer (BD Biosciences) at 4 °C for 15 min. Cells were then washed in wash buffer (BD Biosciences) and incubated, at room temperature, in blocking buffer (Pharmingen staining buffer with 2% goat serum) for 30 min. Blocked cells were seeded onto a flat bottom 96-well plate (treated, sterile, polystyrene, Thomas Scientific) and stained with conjugated primary antibodies (Cone Arrestin-FITC, S-opsin-FITC, RG-opsin-FITC, Recoverin-FITC, Caspase9-FITC, Rhodopsin-FITC, Oct4-APC, PAX6-APC, CMYC-APC, KI67-APC) overnight at room temperature. Primary antibodies were diluted in 200 µl of antibody buffer (TBS, 0.3% Triton X-100 and 1% goat serum). Post overnight incubation cells were washed three times for 15 min, and secondary antibodies (goat-derived anti-rabbit and anti-mouse, DAPI-VioBlue) were diluted 1:200 in antibody buffer (Jackson Immunoresearch Laboratory). Cell were incubated in secondary antibodies and left at room temperature for 3h. Light scatter and fluorescence signals from each sample were measured using the MACSQuant (Miltenyi

Biotech, Germany) flow cytometer (2 x 10^5 events were recorded). The results were analyzed using the MACSQuantify software (https://www.miltenyibiotec.com). For each primary antibody DAPI-positive single cell population was gated. The ratio of positive cells in the gated population was estimated in comparison with blank and species-specific isotype control. Primary antibodies and their dilutions are listed in Table 3.1.

Table 3.1: Primary antibodies and their dilutions used for phenotype analysis.

Antibody	**Isotype**	**Dilution**	**Source**	**Target**
DAPI-VioBlue	IgG2a	1:1000	BD Biosciences	Nuclei
Cone arrestin-FITC	IgG1	1:200	BD Biosciences	Cones
S-opsin-FITC	IgG1	1:200	BD Biosciences	Cones
RG-opsin-FITC	IgG1	1:100	BD Biosciences	Cones
Recoverin-FITC	IgG1	1:100	Abcam	Photoreceptors
Caspase9-FITC	IgG1	1:50	Santa Cruz	Apoptosis
Rhodopsin-FITC	IgG1	1:20	Abcam	Rods
Oct4-APC	IgG2a	1:200	BD Biosciences	Stemness
PAX6-APC	IgG2a	1:100	Santa Cruz	Retinal cells
Cmyc-APC	IgG2a	1:200	BD Biosciences	Stemness
Ki67-APC	IgG2a	1:50	Santa Cruz	Proliferation
Isotype Rabbit	IgG1	1:100	Abcam	Control
Isotype Mouse	IgG2a	1:100	Abcam	Control
Anti-Rabbit		1:200	BD Biosciences	Secondary
Anti-Mouse		1:200	BD Biosciences	Secondary

3.3.6 Rheology and compression measurement of hydrogel stiffness

Oscillatory rheology was performed with a TA instruments AR-G2 rheometer using cone and plate geometry of 40 mm diameter and 2° angle. For each measurement, 200 µl of each sample (Gtn-HPA, IPN90, IPN75, IPN50, IPN25, IPN10 and HA-Tyr) at 2%wt/vol, containing 0.1 U/ml of HRP and varying concentrations of H_2O_2 (ranging from 0.8-1.3 mM) was applied to the bottom plate immediately after mixing. All hydrogels having a gelation time comprised between 30s-3min samples were still liquid when applied onto the bottom plate. The upper cone was lowered to a measurement gap of 51 µm. As soon as a layer of silicone oil was applied, to prevent evaporation, the rheometer was started. All measurements were taken at 37 °C in the oscillation mode with a constant strain of 1% and frequency of 1 Hz. To estimate the gelation rate, the time at which the gel point (as defined by the crossover between storage modulus, G' and loss modulus, G") occurred was measured. G' (storage modulus) and G" (loss modulus) were measured every 2 seconds. Final plateau value of G' and time to reach this plateau were then recorded for each sample. Due to the fast gelation of all samples and time to stick the sample onto the bottom plate and the start of experiment, gel point was not measured with oscillatory rheology. Measurement can be seen in micro-rheology experiments.

Unconfined compression tests were performed using a Zwick/Roell Z2.5 static materials tester (Zwick GmbH & Co., Ulm, Germany) with integrated testing software (testXpert, Zwick). 1 ml of Gtn-HPA, IPN50, IPN75 and HA-Tyr were prepared into 24-well plates to create samples 16 mm in diameter and 3-4 mm in thickness. All hydrogels were left to fully crosslink and stabilize for 2 hours at 37C before performing compression testing. All gels were swelled in PBS for 1 hour before compression testing. Mechanical tests were performed at a constant strain rate of 0.5%/s to a maximum strain of 10% using a 20 N load cell (Part No. BTC-LC0020N.P01, Zwick) sampling at a frequency of 2 Hz. The diameter of the samples at the start of the testing was measured using digital calipers. The compressive modulus was determined by the slope of the true stress-strain curve within the linear regime of the material (0-7%).

Evolution of the Youngs' modulus E, shear modulus G', final plateau value, and critical time to reach this plateau were recorded for each sample. Each sample had n = 5 replicates to minimize the experimental effects of the rapid crosslinking time and oil application.

3.3.7 Differential scanning calorimetry on wet hydrogels

All materials were analyzed for water content using a differential scanning calorimeter (DSC 250) (TA Instruments, New Castle, USA). All hydrogels (Gtn-HPA, IPN90, IPN75, IPN50, IPN25, IPN10 and HA-Tyr) were analyzed from 20 to -60 °C at a cooling speed of 10 °C/min and a heating speed of 5 °C/min. Water transitions were observed at 0 °C and -20 °C for all samples. Water content was measured by analyzing the DSC trace and calculating the integral of the heat flow at both transition temperatures as compared to the normal heat flow of water.

To calculate the heat flow at transition temperatures, each transition was measured by finding the range where the heat flow was higher (or lower) than the control value. Within this range, the integral of the curve, normalized by the control value, was calculated for each transition and each sample. This integral value was then reported as the heat flow corresponding to the free water (0 °C) and bound water (-20 °C) freezing transitions.

As most of our hydrogels were made at 2 wt% solution, the amount of water present in those hydrogels during differential scanning calorimetry was in significant excess. This created a ‘loop artifact’ in the DSC trace around the temperature of melting (or crystallization) of bound water (-20 C). This artifact can be explained by the large exotherm of water crystallization, suggesting a considerable presence of bound water in our hydrogels.

3.3.8 Growth factor encapsulation and release in hydrogels

Human epidermal growth factor and human fibroblast growth factor were obtained from ThermoFisher scientific and dissolved in water to create aliquot of 1 mg/ml. Gtn-HPA, HA-Tyr and different composition copolymer were dissolved at 2wt% in 5ml of PBS. hEGF/hFGF were added to the dissolved polymer to reach a concentration of 10 ug of hEGF in each sample (100 µl). This load was performed before adding the catalyzer and crosslinker to crosslink hydrogels. Gels were then crosslinked and pipetted in 1 ml cryotubes and incubated at 37C for 20 min to reach stability. Then, 200 µl of PBS was added on top of the gel. At time of measurement Gtn-HPA, HA-Tyr and CP were submerged in 400 µl of PBS release buffer. 200 µl of supernatant was collected at the following time points to study the release of hEGF: 15 min, 30 min, 45 min, 1 h, 1.5 h, 2 h, 1 d, 7 d, 9 d, 10 d and 11 d. The 11 days endpoint was chosen based on the degradation rate for these hydrogels in vivo. After 11 days, the Gtn-HPA gel was degraded using Collagenase IV solution for 3 hours at 37 °C. The concentration of EGF at each time point was assessed using an EGF ELISA kit (R&D Systems).

The EGF ELISA kit allowed the samples to be analyzed at each time point with an accuracy of 0.05 µg of EGF release. To measure and collect the supernatant from all samples, PBS buffer was analyzed via ELISA each day with a new control sample. This allowed us to confirm the measurement of active EGF without denaturation. For unknown samples, a 1:600 dilution was used for all time points. The standard curve fit was calculated using a 4-parameter logistic regression curve. The concentration and cumulative EGF release amount over one week were calculated based on the best fit equation using the 4-parameter standard curve for all groups.

3.4 Results

3.4.1 hRPCs resist the Gtn/HA covalent crosslinking

Catalyst (HRP) and crosslinker (H_2O_2) effect

Our main goal, in creating a hydrogel that could be used to improve retinal regeneration, was to prove its biocompatibility by measuring cell viability after 2 days of culture in 3D scaffolds. Cells (suspended in saline) were encapsulated in hydrogels (deprived of nutrients) and, after 2 days, were analyzed to evaluate the efficiency of culture condition using a live/dead assay. The percentage of viable cells was calculated by dividing the number of live cells (green) by the total number of cells in the given area.

One of the most impactful stress that appears on cells encapsulated in Gtn-

HPA and HA-Tyr is oxidative stress due to the presence of hydrogen peroxide as a crosslinker (usually cytotoxic to cells in high doses). We performed a viability assay on cells encapsulated in hydrogels with increasing concentration of H_2O_2 (but constant HRP at 0.1 U/ml) to find the optimal formulation for both homopolymeric networks: this could then be transferred to IPN (Figure 3.2). To accurately quantify the number of viable cells, immunohistochemistry was performed using calcein-AM and ethidium bromide; and DAPI as nuclear marker. For both samples (Gtn-HPA and HA-Tyr) crosslinked with H_2O_2 around 1mM seemed to provide the highest biocompatible hydrogels with viability ranging from 60% in HA-Tyr to 80% for Gtn-HPA. Of note is that we observed, for low concentration of H_2O_2 (<0.8mM), almost no gel formation which is shown by a really high viability at 0.5mM. This is due to the fact that in this case H_2O_2 is not sufficient to form a gel and therefore cells are in a 2D formation, as in the defined protocol. Finally, we increased hydrogen peroxide concentration up to 5 mM in order to look for its cytotoxic effect on cells. Oxidative stress was already high at 2.5 mM with a viability ranging from 20% to 35% while being minimal at 5mM where most cells died (only 5-8% viable). This broad testing of hydrogen peroxide effect on cell viability in both homopolymeric networks suggested that a concentration around 1mM should be used to make the most biocompatible hydrogel. As seen in the next section, we performed a sharper testing for different IPN content with crosslinker concentration ranging from 0.8 to 1.3 mM. The optimal IPN was found to contain at least 30% of Gtn-HPA with a crosslinker concentration of 1mM.

As seen in past studies [77], the catalyst (HRP) concentration was shown to be optimal at 0.1 U/ml to enable encapsulated cells to thrive. In these studies, a live/dead assay on different type of stem cells (MSC, RPE, ES) encapsulated in Gtn-HPA with varying concentrations of HRP was performed. The result show that a concentration of at least 0.1 U/ml was necessary in order to form a hydrogel. Concentration lower than 0.1 U/ml show a significantly low viability of cells (<20%) which is due to the presence of H_2O_2, cytotoxic to cells, not being used to create a gel as the concentration of HRP is too low. Upon using 0.1 U/ml a high viability was observed along

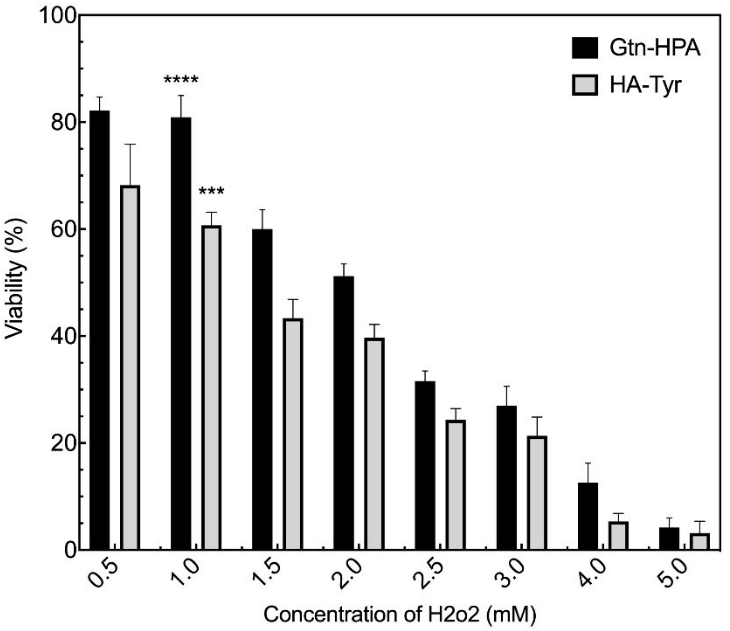

Figure 3.2: Viability assay on hRPCs encapsulated in Gtn-HPA/HA-Tyr with increasing concentration of H_2O_2.
Viability was measured by counting the number of live and dead cells in the viability assay performed with CalceinAM and Ethidium Bromide. Data of each group were calculated from 15 randomly chosen fields in each group using confocal fluorescence microscopy. Viability was observed to be significantly decreasing with the increase of hydrogen peroxide concentration. ****p=0.0001, ***p=0.001.

with the formation of a hydrogel (80%). Increasing the concentration of HRP above 0.1 U/ml does not affect the viability of hRPCs. However, as shown in other studies [116], HRP might have a slight impact on cells phenotype and differentiation. As 0.1 U/ml has been shown to be completely used to catalyze the gelation of our hydrogels, these results suggest that it is the correct concentration to be used.

Live/dead staining of cells encapsulated in IPN (at 1mM crosslinker and 0.1 U/ml catalyst) and grown in PBS are presented in Figure 3.3. Images represent a maximal projection of 200 µm z-stack for hydrogels samples which were seeded at the same concentration. Cells in 2D culture appeared more fibroblastic with a higher number of dead cells. In contrast, cells encapsulated in Gtn-HPA and IPN seemed to retain their phenotypic morphology. Our result clearly demonstrates the effect of oxidative stress and protective nature of Gtn-HPA and IPN for hRGC culture and possible transplantation.

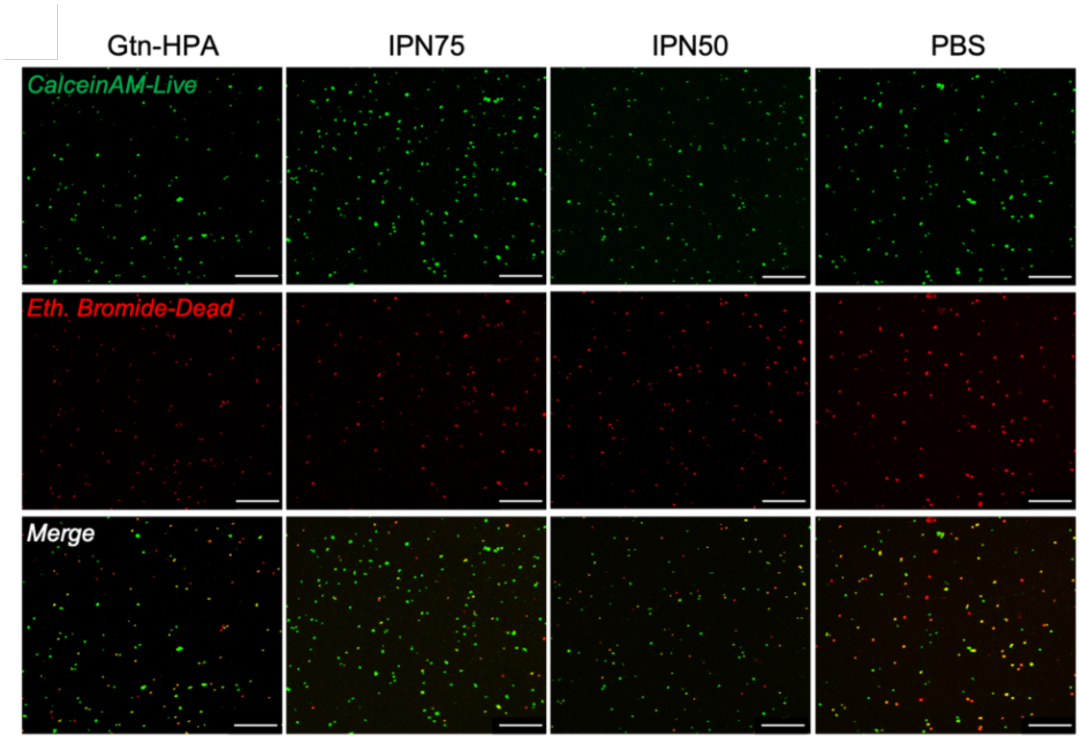

Figure 3.3: Encapsulated human retinal ganglion cells viability assay. Fluorescence images of live (CalceinAM-green) and dead (Ethidium Bromide-red) hRGC encapsulated in hydrogels, maximum projection of 300 µm samples imaged with confocal microscopy. All images were taken at 10X magnification under fluorescence microscopy. Scale bar – 200 µm. ***p=0.001.

Gelatin and growth factor effect on hRPCs

The percentage of viability was calculated by dividing the number of live cells (FITC) by the total number of cells in the given area (live and dead cells added). Cells cultured in media showed the highest viability as expected (Figure 19), since these cells received all the nutrient required for cellular growth. This group is only used as an in vitro control group to check if viability was correctly performed. The viability measured for hRPCs grown in media for 1-3 days ($<$70%) corresponds to values found in previous studies [117], [118]. Using defined media is not approved for transplantation, therefore we considered PBS as a carrier as the control group to further mimic the in vivo conditions. In comparison, in all other groups, cells were deprived from essential nutrients for 1, 3, or 6 days, hence their viability is significantly lower than cells culture in media (without shear stress applied). To test the hypothesis that Gtn-HPA hydrogel can support hRPCs growth, direct comparison between 2D (PBS and hEGF) and 3D cultures (Gtn-HPA) was performed. Even though initial viability of hRPCs in 2D and Gtn-HPA showed no significant difference, the trend changes in long-term culture (Figure 3.4). After 6 days of being deprived from nutrients cells in PBS show a lower viability than cells cultured in Gtn-HPA or with hEGF added. These results suggest that culturing hRPCs in a 3D environment (Gtn-HPA) or adding only hEGF to PBS could greatly improve the viability of cells in vitro.

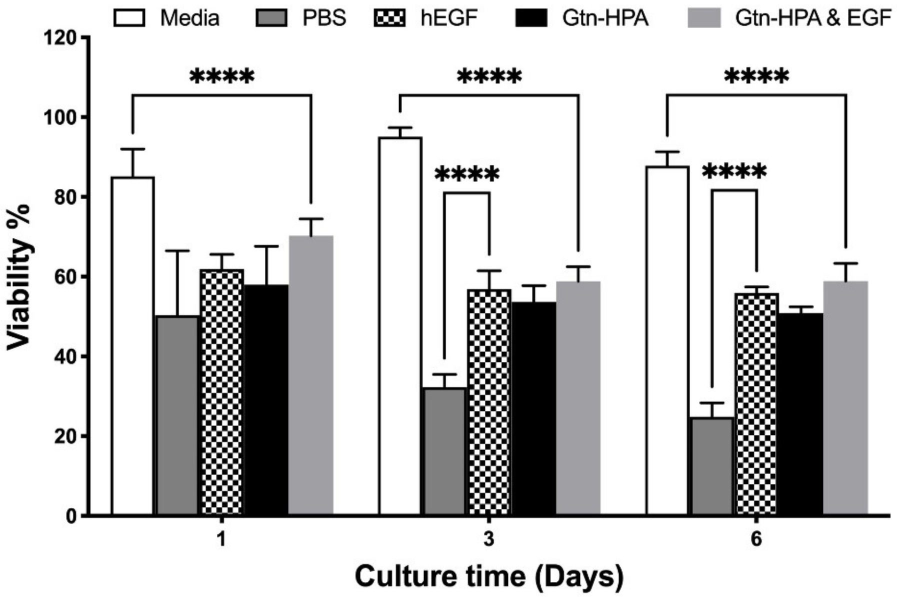

Figure 3.4: Live/Dead assay of hRPCs by immunohistochemistry with different nutrients and tissue culture.
Data analysis of Live/Dead assay for different nutrients and culture conditions (Media, PBS, hEGF, Gtn-HPA). Data shown as mean ± SEM of triplicate wells with 15 different fields for each well. Three-way ANOVA was performed and shows a statistically high significant difference between media alone and all other groups. Significant decrease of viability can be seen between PBS and all other groups starting at day 3 (****p = 0.0001).

To accurately quantify the number of viable cells, immunohistochemistry was performed using calcein-AM (FITC) and ethidium bromide (APC) as live/dead assay. Cells in 2D cultures (PBS, hEGF), deprived from most nutrients, appeared more fibroblastic with higher number of dead cells (Figure 3.5). In contrast, hRPCs embedded in Gtn-HPA were located in different layers (3D structure). It has been shown in multiple studies, that culturing retinal cells in a 3D environment (spheroids, organoids [119] or, hydrogels [120]) improves their viability, development and, phenotypic differentiation and morphology.

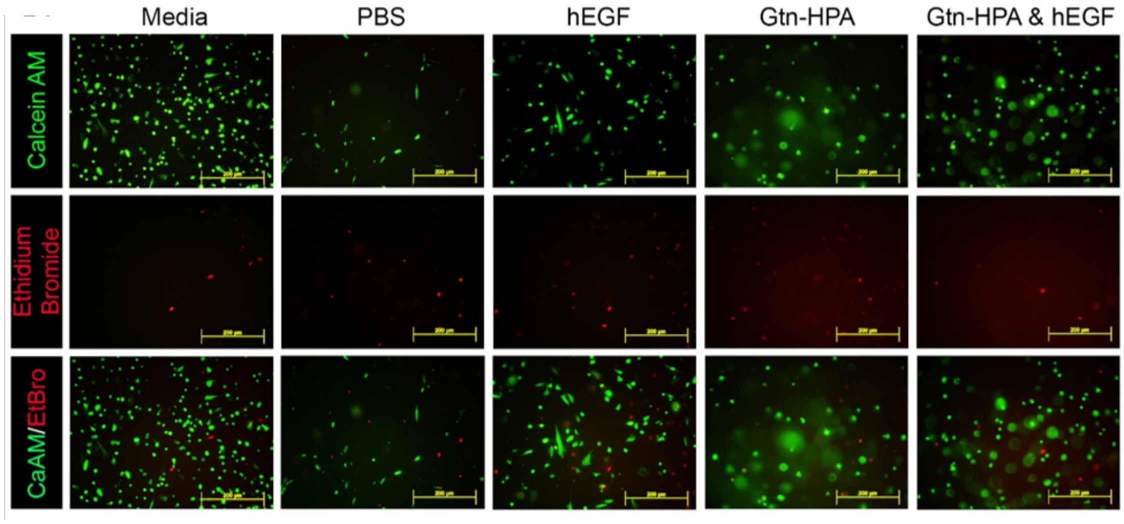

Figure 3.5: Fluorescence images of live/dead assay for hRPCs in different culture conditions.
All images were taken at 40X magnification. Fluorescence images of Live/Dead assay performed on hRPCs with Calcein-AM as live staining (FITC channel), Ethidium Bromide as dead staining (APC channel) and, merged pictures for Media, PBS, hEGF, Gtn-HPA and Gtn-HPA & hEGF. Scale bar is 200 µm in all images. Image modified from [75].

Phenotype analysis across common retinal marker (stemness, proliferation, apoptosis, retinal, cone and rod) was also performed for hRPCs in their normal condition (in 2D culture with media) and encapsulated in Gtn-HPA hydrogels. As seen in Figure 3.6, no significant difference was found for any of the markers. This result suggests that hRPCs maintain their phenotype when encapsulated in hRPCs; phenotype which has been analyzed before [37].

Finally, analysis of the gelatin and HA content effect on encapsulated hRPCs was

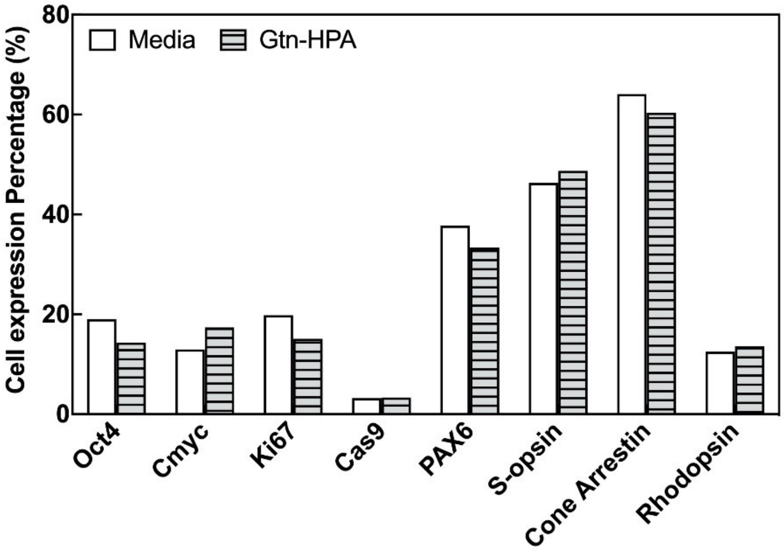

Figure 3.6: Phenotype analysis of hRPCs using flow cytometry.
hRPCs cultured with media or in Gtn-HPA were analyzed for their phenotype with flow cytometry. No significant difference was observed at short time between both groups for all retinal, stemness, rods, cones, proliferation and apoptosis markers.

performed. For this investigation, hRPCs were encapsulated in multiple Gtn-HA IPN gels with selected percentages of Gtn and HA, and various crosslinker concentrations, which have been chosen to be as close as possible to the optimal crosslinker concentration (from 0.8 to 1.3mM) as observed in the previous section. A short-term viability study enabled us to tune the optimal crosslinker (H_2O_2) concentration both in IPN and homopolymeric hydrogels to be exactly 1mM. High viability was found for concentrations close to 1mM, however this optimal concentration was found to be significantly higher than all others. In Figure 22, we also studied the impact of Gtn-HPA content in IPN on encapsulated cell viability. Of note is that the viability of cells cultured in PBS was found to significantly lower than all hydrogel groups. A viability threshold, corresponding to a content of $>$30% of Gtn-HPA, was observed for all crosslinker concentrations demonstrating that hRPCs do not thrive in HA-Tyr. This finding can be related to the understanding that hRGC possess integrins to attach to the gelatin backbone but not to the hyaluronic acid backbone [121], [122]. . This result reduces the number of candidates to IPN possessing a Gtn-HPA content higher than 50% (which include Gtn-HPA itself).

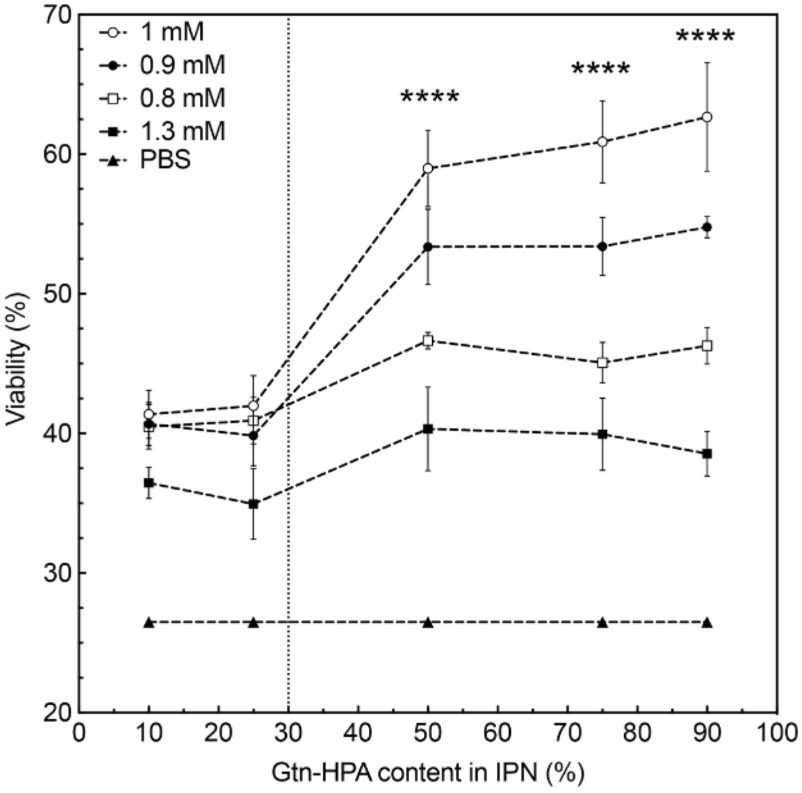

Figure 3.7: Optimal IPN candidate for hRPCs viability and encapsulation.
Viability assay at day 3 of encapsulated human retinal ganglion cells in IPN with different Gtn-HPA content and a range of crosslinker concentration compared with PBS. Data was measured for 10 field of views of live/dead staining. Data shown as mean ± SEM and one-way ANOVA followed by student-t test was performed showing a statistically high significant difference between H_2O_2-1mM and all others for more than 50% Gtn-HPA in the IPN (****$p<0.0001$).

Cell morphology analysis

Counting and analyzing cell size and shape manually is a tedious error prone process. To be able to analyze a large data set from fluorescent confocal microscopy images, we decided to use a basic computer vision technique. This image processing algorithm, previously explained in [115], enables for cell segmentation from a black background image based on cell intensity and staining. The method uses basic morphological operations and the watershed algorithm to segment the cells and was implemented in MATLAB. We chose this method for its simplicity and ease of implementation.

For each sample group we analyzed n=10 fluorescent maximum projection of fields of view obtained from live/dead staining images of cells encapsulated or grown in 2D conditions (Figure 3.8a). We then converted each image to a greyscale (from the specific staining analyzed live: green and red: dead). To be able to analyze cells correctly, multiple image rendering processes were used. The extraction of dimmer cells was performed by contrast adjustments. The elimination of objects on the borders (which can cause noise and be artifacts) was realized with an intrinsic MATLAB function. Noise removal, critical to extract only cells and not artifacts, was done with adaptive filtering (small window). The final image rendering included using a global Otsu's thresholding method to convert the image to binary, filling the image region and holes, performing a morphological opening using a disc kernel and finally removing all small cells (connected components with low number of pixels <10px). The final image can be seen in Figure 3.8b. To further analyze cells, we performed perimeters extraction of cell or cell groups, as seen in Figure 3.8c. Some cells might be grouped and counting their number may be critical for viability results. To extract cells in groups we applied a watershed algorithm, which can divide the groups into distinct cells. The watershed algorithm interprets different levels of gray intensity, in an image, as altitude. It then finds objects which are delimited by their perimeter with a high altitude in their center (high overlapping intensity). To implement the watershed algorithm, we modified the image by finding the maxima (corresponding to the cell nuclei) and transformed the image to show the perimeter and these maxima (Figure 3.8d). We finally applied the watershed algorithm which finds all connected components and enables for an easy cell counting (Figure 3.8e). In the sample image 33 cells were extracted (Figure 3.8f). We also extracted cell size, measured as the longest line drawn inside each object (Figure 3.8g) and the shape factor (Figure 3.8h) which corresponds to the relative shape of an object compared to a circle:

$C = (4 * \pi * A)/(P^2)$ ($C = 1$ being a perfect circle). A cell with a low shape factor could be due to elongated or stellate morphology resulting from the formation of cell processes. Due to small cell size, while most cells have been correctly detected, some have been taken as dust and deleted. Segmenting grouped cells worked well and enabled a coherent cell size and number measurement. Detected cells appear to have a similar size to real cells (broadly measured with scale on confocal microscope). By counting some fields of views manually and comparing to the algorithm result we can suppose that this algorithm has a rate of success of around 95%.

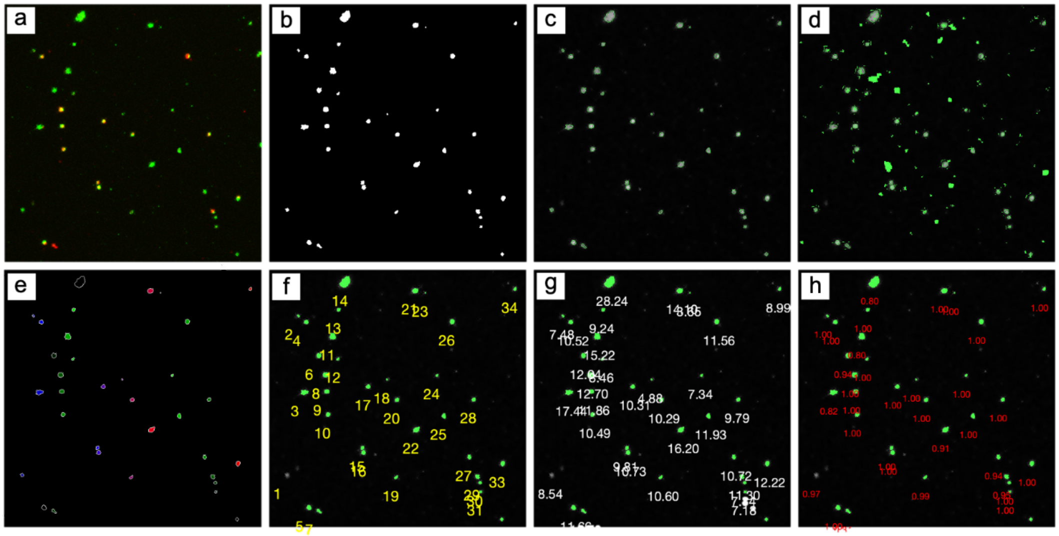

Figure 3.8: Image processing algorithm for measuring cell size and shape. Step by step image processing analysis of live and dead stained hRGC encapsulated in hydrogel or in 2D conditions. **(a)** Initial maximum projection fluorescence image taken with confocal microscopy at 10x magnification. **(b)** First processed image after contrasts adjustments, elimination of objects on the borders, noise removal and threshold with Otsu's method. **(c)** Perimeter cell extraction. **(d)** Image processed with watershed algorithm to separate possible grouped cells. **(e)** Connected components from the watershed results. **(f)** Number of cells extracted per image. **(g)** Cell size for each object. **(h)** Cell shape factor corresponding to its shape compared to a perfect circle.

We applied this image processing algorithm to the viability assay performed on hRPCs in different conditions. All extracted values form the image processing algorithm can be seen in Figure 3.9 for all samples. Live (green) and dead (red) cell size distribution was analyzed for all groups and shows no significant difference in time. The results suggest that dead cells are, on average, 10 µm smaller than live cells. A significantly higher live cell size was found in hydrogel samples (around 15um for Gtn-HPA, 20 µm for IPN75 and IPN50) compared to cells cultured in 2D environment (8-10um for media and PBS). The shape factor was also analyzed for both live and dead cells for all samples and shows no difference between time points. A significantly lower shape factor was observed for cells in hydrogels samples compared to media and PBS. Dead cells, mostly due to the loss of cytoplasm, nucleus, and shape, show a low shape factor for all samples. These findings suggest that Gtn-HPA and IPN can enable cell growth and differentiation due to their higher size while enabling morphological extension of primary processes, as shown with a lower shape factor.

3.4.2 Phenotypic expression controlled by hydrogel stiffness

Stiffness and mechanical characteristics of gels

In order to understand what type of effect our hydrogels can have on hRPCs viability, phenotype and proliferation we analyzed and characterized mechanically all hydrogels ranging from pure Gtn-HPA to pure HA-Tyr. Constant shear rheology was performed on all hydrogels with n=5 replicates, with mineral oil added to the contour to reduce as much as possible the evaporation of hydrogels during measurements. Unconfined compression testing was also performed to measure the Young's modulus of hydrogels.

Mechanical characteristics of IPNs was measured by oscillatory rheology and unconfined compression testing. Hydrogen peroxide, being cytotoxic to cells at high concentrations, has been shown to create biocompatible hydrogels around 1mM (see previous section and [75]). This hinted at the mechanical measurement of HA-Tyr, Gtn-HPA and IPN at crosslinker concentrations equal or close to 1mM as seen in Figure 3.10a. Shear moduli (G') of both Gtn-HPA (red-dashed line) and HA-Tyr (red-dotted line) increase with crosslinker concentration ranging respectively from 160 and 1010 PA at 0.7 mM of H_2O_2 to 910 and 1650 Pa at 1.3 mM. A similar

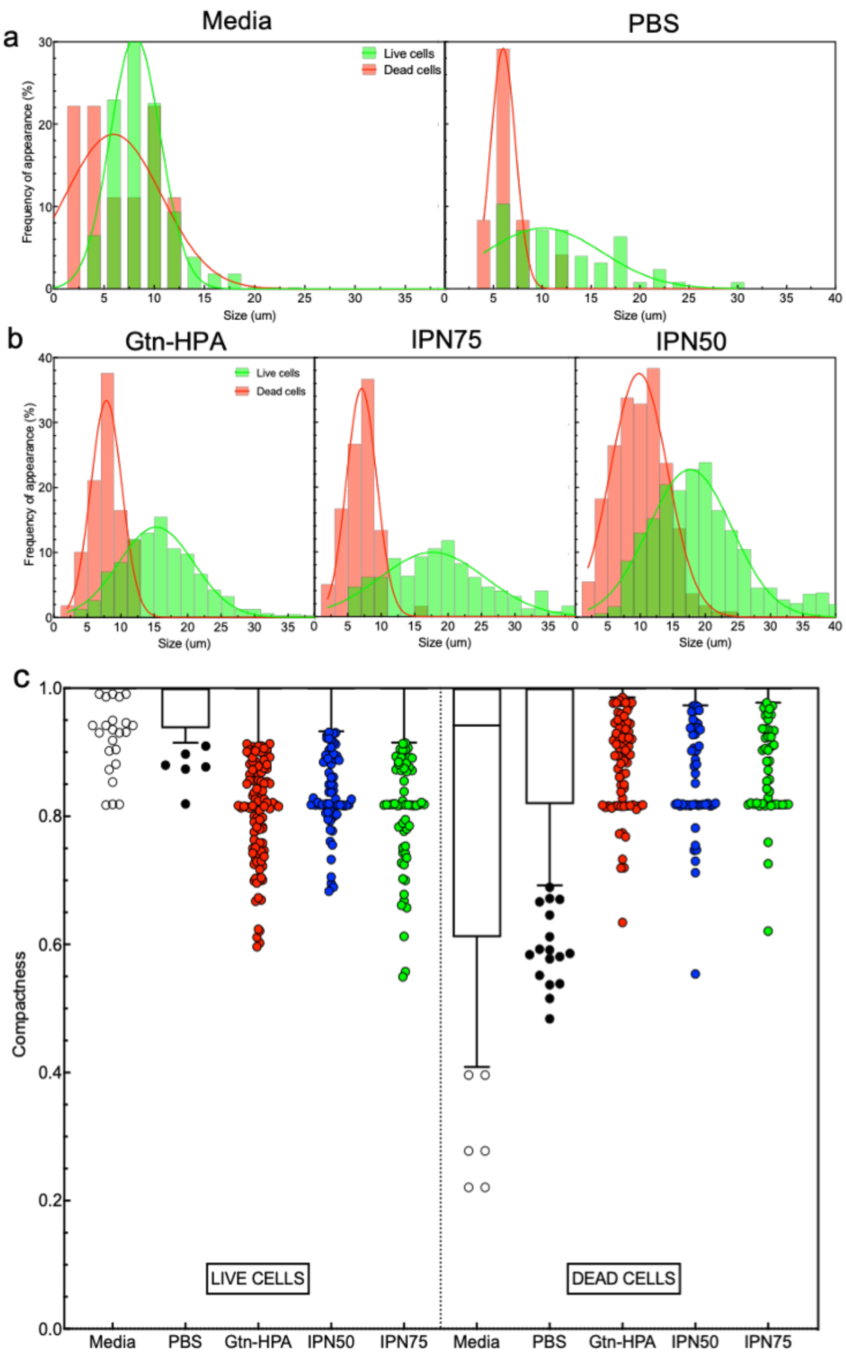

Figure 3.9: Human retinal progenitor cells size and shape quantitative analysis.
Live and dead cell size distribution for hRPC cultured in 2D conditions (media and PBS) **(a)** or in hydrogels (Gtn-HPA, IPN75, IPN50) **(b)**. **(c)** Live and dead cell shape factor quantification for all samples. No statistically significant difference was found in this analysis.

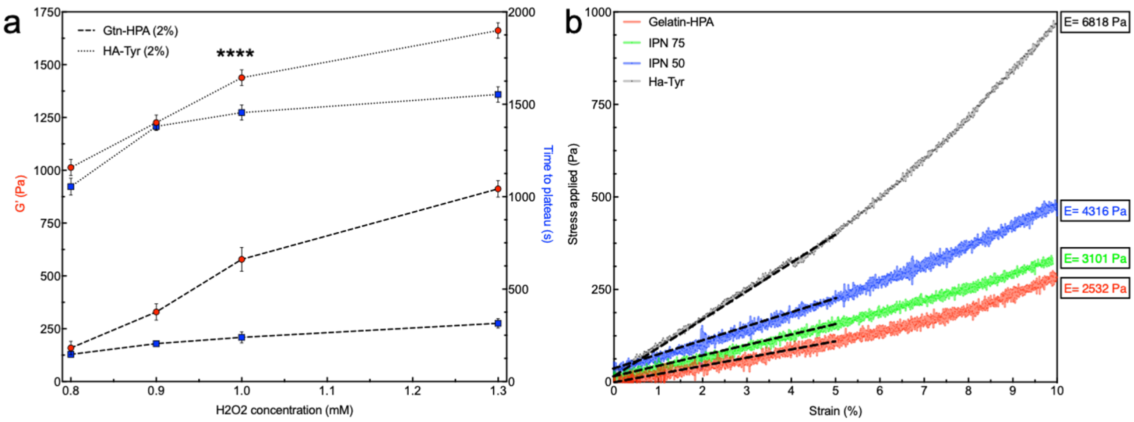

Figure 3.10: Hydrogels (IPN and homopolymers) rheological and mechanical characterization.
(a) Oscillatory rheological measurements of shear modulus (G' in red) and time to reach plateau (in blue) for Gtn-HPA and HA-Tyr for different concentration of crosslinker H_2O_2 (ranging from 0.8mM to 1.3mM). Data shown as mean ± SEM of triplicate measurements. One-way ANOVA, followed by student-t test for each concentration, was performed and shows a significant difference in shear moduli between HA-Tyr and Gtn-HPA (****$p<0.0001$). **(b)** Compression test measurements of Young modulus for Gtn-HPA, IPN75, IPN50 and HA-Tyr. Dashed line shows linear regression performed to measure moduli in the elastic region (strain less than 5%).

trend was observed for the time to reach steady state (blue lines). This high difference could enable to create IPNs with different and controlled stiffness which could greatly impact stem cells differentiation.

A similar trend was observed on the Young's modulus, calculated from maximal 5% strain during unconfined compression (Figure 3.10b). HA-Tyr shows a plastic behavior at low strain (4.5%) with a modulus of 6818 Pa while IPN50, IPN75 and Gtn-HPA stay in the elastic domain for higher strain (8%).

To assess whether mechanical characteristics of these IPN can be controlled by their relative percentages of Gtn and HA, we performed oscillatory rheology and unconfined compression testing on all IPN (HA-Tyr, IPN10, IPN25, IPN50, IPN75, IPN90 and Gtn-HPA). As seen in Figure 3.11, the shear (G') and Young's (E) modulus both decrease monotonically with the increasing amount of Gtn-HPA in the IPN, ranging respectively from 1438 Pa and 6828 Pa for pure HA-Tyr to 578 Pa and 2532

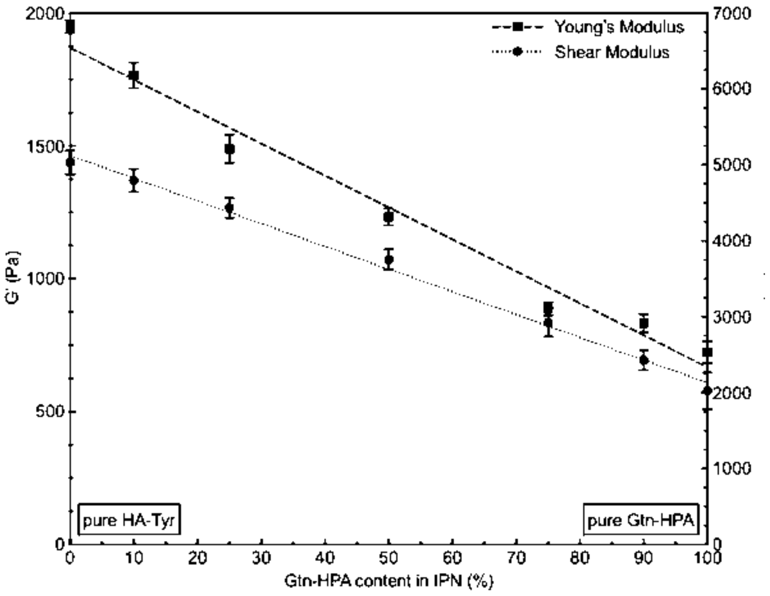

Figure 3.11: Mechanical characteristics of IPNs with ranging Gtn-HPA content.
Shear (dot line) and Young's (dash line) moduli measurements for multiple IPN with different Gtn-HPA content (ranging from 10% to 90%). Linear regression was applied both set of values, with n=15.

Pa for pure Gtn-HPA. This behavior can be explained by homopolymeric networks rheology (Figure 3.10a) which showed that HA-Tyr possesses a shear modulus 2-5 times higher than Gtn-HPA. Mechanical and stiffness characteristics can therefore be controlled by the IPN content of the respective polymers.

Cell Viability and proliferation

Cell growth and viability were measured with Alamar Blue, CalceinAM and Ethidium Bromide, as explained in methods, at day 1, 4, 7, 11 and 14. Figure 3.12 shows the hRPCs growth in different hydrogels and with different nutrients through time. Deprived from any growth factor (no GF) cells tend to have a significantly smaller growth when encapsulated in hydrogels, especially in pure HA-Tyr, compared to culture in 2D (positive control) or in hydrogels with higher Gelatin content. By adding either EGF or FGF to the hydrogels a higher cell growth was observed for groups containing a high content of gelatin and 2D culture. Furthermore, by adding both

FGF and EGF at concentrations present in the defined media (see methods for correct concentration) a significantly higher cell growth was observed for cells cultured in 2D or in pure Gtn-HPA even after 14 days compared to all other groups. Overall, when depriving hRPCs from growth factor a visible decreasing cell growth was observed throughout time (from day 1 to day 14) while by including both growth factors, cells were found to be proliferating at a high pace, increasing almost exponentially for hRPCs encapsulated in pure Gtn-HPA.

To further confirm these results, we performed a Live/Dead staining by mixing CalceinAM (FITC in green) and Ethidium Bromide (APC in red) to hRPCs in different tissue culture, as seen in Figure 3.12B. Live cells are shown in green and dead cells in red. Fifteen randomly chosen fields were chosen in each group to calculate viability data. Cells were seeded in all samples at the same concentration, enabling for a correct measurement of the viability in these different hydrogels. As we have seen with the cell growth experiment, cells tend to be more proliferating and viable when both EGF and FGF are added to the mix. Therefore, we present here only this nutrients groups with different tissue culture and hydrogels: 2D culture, HA-Tyr, IPN25, IPN50, IPN75 and Gtn-HPA. As seen in Figure 3.12A, hRPCs viability increases significantly with the amount of Gelatin in the hydrogel mix. Reaching the highest viability and highest number of live cells (due to a high proliferation) when cells are encapsulated in pure Gtn-HPA. This finding is coherent with the previous experiment on measuring hRPCs viability in changing concentrations of the catalyzer (HPR) and crosslinker (H_2O_2), see previous section. Overall, these results suggest that adding both EGF and FGF into the hydrogels can greatly enhance the proliferation capabilities and viability of hRPCs in vitro. This suggests a specific advantage of using our hydrogels as delivery vehicle for retinal regeneration as it enables the encapsulation of not only cells but also growth factors and other nutrients to improve the viability of cells in vivo and therefore their potential engraftment and survival long term, with the possibility to enhance retinal regeneration. This is impossible to achieve with just saline injection as the nutrients delivered would automatically be dispersed at the injection location and would not impact the fate of the injected stem cells.

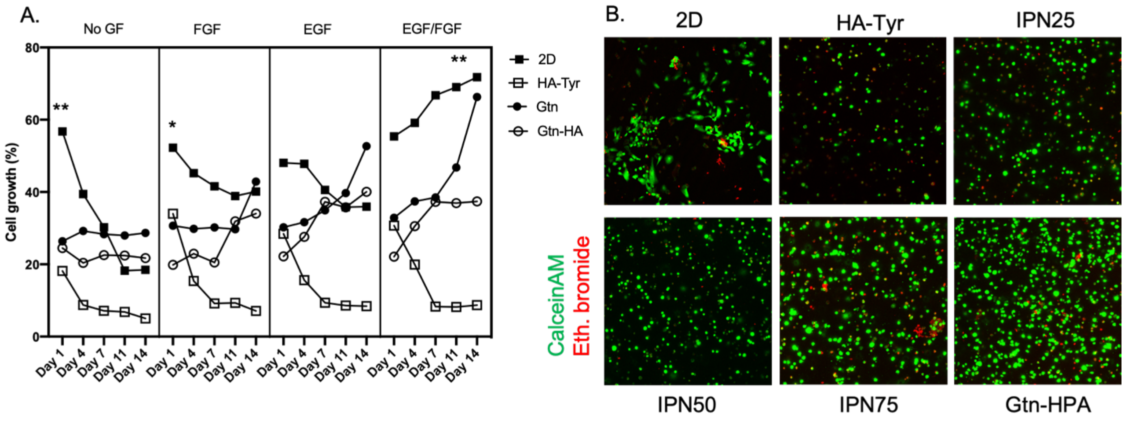

Figure 3.12: Viability and proliferation assay for hRPCs encapsulated in IPNs.
A. Cell growth was obtained with AlamarBlue staining for n=5 replicates using colorimetry. Cells were found to possess a significantly higher growth when encapsulated in pure Gtn-HPA or with media. **B.** Live/dead staining of hRPCs in different tissue culture. Gtn-HPA shows the highest number of live cells while HA-Tyr shows higher number of dead cells.

Phenotype analysis

The main objective of this experiment is presented here: can our hydrogels based on gelatin and hyaluronic acid effect the phenotype and differentiation of hRPCs after 14 days of culture. To answer this question, we performed a phenotype analysis with flow cytometry on hRPCs encapsulated in different hydrogels at day 1, 4, 7, 11 and 14. This phenotype analysis was performed on markers of interest: stemness, retinal, photoreceptor, cone and rod as hRPCs being derived from fetal retina can only differentiate into retinal cells. Our approach was to mainly analyze the phenotype difference in photoreceptors population as the principal objective of hRPCs (in clinical trial at the moment) is to be injected in the subretinal space with a goal to replace degenerating photoreceptors (mainly rods) in diseases such as retinitis pigmentosa or rod-cone dystrophies.

The flow cytometry analysis was performed with the Miltenyi MACSQuant flow cytometer, as explained in methods. The next figures show the result of the phenotype analysis for Oct4-stemness, PAX6-retinal, recoverin-photoreceptor, rhodopsin-rods and R/G opsin-cones. The absence of SEM in Figures 3.13 is due to the average of 10^5 events measured by the flow cytometer after gating the right cell populations. Furthermore, flow cytometry was performed on n=4 replicate however adding SEM on Figure 3.13 would reduce the data visibility due to the 3D graph. For all markers the same gating strategy (population of event or cells to be considered as positive) was applied: gating the cell population (FSC-A vs SSC-A), gating the single cell population (FSC-A vs FSC-H), and then gating the DAPI positive population (VioBlue-A vs FSC-A). This single-cell-DAPI-positive gate correspond to the population of cells we can compare for all different markers (retinal, stemness, photoreceptor, rods, and cones). The data presented in the following figures only shows days 4, 7, 11 and 14 as data in day 1 was not relevant due to the short-term culture of cells in hydrogels. Cells usually need 4-7 days to express a different phenotype due to their response to different environments. Therefore, according times of culture have been used for hRPCs in all different tissue and media culture.

Figure 3.13 shows the expression of Oct4, a key gene that regulate stemness in progenitor cells [123]. The expression of Oct4 was observed to be similar from day 4 to day 14 showing a significant increase with the addition of HA in the tissue culture, being the highest for pure HA-Tyr with 35% compared to Gtn-HPA or 2D with less than 12%. Of note is that the change in nutrients didn't impact the stemness of hRPCs showing almost the same expression for all samples in the same tissue culture. This result can be related to many studies that have shown the importance and effective association of stiffness of biomaterials on stem cell culture [124]. This results further corroborates that by increasing the gelatin content of our hydrogels, one can increase hRPCs differentiation towards specific retinal cells.

As second marker which was analyzed is PAX6, as shown in Figure 3.14, PAX6 which is an early retinal cell marker [125]. The exact opposite trend was observed showing a significantly higher expression of PAX6 for cells cultured in Gtn-HPA and high gelatin content hydrogels. The expression of PAX6 was seen to be increasing with time, reaching a plateau after 10 days. Gtn-HPA and IPN75 show the highest expression with respectively 30% and 28% after 11 days compared to less than 10%

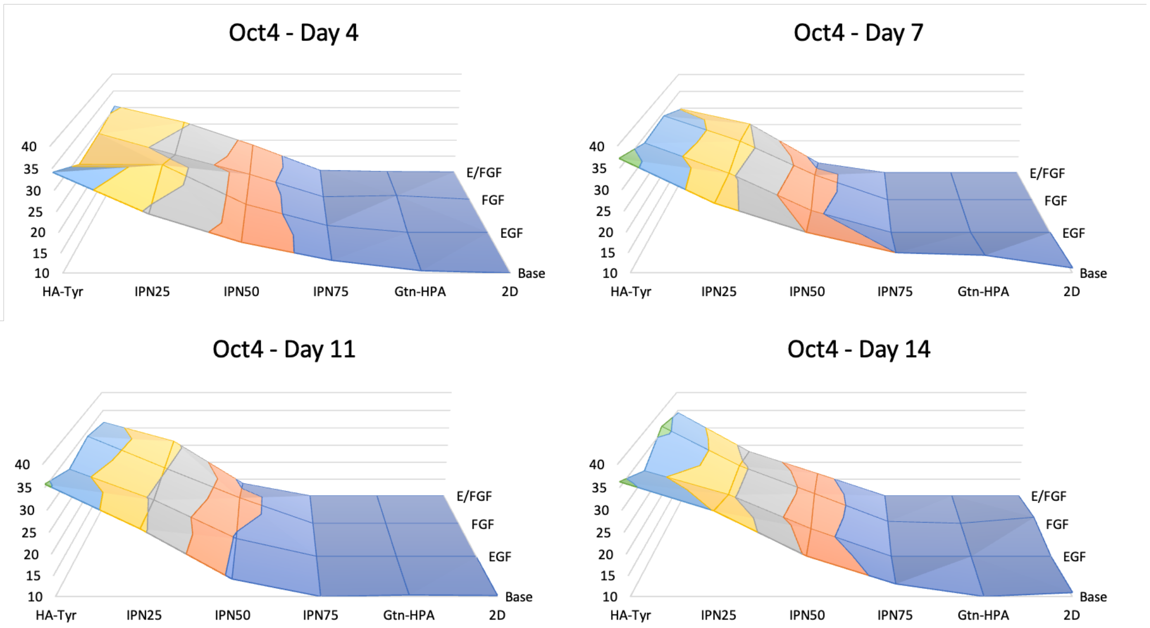

Figure 3.13: Phenotype assay for stemness marker Oct4 of hRPCs in different tissue culture.
Cells were cultured for 2 weeks and phenotype was analyzed at day 4, 7, 11, and 14 for n=5 replicates with flow cytometry. Map surfaces show the media component on the x-axis (base media, EGF, FGF, or both), the tissue culture on the y-axis (2D, Gtn-HPA, IPN75, IPN50, IPN25, and HA-Tyr) and the expression of Oct4 is shown on the z-axis.

for cells cultured in HA-Tyr. A similar trend as for Oct4 was also observed for the nutrients effect on PAX6 expression. The data suggests that there is no impact from EGF or FGF on the early retinal marker expression of hRPCs. This early retinal marker expression differences suggest that hRPCs differentiation could be driven towards retinal cells by using tissue culture with high gelatin content and lower stiffness.

As hRPCs are usually meant to be injected in the subretinal space to replace dead photoreceptor, we analyzed a specific photoreceptor marker: recoverin. This marker is expressed randomly by both cones and rods with no specificity. As seen in Figure 3.15, a clear significant increase in recoverin expression was found from day 4 to day 14. Moreover, a similar trend as for PAX6 was observed with the highest expression for Gtn-HPA and IPN75 after 14 days: respectively 36% and 34%. Of note is that the

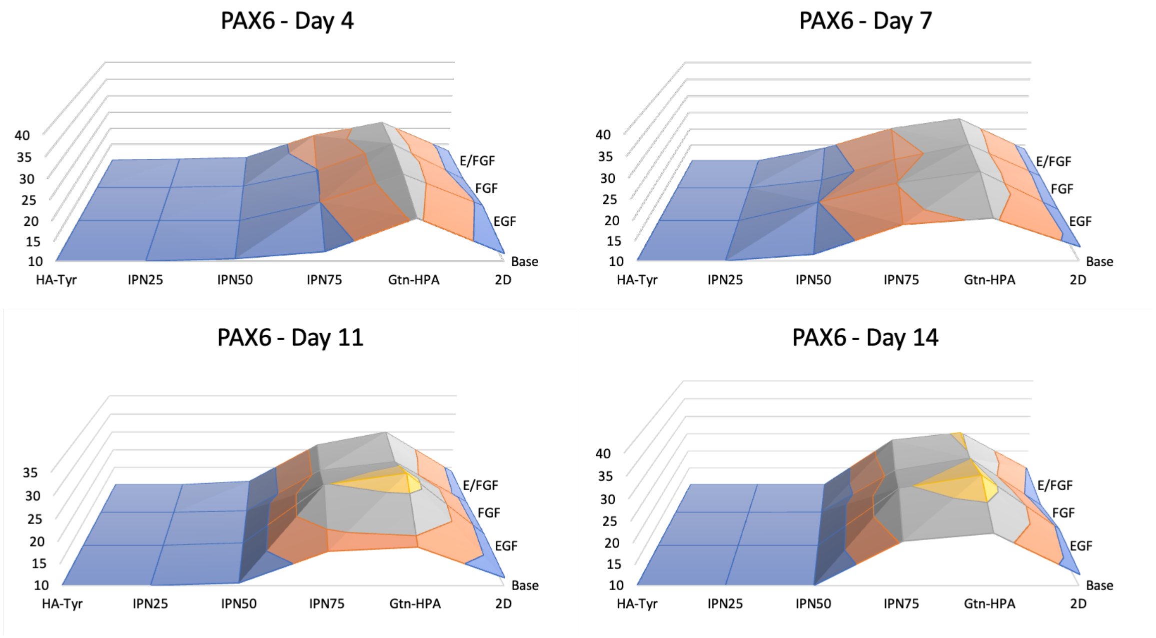

Figure 3.14: Phenotype assay for retinal marker PAX6 of hRPCs in different tissue culture.
Cells were cultured for 2 weeks and phenotype was analyzed at day 4, 7, 11, and 14 for n=5 replicates with flow cytometry. Map surfaces show the media component on the x-axis (base media, EGF, FGF, or both), the tissue culture on the y-axis (2D, Gtn-HPA, IPN75, IPN50, IPN25, and HA-Tyr) and the expression of PAX6 is shown on the z-axis.

marker was deeply affected by the different nutrients added to hRPCs. All samples which did not receive EGF (base media and FGF only) were found to be significantly lower than other samples for all different tissue culture. Therefore both EGF and EGF/FGF samples show higher expression.

Furthermore, we analyzed both a rod marker (rhodopsin) and a cone marker (RGopsin). The data in Figure 3.16 show the same trend as for recoverin with a higher expression for cells cultured in high gelatin content hydrogels, with an increading expression from day 4 to day 14. The same trend for FGF was observed for both rod and cone marker, strongly suggesting that the addition of EGF in the culture of hRPCs signifcantly increase their differentiation towards photoreceptors. A promising result was found when analyzing rod anc cone marker: hRPCs seem have a higher differentiation towards rods for IPN75 while having a higher differentiation towards

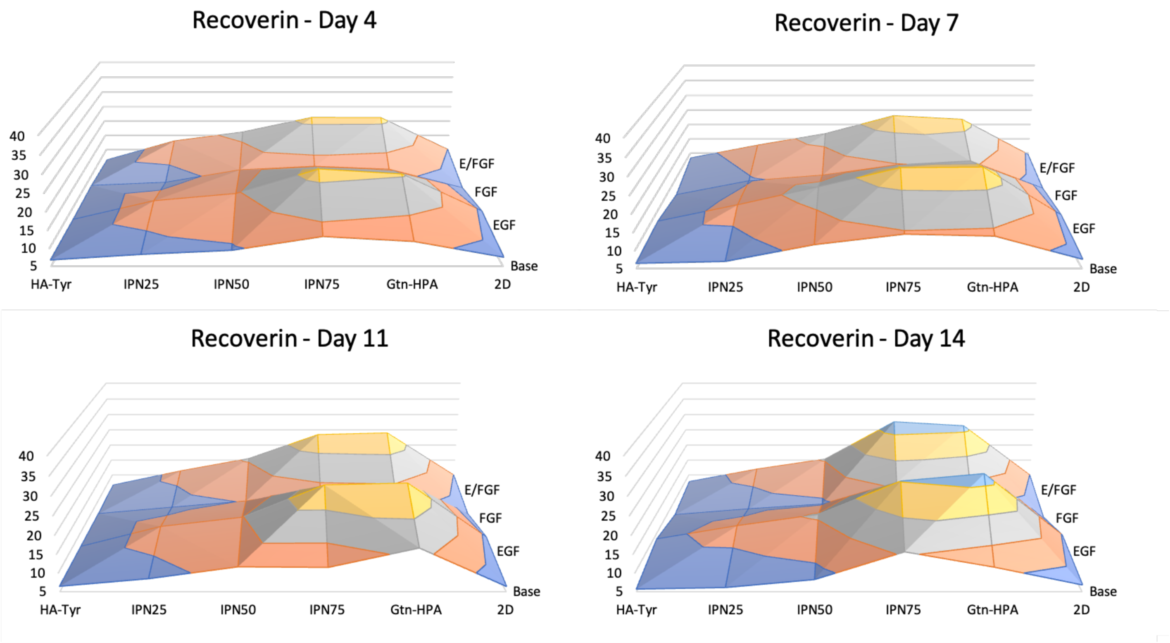

Figure 3.15: Phenotype assay for photoreceptor marker recoverin of hRPCs in different tissue culture.
Cells were cultured for 2 weeks and phenotype was analyzed at day 4, 7, 11, and 14 for n=5 replicates with flow cytometry. Map surfaces show the media component on the x-axis (base media, EGF, FGF, or both), the tissue culture on the y-axis (2D, Gtn-HPA, IPN75, IPN50, IPN25, and HA-Tyr) and the expression of recoverin is shown on the z-axis.

cones for Gtn-HPA.

Of note is that all markers expression were found to be significantly lower for cells cultured in the common 2D tissue protocol compared to encapsulation in hydrogels, suggesting that our hydrogel can greatly impact the differentiation of hRPCs.

Overall, this phenotype analysis of hRPCs encapsulated in different hydrogels with different nutrients added enabled us to show a driven differentiation towards specific type of retinal cells by modulating the stiffness and nutrients added to hRPCs. We showed that stemness expression greatly increases with the addition of HA while early retinal marker decreases. Photoreceptor, rod, and cone markers where found to be significantly higher for cells that received EGF. The rod marker expression was found to be the highest in IPN75 while cone marker expression for Gtn-HPA. Finally, Alamar Blue and viability enabled us to confirm that hydrogel with a high

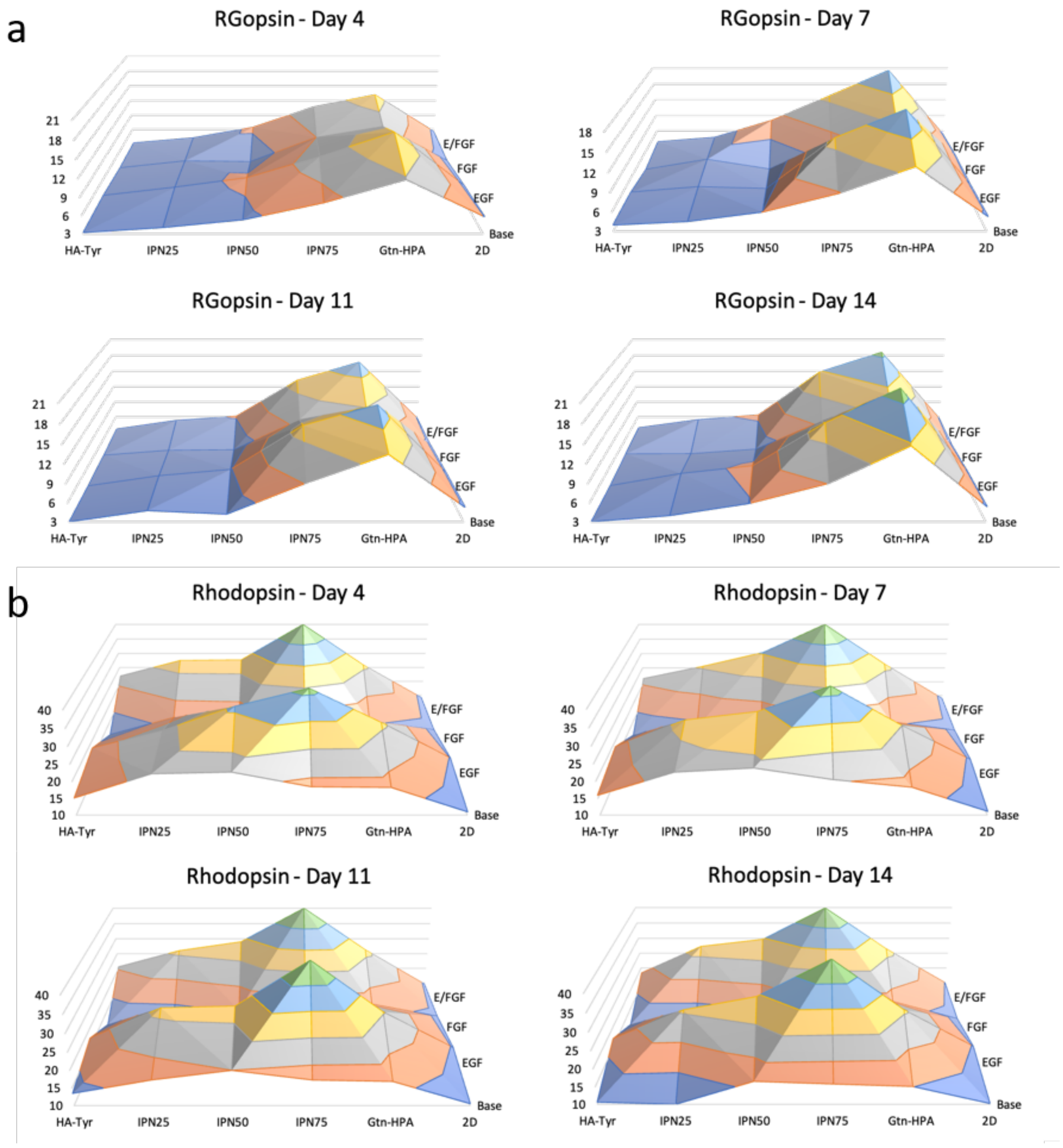

Figure 3.16: Phenotype assay for rod (rhodopsin) and cone (opsin) marker of hRPCs in different tissue culture.
Cells were cultured for 2 weeks and phenotype was analyzed at day 4, 7, 11, and 14 for n=5 replicates with flow cytometry. Map surfaces show the media component on the x-axis (base media, EGF, FGF, or both), the tissue culture on the y-axis (2D, Gtn-HPA, IPN75, IPN50, IPN25, and HA-Tyr) and the expression of **(a)** R/G-opsin **(b)** rhodopsin is shown on the z-axis. Cones show a specific peak for Gtn-HPA while rods show a peak for IPN75.

HA content don't enable cell attachment, proliferation and viability.

3.4.3 Diffusion kinetics of growth factors through hydrogels

Measurement of hydrogel water content

Water in hydrogels can be classified into several types: (i) bound water, which can be divided into strongly bound, weakly bound, and non-bound with nearly bulk water properties; (ii) associated water, which comprises strongly and weakly associated water; and (iii) free water. Previous studies [110] have shown that the water content in hydrogels can be measured by differential scanning calorimetry (DSC). The water fraction can be measured with the following equations:

$$W_{free} = \frac{\Delta H_{gel}(0C)}{\Delta H_{H_2O}} * 100, \qquad W_{bound} = \frac{\Delta H_{gel}(-20C)}{\Delta H_{H_2O}} * 100 \tag{3.16}$$

$$W_{Associated} = W_{total} - W_{free} - W_{bound} \tag{3.17}$$

We performed DSC on homopolymeric and copolymeric networks (IPN50 and IPN75) hydrogels. Freezing and melting transitions of different water types were observed for all samples, as seen in Figure 3.17. A loop artifact (also presented in [126]) was also observed for the bound water heat transition temperature. This artifact is attributed to the extremely large exotherm of bound water crystallization. To try and remove this loop artifact, we turned to computational methods based on theory to remove this artifact. We first used the main trace obtained from 'rapid' DSC to measure the free water heat flow (at 0 ℃, green curve) and differentiate the end of the loop artefact to the normal heat transition (blue and black curves) (Figure 3.18a). We then performed a slow heating and cooling DSC to obtain a more precise loop transition, as seen in Figure 3.18b and 3.18c, the loop artifact was shifted by 5-10 ℃ while the trace for the bound water transition started to take form. This allowed us to create a trace without the presence of a loop artifact by adding all different traces and subtracting the loop artifact in each, which can be seen in Figure 3.18d.

The differential scanning calorimetry performed on wet hydrogels allowed us to

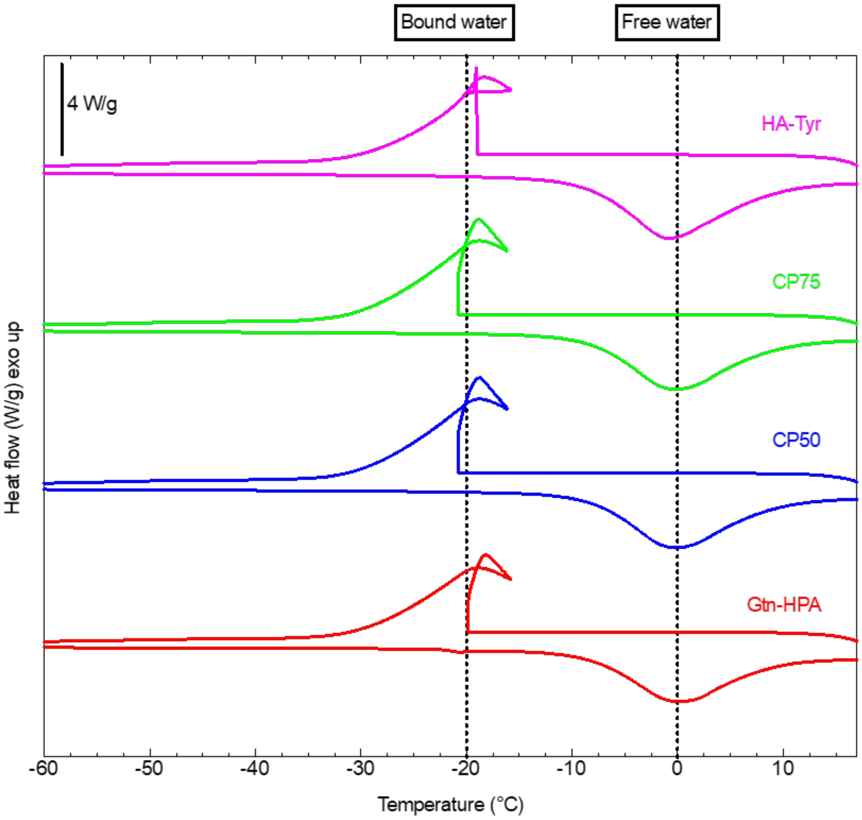

Figure 3.17: Water content measurement in IPNs.
Differential scanning calorimetry traces (heat flow with exotherm up as a function of temperature) for HA-Tyr, CP50, CP75 and Gtn-HPA, ranging from -60 °C to 20 °C showing both bound and free water heat transitions at -20 °C and 0 °C, respectively (dotted lines). The loop artifact is observed in all four samples. The data is shown is one representative run; however, final calculations have been made with heat flow averages. Image reprinted from [61].

quantitatively measure the water content in each of our hydrogel samples using equations 15-17. The hydrogel free water content ranges from 43% (HA-Tyr) to 55% (Gtn-HPA); bound water content ranges from 25% (Gtn-HPA) to 38% (HA-Tyr), while associated water content is mostly constant throughout all samples around 23%.

We, then, examined the water content in relation to hydrogel's stiffness. The hydrogels' shear moduli G' when applying a constant shear rate were measured over time, as seen in Figure 3.19a. Hydrogel stiffness increases with the addition of HA-Tyr to the mixture, starting at approximately 600 Pa for homopolymeric Gtn-HPA, 950 Pa

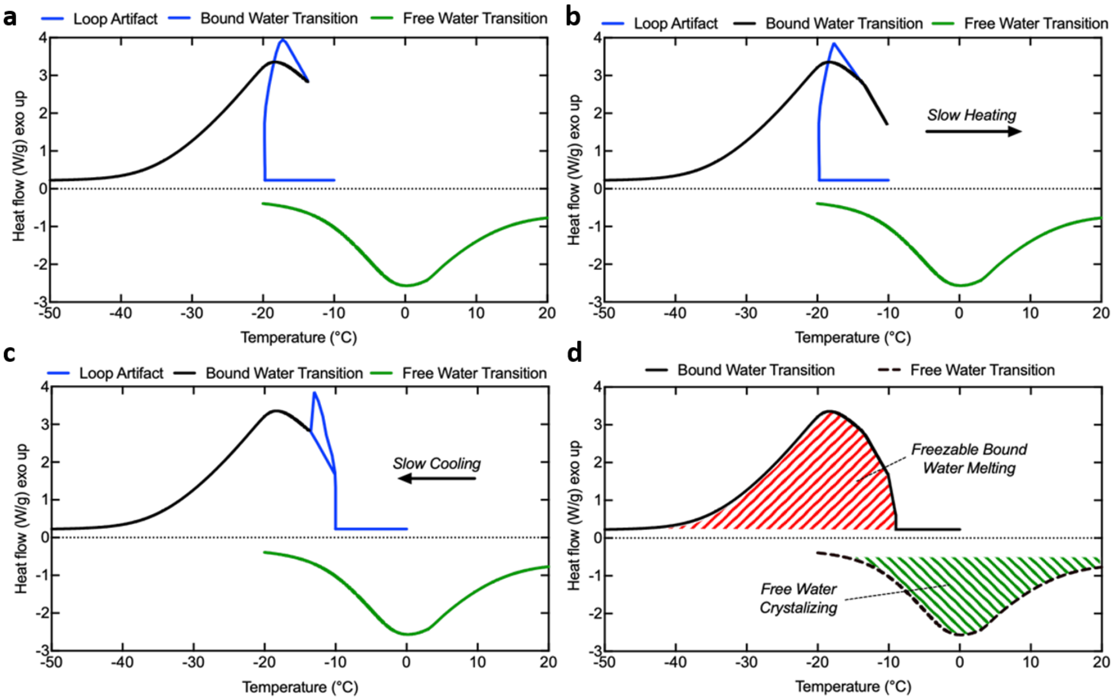

Figure 3.18: Loop artifact removal using computational methods. **(a-d)** DSC traces for Gtn-HPA with different slowing and heating speeds to reduce the loop artifact. **(a)** Normal speed (10 °C/min) cooling trace for Gtn-HPA. **(b)** Slow heating curve (0.1 °C/min). **(c)** Slow cooling curve (-0.1 °C/min). **(d)** Final DSC trace obtained by the addition of all other experiments by subtracting the loop artifact. Image reprinted from [61].

for CP50, and 1440 PA for homopolymeric HA-Tyr. We were finally able to compare the water content of those hydrogels with their respective stiffness for all three water types (trend lines in Figure 3.19b). As expected and explained in many studies [127], the free water content linearly decreases with stiffness while the bound water linearly increases. A statistically significant difference was found between Gtn-HPA and HA-Tyr for both free and bound water. Importantly, the associated water stays constant in all samples, showing an equilibrium relationship between free water and bound water when changing the amount of Gtn-HPA in our copolymeric networks.

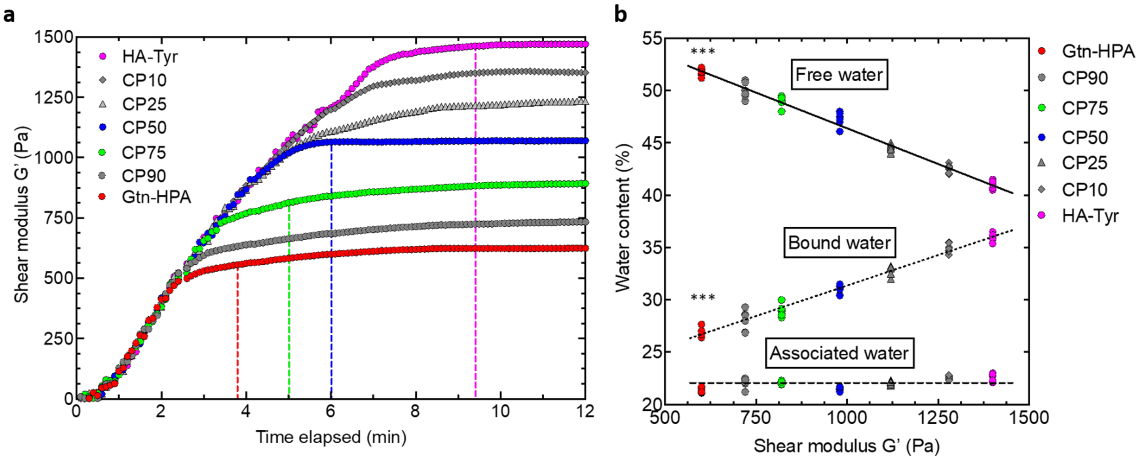

Figure 3.19: Stiffness measurement and relationship to water content. **(a)** Oscillatory rheology measurement of shear modulus G' (Pa) for all samples (Gtn-HPA, CP75, CP50, CP25 and HA-Tyr). The final value was obtained when the plateau was reached. The vertical dotted line shows the time to reach plateau. Values are shown as an average of n = 5 replicates. **(b)** Water content (%) of hydrogel samples as a function of their stiffness (G'). A linear regression was performed for all three water types: solid line for free water, dotted line for bound water, and dashed line for associated water. Values shown as all replicates (n = 5). A statistical difference is observed between Gtn-HPA and HA-Tyr for both free and bound water (***p=0.001). Image reprinted from [61].

Measuring hEGF release from gels

To further understand the mechanism of drug and growth factor release in the eye, we analyzed the release of human epidermal growth factor (hEGF), which is presently used in ophthalmic disease treatments. We performed a bio-release assay with an hEGF ELISA kit for 11 days. As injectable and biodegradable matrices, we also focused on the burst release of the biomaterials with a precise measurement for the first 120 minutes. A 4-parameter logistic curve fit was applied to the standard, which can be seen in the inset of Figure 3.20a. hEGF overall and sustained release for all samples is plotted in Figure 3.20a. We observe no significant difference between all samples in the sustained release period, defined as after one day. We also analyzed faster hEGF release in 15 min increments from hydrogel formation until 90 min. The results of this burst release can be seen in Figure 3.20. Linear, rapid burst release profiles were observed until 45-60 minutes for all samples. Statistical analysis shows a notably significant difference between all samples during this burst release phase. This difference showed that increasing the amount of Gtn-HPA in the mixture increases the burst release rate of hEGF. For all samples, the average mass release of hEGF was around 50 ng (5% of total mass) at 15 min, 90 ng (9% of total mass) at 30 min, and 140 ng (14% of total mass) at 45 min. To compare the burst release value to a diffusion mechanism, we measured the coefficient of burst release normalized by the total mass of release (1 µg) (Figure 3.20b, inset). As observed in Figure 3.20b, Gtn-HPA possesses a higher burst release coefficient than all other samples (0.2), and a statistically significant higher coefficient than HA-Tyr (0.176).

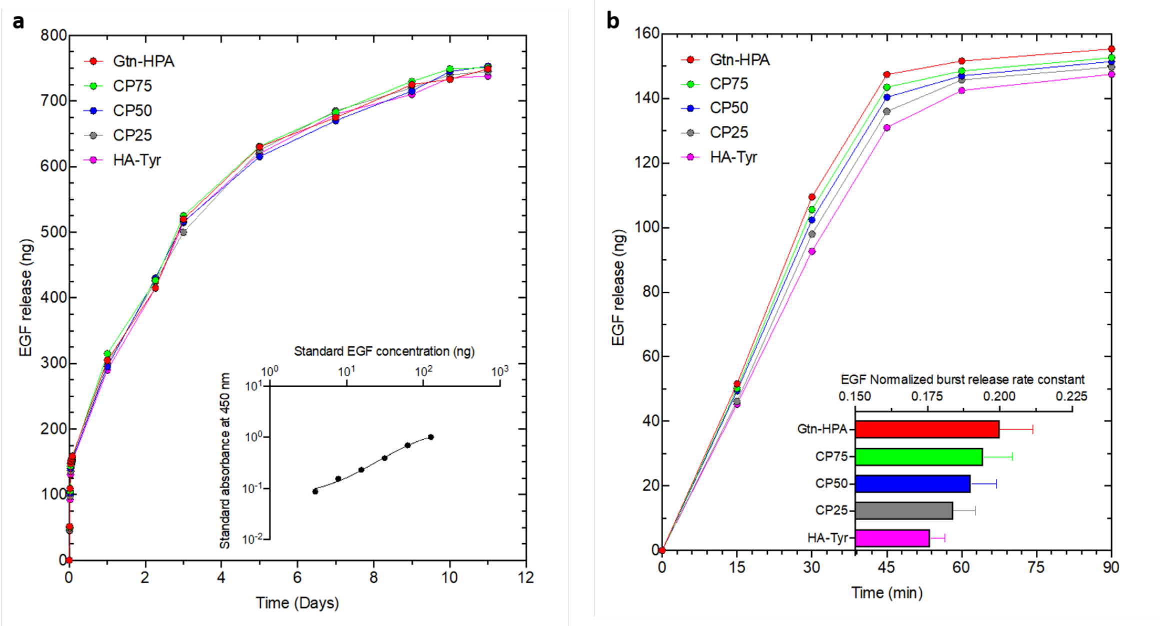

Figure 3.20: Human epidermal growth factor (hEGF) release analysis from hydrogels.
(a) Sustained release of hEGF from hydrogels over 11 days. Inset: standard curve analyzed with a four-parameter logistic fitting curve to convert absorbance into hEGF concentration. **(b)** Burst release period of hEGF from hydrogel over the first 90 minutes. Inset: hEGF normalized burst release constant, measured during the first hour of release. A statistical difference is found between all samples at t = 30, 45 and 60 min, and between Gtn-HPA and HA-Tyr burst release constants (**p=0.005). Image reprinted from [61].

Relating water content with hEGF release and diffusion theories

To finalize our results, we analyzed the relationship between the free water fraction, the stiffness (G'), and the burst release coefficient found in the hEGF release experiment, as seen in Figure 3.21a. The hEGF burst release coefficient from hydrogels was found to be linearly increasing with the free water fraction, ranging from 0.176 at 41% free water in HA-Tyr to 0.2 at 53% free water in Gtn-HPA. A statistically significant difference was found between both homopolymeric networks. Contrarily, stiffer hydrogels display a lower hEGF burst release, with a difference of 0.024 between Gtn-HPA at 600 Pa and HA-Tyr at 1440 Pa. This result suggest that burst release of growth factor is tightly related to the free water fraction and stiffness of hydrogels. Studying the structure formed by the polymeric networks could help us understand the mechanisms of diffusion and growth factor release. The formation of all samples (Gtn-HPA, HA-Tyr and CP) are catalyzed with HRP and crosslinked with H_2O_2 in the same manner via an enzymatically crosslinking reaction, which we expect should create fully random copolymeric networks, for CP. To investigate this hypothesis, we analyzed the network structures with hydrogel degradation assays using collagenase IV. As observed in Figure 3.21b, all Gtn-HPA was degraded after 30 minutes of incubation. Furthermore, we observed that collagenase IV has no impact on HA-Tyr alone. However, CP75, CP50 and CP25 had 30.9%, 49.3% and 77.3% of their volume remaining after degradation, respectively, corresponding to the fraction of Gtn-HPA mixed into the copolymeric network.

Due to the relatively high degree of freedom of Gelatin Hyaluronic fibers in the hydrogels and their low weight fraction of polymer (2 wt%), we can consider these hydrogels as homogeneous. Table 3.2 summarizes the different theories of diffusion and their equations for free volume, hydrodynamic, and obstruction theories for both heterogenous and homogeneous hydrogels. To be able to compare our experimental release of hEGF with theoretical models of diffusion, we normalized the burst release of hEGF. Furthermore, by using the charge, affinity, molecular weight of hEGF, the molecular weight and chemical characteristics of our hydrogels along with values from

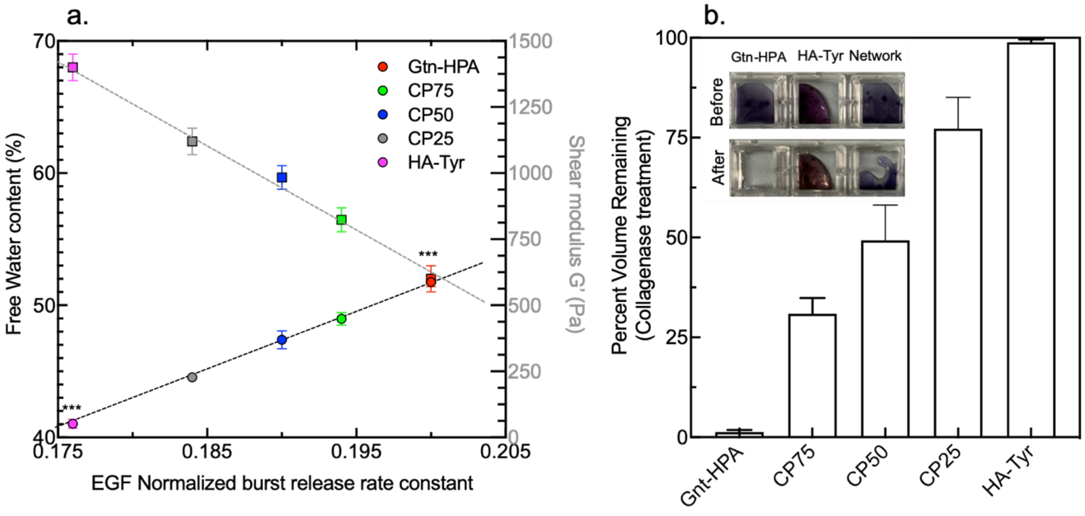

Figure 3.21: Relationship between hEGF release, water content, and hydrogel stiffness.
(a) Final comparison between free water content (circle) and stiffness (square) with normalized burst release hEGF coefficient. The burst release of hEGF was found to increase with free water fraction and decrease with stiffness. A statistically significant difference was found for both variables between Gtn-HPA and HA-Tyr (***p=0.001). **(b)** Degradation assay of pure Gtn-HPA, CP and pure HA-Tyr using a collagenase IV treatment. The percentage of remaining volume post treatment was measured for all hydrogels. HA-Tyr showed little to no volume decrease while all of Gtn-HPA was degraded. Image reprinted from [61].

previous studies [128] and our polymers [116], we were able to predict an average value for the free volume theory as $D_g/D_0 = 0.1$, the hydrodynamic theory as $D_g/D_0 = 0.2$, and the obstruction theory as $D_g/D_0 = 0.4$. These values correspond to the actual diffusion coefficient normalized by the maximum diffusion coefficient of solute (hEGF in our case) at infinite dilution (near-pure water in our case). Experimentally, we observed that all hEGF diffusion release values were around 0.17-0.2, which is comparable to the hydrodynamic theory prediction of 0.2.

Table 3.2: Theories of solute diffusion within heterogeneous and homogenous hydrogels.

Model	**Equation**	**Predicted Value**	**Type**	**Refs**
Free Volume	$\frac{D_g}{D_0} = (1 - k_1 r_s \theta^{0.75}) exp\left(-k_2 r_s^2 \left(\frac{\theta}{1-\theta}\right)\right)$	0.1	Homogeneou hydrogel	[129]
Hydrodynamic	$\frac{D_g}{D_0} = -exp(-k_c r_s \theta^{0.75})$	0.2	Homogeneou hydrogel	[106]
Hydrodynamic	$\frac{D_e}{D_0} = exp\left[-\left(\frac{a\pi L_c N_A}{M_f ln\left(\frac{L_c}{2r_f}\right)}\right) r_s \theta^{0.5}\right]$	N/A	Heterogeneou hydrogel	[106]
Obstruction	$\frac{D_g}{D_0} = exp(-0.84\alpha^{1.09})]$	N/A	Homogeneou hydrogel	[108]
Obstruction	$\frac{D_g}{D_0} = exp\left[-\pi\left(\frac{r_s+r_f}{k_s\alpha^{0.5}+r_f}\right)^2\right]$	N/A	Heterogeneou hydrogel	[128]

3.4.4 Hydrogels protect cells from shear stress applied during injection

Stress and strain modeling in Gtn-HPA and PBS

Velocity profiles were modeled from Poiseuille flow and cell-marginal free layer model as described previously. Due to the non-Newtonian aspect of Gtn-HPA and its property of being in the process of gelation in the syringe, its viscosity and shear modulus are evolving. To characterize a representative value of the shear stress applied on hRPCs, we first calculated the velocity profile (and therefore the maximum velocity) for PBS (Figure 3.22A blue curve), using Poiseuille flow equations, and for different viscosities of Gtn-HPA (Figure 3.22A red curves), using the marginal cell-free layer model, varying from 1.5 mPa.s to >1000 mPa.s. The maximum velocity (located at the center of the syringe) is inversely related to viscosity of Gtn-HPA. Gtn-HPA's viscosity, after full gelation, crosslinking and, stability (30 minutes incubation) has been measured at 400 Pa.s [87], when crosslinked with 0.1 U/ml of horseradish peroxidase and 1 mM of H_2O_2. The modeling we performed here, suggests that, when the viscosity of the pre-gel Gtn-HPA reaches 1000 mPa.s (lowest red curve on Figure 3.22A) the maximum velocity applied on hRPCs remains constant and is minimal (1.71*10-3 m/s). Due to the fast gelation time of Gtn-HPA in our experiments (less than 1 min) and its large viscosity at the end (400 Pa.s) we can consider that minimal velocity was reached almost immediately in the experiments. The marginal cell-free layer model also includes another variable to determine (δ) which corresponds to the size of the cell-free layer. Due to Poiseuille flow, cells will be pushed towards the center of the needle while being pushed through the syringe to reach the subretinal space or during the seeding process. Therefore, the cell-free layer δ is playing a major role in the modeling of shear stress as seen in Figure 3.22B. Different cell-free layer δ will create different velocity profiles for cells in Gtn-HPA. The cell-free layer δ dramatically increases the maximum velocity and the shear stress applied to the cells. Due to the size of hRPCs [114], the gelation process of Gtn-HPA [112] and the low compressive force applied on cells [130], we can assume that only the smallest δ, seen on Figure 3.22B (bottom red curve), can be used in this model.

These velocity profiles enable us to calculate the differences of maximum velocity applied to hRPCs in PBS (V_{max}= 0.535 m/s) and hRPCs embedded in Gtn-HPA (V_{max}= $1.71*10^{-3}$ m/s). By using different constitutive laws [131], and knowing the viscosity of PBS [132] and Gtn-HPA, we have calculated the final shear stress and shear strain applied on the cells in both groups (Figure 3.22C). After calculation, some approximations have been used in order to derive the shear strain exerted on each cell. By using the Young's modulus of hRPCs [101] and Gtn-HPA (described in a previous study [112]), the strain (or elongation) applied on cells can be modeled in PBS (0.7%) and in Gtn-HPA (0.004%). A 300-fold and 200-fold decrease, respectively for shear stress and shear strain, was calculated for cells in PBS compare to Gtn-HPA. The combination of the Poiseuille flow equations and the marginal cell-free layer model clearly suggests the high impact of Gtn-HPA on protecting cells from stress and strain exerted during injection, due to its high viscosity.

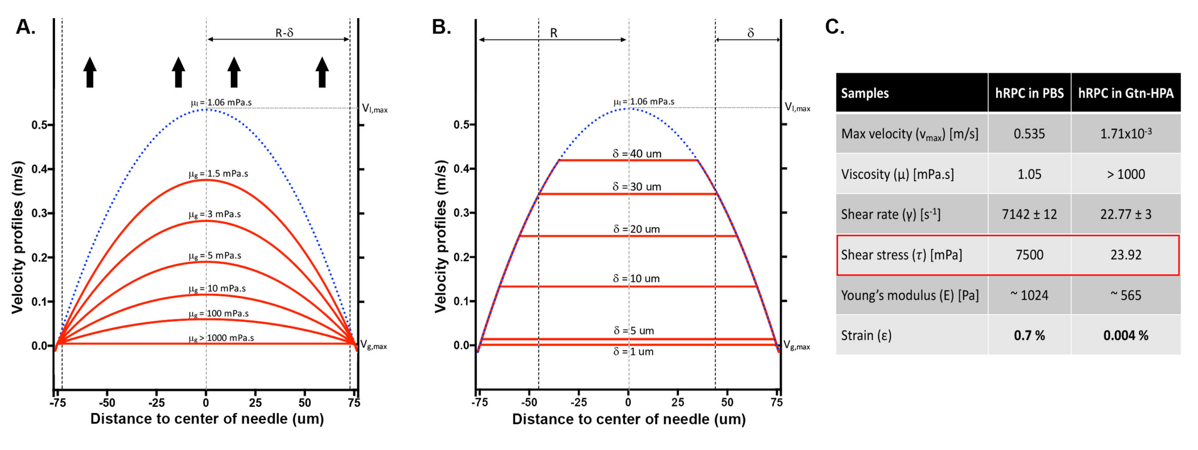

Samples	hRPC in PBS	hRPC in Gtn-HPA
Max velocity (v_{max}) [m/s]	0.535	1.71×10^{-3}
Viscosity (μ) [mPa.s]	1.05	> 1000
Shear rate (γ) [s^{-1}]	7142 ± 12	22.77 ± 3
Shear stress (τ) [mPa]	7500	23.92
Young's modulus (E) [Pa]	~ 1024	~ 565
Strain (ε)	**0.7 %**	**0.004 %**

Figure 3.22: Shear stress/strain modeling for hRPCs embedded in Gtn-HPA and PBS.
Data was modeled according to the marginal cell-layer model and Poiseuille flow using MATLAB code. **A.** Velocity profile for cells in PBS (blue curve) and velocity profiles for cells in Gtn-HPA for different viscosity of gel (red curves), viscosity is labelled on top of each curve. **B.** Velocity profiles for cells in PBS (blue) and velocity profiles for cells in Gtn-HPA for different cell-free layer (δ in red). **C.** Calculation of maximum velocity, shear rate, shear stress and strain applied to hRPCs both in PBS and Gtn-HPA. Image reprinted from [75].

hRPCs viability assay in Gtn-HPA with shear stress

hRPCs cultured in different conditions with shear stress applied were analyzed using a live-dead assay, after 1,3 and 6 days of culture. To measure the protective aspect of Gtn-HPA on cells subjected to shear stress, direct comparison between normal and stressed samples was performed for both PBS and Gtn-HPA group (Figure 3.23a). Shear stress substantially reduced cell viability in all the non-gel groups (media, PBS, and hEGF). hRPCs in Gtn-HPA showed significantly higher viability in comparison to all the other groups. Furthermore, cell viability on 1, 3 and 6 days for the Gtn-HPA group remained constant (no statistical differences) with a drop of less than 5% (Figure 3.23b) after applying shear stress onto the sample. Shear stress applied on cells cultured in PBS significantly decreases their viability even at day 1: from 68% to 28%. hEGF, a known component that helps in cellular growth [133] showed a higher viability than PBS, however, without the protecting covering of Gtn-HPA, the percentage of viable cells drops in hEGF group when shear stress is applied. Our results show that Gtn-HPA gel could make a statistically significant difference on cellular viability even for hRPCs deprived from media, for 6 days, and with shear stress applied at seeding.

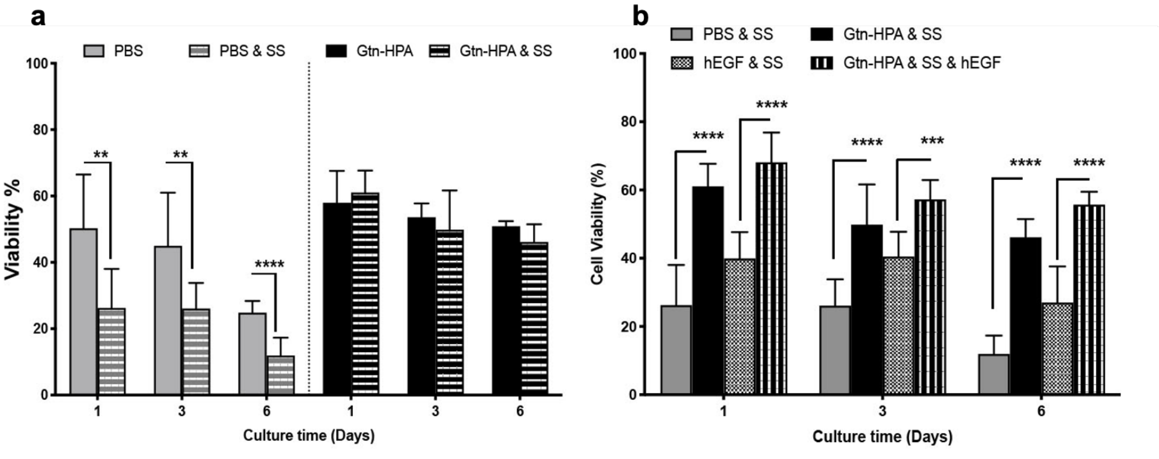

Figure 3.23: Live/Dead assay of hRPCs by immunohistochemistry with applied shear stress.
(a) Data comparison of 2D (PBS) and 3D (Gtn-HPA) cultures on hRPCs seeded with or without shear stress applied. **(b)** Viability data summary of shear stress applied on hRPCs on all different groups. Data shown as mean ± SEM of triplicate wells with 15 different fields for each well. Three-way ANOVA was performed and shows that shear stress reduces significantly cell viability in all 2D culture wells but not in Gtn-HPA wells (***p=0.0005). Image modified from [75].

To accurately quantify the number of viable cells, immunohistochemistry was performed using calcein-AM (FITC) and ethidium bromide (APC) as live/dead assay. Shear stress (Figure 3.24) resulted in significant drop in cell viability across all the groups except Gtn-HPA (with or without hEGF). Indeed, cells embedded in Gtn-HPA show a drop of only 7% in viability when subjected to shear stress while cells in PBS have their viability decreased by almost 30%. To isolate the effect of shear stress, cells in all groups were seeded in same density and cultured in the same buffer. To correlate the in vitro experiments results with the modeling of shear stress the same seeding strategy was applied to all samples. To keep the results consistent, both seeding (with 200 µl pipette and with 31-gauge syringe) were performed at a constant rate (10 seconds injection time was kept constant).

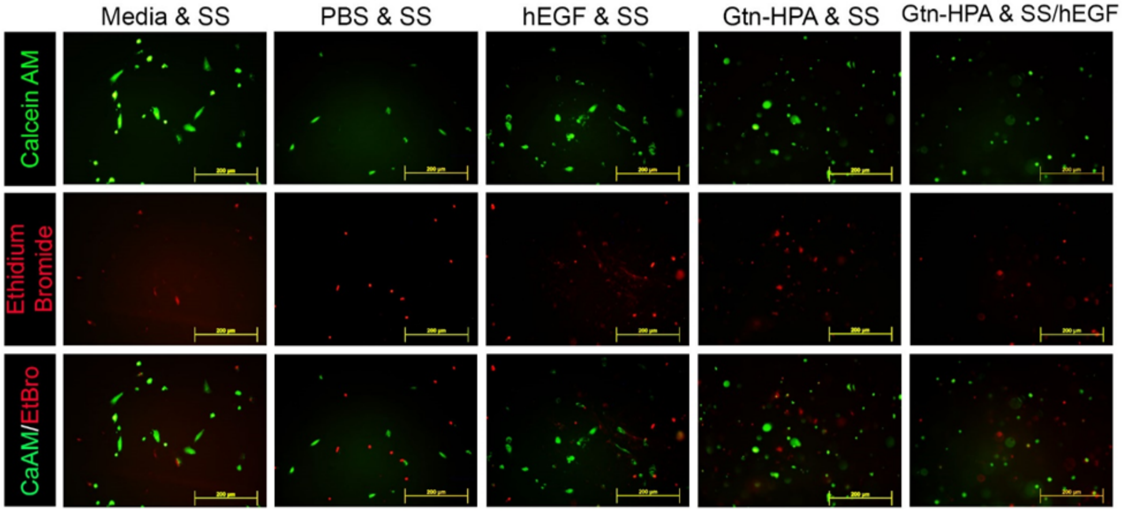

Figure 3.24: Fluorescence images of live/dead assay for hRPCs with shear stress applied.
All images were taken at 40X magnification. Fluorescence images of Live/Dead assay performed on hRPCs with Calcein-AM as live staining (FITC channel), Ethidium Bromide as dead staining (APC channel) and, merged pictures for Media, PBS, hEGF, Gtn-HPA and Gtn-HPA & hEGF all with shear stress (SS). Scale bar is 200 µm in all images. Image modified from [75].

The sharp decrease in cell viability in 2D cultures (PBS or hEGF), deprived from most nutrients, can be directly correlated to the shear stress exerted from the 31-gauge syringe during cell seeding. It is well known that shear stress modulates cellular response and directly affects cell-cell and cell-membrane interactions [134]. This could be the reason that despite the same cell seeding density, dramatically lower number of cells were observed in stressed 2D cultures. Gtn-HPA being a highly porous environment with an open interconnected geometry, it creates a large surface area relative to the scaffold's volume. Therefore, cells are enclosed in a scaffold that allows for better cell-cell interaction which provides time for cells to recover from initial stress experienced during the seeding. Our live/dead assay results clearly demonstrate the harmful effect of shear stress on cell viability and the protective nature of a 3D culture scaffold (Gtn-HPA) for hRPCs undergoing this stress.

hRPCs proliferation and apoptosis assays

hRPCs seeded in PBS and in 3D Gtn-HPA, with and without shear stress applied, were assessed for proliferation and apoptosis. At various time points (1 and 3 days), cell proliferation rate was monitored using Ki-67 staining. Ki-67 is a protein in cells that increases during cell division [135]. Staining process can help measure the percentage of cells expressing this protein and their proliferation index can hence be calculated. Proliferation was significantly higher in cells embedded in Gtn-HPA than cultured in 2D monolayer system (Figure 3.25), for stressed and non-stressed samples, with a drop of approximately 15% in both cases. Furthermore, Ki-67 expression appears to be reduced by a similar margin following shear stress in PBS conditions as it is in Gtn-HPA conditions. Indeed, a reduction of approximately 12% is found from PBS to PBS with shear stress, and 14% from Gtn-HPA to Gtn-HPA with shear stress. These similar findings suggest that Gtn-HPA, being a more favorable culture condition than PBS in terms of viability, has low impact on protecting cell proliferation from shear stress exerted during transplantation.

Mid phase apoptosis is the junction at which 2 different apoptotic pathway converges [136]. However, it is still possible to differentiate between intrinsic and extrinsic pathways using specific stains. This is a critical point as it helps to determine if the cell death is due to necrosis or apoptotic process. At this apoptotic phase, mitochondrial outer membrane permeabilization (MOMP) is followed by cytochrome-c and apoptotic protease activating factor-1. They join together to form the apoptosome and activate Caspase-9 (Cas9) [137]. Cas9 staining has been performed on hRPCs seeded in PBS and Gtn-HPA with or without shear stress applied. In the experimental groups, the highest apoptosis was observed in the hRPCs cultured in PBS under shear stress. All other groups show a similar fraction of apoptotic cells around 6-7% (PBS, Gtn-HPA and Gtn-HPA with shear stress). These results indicate the impact of shear stress on hRPCs. Furthermore, it promotes the aspect that Gtn-HPA protects cells from apoptosis due to this shear stress.

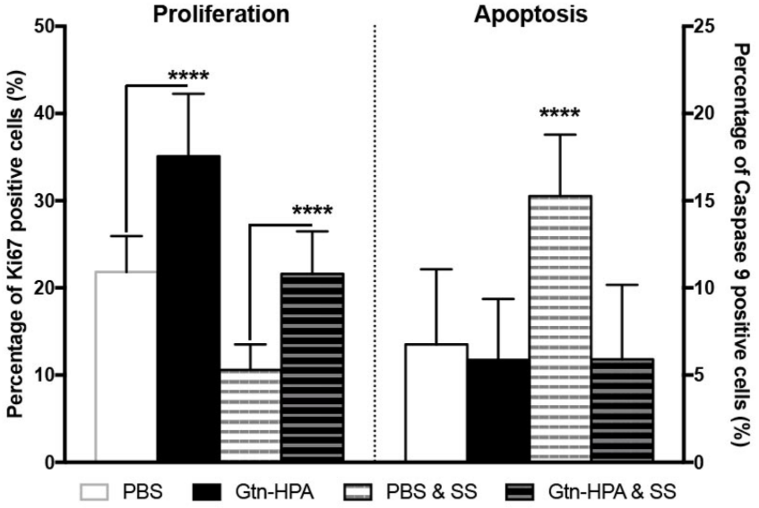

Figure 3.25: Apoptosis and Proliferation assay of hRPCs.
Data analysis of proliferation (Ki-67) and apoptosis (Cas9) staining. Data shown as mean ± SEM of triplicate wells with 15 different fields for each well. One-way ANOVA was performed and shows a significant difference between hRPCs in PBS and hRPCs in Gtn-HPA for proliferation (p=0.0001). Apoptosis is significantly higher for cells in PBS with shear stress compare to all other groups (p=0.0001). Image reprinted from [75].

hRPCs subjected to shear stress phenotype analysis

We quantified hRPCs expression using a flow cytometer to analyze up or down regulation of key retinal markers along with stemness and proliferation markers. Oct4 and C-myc are key genes that regulate stemness in progenitor cells [123]. Without shear stress about 15-18% of hRPCs were expressing both the markers in PBS and Gtn-HPA samples. The cell expression of these stemness markers dropped to 5-7% in both groups when shear stress was applied. This result indicates that stemness is significantly affected by shear stress and that Gtn-HPA alone is not sufficient to protect stemness expression in hRPCs. However, when cultured in presence of Gtn-HPA and hEGF, cells were able to retain their stemness with 30% of cells expressing Oct4 and C-myc (Figure 3.26A) even after shear stress was applied. This result confirms that hEGF (together with a protective hydrogel Gtn-HPA) is a growth factor that has the ability to maintain the differentiation potency of stem cells [81].

Next, we quantified hRPCs expression for typical retinal markers (Figure 3.26B) such as S-opsin and cone arrestin [138]. Opsins are a group of proteins, light-sensitive, found in photoreceptors (rods and cones) which regulate the conversion of photons into electrochemical signal. Interestingly, a higher percentage of cells expressing cone arrestin was observed in PBS than Gtn-HPA. However, this percentage drops (from 60 to 35%) once hRPCs are stressed, suggesting cells behavior is altered in PBS but their behavior remains unchanged when cells are encapsulated in Gtn-HPA (40% cone arrestin expression with and without shear stress). S-opsin expression was significantly higher in Gtn-HPA compare to PBS, and shear stress doesn't seem to impact its expression. Similar trends were observed with PAX6 which is an early retinal cell marker [125]. PAX6 expression was high in samples without shear stress and significantly reduced when cells were stressed (Figure 3.26C). A sharp decrease of PAX6 expression was seen in PBS when shear stress was applied (from 38 to 8%) as compare to the Gtn-HPA samples which expression remained constant (from 27 to 23%). Finally, Ki-67 expression was studied to confirm the results found in immunohistochemistry. About 40% of hRPCs were expressing Ki-67 in Gtn-HPA and hEGF cultures but less than 10% of cells were found positive in the PBS group. These results further drop to 20% and 5% respectively after applying shear stress.

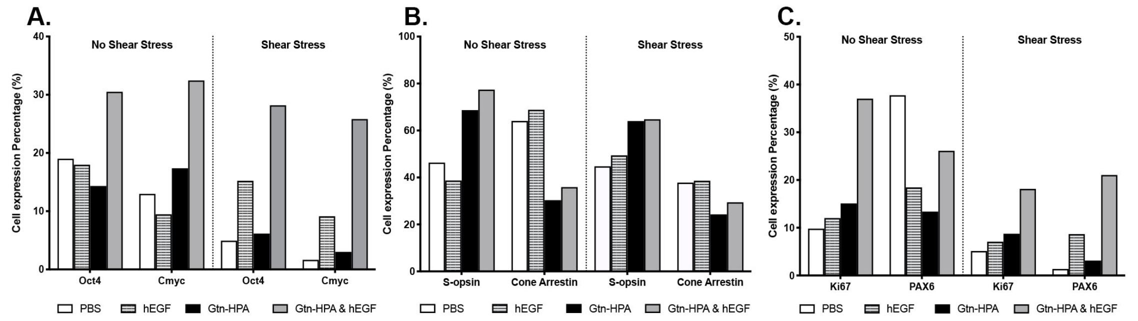

Figure 3.26: Flow cytometry data for hRPCs in 2D or 3D cultures.
hRPCs cultured in PBS, within 2%wt Gtn-HPA and, within 2%wt Gtn-HPA with 20 ng/ml hEGF were analyzed with and without shear stress applied (n=3). **A.** Percentage of positive hRPCs which express stemness markers (C-myc and Oct4). **B.** Percentage of positive hRPCs which express cone cell markers (S-opsin and cone Arrestin). **C.** Percentage of positive hRPCs which express retinal and proliferation markers (respectively PAX6 and Ki67). Image reprinted from [75].

Flow cytometry data shows a clear pattern in which the percentage of cells expressing stemness marker drops upon experiencing shear stress, which is also indicated by a decrease in Ki67 positive cells. Furthermore, in Gtn-HPA cultures, the stemness, retinal and proliferative markers quantification suggest that hydrogel increases hRPCs expression in comparison to the PBS only culture. Finally, Gtn-HPA (in combination with hEGF) can maintain specific photoreceptor marker expressions in cells subjected to shear stress. All cells were deprived of most nutrients (no media culture for flow cytometry assay) but were still proliferative and expressing retinal markers. This also provides an added advantage for cells during transplantation.

3.5 Discussion

Recently, it has been identified that the natural ECM of retina is composed of collagen, hyaluronic acid and chondroitin sulfate [139]. Using gelatin, which is natural derivative of collagen, reduces the immunogenicity associated with the collagen polymer. Gelatin also retains the RGD motif that helps in cellular attachment and signaling via integrin receptor. This further promotes cell survival and differentiation [140]. Using HA can help in tuning the hydrogel for mechanical characteristics and further driving cell differentiation. To understand the effect of the scaffold on cells, numerous studies have been performed which have clearly demonstrated scaffolds can alter cellular behavior [141], [142]. Using apparatus that imparts mechanical strain to cells in vitro, it has been found that mechanical stress affects cardiac stem cells by inhibiting cell growth and increasing apoptosis [143]. Furthermore, mechanical strain increases inflammatory cytokines and angiogenic growth factors production. So far, no such studies have been performed on retinal cells to evaluate the effect of hydrogel encapsulation on these cells.

In this study we have observed and analyzed the effect of Gtn-HPA and HA-Tyr on encapsulated hRPCs for short and long-term. We were able to prove that by optimizing our hydrogels with the right catalyst (HRP), crosslinker (H_2O_2) and gelatin concentration, we were able to obtain hRPCs with a high viability, proliferation and a maintain phenotype and morphology compared to hRPCs culture in defined protocol (2D). Higher cell survival could also be attributed to the fact that hydrophilic Gtn-HPA promotes protein adsorption leading to better cell attachment and survival [87]. By changing the hydrogel content (different mixing of Gtn-HPA and HA-Tyr) we were able to observe different phenotype in hRPCs encapsulated for more than 14 days. As suggested in many studies [144], stiffness has a critical impact on stem cells differentiation. Of note is that we were able to observe specific differentiation of hRPCs into retinal subpopulation (such as rods or cones) by only changing our hydrogels content and therefore their stiffness, without any modification of hRPCs viability. This result offers the possibility to tune these hydrogels to further differentiate hRPCs into the specific retinal cell needed for retinal regeneration.

Analysis of the amount and state of bound and un-bound water content in 3D gels provides valuable information about the architecture and characteristics of hydrogels. In the case of macroporous materials, unbound water can form an interconnected network of pores that facilitates the nutrient movement. Researchers have shown that the presence of macroporous walls allows the ingrowth of cells that over time can assist in in vitro neo-tissue formation [145]. Designing hydrogels with high volume fractions of unbound water provides a route to biomaterials that overcomes this limitation through facile nutrient transport. It has been shown in multiple studies [146] that the diffusion of small particles, drugs, or cells inside hydrogels happens mostly through free water, as bound and associated water is either too close or too attached to polymer chains to allow solute diffusion. Our results, suggesting that free water content increases with the addition of Gtn-HPA in the mix enable the creation of a tunable copolymeric network where free or bound water fraction can be selected by simply changing the fraction of each polymer in the network. Understanding the state of water in hydrogels allows us to probe their nanoarchitecture and predict the thermodynamic properties of the matrix, which in turn impacts the diffusion of the loaded particles. In our experiments with hEGF, we established that a sustained, controlled release of growth factor is possible without compromising the biocompatibility or mechanical property of the gel. Thus, it is possible to tailor make the hydrogel to achieve growth factor or drug release depending upon the end application.

Stem and retinal progenitor cells are promising sources for replacing degenerated photoreceptors in many retinal diseases [30], [31]. However, the efficiency of the cell delivery vehicle and its influence on the grafting of the exogenous cells with the host has remained a major challenge in the field [60], [147]. One of the critical aspects of cell therapies that needs to be addressed is the stress that these cells experience during the injection [93]. In the in vitro system, cells are cultured in abundance with medium and growth supplements without any stress. However, these cells subsequently experience a substantial shear stress as they are injected into the eye (subretinal space for photoreceptors) in a small bore needle [94]. The diameter of these needles is usually around 31-gauge, with the cells mostly suspended at a concentration of 100k per microliter. Cells cultured in vitro are usually seeded using pipette tips that have an orifice around 1.2 mm allowing easy flow of cells. However, for injection in vivo, the 31-gauge needle inner diameter is about 0.15 mm resulting in 100 times more shear stress on cells (due to the R2 dependence of the maximum velocity found in our model). This could lead to a higher cell death and failure to integrate with the host tissue.

In this study, we have tried to mimic the stress experienced by cells in a clinical setting [53] by mimicking transplantation in vitro. Different culture conditions were used to optimize the best suited condition for hRPCs culture. This in vitro approach allowed us to isolate the effect of shear stress from other in vitro factors that affect stem cell-based therapies [81], [148]. Cells, cultured in vitro, in a 2D environment with PBS showed the lowest cellular proliferation and the highest apoptosis when shear stress was applied. In contrast, the 3D culture using Gtn-HPA showed 4 times higher proliferative and 2 times less apoptotic cells. There could be two reasons for this: 1) the surface area provided by Gtn-HPA is much higher than 2D culture [149]; and 2) cells were mixed in pre-gel when casted onto the coverslip, hence, as the gelation occurred, cells were subjected to a 300 times lower shear stress than when seeded without the gel (marginal cell-free layer modeling). Because the survival and engraftment of these cells directly correlate with the functional recovery of the retina, shear stress can alter the behavior of these cells by reducing the survival and proliferation of hRPCs post transplantation. This shear stress, exerted during transplantation, has a significant effect on the growth, proliferation, and differentiation of hRPCs, as observed with the live/dead assay and flow cytometry results. We found that shear stress significantly inhibited stemness and retinal cell expression along with suppressing Ki-67 (proliferation marker). This is critical as the in-vitro setup mimicked implantation condition. It clearly suggests that using Gtn-HPA aided in protecting cells from shear stress that was exerted from the needle in the in vitro seeding.

Chapter 4

Optimization of retinal cells culture and NF1-OPG animal model

4.1 Introduction

One important objective to be able to study retinal regeneration using different stem cells and biomaterials is to optimize cell culture but also the animal models to be used for in vivo studies. The aims of this following study are to first: optimize the cell culture protocol, oxygen content and nutrients of hRPCs in order to obtain the highest viability and controlled differentiation of these cells in vitro; second: to create a short-term animal model for NF1-OPG by injecting C6 cells in the optic nerve of rats that would lead to tumor formation, which is typical in NF1-OPG.

Human retinal progenitor cells (hRPCs) hold great promise as potential candidate that can be isolated from fetal neural retinal tissue and possess the capacity to proliferate, survive, differentiate, and ultimately integrate within the host retina following transplantation, as previously described [111], [150], [151]. However, hRPCs have limited proliferation and differentiation index which can restrict its usage in large scale clinical application, hence, different techniques need to be explored to overcome this barrier. For stem cells to be useful in the clinical medicine the differentiation protocol needs to be devised in a way that allows large scale production of retinal cell types. Various groups have used different nutrients combinations [37],

[39], [147], [152]. This indicates that the culture conditions for such cells play a vital role determining the fate and eventual differentiation of these cells. Using a combination of nutrients/growth factors makes it difficult to understand the effect of one condition and to obtain the highest yield of cells that express stage-specific markers. When oxygen level offered to stem cells is not at the same level as its niche, it induces cellular alterations such as metabolism turnover, increased oxidative stress and reduced cellular proliferation and self-renewal properties [153]. Furthermore, it effects its motility and changes differentiation potentials along with loss of its potential stemness. The most commonly used small molecule component in stem cell culture is knock-out serum (KOSR) which has been shown to facilitate the generation of embryonic stem cells. It serves as a replacement for fetal bovine serum that can greatly enhance alkaline-phosphate positive colonies. In our study, we compared the effect of hypoxia and KOSR on human retinal progenitor cells (hRPCs). Cells were cultured in defined media with and without KOSR in normoxia and hypoxia conditions and cellular expression and viability, using live dead assay, immunostaining and flow cytometry, were assessed to evaluate the effect of environmental and chemical conditions on these cells.

The most common form of optic neuropathy is Neurofibromatosis type 1, NF1 (also known as peripheral neurofibromatosis or Recklinghausen's neurofibromatosis), with an incidence of approximately about 1 in 3,500 per year [154]. It is known to occur due to a mutation in the NF1 gene located on chromosome 17. Young children effected by NF1 are prone to developing low-grade astrocytomas which typically involve the optic nerves chiasm, and optic radiations and have been termed called optic pathway gliomas (OPG) [19]. To develop a transplantation-based model of OPGs in a larger animal (vis-à-vis mouse) we have injected C6 cells in the optic nerve of Long Evans rats. Two-week post injection, eyes were enucleated and tested using different histologic and immunostaining to confirm formation of gliomas in the optic nerve. In this experiment, we have created a simple glioma model that can be used to test various tumoricidal agents that may serve as treatments for NF-1-OPG patients.

4.2 Experimental design

4.2.1 Overview of animal experiments

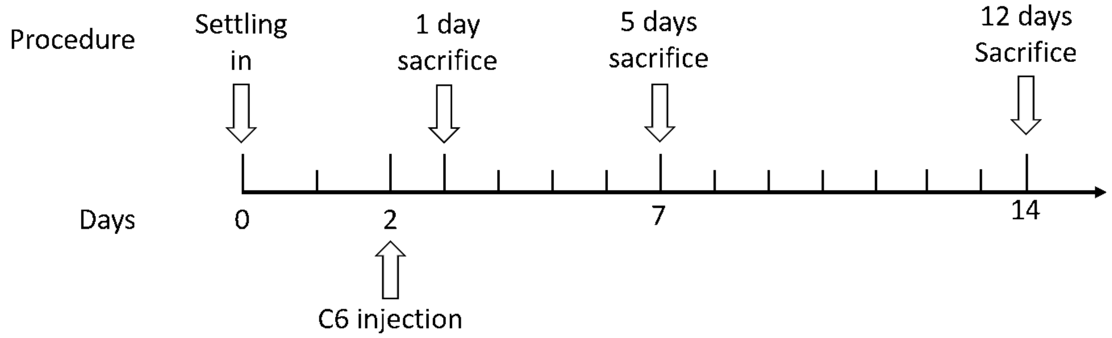

Figure 4.1: Experimental design of C6 cell injection.
Rats are left to settle down for 2 days after arrival, then C6 cells are injected. Sacrifice is performed 1, 5, and 12 days post-injection.

4.2.2 Control and measured outcomes

The control group consisted of healthy rats which had no surgery. These rats were sacrificed at the same time points as the experimental groups. Outcomes for this study were based on direct examination and image processing analysis of retinal and optic nerve sections of injected rats. The measured outcomes were:

- Tumor size at all time points/Optic nerve diameter
- Glioblastoma and neoplastic cells presence with H&E
- Retinal structure (retinal layers)
- % of C6 cells presence and infiltration
- Presence of C6 cells expressing S100 (tumor)
- Presence of C6 cells expressing Foxp3 (tumor genesis)
- Presence of C6 cells expressing Ki67 (proliferation)

- % of cells engrafted expressing DAPI (Nuclei)

4.3 Materials and Methods

4.3.1 C6 cell culture

C6 cells were cultured based on the protocol provided by ATCC (culture method, CCL-107). Briefly, confluent T75, fibronectin (Akron)-coated flask (surface 75 cm^2, vented cap, sterile, Nunclon Delta) were washed with HBSS (Hank's Balanced Salt Solution, without calcium and magnesium, ThermoFisher) to remove any trace of serum before treating with 0.25% (w/v) Trypsin – 0.53 mM EDTA (Sigma-Aldrich). Flasks were observed under an inverted microscope and incubated for 5 mins at 37°C to reach complete detachment of cells. Cells were then collected, centrifuged, and resuspended in 1ml culture media containing: F-12K medium (ATCC-formulated), 2.5% of fetal bovine serum (Sigma) and 15% of horse serum (Sigma). Appropriate amount of the cell suspension was seeded into new culture flasks (usually $2x10^5$ per flask). Once confluent cells were further detached with Trypsin and frozen in 95% culture media and 5% dimethyl sulfoxide (DMSO, Sigma) until further experiment. Cell number and viability were estimated, after each passage, using Trypan blue (Sigma-Aldrich) and a hemocytometer (Countess™ II FL Automated Cell Counter, Thermo Fischer scientific). To prepare for injection, C6 cell suspension was prepared in HBSS at the 10,000 cells/µl.

4.3.2 Knock-out serum replacement and normoxia

To test the effect of different conditions, hRPCs were cultured in Ultraculture medium in hypoxia condition (37 C, 5% O_2, 5% CO_2, 100% humidity), Ultraculture supplemented with KOSR in hypoxia, hRPCs in Ultraculture medium in normoxia condition (37C, 20% O_2, 5% CO_2, 100% humidity), and Ultraculture supplemented with KOSR in normoxia: Normoxia, KOSR-Normoxia, Hypoxia and, KOSR-Hypoxia. Cells were seeded with cell surface density of 20,000 cells/cm^2.

4.3.3 Optic nerve injection in Long Evans rats and tissue processing

Twenty-four domestic rats of the Long Evans strain (age 4 weeks with approximate weight of 150g) were used as control and test recipients in the experiment. Rats were sedated using 2-4% isoflurane (Abbott, Solna, Sweden), followed by intraperitoneal injection of ketamine (40-80mg/kg) and xylazine (10mg/kg) combination for anesthesia. A drop of lidocaine (Sigma-Aldrich) was placed on surgical eye and artificial tears were used every 5 mins to prevent dryness of eyes during the surgical procedure. Before starting rats were placed on stereotaxic frame with heating pad to keep them warm throughout the procedure. A 1-inch incision was made in the skin overlying orbital ridge using size 12 scalpel. Skin was retracted exposing underlying fascia which was carefully dissected away. Utmost care was taken to avoid blood vessel which could cause excessive bleeding and cotton swab was used to maintain hemostasis during dissection of fascia. Furthermore, with lightly traction on the conjunctiva while pulling eye downwards out of eye socket superior orbital muscle was exposed. Using a fine tip needle the muscles was teased out which gave complete access to the optic nerve fascia.

C6 cell suspension was prepared to contain 10,000 cells/µl and each test animal received 1 µl of injection using a glass micropipette of 105 µm diameters. The glass needle was mounted onto a micromanipulator attached to Hamilton syringe stand. After completion, the microneedle was retracted, and eyes were gently pushed back. The skin was sutured, and the animal was return to cage after full recovery. The research protocol was reviewed and approved by the Schepens Eye Research Institute Animal Facility and was in accordance with the Association for Research in Vision Ophthalmology Statement for the Use of Animals in Ophthalmic and Vision Research. Day 1, 5 and 12 were the time points to check the effect of C6 injection and its tumor formation ability. Both control and test animals were sacrificed by using CO_2 suffocation and secondary step of puncturing major organ was used to ensure death. Eyes were enucleated by dissecting from the superior orbital side to obtain part or complete optic nerve and placed in 4% paraformaldehyde for 12 hrs. Tissues were subsequently treated with sucrose in increasing concentration (5%, 10%, 20%) containing Sorensen phosphate buffer. One day before dissection eyes were transferred into sucrose: OCT solution (1:1) and, before mounting, with compete OCT media. About 15 µm sections were collected in poly-lysin coated slides.

4.3.4 Histological and immunostaining of ONG

Both control and test slides were examined using different stains. For histology, Thermo-scientific Rapid-Chrome H&E staining kit was used. This was 18 step process which permanently stains cytology specimens. Slides were dipped into series of solution containing 95% alcohol, distilled water, Hematoxylin, Bluing reagent, and Eosin-Y stain followed by series of wash before final fixing step. Slides were then mounted and observed under upright microscope (Leica DM2500). Sections were stained with Luxol blue staining kit (Abcam ab150675). Slides were washed with PBS and incubated with Luxol blue solution for 2 hours at 60℃. Following which slides were rinsed with distilled water and differentiated by dipping into lithium carbonate solution. To develop further differentiation slides were dipped in alcohol reagent provided with the kit. For the final staining slides were dipped in Cresyl Echt Violet for 2-5 min following which rinsing and dehydration was performed before mounting the slides for visualization.

For IHC staining, cryosections from Long Evans rats left eyes, were fixed with 4% paraformaldehyde in 0.1 M PBS (Irvine Scientific) at room temperature for 20 min. These sections were blocked and permeabilized with a blocking solution [(Tris-buffered saline (TBS), 0.3% Triton X-100 and 3% goat serum (Jackson Immunoresearch Laboratories, West Grove, PA, http://www.jacksonimmuno.com)] for 15 min. Samples were then rinsed twice with 0.1 M TBS buffer for 15 min each time, mounted on polysine microscope slides and incubated with primary antibodies overnight at 4℃: S100-FITC (major protein expressed by C6 cells [155]); Beta-tubulin III-FITC (neurofibroma presence); Ki67-FITC (proliferation marker); Vimentin-APC (expressed by C6 cells [156]); Foxp3-APC and CD45 (Immune response markers). After overnight incubation, samples were rinsed three times with TBS for 15 min. Secondary antibodies (goat-derived anti-mouse and anti-rabbit, DAPI-VioBlue) staining was performed for 1h at room temperature. Samples were then washed a final time with TBS before being mounted on poly-l-lysine microscope slides with low viscosity slide mounting medium. Digital images were obtained with an epifluorescence microscope using 20x objective (Leica, DM2500). Electronic image files were processed using MATLAB software (MathWorks Inc., R2019a).

4.3.5 Flow cytometry assay of C6 cells

The phenotype of C6 cells was analyzed using flow cytometry with the MACSQuant flow cytometer (Miltenyi, San Diego). Cells were collected and fixed with Perm/Fix buffer (BD Biosciences) at 4 ℃ for 15 min. Cells were then washed in wash buffer (BD Biosciences) and incubated, at room temperature, in blocking buffer (Pharmingen staining buffer with 2% goat serum) for 30 min. Blocked cells were seeded onto a flat bottom 96-well plate (polystyrene, Thomas Scientific) and labeled overnight at room temperature with the following conjugated primary antibodies as seen in Table 4.1: S100-FITC, Vimentin-FTIC, CD45-APC, Ki67-APC, GFAP-APC. Primary antibodies were diluted in 200 µl of antibody buffer (TBS, 0.3% Triton X-100 and 1% goat serum). After overnight incubation cells were washed three times for 15 min and incubated in secondary antibodies (goat-derived anti-rabbit and anti-mouse, DAPI-VioBlue) which were diluted 1:200 in antibody buffer (Jackson Immunoresearch Laboratory). Incubation was performed at room temperature for 3h. Forward and side scatter and fluorescence signals from each sample were measured using the MACSQuant (Miltenyi Biotech, Germany) flow cytometer. The results were analyzed using the MACSQuantify software (https://www.miltenyibiotec.com). For each primary antibody the DAPI-positive single cell population was gated. The ratio of positive cells in the gated population was estimated in comparison with blank and species-specific isotype controls.

Table 4.1: Primary antibodies used for analysis of gliomas.

Antibody	Isotype	Dilution	Source	Target
DAPI-VioBlue	IgG1	1:1000	BD Biosciences	Nuclei
S100-FITC	IgG1	1:200	BD Biosciences	Tumor
Vimentin-FITC	IgG1	1:200	BD Biosciences	Filament
CD45-PE	IgG H&L	1:100	Abcam	Macrophage
GFAP-PE	IgG H&L	1:50	TakaraBio	Muller cells
Ki67-APC	IgG H&L	1:50	Santa Cruz	Proliferation
Isotype Rabbit	IgG1	1:100	Abcam	Control
Isotype Mouse	IgG H&L	1:100	Abcam	Control
Anti-Rabbit		1:200	BD Biosciences	Secondary
Anti-Mouse		1:200	BD Biosciences	Secondary

4.3.6 Image processing and analysis of ONG sections

Seven randomly selected images were taken for each sample. To statistically analyze the field of view, an image processing MATLAB code was created., based on Otsu's method [157] (thresholding algorithm). For each image taken, the code calculates (with a tolerance of 0.01%) the surface covered by the cells of interest (in images taken with 20x magnification). The number of colored pixels (Green for FITC channel and Red for APC channel) were counted, and a percentage of cell surface coverage was created.

4.3.7 Statistical analysis

All experiments were conducted in n= 5 set. Values were expressed in graphs is mean ± standard error mean (SEM) using GraphPad software. One-way ANOVA was used following student's t-test for statistical analysis. The $p < 0.005$ value was considered as significant difference.

4.4 Results

4.4.1 Viability and phenotype of hRPCs in hypoxia

Cells cultured in different condition were assessed for viability using calcein-AM and ethidium bromide for live/dead staining (N=4 replicates). Four different hRPCs groups are analyzed throughout all the experiments: Normoxia, KOSR-Normoxia, Hypoxia, KOSR-Hypoxia. Live & dead results (Figure 4.2) show that hRPCs cultured in hypoxic conditions have a significantly higher number of viable cells compared to normoxia condition, both with and without KOSR. However, no difference was found between cells cultured with or without KOSR supplement. Statistical analysis performed using two-way ANOVA, followed by Tukey's test, indicates a significantly higher viability (5-7%, p=0.006) in KOSR-hypoxia and hypoxia when compared, respectively, to the KOSR-normoxia and normoxia groups (Figure 4.2). At all-time points the viability of cells was above 80%. The cells were more elongated and fibroblastic, morphologically, in both Normoxia and KOSR-Normoxia groups when compared to the hypoxic conditions.

Proliferation of hRPCs in all groups was monitored using Ki67 (N=4 replicates). By day 3, immunostaining suggest that the percentage of proliferating cells decreased in normoxia condition (with or without KOSR) when compared to cells in hypoxia (Figure 4.3). A quantitative measurement of the percentage of Ki67 expression is performed using flow cytometry analysis.

Markers for stemness, like Oct4 and C-myc, are key genes that maintain and regulate cells in the progenitor state. A qualitative difference in expression of these markers was found between groups of different oxygen tension. hRPCs cultured in hypoxic conditions, with and without KOSR, showed the highest Oct4 expression and cells in normoxia showed the least expression (Figure 4.4).

The opposite trend can be seen for Recoverin expression, where cells in normoxia shows a higher expression than cells in hypoxic conditions, suggesting that lower oxygen tension tends to decrease the maturation of hRPCs (Figure 4.5).

Flow cytometry analysis showed that less than 5% of the cells cultured in normoxia

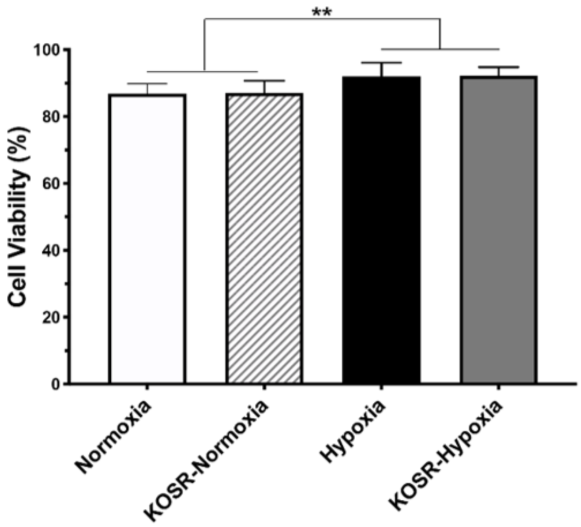

Figure 4.2: Live/Dead assay performed on hRPCs using immunohistochemistry for different culture conditions.
Quantitative analysis of viability in all groups. Data shown as mean ± SEM of N=15 field of views. Two-way ANOVA was performed and shows a statistically significant difference, **p=0.008. Scale bar 200 µm. Image reprinted from [158].

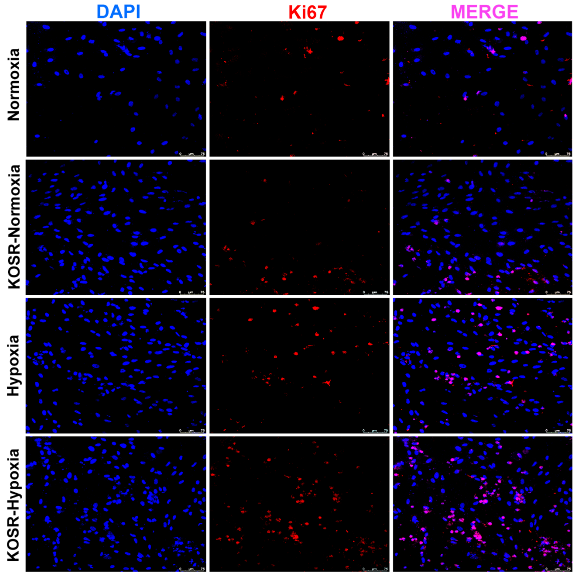

Figure 4.3: Ki67 staining for proliferation assay using immunohistochemistry for different culture conditions.
Hypoxia shows more proliferative cells than normoxia. Cells cultured in KOSR shows higher proliferative cells indicating its effect on cells. Images taken on 3rd day of culture at 20x magnification. Scale bar 75 µm. Image reprinted from [158].

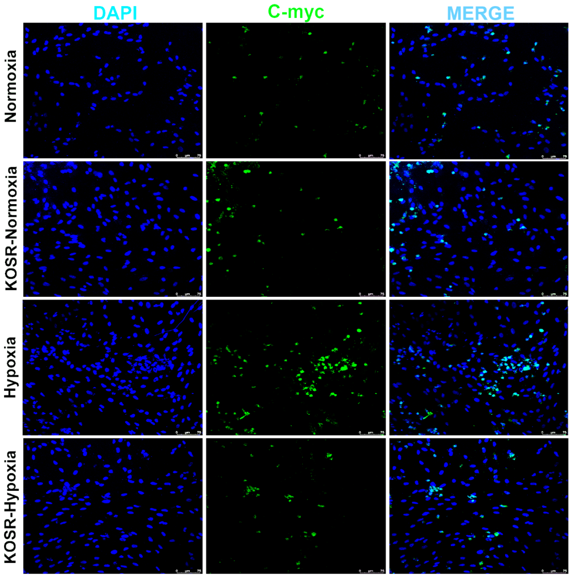

Figure 4.4: Stemness marker C-myc was used to identify the effect of culture condition of hRPCs.
Oxygen gradient affects the stemness of hRPCs as significantly fewer positive cells were seen in hRPCs in normoxia in comparison to hypoxia and KOSR-hypoxia conditions. Images taken on 3rd day of culture, at 20x magnification. Scale bar 75 µm. Image reprinted from [158].

(with or without KOSR) were expressing C-myc and even lesser percentage of cells expressed Oct4 which was significantly different from hRPCs cultured in hypoxic condition (from 4% to 7%, p=0.0001). No significant difference was found between hRPCs with KOSR (in both oxygen tension conditions) and without KOSR (Figure 4.6). These results, in addition to the immunostaining, suggest that stemness is driven by the oxygen tension (hypoxic conditions increasing the stemness in hRPCs cultures) while KOSR has little effect on the differentiation.

C-myc expression was found highest in both Normoxia conditions compare to both Hypoxia conditions. The stemness marker Oct4 shows a similar trend. The mature retinal markers Rhodopsin and Recoverin was significantly increased in Normoxia, compared to KOSR-Normoxia, and even more compared to both Hypoxia conditions. This suggest that differentiation of hRPCs from progenitor to mature state is driven by normoxia conditions and that KOSR helps in keeping cell in an undifferentiated state. The opposite trend is seen for proliferation, where both Hypoxia conditions

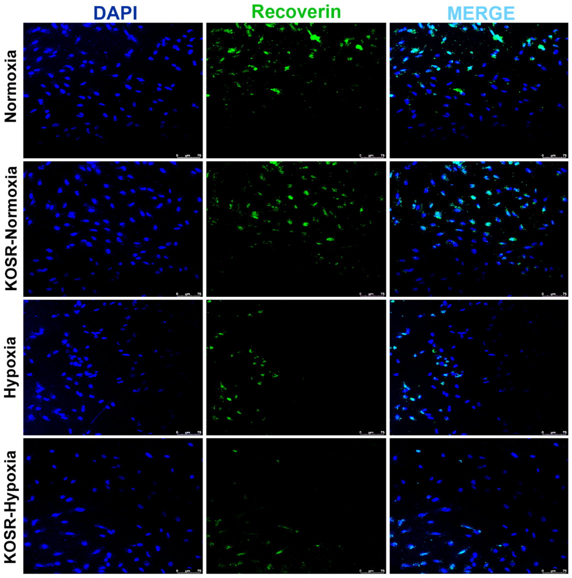

Figure 4.5: . Differentiation assay performed with recoverin (photoreceptor marker) to identify the effect of culture condition on hRPCs fate.
Normoxia and KOSR-Normoxia cultures show the highest Recoverin expression and the least expression was observed in hypoxia conditions. Oxygen tension and KOSR influences Recoverin and therefore the differentiation of hRPCs. Images taken on 3rd day of culture, at 20x magnification. Scale bar 75 µm. Image reprinted from [158].

have an increased expression of Ki67 compare to Normoxia.

Maturation markers of retinal lineage like rhodopsin and NRL, which are characteristic of rod photoreceptor cells, recoverin (rod and cone photoreceptor and some bipolar neurons) and, PAX6 (retinal marker) was used to identify and quantify effects of culture condition on maturation and differentiation of hRPCs. Expression of these key differentiation markers were significantly higher in normoxia conditions (rhodopsin, recoverin and, PAX6 positive 15%, 10% and, 14% respectively, p=0.0003) compare to hypoxia groups (respectively 7%, 4% and, 9%). A significant difference was seen by the addition of KOSR for the rhodopsin expression. hRPCs cultured in Normoxia-KOSR shows a significantly lower expression of rods markers compare to Normoxia (respectively 15% and 18%, p=0.003). However, no other difference in differentiation markers was found by the addition of KOSR supplement. Proliferation measurement (Ki67) shows higher value for cells cultured in hypoxic conditions with

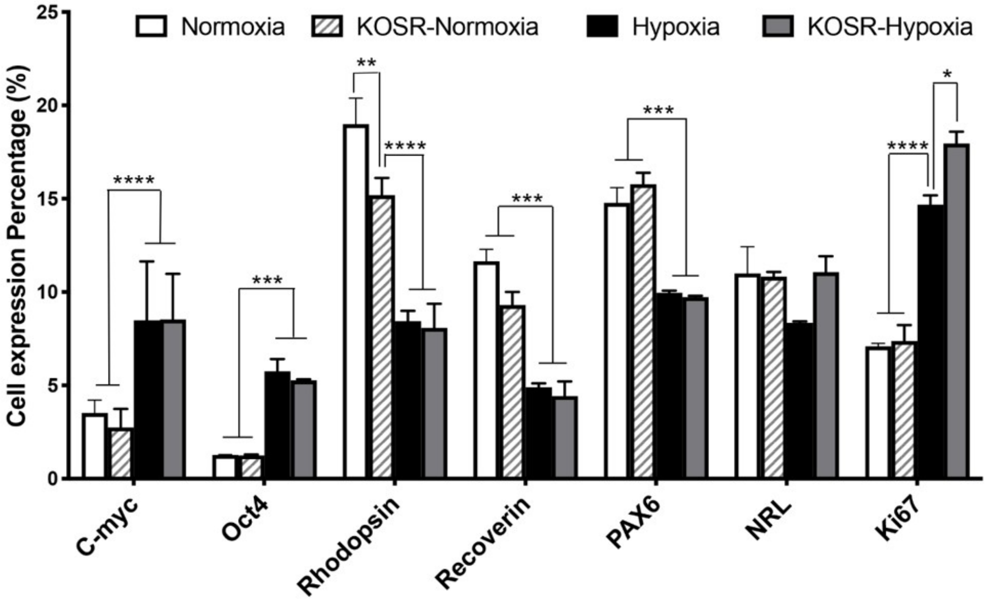

Figure 4.6: Statistical analysis for flow cytometry assay for hRPCs expression in different culture conditions.
Data shown as mean ± SEM of N=3 replicates. Two-way ANOVA was performed followed by Tukey's multiple comparison test.(*p=0.01, **p=0.003, ***p=0.0003, ****p=0.0001). Image reprinted from [158].

KOSR supplement than without KOSR (respectively 18% and 15%, p=0.01). hRPCs in normoxia with and without KOSR shows a significantly lower proliferation.

4.4.2 Mouse animal model for NF1-OPG

CD6 cells tumor formation and phenotype analysis

C6 cells were injected into the optic nerve anterior of the optic chiasm of the left eye (test) of each animal (right eye serving as control) as shown in the diagram in Figure 4.7A. Macroscopic examination (using a surgical microscope) was performed at day 1, 5 and 11 after surgery. At day 1 after C6 injection in the optic nerve, no visible difference was noted between the control and tumor injected test group. However, 11 days post injection, upon macroscopic examination, significant lens opacity was observed, likely due to increased intraocular pressure (Figure 4.7B). This along with slight proptosis that is typical of optic nerve glioma was only be observed in the test animals. Post-enucleation, large tumors were observed in the test animals, while control eyes showed normal sized optic nerve (Figure 4.7B). The macroscopic examination suggests tumor evolution from day 1 to day 11 after tumor induction. Quantification of tumor size and formation at day 11 was performed by measuring the size of the tumor in each test eye and compare it to the healthy optic nerve in the control eye (n=5). Tumor surface coverage analysis was performed using student t-test and was significantly larger than control animals which did not received any injections (Figure 4.7C). The actual area measured for the control eyes corresponded to the area of the healthy optic nerve. This examination suggests the presence and formation of a large tumor, after 11 days post C6 cells injection in the optic nerve.

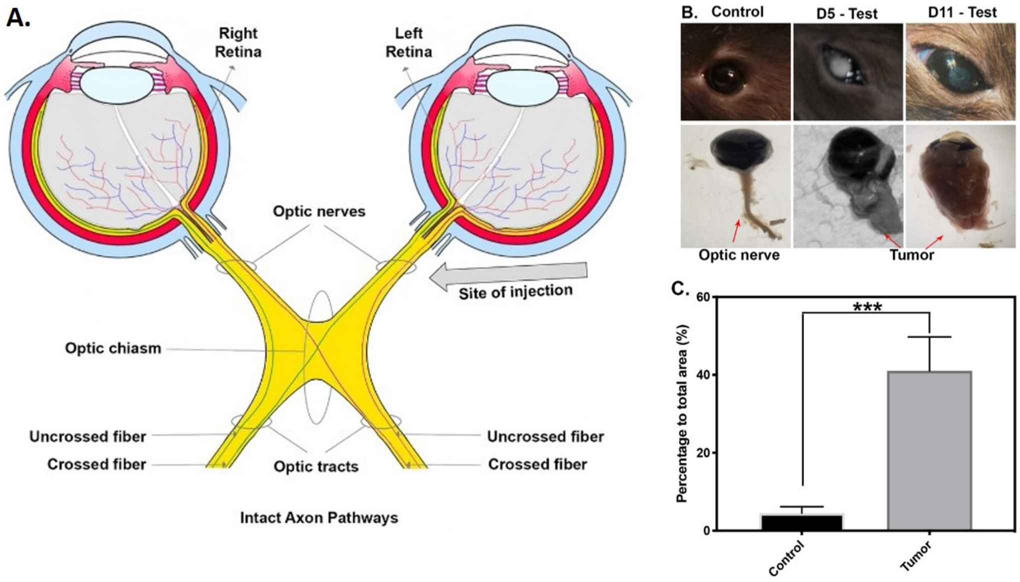

Figure 4.7: Macroscopic examination of ONG formation and statistical analysis.
A. Diagram of optic nerve anatomy and injection site of C6 cells. **B.** Photography, in brightfield, of rat eye, optic nerve and tumor for control eye and at day 5 and 11 post-surgery. **C.** Analysis of tumor size by measure of visible area around the optic nerve. Statistically significant differences were observed in the size of the tumor between control and test group ($p<0.005$). Image reprinted from [159].

We quantified C6 expression using flow cytometry to analyze up- or down-regulation of key tumor and immune cell markers along with stemness markers (Figure 4.8). The absence of standard errors of the mean in Figure 4.8B is due to the methodology of averaging events measured by the flow cytometer. The same gating strategy (i.e., the population of events, to be considered as positive) was applied for all markers: gating the cell population (FSC-A vs SSC-A), gating the single cell population (FSC-A vs FSC-H), and then gating the DAPI positive population (VioBlue-A vs FSC-A), as seen in Figure 4.8C. The single-cell-DAPI-positive gate yielded the number of cells to be employed for comparison of all of markers. Both GFAP (glial fibrillary acidic protein - an activated muller cell marker,) and CD45 (immune cell marker) expression were lower than the isotype control used. This finding indicates that, as seen in other studies [156], C6 cells do not express GFAP nor immune cell markers. However, S100 (tumor cell markers) was expressed in about 25% of the population, indicating the expression of tumor markers in C6 cells while Ki67 (proliferative marker) was expressed in 47% of the population, indicative of their ability to rapidly proliferate. Finally, Vimentin was found to be expressed in almost all C6 cells analyzed (98%), which is consistent with other studies stating the high expression of Vimentin in C6 cell population. Overall, the phenotype analysis of C6 cells suggest their ability to proliferate and their specific tumor cell phenotype, suggesting this cell line may be a suitable candidate for induction of optic nerve tumors through transplantation and creating a model for studying NF1-OPG conditions in a rat.

Histological and immunostaining analysis of gliomas

Histological analysis was done using hematoxylin-eosin (H&E) and Luxol Fast Blue staining on control and test ocular tissue 11 days post-injection. H&E staining of the control tissue showed normal optic nerve fibrous structure with well-defined cell nuclei (Figure 4.9A). The histopathology patterns of glioma tumors with diffused astrocytoma characterized by highly pleomorphic nuclei with low cell density was observed. Distinct areas of high cell density show clear protoplasmic area with round bland nuclei indicating few oligodendroglioma (Figure 4.9B). Near the injection site, large irregular shaped neoplastic cells could be clearly seen (Figure 4.9 right panel). Prominent areas of necrosis around the injection site were visible with palisades of

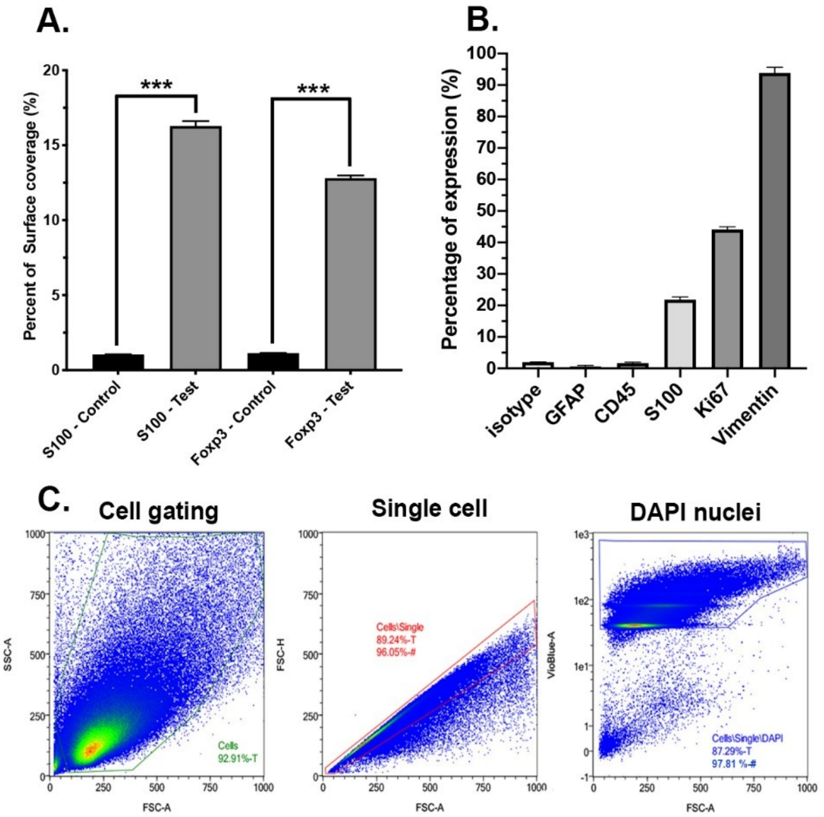

Figure 4.8: In vitro and in vivo phenotype assay of C6 cells. C6 cells were analysis by flow cytometry using MACSQuantify software.
A. Surface coverage analysis of C6 cells in vivo for control and test group for S100 and Foxp3 markers. High statistical difference was observed between control and test groups for both markers ($p<0.005$). **B.** In vitro phenotype analysis of C6 cells with flow cytometry. Markers analyzed: Isotype control, GFAP, CD45, S100, Ki67 and Vimentin. **C.** Cell, single cells and DAPI gating for flow cytometry analysis. High number of events was observed in all population. Image reprinted from [159].

neoplastic cells nearby. This morphological analysis suggests the formation of a glioma in the optic nerve, near to the injection site, 11 days post C6 cells injection.

H&E staining of retina was also performed to look at possible tumor formation in retinal layers, however, we have looked extensively at retina slices and tiling and did not find any tumor formation. Luxol fast Blue staining (Figure 4.10A) shows no sign of demyelination and the lamellar structure was found to be intact in control tissues. However, Luxol Fast Blue images of test tissues (Figure 4.10B) shows significant difference suggesting demyelination after C6 injection.

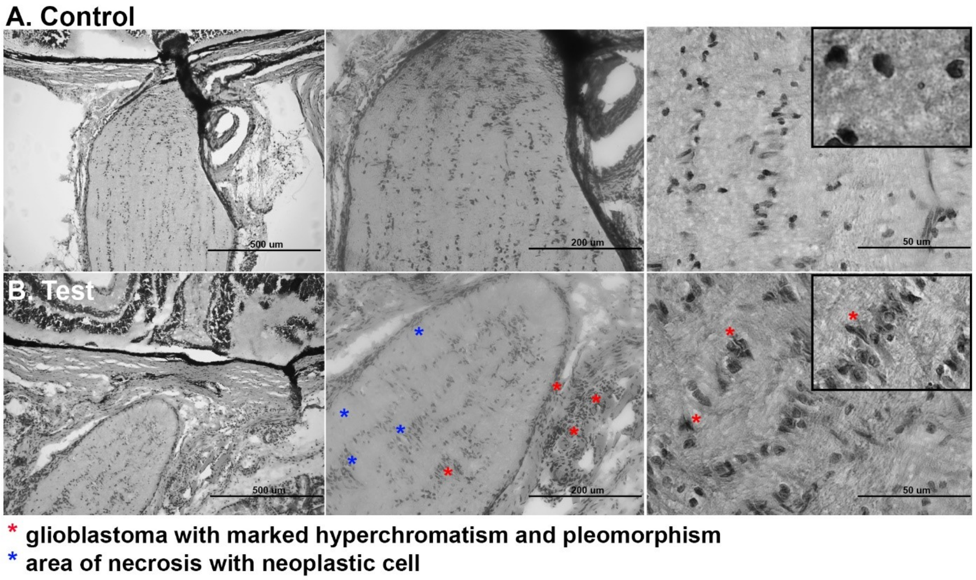

Figure 4.9: Hematoxylin-eosin staining and analysis of injected and control tissues.
H&E staining was performed, and slides were observed under brightfield with upright microscope. Control tissue. **A.** shows healthy optic nerve with normal and uniformly distributed nuclei while test tissue. **B.** suggest the presence of necrotic areas with neoplastic and infiltrating cells. Image reprinted from [159].

Different stains were used to evaluate expression of tumor markers in resultant gliomas. The S100 protein family are useful as markers for certain tumors and epidermal differentiation. It can be found in melanomas, 100% of schwannomas, 100% of neurofibromas (weaker than schwannomas), 50% of malignant peripheral nerve sheath tumors (may be weak and/or focal), paraganglioma stromal cells, histiocytoma and clear cell sarcomas [155]. S100 protein is secreted at high levels by glial tumors and was found to be highly expressed in the C6 injected test animals (Figure 4.11B). Negative control eyes, which were not injected with C6 cells, showed no S100 expression. The macrophages, microglia and immune surveillance cells of the Central Nervous System (CNS) are largely quiescent in normal conditions but become activated in injured neural tissue and can be detected by antibodies directed against CD45 [160]. CD45 staining of the test animals shows typical minimal staining usually seen in the rodent models in which resident microglial are not highly activated for low-grade tumors, while control eyes show no presence of CD45 expression (Figure 4.11A). These

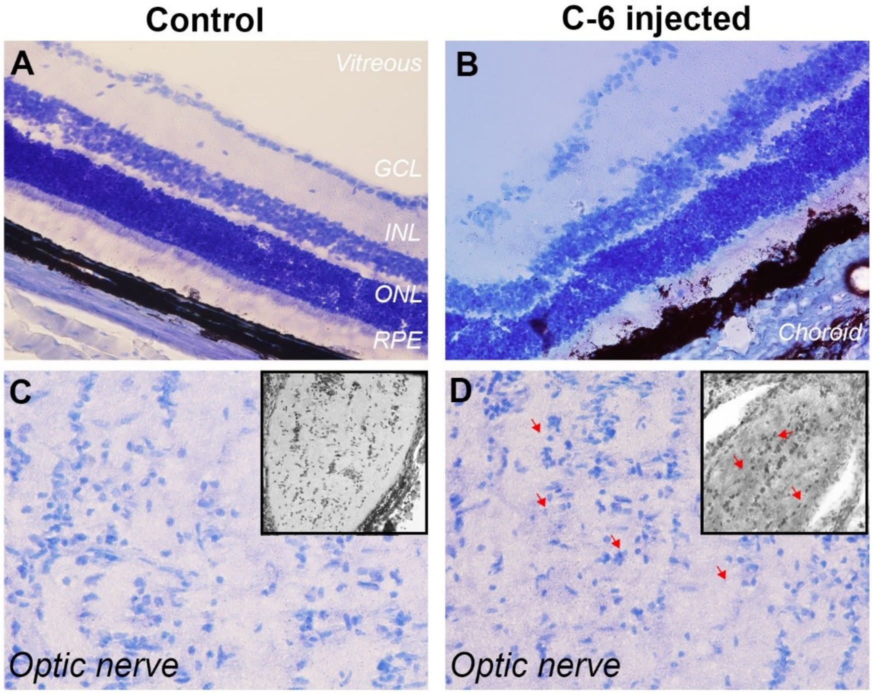

Figure 4.10: Luxol Fast Blue/Cresyl Violet staining and analysis of injected and control tissues.
Luxol Fast Blue staining was performed, and slides were observed under brightfield with upright microscope. Control tissue **A.** and test tissue **B.** images of retina show effect of C6 injection on retina with ganglion cell layer showing sign of degeneration in the test tissue **C**. Optic nerves staining show increased cell infiltration in C6 injected rats (red arrow) **D**. Image reprinted from [159].

staining suggest the formation of glial tumor next to the injection site with a minimal immune response.

Foxp3 (forkhead box P3), also known as scurfin, is a protein involved in immune system responses. Foxp3 expression was not detected in the control eyes (Figure 4.12A) while relatively high marker expression was found in test tissues. Beta tubulin III is a useful marker to corroborate neurofibroma diagnosis (Figure 4.12B). Co-localization of Foxp3 and beta tubulin III was observer in the test eyes next to the injection site while control eyes were found negative for both markers. The expressions of these markers in the test group suggest the formation of neuroglioma with a low-level immune response. Quantitative analysis of S100 and Foxp3 was performed using Otsu's method of image processing. Analysis of the surface coverage of each marker

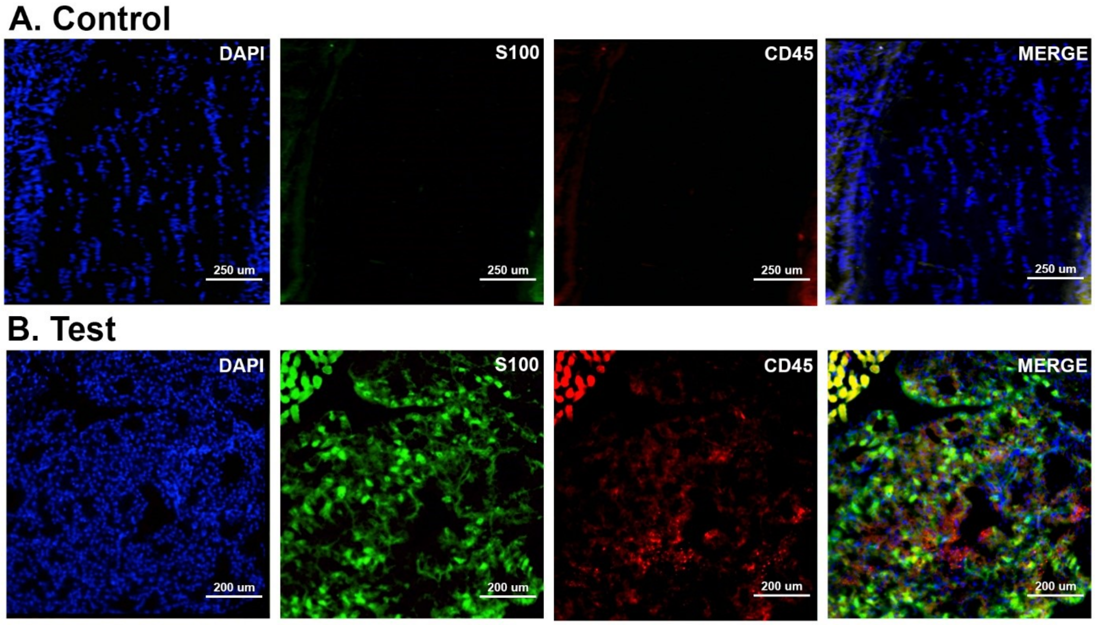

Figure 4.11: Immuno-staining for optic nerve tumor presence (S100) and immunoreaction of the host (CD45).
Images taken under fluorescence microscopy to assess presence of tumor and immune reaction due to injection of C6 cells. All images were taken at 20x magnification. DAPI (VioBlue) staining was performed to show cell nuclei, S100 (FITC) staining for optic nerve tumor and CD45 (APC) staining for host immune reaction. **A.** Control tissue. **B.** Test tissue. Image reprinted from [159].

was performed for the test and control tissues (n= 7 fields of view). S100 surface coverage was significantly higher in the test tissue (16%) compare to the control test (1.4%). The same expression pattern was seen with Foxp3 (respectively 12% and 1.5%). This quantitative data confirms the immunostaining results found – C6 cells injection promotes tumor formation with a low-level immune reaction.

Finally, to determine if these effects were due to the injection of C6 cells in the optic nerve, we analyzed the proliferation and Vimentin (type II intermediate filament) expression near the injection site. Ki67, proliferation marker, expression was found to be high in the region near the injection site while being negative in the control eyes (Figure 4.13A). Vimentin is highly expressed in C6 cell line [156]. Co-localization of proliferative and Vimentin positive cells were found in the test eyes (Figure 4.13B) suggesting the presence of C6 cells creating a tumor near the injection site.

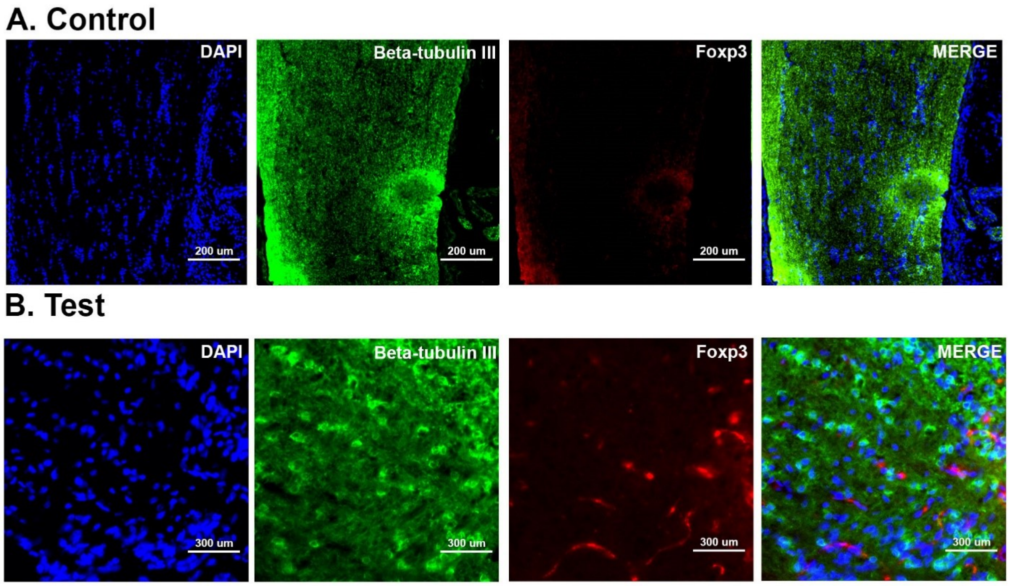

Figure 4.12: Immuno-staining to confirm neurofibroma diagnosis.
Images taken under fluorescence microscopy to assess immune response (Foxp3) and neurofibroma (β-tubulin) presence. **A.** Control tissue. **B.** Test tissue. Image reprinted from [159].

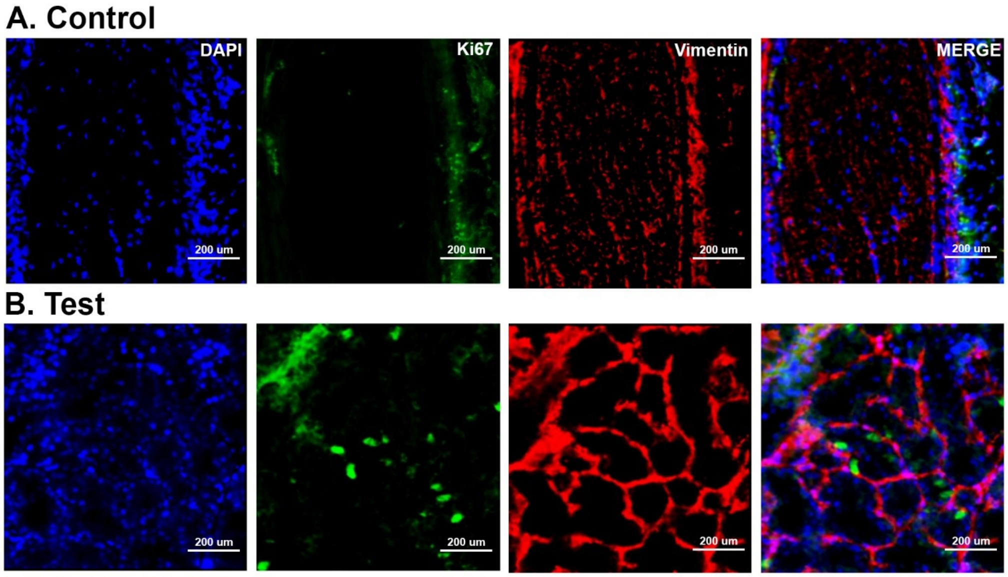

Figure 4.13: In vivo immunostaining of C6 cells with vimentin.
Images taken under fluorescence microscopy to assess C6 cells proliferation (Ki67) and Vimentin expression. **A.** Control tissue. **B.** Test tissue. Image reprinted from [159].

4.5 Discussion

Optic nerve glioma is termed as pilocytic astrocytoma WHO grade I [161]. These are extremely benign compared to other types of astrocytoma, with the most aggressive form reported being glioblastoma multiforme. OPG primarily involves and impacts astrocytes. Tumors are architecturally well defined and can be found at almost any site within the CNS. This is a gene abnormality that causes overproduction of astrocytes and can be linked to the malfunction of a gene that controls proteins in several cell proliferation pathways such as mTOR and MAPK [20]. Most OPG cases present in first two decades of life and can form anywhere along the optic pathway including nerves, chiasm and post-chiasmatic tracts. Depending upon the location of the tumor, signs and symptoms of the disease varies. Most of the OPG models in mice or rats have described C6 cells injection into the brain [162], [163], however, to simulate the optic nerve glioma we have injected C6 directly into the optic nerve and allowed C6 cells to invade the host tissue. The growth characteristics resemble that of human glioma and these models can be readily made at lower cost and shorter time than comparable large animal models. Moreover, the larger size of the rat eye compared to mouse enables surgical and other interventional studies. This technique has advantages over brain inoculation, which often causes a degree of brain damage due to the surgical procedure and growth into adjacent structures. In our experiment, 2 weeks post injection, all animals showed formation of cataract and cloudy lens due to increase in the intraocular pressure [164]. Out of 30 rats injected 27 showed varying form of proptosis. Upon enucleation, fusiform appearance is noted in the C6 injected rats which is typically noted in optic nerve gliomas. Besides the gross examination, statistical analysis was performed to evaluate the surface coverage of tumors. In all the test animals the tumor was noted, however, in 3 animals the size of tumor was smaller in diameter in comparison to the other test tissues. Post sectioning, H&E was performed and showed massive infiltration of cells with hyperchromatism and pleomorphism markers. The large multi-lobe, irregular nuclei showing neoplastic characteristics were observed. A prominent area of necrosis could also be seen in the test animals. Direct comparison between control and test optic nerves indicated alteration in lamellar structure.

One of the most common markers to study the immune response is CD45 staining for infiltrating cells [160]. FOXP3 staining of the C6 injected animals showed high expression along the entire length of optic nerve. FOXP3 (forkhead box P3), also known as scurfin, is a protein involved in immune system responses. A member of the FOX protein family, FOXP3 function as a master regulator for the regulatory pathway involved in development and function of regulatory T cells. In C6 injected tissues, vimentin positive areas colocalizing with ki67 positive cells were observed. In case of neurodegeneration, inflammation or trauma upregulation of cytoskeletal components like vimentin and GFAP can be seen [165]. Vimentin filament protein is often used as marker of tumor cell invasion. In this experiment, vimentin expression was negative in control eyes whereas in area of tumor (test), necrosis vimentin staining was high suggesting initial phase of astrocyte activation. In conclusion, the pathological mechanism of OPG development in NF1 is not completely understood and this has made the development of effective therapeutics difficult. One limitation is due to limited availability of biological samples due to low rate of surgery, therefore patient-derived models for these tumors remain sparse. There is no one model that can fully recapitulate the NF-1 OPG phenotype, but a combination of animal models using patient derived or engineered cells can aid development of future translational science. Developing a rat model for NF-1 OPG is potentially useful as it provides a relatively small and rapidly developing target to test novel therapeutics. A preclinical model for this disease can help understand the pathophysiology and promote clinical trials for biological drugs and small molecules that are presently difficult to advance. Our aim for this OPG study for creating a simple and short-term model for drug screening. The NF-1 OPG is an extremely slow growing tumor and we have tried to create a model that can replicate the disease progression in short duration that makes testing therapeutics more feasible.

The principal objective of the hRPCs study was to investigate the effects of oxygen tension (especially hypoxia) and knock-out serum replacement (KOSR) on human retinal progenitor cells (hRPCs). The role of these two factors on viability, proliferation, maintenance of stemness and, driven differentiation was evaluated in vitro in four different conditions: Normoxia, KOSR-Normoxia, Hypoxia and, KOSR-Hypoxia. Hypoxic conditions (usually 5-10% O_2) are known to be beneficial for stem and progenitor cell culture [34]. They are, in fact, physiologically normal for many stem cells niches [117]. A number of studies have shown significant benefits in terms of cellular expansion and viability using lower than 20% oxygen tension. In the case of embryonic stem cells specifically, low oxygen tension appears to favor cell growth more efficiently than standard oxygen concentration. Our current work confirmed this effect with a significantly higher viability seen in hRPCs cultured in both Hypoxia conditions (with or without KOSR). However, the addition of KOSR seems to have a low effect on hRPCs viability in both oxygen tension conditions.

It is well established that mammalian cells have limited proliferative potential when in culture condition. There is progressive loss of mitotic activity with increased cellular division that is referred to as senescence [166]. Due to this, many researchers have developed protocols to maintain and increase the proliferative capacity of cells in culture conditions [81], [87]. However, both genetic and environmental factors play vital roles in cellular behavior in in vitro conditions. Rubin et al., postulated that the limited proliferative capacity of cells in vitro could be attributed to inability of cells to survive dissociation and culture conditions [167]. These and other such studies suggest that improving the methods used to culture progenitor cells would have a major influence on their proliferative and differentiation efficiency [117]. In this study, we have examined chemical (KOSR) and environmental (Hypoxia vs Normoxia) effects on human retinal progenitor cells. Flow cytometry and immunostaining, in our study, suggest that hypoxia can significantly improve the proliferation (measured with Ki67 expression) of hRPCs: expression doubles by culturing cells in hypoxic conditions compare to both normoxia conditions (with and without KOSR). Furthermore, KOSR supplement enables a higher proliferation by combining it with hypoxic conditions (KOSR-Hypoxia) compare to all other conditions. In addition, hypoxia can improve differentiation of stem and progenitor cells into specific lineages, and has been shown to increase differentiation of adipose stem cells into functioning smooth muscle cells [168], implying that the impact of hypoxia is complex, and a more complete understanding its influence of cultured cells would benefit the field of developmental biology, and improve our ability to translate stem cells into treatment for disease. While improving the viability and proliferation of cell cultures, it has been shown that hypoxia can also preserve the stemness expression of embryonic stem cells [117], [169]. Here, we have evaluated this effect of hypoxia and KOSR on specific stemness markers (Oct4 and C-myc) for hRPCs [170]–[172]. We confirm that hRPCs specifically require hypoxic conditions to maintain proliferation and may be providing a biomimetic environmental niche for these cells by mimicking in vivo conditions. There was no significant effect seen using KOSR on the preservation of hRPCs stemness.

Oxygenation of the inner retina is usually achieved through the intraretinal microvasculature and RPE and photoreceptor oxygenation is by diffusion from the choriocapillaris [173]. Due to these different vascular sources, there is an uneven oxygen tension across the retina with significantly less oxygenation at the level of the outer nuclear layer (ONL). This fluctuation is also due to divergent oxygen utilization by retinal neurons and glial cells. Since photoreceptors are highly metabolically active, they utilized high amounts of retinal oxygen [174], [175]. As hRPCs are primary rod progenitor cells, there is likely to be a significant effect of oxygen tension on these cells. hRPCs and their rhodopsin expressing progeny are cells that are most active during dark conditions with high cytoplasmic calcium levels maintained through cGMP-gated calcium channels. This process is extremely ATP-dependent and it has been suggested these retinal neurons can consume about 4 times more oxygen under scotopic condition [176]. Expression of mature retinal lineage markers such as rhodopsin and recoverin was evaluated to examine the cell differentiation profile under different physiological conditions. Immunostaining and flow cytometric analysis show there is a significant increase in rhodopsin (15%) positive cells in both normoxia conditions compare to hypoxia, with less than 8% positive cells found. Similarly, recoverin expression was significantly higher in the normoxia conditions than hypoxia. In retinitis pigmentosa, loss of rod photoreceptors leads to a reduced metabolic demand that in turn causes reduction of retinal oxygen consumption [177]. Higher expression of both rhodopsin and recoverin in normoxia conditions indicates the tendency of hRPCs to leave exit the cell cycle and differentiate into mature cells when exposed to higher oxygen tension. There was no significant difference with the addition of KOSR, which may be due to the fact these are normally cultured in serum-free condition hence, KOSR shows no differentiation effect on hRPCs. This study demonstrates the effect oxygen tension has on hRPCs. Hypoxia may provide environmental cues that helps hRPCs maintain their progenitor cell state, while the addition of KOSR can improve their proliferation. Normoxia might be used as one mechanism to differentiate these cells into mature phenotypes without their need for exogenous chemical stimulus.

Chapter 5

Human retinal progenitor-seeded hydrogels in vivo transplantation

5.1 Introduction

Human retinal degeneration caused by age-related macular degeneration and retinitis pigmentosa results in irreversible loss of vision [178]. Due to the lack of self-renewal ability of this tissue, replacing photoreceptors and other retinal cells is critical [37], [179]. Numerous cell therapy techniques have been explored to regenerate or replace affected tissue or cells [180], [181]. Rescue treatments yield some improvement in vision, but it requires some number of surviving host photoreceptor cells for the technique to be successful. For cell replacement to become reality, functionally competent neural retinal cells in therapeutically applicable quantities is vital. To achieve this goal, human retinal progenitor cells (hRPCs) have demonstrated ability to survive, differentiate and, engraft into the host retina promoting host photoreceptor rescue thereby, improving the visual function in animals [111]. Presently, hRPCs are in a multi-center phase 2 clinical trials and have shown early indication of improving visual acuity [53].

Failure during transplantation is largely attributed to the cells themselves, but other major factor could be the lack of a suitable carrier capable of forming a protective envelope around the cells. Most cells when delivered using conventional injection techniques show decrease in viability and poor integration with the host tissue. There is a lack of proven polymeric cell carrier that could aid in the delivery of cells into the subretinal space of patients. An ideal polymer would enhance cell survival and degrade within an acceptable time frame without triggering an inflammatory response from the host [65]. Moreover, the environment at the degenerative site in the eye is highly unfavorable for the induction of progenitor cells [182]. Without structural support within the retina, transplanted cells lack matrix protection and may undergo apoptosis. Of the cells that survive, most lack a matrix to be spatially retained and organized within the lesion and typically leave the lesion for the surrounding viable host tissue [67]. Therefore, it becomes even more critical to identify the suitable scaffold for retinal regeneration [183]. Moreover, biomaterial properties have been shown to play major roles in maintaining cell phenotype, proliferation and differentiation. Various studies have shown that material properties such as stiffness can influence and even direct stem cell differentiation [144], [184]. The principal objective of this study was to use our in-situ crosslinking hydrogels and analyze its effect on the in vivo transplantation of hRPCs into the subretinal space of Long Evans rats at short and long time points. We formulated a Gtn-HPA and HA-Tyr hydrogel with gelation time of 30 to 180 seconds. The aim of this study is to explore the use of a hydrogel as a “protective envelope” for cells that experience high stress during injection. We performed an in vivo xenograft transplantation of hRPCs, in PBS, in Gtn-HPA, and in IPN75 into the subretinal space of immunosuppressed rats of the Long Evans strain. Injected retinas were analyzed 3 days and 3 weeks post-surgery for the presence, engraftment and viability of hRPCs.

5.2 Experimental design

5.2.1 Experimental groups

Table 5.1: Long Evans experimental groups for subretinal injection of hRPCs.

3 days injection groups	Total no of injected rats	Successful injections	No of rats with presence of cells
Gtn-HPA	5	4	4
Gtn-HPA & EGF	6	5	5
PBS	6	5	3
SHAM	4	4	N/A
Control	3	3	N/A
3 weeks injection groups	**Total no of injected rats**	**Successful injections**	**No of rats with presence of cells**
Gtn-HPA	4	3	3
Gtn-HPA & EGF	4	3	3
IPN75	4	3	3
IPN75 & EGF	4	3	3
PBS	4	4	3
SHAM	4	4	N/A
Control	3	3	N/A

5.2.2 Overview of animal experiments

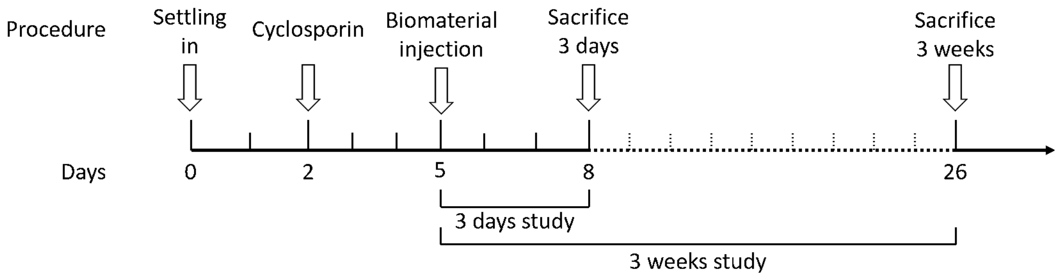

Figure 5.1: Experimental design of hRPC injection in Long Evans rats.

5.2.3 Control and measured outcomes

The control group consisted of healthy rats which had no surgery. The SHAM group consisted in rats which had only a minimal surgery consisting in poking the eyeball with a 31-gauge needle without injecting anything. This is performed in order to replicate the trauma of needle injection itself. These rats were sacrificed at the same time points as the experimental groups. Outcomes for this study were based on direct examination, image processing and machine learning analysis of retinal sections of injected rats. The measured outcomes were:

- % of cells engrafted expressing STEM121 (human)
- % of cells engrafted expressing Cone Arrestin (Cones)
- % of cells engrafted expressing R/G opsin (Cones)
- % of cells engrafted expressing DAPI (Nuclei)
- Position of engrafted in cells in retinal layer
- % area of IBA1 (immune cells)
- % area of CD45 (macrophages)

5.3 Materials and Methods

5.3.1 In vivo xenograft study - animals and surgery

Thirty-seven male rats of the Long Evans strain (age 12 weeks, approximate weight 200g), from Charles River (Wilmington, MA) were used as recipients in the experiment. Transplantation was performed on cyclosporin immuno-suppressed rats. Rats were sedated using 2%-3% isoflurane (Abbott, Solna, Sweden, http://abbott.com) in combination with oxygen by placing the rats in the inhalation chamber, followed by intraperitoneal injection of ketamine (40-80mg/kg) and xylazine (10mg/kg) for anesthesia. Eyes were first anesthetized using topical ophthalmic proparacaine (0.5%) followed by Genteal to keep the lens moist during the surgery.

Recipient rats were injected in sub-retinal space with hRPCs encapsulated in composite suspension of hydrogels or single-cells injections (in PBS). A conjunctival incision and a small sclerotomy were performed using a fine disposal scalpel. Cells were injected into the subretinal space using a glass pipette (internal diameter, 150 µm) attached to a 10 µl Hamilton syringe via a polyethylene tubing. The hRPCs were injected into the retina bleb as a single-cell suspension in PBS (n=10), encapsulated in 2%wt Gtn-HPA (n=9), encapsulated in 2%wt Gtn-HPA with 20 ng/ml hEGF (n=10), encapsulated in 2%wt IPN75 (n=4), encapsulated in 2%wt IPN75 with 20 ng/ml hEGF (n=4). All samples contained approximately 1 x 10^5 cells and the injection volume were 2 µl for all replicates. Using a glass coverslip applied on the eye bleb presence was checked. Subretinal space injection was considered successful if a shiny bleb was seen under the dissection surgical microscope (Alcon Vitreoretinal, Constellation Vision System). Triple antibiotic (Bac/Neo/Poly) was given locally at the end of the surgery to prevent infection. The rats were then placed in their cages for 3 days or 3 weeks. 100 mg/L of Cyclosporine was added to the water container of all cages and was changed every 3 days.

The research protocol was reviewed and approved by the Schepens Eye Research Institute Animal Facility and was in accordance with the Association for Research in Vision Ophthalmology Statement for the Use of Animals in Ophthalmic and Vision Research.

5.3.2 Tissue processing

Three days or three weeks post transplantation rats were sacrificed by CO_2 suffocation for 5 min. Cervical dislocation was performed to certify death. Eyes were enucleated and placed in 4% paraformaldehyde for 24 hours. Tissues were subsequently saturated with increased concentrations of sucrose (5%, 10%, 20%) containing Sorensen phosphate buffer. Eyes were left in 30% sucrose overnight or until dissection. The tissues were embedded in cryosection gelatin medium overnight and sectioned at 18 µm thickness on a cryostat. During the sectioning process, every 5th section was stained and examined by epifluorescence for hRPCs presence with STEM121-FITC (human cells marker), Cone Arrestin-APC (host photoreceptor marker) and DAPI-VioBlue (cell nuclei), every 6th section was stained with RGopsin-APC (photoreceptor marker) instead of Cone Arrestin and every 7th section was stained with CD45-PE (leukocytes marker), Cone Arrestin-FITC and DAPI-VioBlue.

5.3.3 Immunofluorescence staining

Cryosections from Long Evans rats left eye were fixed with 4% paraformaldehyde in 0.1 M PBS (Irvine Scientific) at room temperature for 20 min. These fixed cells and sections were blocked and permeabilized with a blocking solution [(Tris-buffered saline (TBS), 0.3% Triton X-100 and 3% goat serum (Jackson Immunoresearch Laboratories, West Grove, PA, http://www.jacksonimmuno.com)] for 15 min. Samples were then rinsed twice with 0.1 M TBS buffer for 15 min each time, mounted on polysine microscope slides and incubated with primary antibodies overnight at 4℃ (Cone Arrestin-FTIC, Cone Arrestin-APC, RG-opsin-APC, CD45-PE, STEM121-FITC) at concentrations determined in laboratory (Table 5.2). Post overnight incubation, samples were rinsed three times with TBS for 15 min. Secondary antibodies (goat-derived anti-mouse and anti-rabbit, DAPI-VioBlue) staining was performed for 1h at room temperature. Samples were then washed one last time with TBS before being mounted on poly-l-lysine microscope slide with low viscosity slide mounting medium. Digital images were obtained with an epifluorescence microscope using 20x objective.

5.3.4 Image processing and analysis

Seven randomly selected images were taken for each sample. To statistically analyze the field of view, an image processing MATLAB code was created. For each image taken, the code calculates (with a tolerance of 0.01%) the surface covered by the cells of interest (in images taken with 20x magnification). The number of colored pixels (Green for FITC channel and Red for PE or APC channels) were counted and a percentage of cell surface coverage was created. The code can be seen in Appendix A.1.

Table 5.2: Primary antibodies used for testing of injected hRPCs.

Antibody	Isotype	Dilution	Source	Target
DAPI-VioBlue	IgG2a	1:1000	BD Biosciences	Nuclei
Cone arrestin-FITC	IgG1	1:200	BD Biosciences	Cones
Cone arrestin-APC	IgG2a	1:200	BD Biosciences	Cones
RGopsin-APC	IgG1	1:200	BD Biosciences	Cones
CD45-PE	IgG1	1:100	Abcam	Macrophage
STEM121-FITC	IgG1	1:100	Abcam	Human cells
Isotype Rabbit	IgG1	1:100	Abcam	Control
Isotype Mouse	IgG2a	1:100	Abcam	Control
Anti-Rabbit		1:200	BD Biosciences	Secondary
Anti-Mouse		1:200	BD Biosciences	Secondary

5.3.5 Statistical analysis

All experiments were performed with n=4-6. Values were expressed as mean ± standard error mean (SEM) using GraphPad software (https://www.graphpad.com/). Analysis of variance (one-way and two-way ANOVA) followed by Student's t-test were performed for statistical analysis. Statistical significance was set at $p < 0.01$.

5.4 Results

5.4.1 Short-term effect of Gtn-HPA on hRPCs injected in the subretinal space

Survival and engraftment of hRPCs into the subretinal space

Short-term survival of transplanted hRPCs (in PBS or Gtn-HPA) was evaluated using immunohistochemistry and statistical analysis, for every 5th section of each enucleated rat eye of each group. To identify hRPCs, STEM121-FITC staining, a mouse monoclonal antibody that is normally used to detect migration, engraftment, and differentiation of human cells after in-vivo transplantation in animal models, was used. The STEM121 antibody is specific to a human cytoplasmic protein expressed in brain, liver, pancreas, and central nervous system (CNS) cells. Cone Arrestin

(APC) was used to distinguish host cone photoreceptor architecture in the animal from transplanted hRPCs. It belongs to super family of multi-functional proteins, which regulates signaling and trafficking of G-protein coupe receptor (GPCRs) along with sub-cellular localization of many other proteins critical to visual cycle [138]. DAPI was used as a counter stain for cell nuclei and is important to separate cells from auto-fluorescence signal in immunohistochemistry. Upon triple staining of the retina, we observed that hRPCs injected in PBS showed poor engraftment and were mostly localized near the retinal ganglion cell layer or in the vitreous (Figure 5.2A). However, cells injected in pre-Gtn-HPA solutions showed higher survival and engraftment in the subretinal space (Figure 5.2B). Using hEGF showed no significant improvement in cell engraftment compare to Gtn-HPA alone (Figure 5.2C). The gel used as cell carrier is an in-situ crosslinking hydrogel and as the gelation occurs in the syringe, we were able to entrap cells in pre-gel station. This viscous microenvironment, injected between the RPE and photoreceptor layers, ensures that hRPCs will stay in the subretinal space for longer duration. This improves the chances of cell interacting with the host retina thereby leading to higher engraftment. Gtn-HPA degradation rate [116], in this study, is relatively fast and only small islands of gel (Figure 5.2D) can be seen after a short period of time in vivo (3 days).

Presence of hRPCs was measured, 3 days post injection, by calculating the cell surface coverage for the 3 different groups. Surface coverage by hRPCs in the control was significantly lower than hRPCs-Gtn-HPA and hRPCs-Gtn-HPA-hEGF (Figure 5.3). However, even though hEGF plays major role in the in-vitro culture there seems to be no major advantage of injecting cells with hEGF in the short-term in-vivo xenografts. This short-term survival study aims at showing the rapid death of hRPCs when injected in PBS (pre-clinical and clinical trial approved solute) compare their encapsulation in an in-situ crosslinking hydrogel (Gtn-HPA) which can protect them from the shear stress exerted during transplantation. Adding this polymeric material in the transplantation process improves the localization of cells in the right layers (INL and ONL layers of photoreceptors) and reduces the rapid cell-death happening less than 3 days post transplantation.

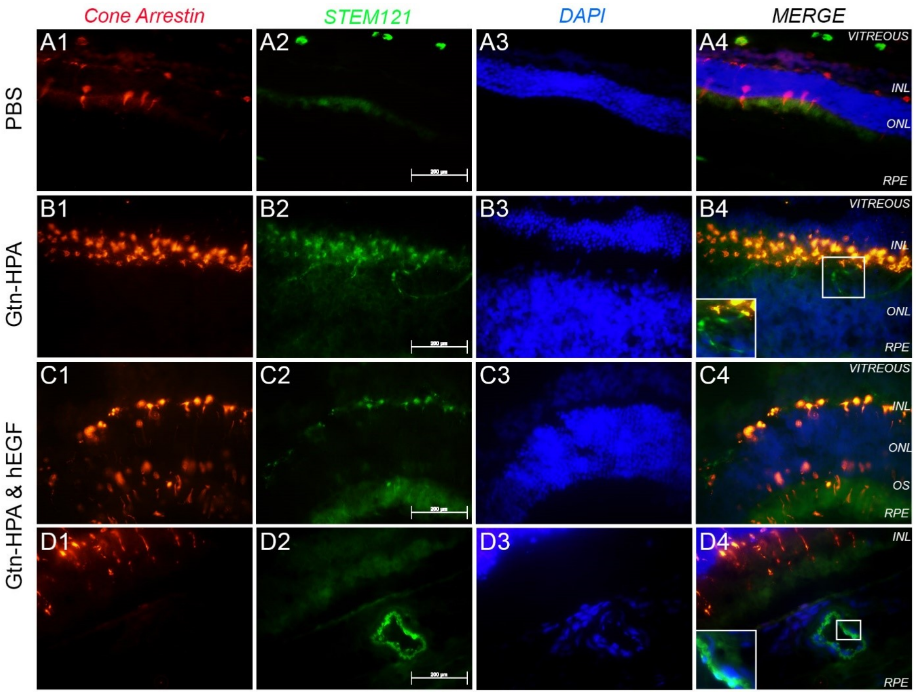

Figure 5.2: Transplantation of hRPC in PBS & Gtn-HPA.
hRPCs survived in the non-immuno-suppressed rat for 3 days following subretinal injection. Images taken under fluorescence microscopy to assess transplanted human cells and host photoreceptors presence. All images were taken at 40X magnification. **A1-D1** are different test conditions stained with cone Arrestin (red) for photoreceptor orientation in the retina, **A2-D2** shows Stem 121 (green) staining for human cells. Nuclei are counterstained with DAPI in **A3-D3** and the last column (**A4-D4**) shows the merge overlay image. Scale Bar-200 µm. Image reprinted from [75].

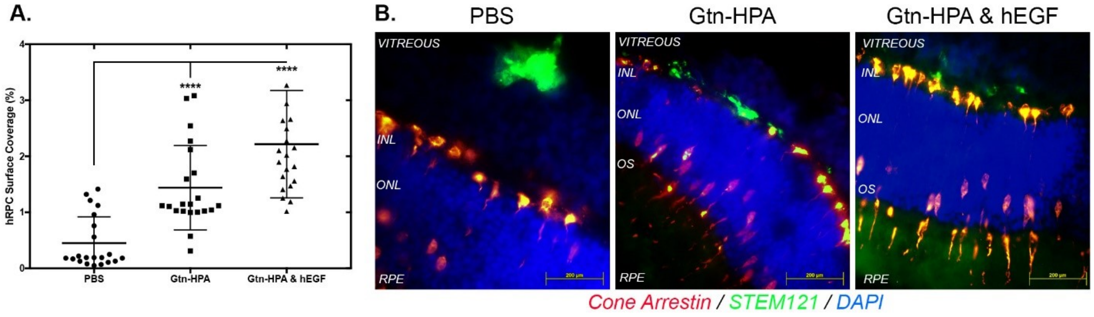

Figure 5.3: hRPCs survival and engraftment.
A. Statistical analysis, using one-way ANOVA, of the percentage of cell surface coverage for the 3 in injected groups. ****$p<0.0001$. **B.** Immunohistochemistry of 5th slide, for each group, stained with Stem121 (green), cone Arrestin (red) and DAPI (blue). Scale Bar-200 µm. Image reprinted from [75].

Immunologic response to xenograft transplantation

We entrapped hRPCs in pre-gel and the protective nature of Gtn-HPA by implanting them into the sub-retinal space of non-immuno-suppressed rats from the Long Evans strain. Three different hRPCs groups were injected: PBS, Gtn-HPA and, Gtn-HPA with hEGF with n=6 replicates in each group. Most FDA approved stem-cell therapies [33], [38] and current clinical trials [42], [47], [53] rely on retinal stem cells injected in HBSS or PBS, deprived from nutrients or scaffolds. In order to mimic the pre-clinical trial conditions, we considered injected hRPCs with a 31-gauge syringe in PBS as the control group in the in vivo experiments. After injecting the cells into the subretinal space, eyes were harvested, cryo-sectioned and stained for CD45 (APC) for leukocytes, cone Arrestin (FITC) to reveal the location of host photoreceptors, and DAPI (VioBlue) for retinal structure. The goal of this short-term study (eyes harvested 3 days post injection) is less to prove the long-term effect of Gtn-HPA and hRPCs treatment rather than showing the immune system response to such an injection. A xenograft transplantation of human cells (in PBS or gel) into the subretinal space of non-immuno-suppressed rats may be able shows the immediate differences in immune response from the host.

The Overall success percentage is defined as the number of times a successful bleb is formed and cells are delivered into the sub-retinal space in function of the total number of animals used in the study. Success rate of transplantation was around 75% in hRPCs in PBS and 50% for hRPCs in Gtn-HPA. The gelation time for Gtn-HPA is about 30 seconds which sometimes resulted in clogging of the syringe and subsequent reduction in the total success rate.

Three days after transplantation, presence of CD45 positive cells was observed near the sub-retinal space and at Bruch's membrane (interface between RPE and choroid). Sub-retinal grafts, irrespective of the carrier (PBS or Gtn-HPA) showed infiltrating CD45+ cells in the inner nuclear layer (INL) or the retina. However, significantly lower leukocytes staining was observed in the Gtn-HPA groups (Figure 5.4A). Furthermore, the retinal architecture was found intact, and no cell layer degradation was observed in the animals injected with success (Figure 5.4). Statistical analysis was performed using one-way ANOVA and shows significant differences between control (hRPCs in PBS) and hRPCs in Gtn-HPA groups. There was no difference between Gtn-HPA and Gtn-HPA with hEGF, suggesting that hEGF has a low immunogenic impact. Percentage cell surface coverage, measured by calculating the number of APC positive pixel per area, in both these groups was found to be in 0.2 range. CD-45 staining, in the PBS group, was mostly localized in the sub-retinal space and ganglion cell layer (Figure 5.4B) while localized in the INL and ganglion cell layer (GCL) for both Gtn-HPA groups. Only 3 days post injection (short-term study) these results suggest that the immediate immune response is lowered by the presence of Gtn-HPA as a carrier for hRPCs. This data can be explained by the biocompatibility and biodegradability of Gtn-HPA, but also by its capability of hiding xenogeneic cells from the host immune system. Indeed, the longer hRPCs are embedded in Gtn-HPA (in the subretinal space) the slower the immune system will react to the presence of exogeneous transplantation.

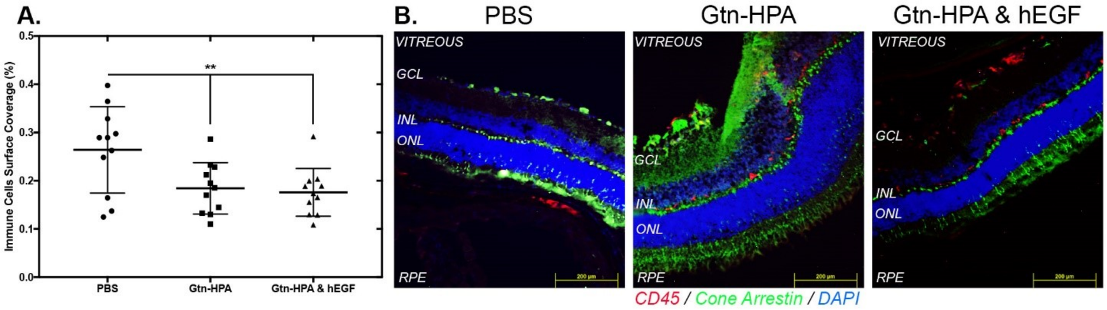

Figure 5.4: Immune response staining of xenografts.
Images taken under fluorescence microscopy to assess leukocytes and host photoreceptors presence. All images were taken at 40X magnification. **A.** CD45 staining data, obtained from number of colored pixels, analyzed using One-way ANOVA (**$p<0.006$). **B.** Immunohistochemistry staining of 3 different groups (PBS, Gtn-HPA and Gtn-HPA with hEGF) for CD45 (APC), Cone Arrestin (FITC) and, DAPI (VioBlue). Scale bar- 200 µm. Image reprinted from [75].

5.4.2 Subretinal transplantation of encapsulated hRPCs in gel with different stiffness

The second timepoint of this in vivo experiment (three weeks) enabled the study of a long-term survival of transplanted hRPCs (in PBS, Gtn-HPA, or IPN75). hRPCs engraftment was evaluated using immunohistochemistry and statistical analysis, for every 4th or 6th section of each enucleated rat eye of each group. Sections were triple stained, as previously described, with DAPI-VioBlue (nuclei stain), STEM121-FITC (human marker), and either Rhodopsin-APC (rod marker) or RGopsin (cone marker). These different stains enable us to analyze not only the engraftment of hRPCs (by using the human marker) but also their different expression in each group. The different injection groups are: hRPCs in PBS, in Gtn-HPA, in Gtn-HPA with hEGF, in IPN75 or in IPN75 with hEGF. These groups were chosen due to the result of in vitro phenotype assay, shown in chapter 3. By analyzing the result of this long-term in vivo injection at 3 weeks, we have been able to measure the effect of stiffness (due to different biomaterials) and nutrients.

Upon triple staining of the retina, we observed in all groups, engrafted hRPCs in the subretinal space of Long Evans rats with different morphology and phenotypic expression. Cells were analyzed for DAPI, human marker and cone marker to measure overall engraftment (Figure 5.5). Specifically, cells injected in PBS showed poor engraftment with a low number of cells expressing STEM121 and being clustered at the injection site with really slow migration, as seen in Figure 5.5A. Cells encapsulated in Gtn-HPA and IPN75 show high survival and engraftment in the subretinal space. These cells have a morphology close to photoreceptors and have a higher surface coverage, showing a higher migration from the injection site (Figure 5.5B and 5.5D). This suggests that encapsulating hRPCs in hydrogel could enhance the regeneration by increasing the migration of cells, therefore improving the surface of engraftment of stem cells. The addition of hEGF showed little to no significance in the overall engraftment of hRPCs. However, as seen in Figures 5.5C and 5.5E, we observed that hEGF increased the presence of double stained cells (expressing both cone and human marker), with cells showing a yellow color (red arrows). This result is coherent with our in vitro experiment, showing that hEGF doesn't impact the viability of hRPCs but can drive their differentiation in vitro and in vivo.

These long-term results confirm our findings for the short-term in vivo experiments: hRPCs encapsulated in gel show higher engraftment than those injected in PBS. However, due to the result of the in vitro data, we also analyzed the specific expression of injected cells with two specific markers: Rhodopsin and RGopsin. Rhodopsin is a biological pigment found in the rods of the retina and is a G-protein-coupled receptor (GPCR). It is extremely reactive to light. Opsins are a group of proteins made light-sensitive via the chromophore retinal (or a variant) found in photoreceptor cells of the retina. RGopsin targets a specific class of cone reacting to red/green light.

To analyze the co-localization and engraftment of hRPCs expressing both human and either rod/cone marker we used an image processing algorithm explained previously which relies on Otsu's method of thresholding. The analysis of RGopsin and STEM121 co-localization showed high significant difference between group, as seen in Figure 5.6B. Figure 5.6A shows an example of a field of view with hRPCs engrafted in the subretinal space and expressing both human marker (in green) and RGopsin (in red). By analyzing the surface coverage of the cells expressing both markers we are able to compare not only the engraftment of hRPCs but the presence of specific sub-population of hRPCs between different injection groups. By normalizing the surface coverage of double-stained hRPCs we observed that cells encapsulated in Gtn-HPA with hEGF shows the highest amount of cone-hRPCs which is followed by the group of IPN75 with hEGF. Those two groups are significantly higher than both gel groups without hEGF. Finally, all groups with gel are significantly higher than cells injected in PBS. This is a really important result which strongly confirms the results we observed in the invitro study: encapsulating hRPCs in Gtn-HPA with hEGF shows the highest controlled differentiation into cone-hRPCs in vitro and in vivo at long-term time points. Of note is that a low amount of RGopsin cells was observed in the PBS groups, which is coherent with the fact that hRPCs are mostly rods.

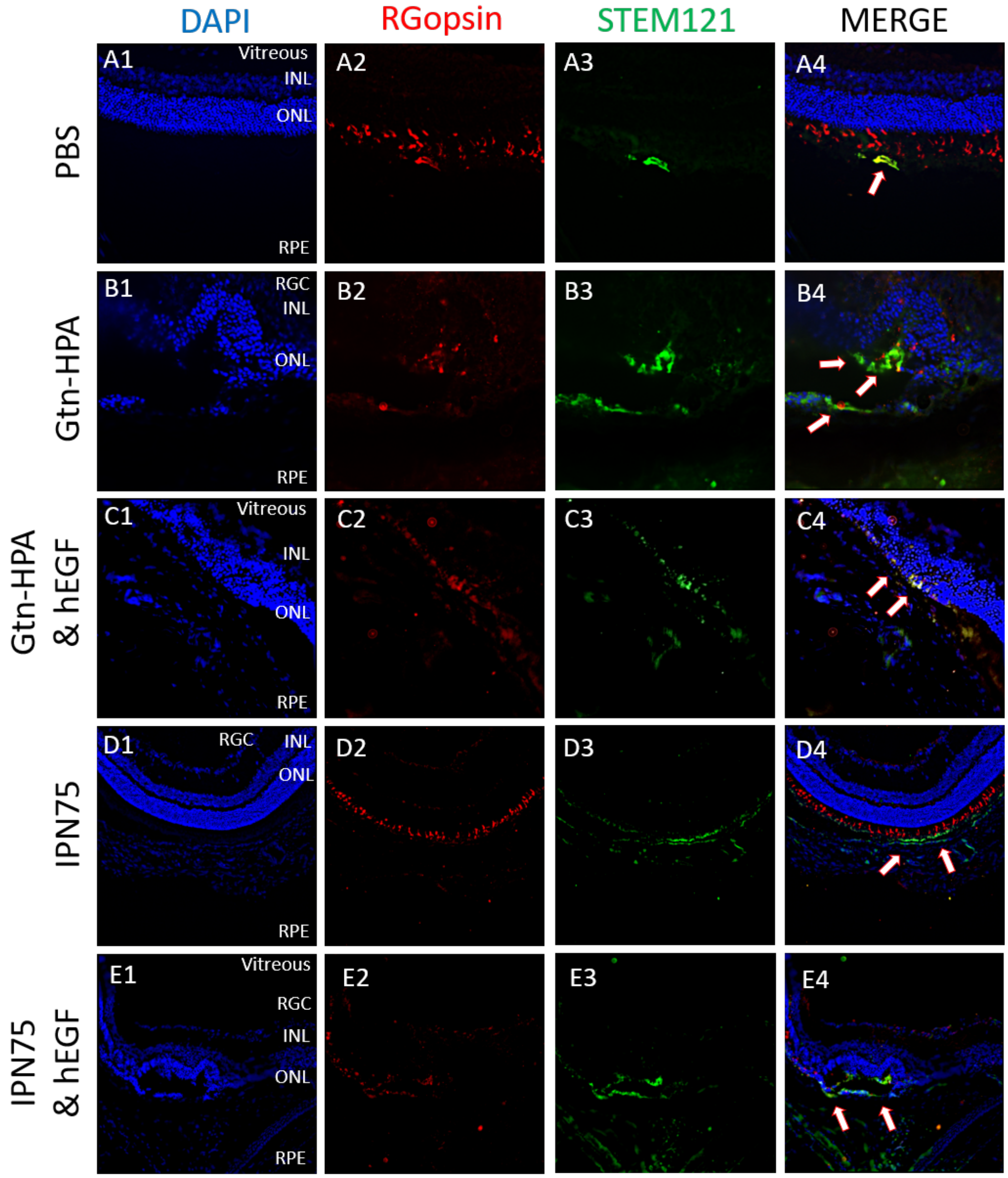

Figure 5.5: Long-term transplantation of hRPC in IPN & PBS. hRPCs survived in immuno-suppressed rats for 3 weeks following subretinal injection. All images were taken at 40X magnification. **A2-E2** are different test conditions stained with RG-opsin (red), **A3-E3** shows Stem 121 (green) staining. Nuclei are counterstained with DAPI in **A1-E1** and the last column shows the merge overlay image. Red arrows show engrafted hRPCs aligned with DAPI near the ONL layer. Scale Bar-200 µm.

The second marker we analyzed for co-localization is rhodopsin, which should be significantly higher due to the high presence of rods in hRPCs. As seen in Figure

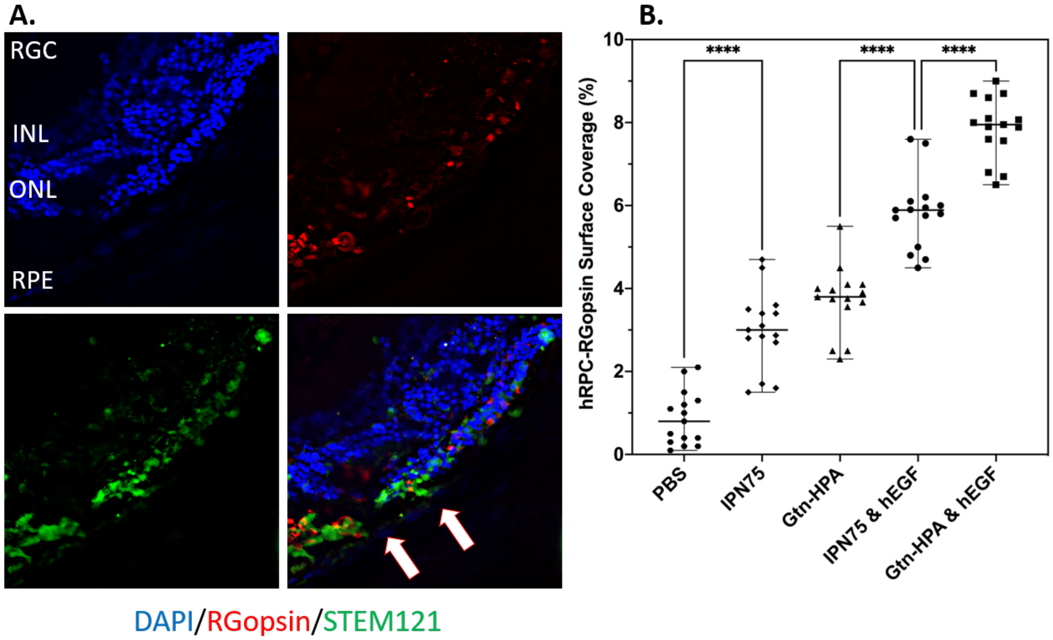

Figure 5.6: hRPCs survival, engraftment, and cone expression post-transplantation.
A. Immunohistochemistry of 5th slide, for Gtn-HPA with hEGF group, stained with Stem121 (green), RG-opsin (red) and DAPI (blue). Scale Bar-200 µm. **B.** Statistical analysis, using one-way ANOVA, of the percentage of cell (expressing RG-opsin) surface coverage for the 5 in injected groups. ****$p<0.0001$.

5.7A, we were able to observe hRPCs engrafted in the subretinal space and expressing both human and rod marker in all groups, which allowed us to measure their surface coverage and statistically compare it. The results, showed in Figure 5.7B, are different from the results we got for RGopsin, with, for rhodopsin, the highest group being cells encapsulated in IPN75 with hEGF. Of note is IPN75 and Gtn-HPA with hEGF had a similar cell surface coverage being higher than Gtn-HPA. All gels groups were significantly higher than cells in PBS. This result confirms the in vitro phenotype assay which suggested that cells encapsulated in IPN75 with hEGF show the highest expression of rhodopsin.

Overall, our findings in the long-term in vivo experiment are crucial as they confirm all our results in the in vitro phenotype assay. Finally, we found that, to enhance hRPCs in vivo differentiation into cones Gtn-HPA with hEGF was the optimal

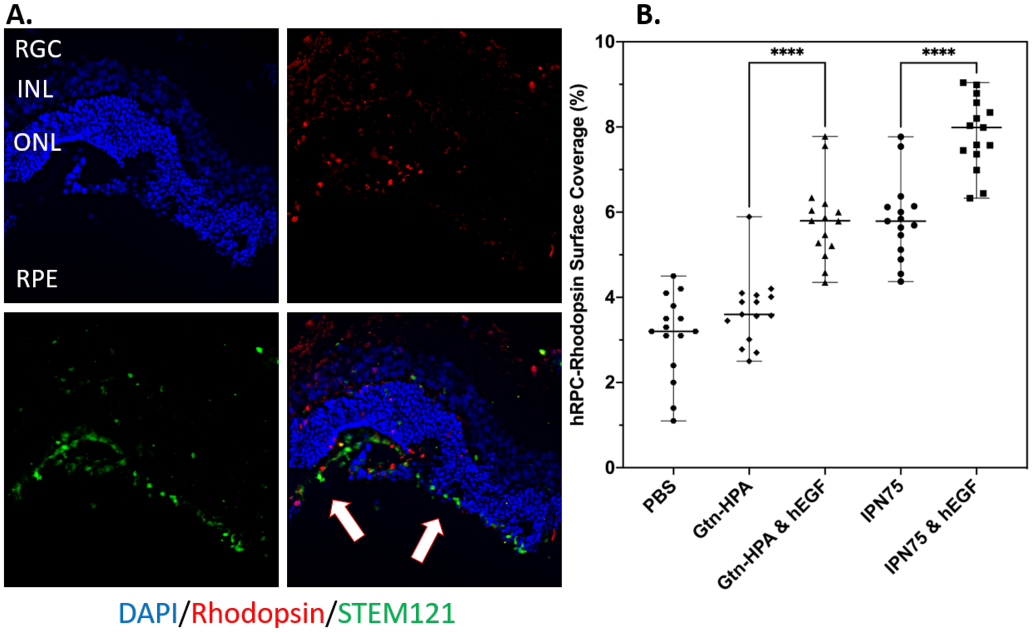

Figure 5.7: hRPCs survival, engraftment, and rod expression post-transplantation.
A. Immunohistochemistry of 5th slide, for Gtn-HPA with hEGF group, stained with Stem121 (green), rhodopsin (red) and DAPI (blue). Scale Bar-200 µm. **B.** Statistical analysis, using one-way ANOVA, of the percentage of cell (expressing rhodopsin) surface coverage for the 5 in injected groups. ****$p<0.0001$.

hydrogel while to promote cell differentiation into rods IPN75 with hEGF was optimal. These findings can be related to the difference in stiffness in our hydrogels (as measured previously in chapter 3) but also their chemical composition with HA-Tyr present in IPN75 compared to pure Gtn-HPA. We also confirmed that our hydrogels can strongly enhance regeneration by acting as passive carrier in which a growth factor (hEGF in this case) can be added. This addition strongly enhanced the controlled differentiation of hRPCs into either rods or cones.

5.5 Discussion

In this study, we have tried to analyze the short- and long-term in vivo injection of hRPCs in rats. We injected hRPCs in PBS, Gtn-HPA, IPN75 with or without hEGF in the subretinal space of non-immunosuppressed rats of the Long-Evans strain. Cell suspensions (in PBS), injected into the subretinal space, showed the least viability and engraftment. In contrast, cells encapsulated in Gtn-HPA or IPN75 show evidence of better engraftment and cellular migration in the host retina. Cells were found migrating in the ONL and INL layers in the retina, while cells in PBS were clustered in the vitreous or RGC side of the retina. The percentage of cells that survived in the host retina was higher in Gtn-HPA grafts than in cell suspensions, suggesting Gtn-HPA was a superior cell carrier. The short-term (3 days post transplantation) immune reaction showing the injury caused due to the injection was also analyzed. hRPCs injection (independent on the carrier) can trigger a reaction from the host as seen with leukocytes staining. In the control group (PBS), hRPCs suspension are exposed to the invading leukocytes especially in non-immunosuppressed animals. Gtn-HPA is an FDA approved biocompatible and bio-degradable polymer [183] that forms a protective barrier for hRPCs, therefore protecting them from the migrating immune cells. This short study aimed at proving the significant decrease of hRPCs presence, viability and migration right after transplantation when injected in PBS compare to Gtn-HPA. The formulation we are proposing here (2wt% Gtn-HPA or IPN75, 0.1 U/ml HRP and 1 mM H_2O_2) showed the highest viability assay for multiple cell lines. Indeed, it is known that hydrogen peroxide can greatly affect cell viability and proliferation even at low doses [87], [185], [186]. This This suggest that we have found an optimal hydrogel to enhance the engraftment of hRPCs and increase the possible regeneration process. As explained in the next chapter we have been able to modify the stiffness but more importantly the gelation time of our pure hydrogel made of Gtn-HPA by mixing it with a different biodegradable and biocompatible hydrogel which possess a higher gel point (HA-Tyr). Therefore, we observed the creation of an IPN, as explained in chapter 2, with is included in the class of in-situ crosslinking hydrogels catalyzed with horseradish peroxidase that possess a high gelation time while keeping cell viability and proliferation at an acceptable level [77], [88]. The long-term (3 weeks post transplantation) in vivo experiment allowed us to compare our in vitro phenotype analysis explained in chapter 3, with the possible phenotype expression of injected hRPCs in the subretinal space of Long Evans rats.

We were able to confirm our in vitro results by showing a similar trend for hRPCs encapsulated in different hydrogels with the addition of hEGF in the mix. Specifically, using Gtn-HPA with hEGF can enhance the differentiation of hRPCs into cones both in vitro and in vivo while IPN75 with hEGF promotes rods differentiation. These results are of utmost importance due to the high heterogeneity of hRPCs [111] which are derived from fetal source and therefore can differentiate into any type of retinal cells (photoreceptors, RGC, bipolar, amacrine or horizontal cells). Being able to control their differentiation in vivo could lead to new therapies focused on specific cell replacement, such as retinitis pigmentosa or rod-cone dystrophy.

To explain these in vivo results we analyzed, in previous chapters, the stiffness of our different hydrogels. We measured that the addition of HA-Tyr in the hydrogel mix can linearly increase the shear and Young's moduli of our gels. Therefore, by increasing the stiffness of our hydrogels and using IPN75 we were able to control the differentiation of hRPCs into rods progenitors. The stiffness effect on stem cells in vitro and in vivo has been analyzed and observed in a lot of studies [187]. Here, we have considered stiffness which is one of the many factors which can influence the fate of hRPCs in vitro and in vivo. Other factors, such as oxygen content, chemical content, ligand density, can also influence hRPCs fate and should be analyzed in our hydrogels to understand their exact effect. The addition of hEGF into our hydrogels can greatly improve the differentiation of hRPCs into rods or cones. hEGF is already being used in the defined media of many stem cell types, especially in the retina [188]. Our hydrogels serve as passive carrier in which we can include growth factor to promote cell viability, proliferation, and differentiation. In our in vitro study we have looked at both hEGF and hFGF which are used to culture hRPCs, however, many other growth factors could be used in order to drive the in vivo differentiation of hRPCs into rods, cones or other type of cells in the retina (such as GDNF) [189].

Chapter 6

Human retinal ganglion cells encapsulated in IPN vitreal injections

6.1 Introduction

Biomaterial-based cell replacement approaches to regenerative medicine are emerging as promising treatments for a wide array of profound clinical problems. Cell replacement therapies critically depend on: the viability of the cells being delivered; maintenance of their phenotype; and their engraftment in the targeted tissue [32], [190]. Many cell therapies have failed to achieve desired outcomes, partly due to low cell viability and failure to attach to the site of injury or disease [191]. In most cases, the exogenous cells are delivered to the target site in a buffered saline solution, raising questions: are the cells receiving the necessary physical and chemical stimuli; and are the cells being retained at the target site long enough for them to bind to the host cells or extracellular matrix to become integrated into the tissue (i.e., engraft)? [192]

Several neurodegenerative diseases including Glaucoma and NF1-OPG, a leading cause of blindness [193], result in a progressive loss of retinal ganglion cells (RGC) requiring an investigation of the intravitreal injection of neuro-modulatory cells [194] or RGC [195], [196]. While all cell replacement therapies, require the exogenous cells to migrate from the delivery site to their natural location within the host, RGC replacement therapy faces special challenges [58], [197]: intravitreally delivered RGC need to penetrate the inner limiting membrane (ILM), extend afferent processes to connect with bipolar and amacrine cells; and extend efferent processes (axons) to connect with specific targets in the brain. Migration of exogenous RGCs through the ILM into the ganglion cell layer and their adhesion to other retinal and brain cells is dependent on the cell adhesion molecules that they express. Transplantation of RGC into the vitreous, a large Interpenetrating network made of collagen fibers and hyaluronic acid [84], could be regulated by an injectable polymeric network. The molecular framework of a composite gel could provide adhesion ligands for cell integrins [121], as well as facilitate attachment of the gel to tissue structures: e.g., to the ILM of the retina. Toward those ends we formulated a gel comprising Gtn-HPA and hyaluronic acid tyramine (HA) . In order to enable enzyme-induced covalent crosslinking of HA, it was conjugated with tyramine (Tyr) [198]. Horseradish peroxidase and hydrogen peroxide incorporated into the gel enabled the independent control of gelation rate and cross-link density of Gtn-HPA/HA-Tyr (Gtn-HA) formulations.

Here we show that by designing a hybrid IPN composed of gelatin-hydroxyphenyl propionic acid and hyaluronic acid-tyramine suitable for vitreal injection, we are able to transplant, grow and engraft hRGC which eventually display signs of regenerating processes along the optical nerve. By precisely matching the chemical and mechanical properties of our hydrogel with the vitreous we achieved attachment to the retina (overcoming the ILM barrier) and enhanced cell migration, engraftment and retinal regeneration. By tuning our bioinspired hydrogel to mimic the vitreous chemical composition and mechanical characteristics we were able to improve in vitro and in vivo viability of human retinal ganglion cells (hRGC) incorporated into the IPN. In vivo vitreal injections of cell-bearing IPN in rats showed extensive attachment to the inner limiting membrane of the retina, improving with hydrogels stiffness. Engrafted hRGC displayed signs of regenerating processes along the optic nerve. Of note was the decrease in the immune cell response to hRGC delivered in the gel. The findings compel further translation of the gelatin-hyaluronic acid IPN for intravitreal cell therapy. Our work will be useful for regenerating vision in patients suffering from retinal diseases, but more generally, the materials design principles herewith put forward should help other stem cell therapies.

6.2 Experimental design

6.2.1 Experimental groups

Table 6.1: Long Evans experimental groups for subretinal injection of hRGCs.

Injection groups	Total no of injected rats	Successful injections	No of rats with presence of cells
Gtn-HPA	5	4	4
IPN75	5	3	3
IPN50	5	4	4
PBS	5	4	4
SHAM	4	4	N/A
Control	3	3	N/A

6.2.2 Overview for SD-OCT

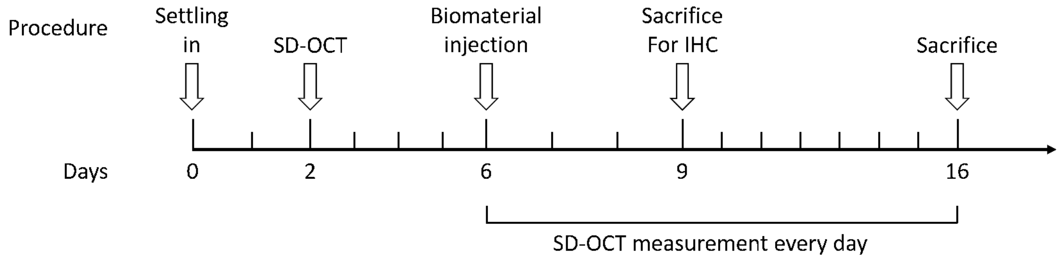

Figure 6.1: Experimental design of hRGC injection in Long Evans rats.

6.2.3 Control and measured outcomes

The control group consisted of healthy rats which had no surgery. The SHAM group consisted in rats which had only a minimal surgery consisting in poking the eyeball with a 31-gauge needle without injecting anything. This is performed to replicate the trauma of needle injection itself. These rats were sacrificed at the same time points as the experimental groups. Outcomes for this study were based on direct examination, image processing and machine learning analysis of retinal sections of injected rats. The measured outcomes were:

- % of hydrogel mass present on top of retina (SD-OCT)
- % of hydrogel mass present in vitro (degradation assay)
- % of gel-retina interface (attachment)
- % of cells engrafted expressing STEM121 (human)
- % of cells engrafted expressing Brn3B (RGC)
- % of cells engrafted expressing DAPI (Nuclei)
- Position of engrafted in cells in retinal layer
- Orientation and size (including processes) of engrafted cells
- % area of IBA1 (immune cells)
- % area of CD45 (macrophages)
- % area of GFAP (Muller cells)

6.3 Materials and Methods

6.3.1 Passive microrheology and PLGA microbeads tracking

All samples having an extremely short gelation time, common oscillatory rheology was not able to capture their gel point. Hence, to characterize this specific viscoelastic characteristic passive microrheology was performed. A volume of 10 µl of 10-20 µm PLGA microbeads (Sigma-Aldrich), at a concentration of 105/ml, were thoroughly added and mixed with all polymers. Then, after addition of the catalyst (HRP) and the crosslinker (H_2O_2), 200 µl of each sample was pipetted as fast as possible onto a microscope slide and particles movement were tracked for a period of approximately 4 minutes by taking a video of their Brownian motion inside the hydrogel in process of gelation. ImageJ (Fiji, NIH) was used to track the center of n=15-17 particles for each sample for 6 minutes. A MATLAB program was then used to calculate the mean square displacement and fit the data with an exponential function as presented in [199]. This fit function was then used to calculate the complex modulus by feeding the data into a MATLAB function that fits this data with a second-order polynomial function from which the first- and second-time derivatives are computed and from that the complex modulus [200]. Finally, the storage modulus (elastic) G' and loss modulus (viscous) G" were measured to calculate the gel point (defined by the crossing of G' and G").

6.3.2 Source, viability and phenotype analysis of hRGCs

Human retinal ganglion cells (hRGC), gifted from Dr. Donald Zack laboratory, were described in previous studies [80], [201], being Brn3b-TdTomato positive. Cells at 1 x 10^5/ml, suspended in saline or medium (mTeSR1 media: Stemcell Technologies) were added to 1 ml of the IPN formulations, along with different catalyst and crosslinker concentrations and were pipetted onto fibronectin-coated round glass coverslips (thickness 5mm, diameter 1 cm, VWR). After 1,3,5 and 7 days of incubation with medium or PBS, they were incubated with 2.5 µM calcein AM (FITC) and 10 µM ethidium homodimer-1 (Cy3) in PBS for 15 min at 37 ℃ and 5% CO_2. hRGC were then washed three times with PBS for 10 min, at room temperature. Coverslips with cells encapsulated in hydrogels were mounted on poly-l-lysine microscope slides (thickness 1mm, L x W 75 x 25 mm, Thermo Scientific Shandon) with low viscosity slide mounting medium (Fisher Scientific) before imaging with an epifluorescence confocal microscope (Leica SP8, USA), in order to capture the 3D configuration of cell distribution through the different hydrogels. hRGC were harvested for immunohistochemistry and flow cytometry with the same protocols explained previously. Primary antibodies and their dilutions are listed in Table 6.2.

Table 6.2: Primary antibodies used for testing of injected hRGCs.

Antibody	Isotype	Dilution	Source	Target
DAPI-VioBlue	IgG2a	1:1000	BD Biosciences	Nuclei
STEM121-FITC	IgG1	1:200	Abcam	Human cells
Brn3a-FITC	IgG1	1:100	ThermoFisher	RGC
RBPMS-APC	IgG2a	1:100	EMD Millipore	RGC
Thy1.1-APC	IgG2a	1:100	Miltenyi	RGC
NeuN-APC	IgG2a	1:100	Abcam	Neural cells
Caspase9-FITC	IgG1	1:50	Santa Cruz	Apoptosis
IBA1-FITC	IgG1	1:100	Abcam	Immune cells
CD45-PE	IgG2a	1:100	Abcam	Macrophage
GFAP-PE	IgG2a	1:50	TakaraBio	Muller cells
Oct4-APC	IgG2a	1:200	BD Biosciences	Stemness
C-myc-APC	IgG2a	1:200	BD Biosciences	Stemness
Ki67-APC	IgG2a	1:50	Santa Cruz	Proliferation
Isotype Rabbit	IgG1	1:100	Abcam	Control
Isotype Mouse	IgG2a	1:100	Abcam	Control
Anti-Rabbit		1:200	BD Biosciences	Secondary
Anti-Mouse		1:200	BD Biosciences	Secondary

6.3.3 In vivo xenograft study - animals, surgery and tissue processing

The research protocol was reviewed and approved by the Schepens Eye Research Institute Animal Facility and was in accordance with the Association for Research in Vision Ophthalmology Statement for the Use of Animals in Ophthalmic and Vision Research. Twenty-seven female Long Evans rats (age 12 weeks, approximate weight 200g, Charles River. Wilmington, MA) were used in the experiments. Transplantations were performed on Cyclosporine (Atopica, oral solution 100 mg/ml, Novartis, USA) immunosuppressed rats. Animals were sedated using 2%-3% isoflurane (Abbott, Solna, Sweden, http://abbott.com) in combination with oxygen by placing the rats in an inhalation chamber, followed by intraperitoneal injection of ketamine (40-80mg/kg) and xylazine (10mg/kg) for anesthesia. Eyes were first anesthetized using topical ophthalmic proparacaine (0.5%) followed by Genteal to keep the lens moist during the surgery. A conjunctival incision and a small sclerotomy were performed using a fine disposal scalpel in all rats. A 2%wt Gtn-HPA/hRGC hydrogel (n=5), 2%wt IPN75/hRGC (n=5), 2%wt IPN50/hRGC (n=5) or a cell suspension in PBS (n=5), were injected into the vitreous of the rats. 3 rats were taken as control and n=4 rats were subjected to only SHAM injection. All injections were performed using a glass pipette (internal diameter, 150 µm) attached to a 10 µl Hamilton syringe via a polyethylene tubing. Approximately 5 x 104 cells in an injection volume of 3 µL were used in each of the 4 groups. The presence of islands of gels onto the back of the eye was checked using a glass coverslip applied to the eye. Vitreal injection was considered successful if shiny islands were seen under the dissection surgical microscope (Alcon Vitreoretinal, Constellation Vision System). Triple antibiotic (Bac/Neo/Poly) was given locally at the end of the surgery to prevent infection. The rats were then placed in their cages for 4 weeks. 100 mg/L of Cyclosporine was added to the water container of all cages and was changed every 3 days.

Four weeks post transplantation, immunosuppressed rats were sacrificed by CO_2 inhalation for 5 min. Cervical dislocation was performed to certify death. Eyes were enucleated and placed in 4% paraformaldehyde for 24 hours. Tissues were subsequently saturated with increased concentrations of sucrose (5%, 10%, 20%) containing Sorensen phosphate buffer. Eyes were immersed in 30% sucrose overnight or until dissection. The tissues were embedded in cryosection gelatin medium overnight and sectioned at 15 µm thickness on a cryostat. Cryosections from Long Evans rats left eyes, were fixed with 4% paraformaldehyde in 0.1 M PBS (Irvine Scientific) at room temperature for 20 min. These fixed sections were blocked and permeabilized with a blocking solution (Tris-buffered saline (TBS), 0.3% Triton X-100 and 3% goat serum (Jackson Immunoresearch Laboratories, West Grove, PA) for 15 min. Samples were then rinsed twice with 0.1 M TBS buffer for 15 min each time, mounted on polysine microscope slides. During the sectioning process, every 4th section was stained and examined by epifluorescence for hRGC presenting with STEM121-FITC (human cell marker) and DAPI-VioBlue (cell nucleus). Every 5th section was stained with CD45-PE, IBA1-FITC (immune cell marker) and DAPI-VioBlue. Every 6th section was stained with GFAP-PE (Muller cells marker) and DAPI-VioBlue. After overnight incubation, samples were rinsed three times with TBS for 15 min. Secondary antibodies (goat-derived anti-mouse and anti-rabbit, DAPI-VioBlue) staining was performed for 1h at room temperature. Samples were then washed a final time with TBS before being mounted on poly-l-lysine microscope slides with low viscosity slide mounting medium. Digital images were obtained with an epifluorescence confocal microscope (Leica SP8) using 63x-oil objective.

6.3.4 Vitreal injections and optical coherence tomography imaging

The same protocol for sedation and anesthesia as for the xenograft study was used for vitreal injections of hydrogels and SD-OCT imaging. Rats left pupils were dilated with tropicamide (VetRXDirect, USA). Animals were then anesthetized and a conjunctival incision and a small sclerotomy were performed using a fine disposal scalpel in all rats. A 2%wt Gtn-HPA hydrogel (n=5), 2%wt IPN75 (n=5) and 2%wt IPN50 (n=5), all samples without cells, were injected into the vitreous of the rats. Animals were then placed in front of the SD-OCT imaging device (Spectralis HRA+OCT, Heidelberg Engineering, MA, USA). Eyes were kept moisturized with HBSS during the whole procedure. Images were taken before, right after injections, 1h after and each day until no more gel was visible. Presence of gel was assessed by visible islands of gel sitting on top of the retina in IR images. Images of the back of the eye with 4B-scans 30 frames were taken and retinal sections with 4B-scans 60 frames, all done in rectangular scan. Acquired images were saved as .tiff files. First, image artifacts due to breathing movements were eliminated by using the StackReg Plugin. Then, all frames were converted into a single image by applying the z-projection. This average enables for the elimination of most of the noise observed on individual images, which help to see the presence of gel and its volume, or degradation time. Comparison before and after injection was performed to see the impact of gel injection on retina morphology and detachment.

Three days post vitreal injection, rats were sacrificed by CO_2 inhalation for 5 min. Cervical dislocation was performed to certify death. The same protocol as for xenograft study was applied to enucleated eyes. After sectioning, every other section was stained and analyzed with Hematoxylin and Eosin (H&E) in order to measure and locate the different gels on top of the retina. Thermo-scientific Rapid-Chrome H&E staining kit was used. This consists in an 18-steps process which permanently stains cytology specimens. Slides are dipped into a series of solutions containing 95% alcohol, distilled water, Hematoxylin, Bluing reagent and Eosin-Y stain followed by a series of washings before the final fixing step. Slides were then mounted and observed under an upright microscope (Leica DM2500) at different magnifications.

6.3.5 Confocal microscopy and cell analysis via image processing

All stained samples (except H&E staining) were analyzed, and images were taken using Leica SP8 confocal microscope. Images were taken with sequential scanning at 1024x1024 or 2042x2042 resolution with the following lasers intensity and characteristics: VioBlue-PMT at 5.4% with line average of 3 and gain of 875 V, FITC-HyD at 2.3% with line average of 3 and gain of 77%, PE-HyD or APC-HyD at 3.7% with line average of 3 and gain of 85%. hRGC viability images were taken at 20x magnification with a z-stack of 300 µm and 22 steps. A 3D projection was used for qualitative analysis while maximum projection was applied as quantification. Cells in 15 randomly-selected maximum-projected fields of view were counted under 20x objective lens magnification with a cell counting and analyzing image processing algorithm [115] (Appendix A.2). Cells number (green for live and red for dead), size (area of positive pixels) and shape factor (e.g., round versus elongated morphology) were measured for each field of view. After 1, 3, 5 and 7 days of culture, the percentage of viable cells was calculated by dividing the number of live cells (FITC) by the total number of cells in the given area (live and dead cells added). The same z-stacks images were used to measure the distribution of the cells through the hydrogels. LASX Leica software enables to measure the average intensity of a marker along each (x,y,z) direction. These intensities were measured for each z-stack, in each group after normalization, and used averaged.

Qualitative immunofluorescence staining (RGC, stemness, neuronal, proliferation and apoptosis markers) along with immune and Muller cell activation markers were taken at 20x of 63x with oil objective magnification with a z-stack of 15 µm and 25 steps. Images, after maximum projection, in 15 randomly selected fields of view were used to quantify the surface coverage of specific markers (IBA1, GFAP and CD45). To do so a MATLAB algorithm was created that consisted in calculating and counting (with a tolerance of 0.01%) the number of colored pixels (Green for FITC channel and Red for PE or APC channels) for each marker. Then, a percentage compared to the total size of the image was created which corresponded to the surface coverage of the specific marker.

Entire tiling of the retina was performed on all injected groups (Gtn-HPA, IPN75, IPN50 and PBS) at 63x with oil objective magnification and z-stack of 20 µm with 50 steps. The tiling square size was 25x10 fields of views, which was reduced by only choosing the field of views containing parts of the retina as seen in Figure 6.12. Finally, in order to be able to quantify the improvement of injected cells migration and engraftment into the retina of rats, STEM121-FITC with DAPI-VioBlue and TdTomato-PE staining were analyzed in a larger quantity than all other images. Images were taken at 63x magnification with a 15-µm z-stack and 22 steps. For each group, 60 fields of view, chosen in the center of the retina (where the injection was performed) were analyzed.

6.3.6 Hydrogels-ILM interface and OCT analysis algorithms

Each slide, stained with H&E, was analyzed under brightfield light microscopy at 20x magnification to find the location and size of the different hydrogels after three days. To quantify this measurement, 10 fields of view were used to look at the interface of retina and vitreous. Interfaces were analyzed as follow: where gel was visible (attached or not to the retina) the interface was split into 200 µm parts (usually 2-3 per image); the interface of each part was then characterized by looking at the region of attachment (red regions in Figure 6.9a) and the others (white regions in Figure 6.9b). Afterwards, the percent of attachment for each interface (proportion of red regions compared to white regions) and the distribution of the gel at the interface (holes in the red regions) were calculated using a MATLAB algorithm. This enables for the characterization and measurement of the attachment of the different gels to the retina after three days. Islands of gels were visible during SD-OCT data acquisition and a quantification of gel presence was performed by applying an image processing thresholding algorithm. This algorithm was based on Otsu's method of thresholding [202] and enables a specific quantification of the gel degradation in vivo. After taking the OCT images of the section of the retina, 10 fields of views were analyzed for each group. In order to apply and use Otsu's method, the retina and the noise were processed to be considered as the background while the gels were processed to be considered as the foreground. Most of the noise was deleted by the plugin in the SD-OCT software, hence the rest of the image was just composed of a bright retina (curved with different layers) and islands of gel on top of it. In order to process the retina as background, different values of the presence of the retina with no injections were calculated: this consists in counting the number of foreground pixels found with Otsu's algorithm in OCT images without injection. These values were used as a normalization in order to find the surplus of foreground pixels where gel was present. This quantification was performed for all groups at all time points and an in vivo degradation curve (which was confirmed with in vitro degradation) was calculated.

6.3.7 Image processing algorithms for detection of cell migration, co-localization and orientation in the retina

The improvement in engraftment of encapsulated hRGC was quantified by measuring cell migration (location in retinal layers after 1 month), co-localization (expressing both Brn3b intrinsically and STEM121 human markers) and, for large cells, orientation (angle formed by extended processes and retina). After using Leica SP8 confocal microscope to image the test groups (60 fields of view per group), as explained earlier, colored images (VioBlue for DAPI, FITC for STEM121 and PE for TdTomato) were analyzed.

To segment cells from images, we designed a two-step algorithm (Appendix C). We first normalized pixel intensities of input images from 0 to 1. Due to the large amount of noise in the image, we started the segmentation pipeline with a small amount of gaussian blur to smooth the image. Part of the cells were very dim, therefore, to segment them, we used a 1^{st} low threshold (around 10% of intensity) to segment cells. To remediate cells which displayed small holes, we incorporated a closing morphological operation (consisting of a dilation followed by an erosion). We also ran an opening (an erosion followed by a dilation) to remove small clusters of pixels that were most likely noise. For large cells, the low threshold followed by morphological operation led to a high recall for cell pixels. We then segmented the brightest part of cells using a 2^{nd} larger threshold (around 0.3). To merge those two segmentations, we designed a fusion algorithm. Using the rough segmentation obtained from the 1^{st} threshold, we employed a connected component algorithm to label each independent group of segmented pixels. Then, we eliminated each labeled group of segmented pixels which did not contain pixels from the high threshold segmentation. The final result had a high precision (high threshold) and a high recall (low threshold). We used labelled groups of segmented pixels to compute the area of segmented cells.

All images were manually annotated using an online annotation tool (Makesense.ai). This enabled the localization of each layer of the retina and therefore, by fitting labelled groups, the migration of injected cells and their location in the retina. The orientation of both retinal layers and cells was measured by fitting each group with the smallest enclosing ellipse. To make sure that STEM121 human staining and intrinsic Brn3b expression were co-localized in regions of interest (cells) we used a co-localization algorithm previously described [203]. Using MATLAB as a basis, the co-localization program analyzed the content of images taken with confocal microscopy. First, images were filtered, normalized, and analyzed with co-localization and Pearson's and Mader's algorithms. Co-localization consists in finding the fraction of pixels which possess a high intensity in both colors (green and red in our case) with linear approximation. P-value, Pearson and Mader's coefficient and co-localization number were then calculated and reported.

6.3.8 Statistical analysis

All experiments were performed with n=10-15 (except image processing for cell location and migration which had n=60 for each group). The power calculation was based on detecting a significant difference in the means between groups of 30-40% with a standard deviation of 15%. Values were expressed as mean ± standard error mean (SEM) using GraphPad software (https://www.graphpad.com/). Analysis of variance (one-way and two-way ANOVA) followed by Tukey's and Student's t-test were performed for statistical analysis. Statistical significance was set at $p < 0.01$.

6.4 Results

6.4.1 Tunable IPN for hRGCs encapsulation

IPN surgical tunability

For our system, both the Gtn and HA networks are in-situ enzymatically crosslinked with horseradish peroxidase (HRP) and H_2O_2 (see details in methods) [88]. For in-situ crosslinking hydrogels, controlling the gel point is critical in terms of surgical performance: to avoid needle clogging. In order to prove that gel point and stability of gels can be tuned by controlling the content of IPN we needed to be able to quantify the elastic nature of gels in the crosslinking process. To measure the gel points of our samples we employed microrheology to deal with the extremely fast gelation of these IPN. To obtain this measurement we utilized passive microrheology by preparing uncrosslinked IPN and homopolymer mixed with 10-20 µm PLGA passive microbeads. To characterize the viscoelastic nature of these gels the mean square displacement (MSD), due to Brownian motion, of the particles were tracked for a period of approximately 4 minutes (Figure 6.2a).

A MATLAB program was then used to track the particles, calculate the instantaneous mean square displacement (MSD) and fit the data with a double exponential decay. While all samples (Gtn-HPA, IPN75 and IPN50) demonstrated a double exponential decay of microbeads MSD (Figure 6.2a), a positive correlation was found between the gel point time and the HA-Tyr content of the IPN. The MSD of n=15 particles was calculated and averaged every 2s. This fit function was then used to calculate the average complex modulus (every 2s) by feeding it into MATLAB. The data is fitted with a second-order polynomial function from which the first- and second-time derivative are computed and from that the complex modulus. The storage modulus (elastic) G' and loss modulus (viscous) G" are then calculated and plotted in function of time post mixing (addition of crosslinker) as seen in Figure 6.2b. G' and G" measurements confirm the dependency of gel point on the Gtn-HPA content. Gel point ranges from 42s for Gtn-HPA, being far too quick for surgical needs, to 147s for IPN75 and 162s for IPN50. By measuring the time for G' to reach plateau in oscillatory rheology (inset in Figure 6.2a) we could detect the time required for hydrogels to reach steady-state equilibrium (stability of IPN), which increased with the percentage of HA-Tyr.

This is a crucial result as it confirms the hypothesis that these biocompatible IPN can be tuned to fulfill surgical needs. These findings enable us to consider these hybrid IPN, made of Gtn-HPA and HA-Tyr, potential candidates for cell encapsulation, in vivo injection and enhancement of retinal regeneration.

hRGCs encapsulation and analysis

To compare the efficacy of various IPN formulations, we proceeded to in vitro and in vivo experiments with Gtn-HPA, IPN75, and IPN50. In vitro viability assay was performed (1,3 and 7 days) by leaving cells in PBS or adding defined medium in hydrogels (Figure 6.3a). hRGC receiving medium, were significantly more viable than those in monolayer receiving PBS, even after 7 days, suggesting a favorable diffusion of nutrients through the IPN. However, when cells received no nutrients viability decreased significantly with time, reaching <7% for the PBS sample after 7 days.

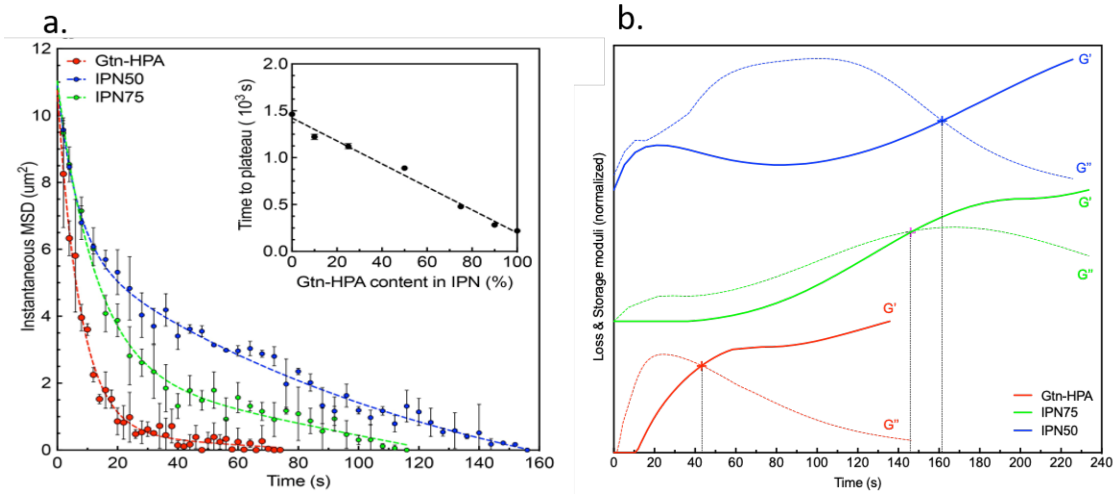

Figure 6.2: IPN microrheological measurements.
(a) Mean square displacement measurements of PLGA microbeads encapsulated in materials during micro-rheology assay for Gtn-HPA (red), IPN75 (green) and IPN50 (blue). N=15 microbeads were tracked for each sample and the data was fitted with a double exponential decay regression. Inset **(a)** shows the time to reach stability of the different IPN during the gelation process. Linear regression was applied to the data confirming the increase of gelation time with the addition of HA-Tyr in the mix. All data is shown as mean ± SEM. **(b)** Loss (G" dashed lines) and storage (G' plain lines) moduli calculation from micro-rheological measurements for Gtn-HPA, IPN75 and IPN50. Gel point is represented with crossing of G' and G" by vertical dotted lines.

Notably, IPN reduced this drop of viability by protecting the cells from the lack of nutrients for all time points, being significantly higher for all IPN groups compared to PBS samples (35-45% viable after 1 week of medium deprivation). This result [204] suggests that these IPN are compelling candidates for enhancing the ability of encapsulated cells to contribute to restoration of retinal function. To determine the distribution of cells throughout hydrogels, the intensity of live (CalceinAM-FITC) and dead (Ethidium Bromide-APC) cells was averaged, normalized and measured as a function of location (cubic regions: 150 μm on a side), Figure 6.3b. The microscope slide samples displayed a peak in intensity around its zero position with a quickly decaying intensity while all hydrogel samples show a constant intensity in all directions. This suggests a uniform distribution of both live and dead cells inside the IPN which is critical for the constant release of cells at the injection site due to the enzymatic and surface degradation of our in situ-crosslinking hydrogels.

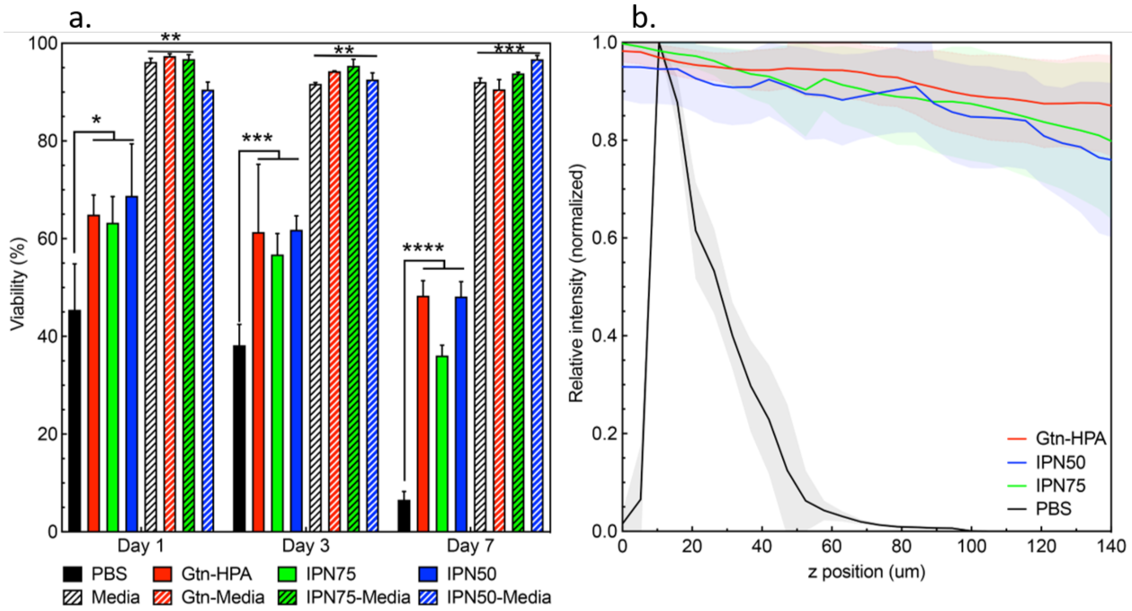

Figure 6.3: Optimal IPN for hRGC encapsulation and in vivo release. **(a)** Viability assay through time of encapsulated hRGC in hydrogel candidates (Gtn-HPA, IPN75 and IPN50) with media or PBS. Plain bars show cells deprived from nutrients while hashed bars represent cells in their defined medium. Data shown as mean ± SEM of triplicate wells with 15 different fields. Two-way ANOVA, followed by Tukey's test, was performed and shows a statistically high significant difference between samples including media and all other groups (**p=0.005 and ***p=0.0001) at all time points; and between hydrogels groups deprived from nutrients compared to PBS (*p=0.01 and ****p<0.0001). **(b)** Relative fluorescence intensity of hRGC stained with live/dead assay, imaged with confocal microscopy for Gtn-HPA, IPN75, IPN50 and PBS, on 150 µm thick slides, in function of their z position.

Confocal microscopy enabled the visualization of the size, morphology and distribution of hRGC (after live/dead staining) throughout 300 µm thick sections of the gels (Figure 6.4). Image processing algorithms (as explained previously) permitted the quantification of live cell size and shape factor in all samples. hRGC in the gels were significantly larger compared to 2D, and their shape factor was lower reflecting a more elongated morphology. This finding suggests that hydrogels may enable certain cell behavior, including the formation of cell processes [205], which are not seen with cells cultured in monolayer in PBS or medium.

Phenotype was checked by flow cytometry and immunohistochemistry on cells

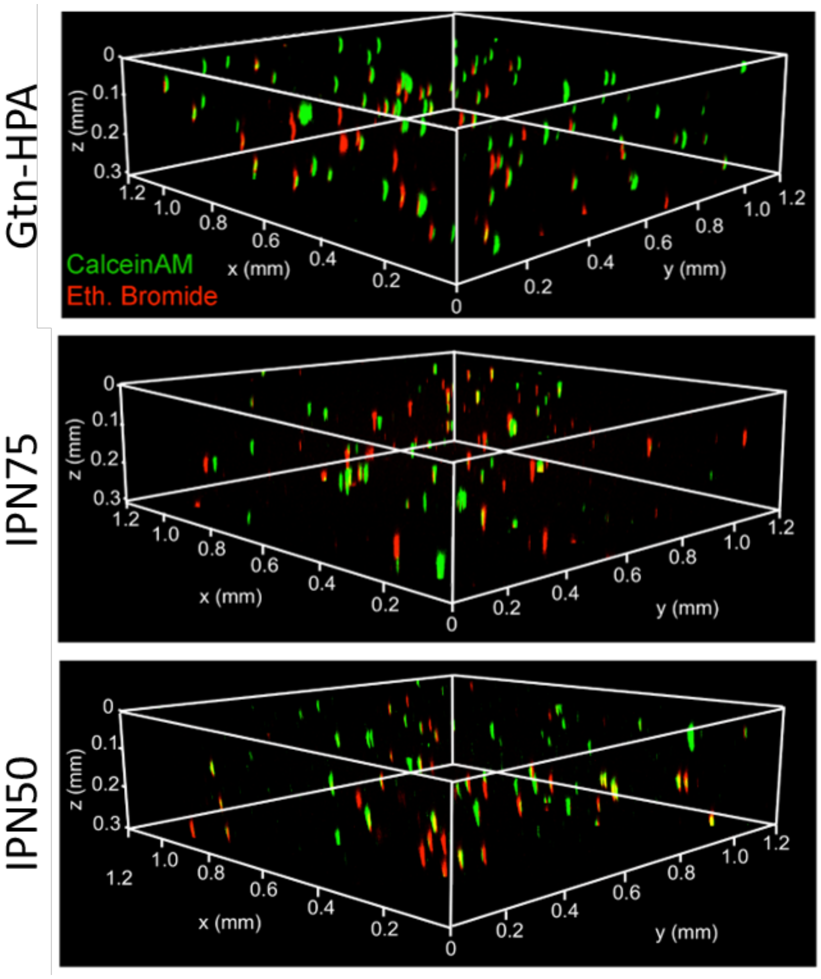

Figure 6.4: 3D scanning of hRGCs encapsulated in IPNs.
3D fluorescence image of live (CalceinAM-green) and dead (Ethidium Bromide-red) hRGC encapsulated in the hydrogel candidates, imaged with confocal microscopy on 1.2x1.2x0.3 mm samples. All images were taken at 10X magnification under fluorescence microscopy.

cultured for 5 days in 2D (media) or 3D (Gtn-HPA, IPN75 and IPN50 with media) conditions. Our hRGC phenotypic expression was measured in previous studies [80] and was shown to have a high positive cell population expressing early RGC markers (such as Brn3a and Brn3b) with a moderate population of late retinal ganglion cells. The gating strategy for flow cytometry is presented in Figure 6.5a-c; and consisted in: gating the cell population with FSC-SSC, then gating the single cell population with the linear representation FSC-H/FSC-A and finally gating the DAPI positive population in VioBlue-FSC. This final population was then analyzed for each isotype control where the gate was put at 2.5% and pasted on all other markers. As explained in previous study [201], our hRGC are labelled and isolated with intrinsic Brn3B-TdTomato expression, this result in a high expression of Brn3B in phenotypic analysis. Percentage of expression of retinal ganglion cells (Brn3b, Brn3a, RBPMS and Thy1.1), neuronal (NeuN), apoptosis (Cas3), proliferation (Ki67) and stemness (Cmyc and Oct4) was measured and is reported in Figure 6.5d while actual cell expression is shown with confocal microscopy fluorescent images (Figure 6.6). Images were taken at field of views presenting a high expression of each marker and are not representative of overall marker percentage of expression. Of note is that a critical factor of using a scaffold to encapsulate cells is to ensure the maintenance of phenotype throughout the entire experiment.

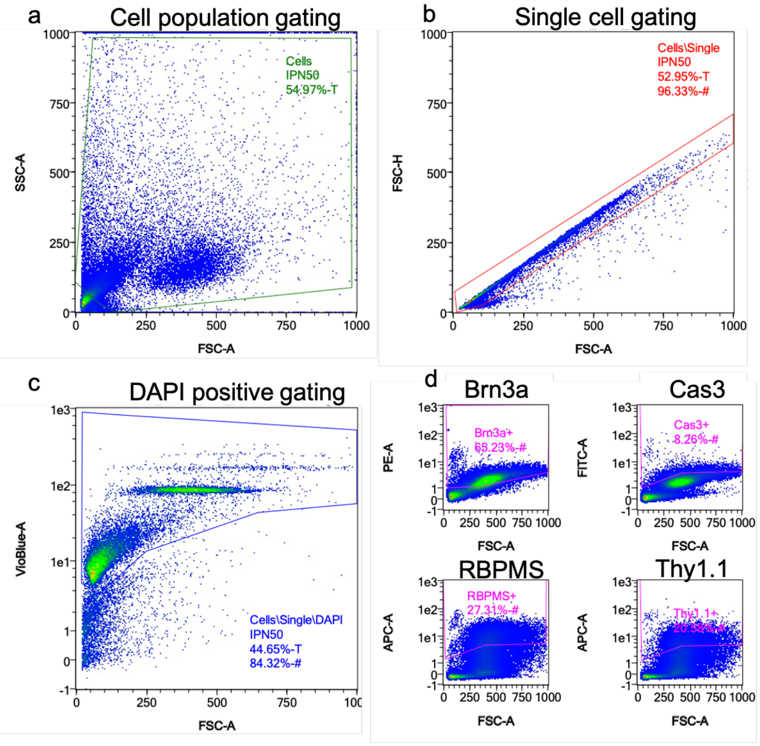

Figure 6.5: Flow cytometry gating strategy for hRGC.
Gating strategy for flow cytometry performed on hRGC to check their phenotype. **(a)** Cell population gating on SSC-A/FSC-A channels. **(b)** Single cell population gating on FSC-A/FSC-H channels. **(c)** DAPI positive population on VioBlue-A/FSC-A. **(d)** Examples of markers gated (RBPMS, Brn3a, Thy1.1 and Cas3). Gates are placed at 2.5% on isotype controls and then applied on all other markers.

Stemness, proliferation and apoptosis expression were remarkably low in all samples. This suggests an already differentiated cell population (with low number of pluripotent stem cells) which is past mitosis. A low apoptosis expression in all samples enables us to consider the hydrogels non-toxic and confirm the viability assay performed on all IPN with healthy cells in 2D and 3D environments.

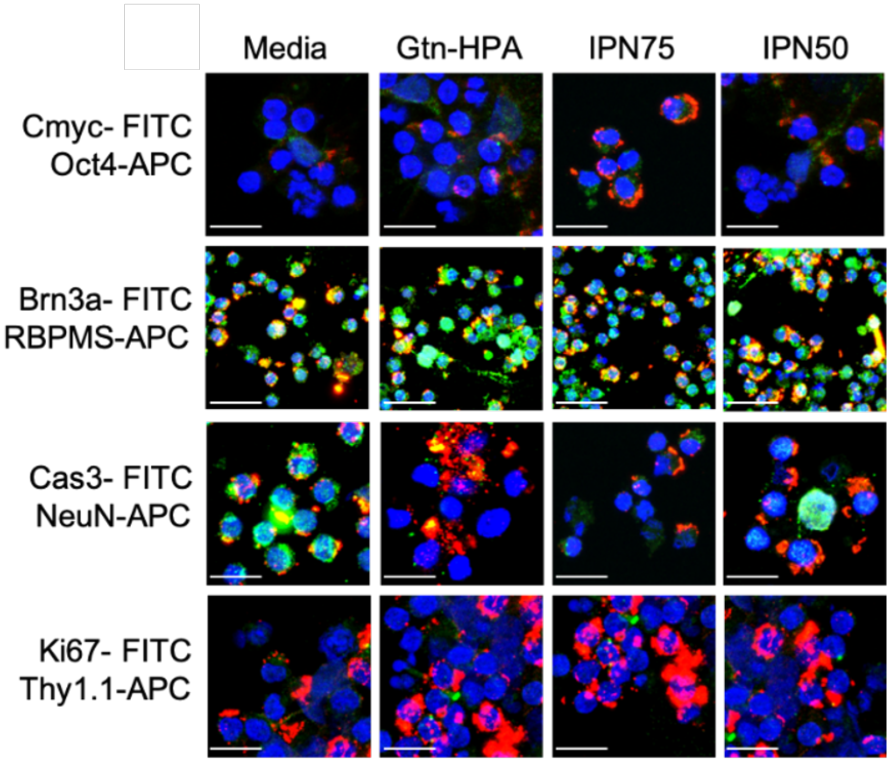

Figure 6.6: Human retinal ganglion cell immunohistochemistry. Fluorescence images of markers analyzed with flow cytometry, with DAPI as nuclear staining (VioBlue channel) for all samples (Media, Gtn-HPA, IPN75 and IPN50). Merged images only. Scale bar is 40 µm in all images. Images taken under fluorescence microscopy 63X magnification.

As explained in methods, cells being Brn3b-Tdtomato positive, Brn3b expression was primordial to confirm cells phenotype maintenance by hydrogels and protocols. This expression is critically high for all samples (around 80%) which also indicate the possibility of locating injected cells in tissue without the need of many staining (Figure 6.7). Brn3a is a marker which overlaps with Brn3b and is shown here to be relatively high for all samples (around 50%) indicating a high percent of early retinal ganglion

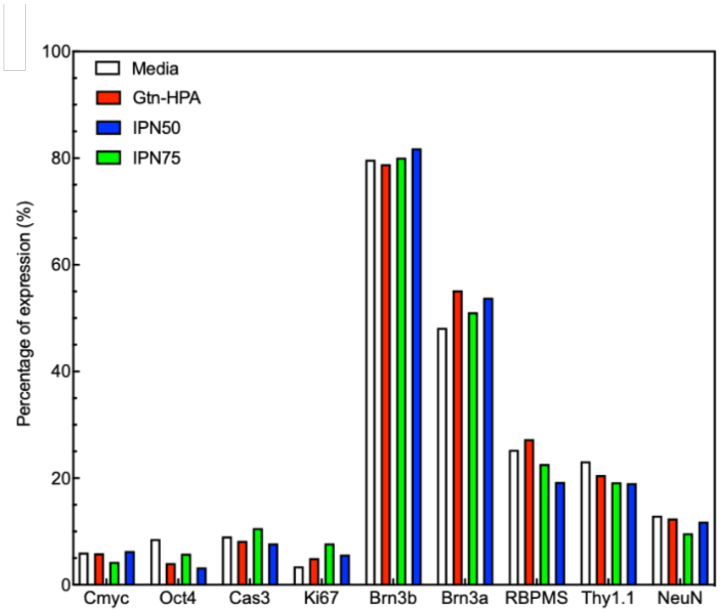

Figure 6.7: Human retinal ganglion cell flow cytometry assay.
hRGC phenotype were analyzed using fixed flow cytometry assay. Percentage of positive hRGC which express stemness markers (Cmyc and Oct4), apoptosis and proliferation markers (respectively Cas3 and Ki67), ganglion cells markers (Brn3b, Brn3a, RBMPS and Thy1.2) and neuronal markers (NeuN) is presented for each sample.

cells in the population. RBPMS and Thy1.1 are markers for late retinal ganglion cells, already fully differentiated. Part of the hRGC population (around 20%) is expressing those two markers, suggesting cells differentiated already present. Finally, retinal ganglion cells' main objective is to extend processes (axons) that merge into fibers to form the optic nerve. These fibers express some neuronal markers such as NeuN. A small part of the hRGC population already expresses NeuN after 5 days in gels (10%) which suggest that injected cells could potentially be able to extend processes that could attach the retina and regenerate a dying RGC layer. This phenotype assay were consistent with previous studies [80] and show no significant difference in proliferation, apoptosis or stemness markers between groups. Our results advocate for the use of IPN50, IPN75 and Gtn-HPA for in vivo transplantation and injection of hRGC.

6.4.2 IPN adherence to the inner limiting membrane of the retina

Gel-ILM interface analysis with H&E staining

Due to the viscous nature of the vitreous, vitreal injections of retinal stem/progenitor cells or drugs pose certain problems, including: how to control their location and release onto the retina? To begin to investigate whether our gels can enhance intravitreal cell therapy, we injected Gtn-HPA, IPN50, and IPN75 (with no cells) into the vitreous of Long Evans rats and assessed, noninvasively, daily changes in their vitreous and retina using SD-OCT. At sacrifice, 3 days post-injection, we evaluated the retina histology with H&E staining (Figure 6.8). Histological images showed the presence of islands of gels present in the vitreous and attached to the inner limiting membrane (ILM) of the retina [206]. By incorporating the hRGC into these Gtn-HA gels, a controlled and constant release of the cells to the ILM could be achieved. Of note, no detachment or injury to the retina was observed throughout the experiment suggesting that no harm was caused to the retina during the injection of gels.

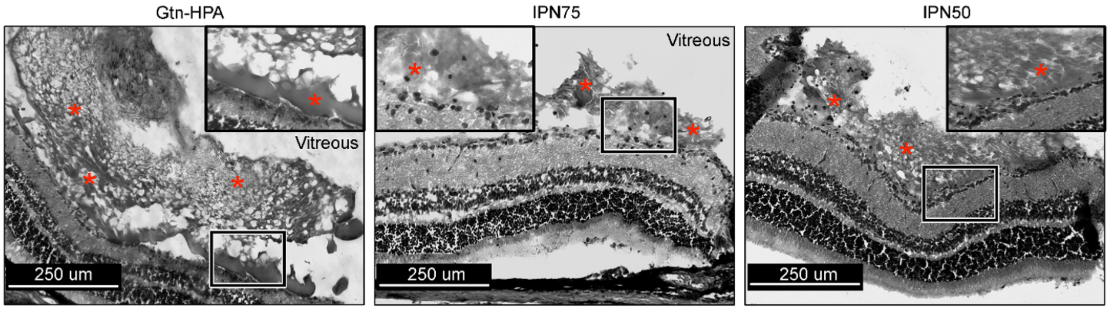

Figure 6.8: H&E staining of invitreal injection of gels 3-days post-transplantation.
H&E staining of rat's retina 3 days post hydrogel injections for Gtn-HPA, IPN75 and IPN50 groups. Images were taken under bright field microscopy at 10X and 63X magnification for respectively large image and inset. Hydrogel presence is observed and labelled with red stars. Inset shows higher magnification and interface of gel with ILM to prove attachment. Scale bar is 250 µm.

To quantify the presence and attachment of IPN we measured the contact between IPN and retinal layers for n=10 fields of view for each sample. As seen in

Figure 6.9a, 200 µm portions of sectioned retina were analyzed (H&E staining) by outlining the interface and calculating contact (in red) or not (in white). Percentage of attachment was calculated for each portion and summed over all replicates which gave for Gtn-HPA, IPN75 and IPN50 respectively 50%, 59% and 79%. By summing over all replicates, we were also able to obtain the actual distribution of attachment which suggests the presence of holes at the interface (see Figure 6.9b). These findings suggest that a higher stiffness and mechanical strength (as in IPN50) could enable a better attachment of injected hydrogels to the retina: higher average attachment and less holes at the interface. When injected cells in saline in the vitreous, cells don't have matrix to stay at the site of injection (usually ILM or RGC layer) and can potentially leave the site and start the process of apoptosis, not being able to attach to other cells. Using these tunable IPN we can encapsulate cells and inject them at the interface where stiffer hydrogels could then attach and release cells directly onto the targeted layer of the retina.

Of note is that we performed H&E staining 1- and 10-days post injections. In the first case gel was not fully attached to the eye but was present in the vitreous cavity, while in the latter most gel was already degraded without any detachment of the retina or its layers.

Optical coherence tomography analysis

When injecting in vitreous Gtn-HPA, IPN75 and IPN50 we performed live Spectral Domain Optical Coherence Tomography (SD-OCT) to image the back of the eye with infrared (IR) and sections of the retina without sacrificing animals. We were able, for the first time, to image and observe vitreal injected gel live in vivo. As seen in Figure 6.10, we acquired images of the back of the eye showing healthy blood vessels, the core of the vitreous and multiple sections of the retina before, after and each day post-injection.

Due to the size of the animals, and the SD-OCT apparatus not made for rodents the quality of SD-OCT images were lower than expected. However, we still observed the presence of islands of gels present in the bulk of the vitreous right after injection for

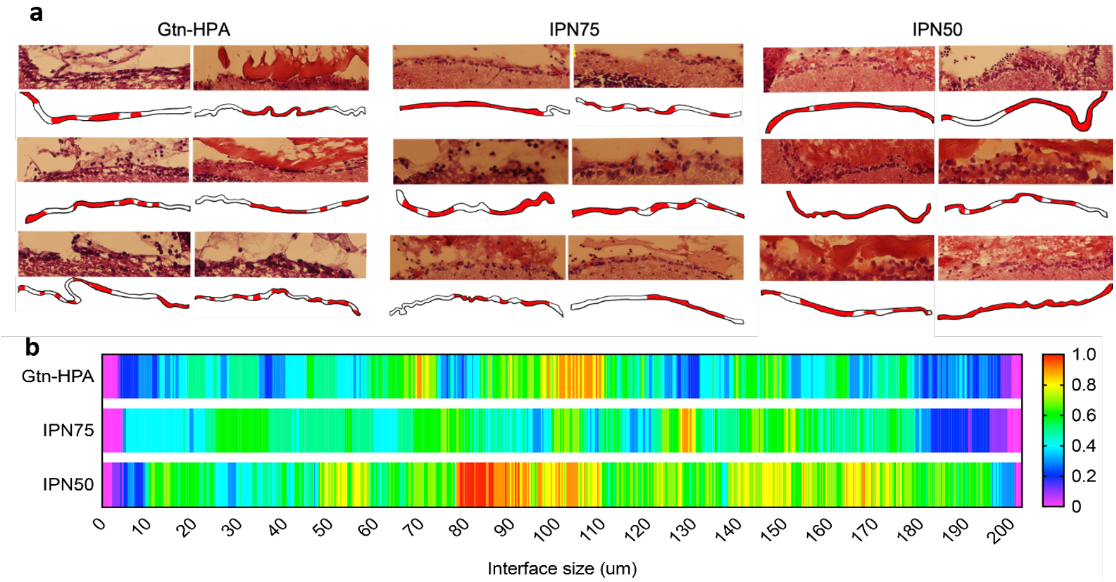

Figure 6.9: Hydrogel-ILM interface analysis after injection of gel in Long Evans rats.
(a) H&E stained 200 µm sections of the retina, centered on the interface hydrogel-ILM for all groups. Analysis of attachment shown below each image with black lines delimiting the interface and red regions showing attachment of gels to the retina. **(b)** Analysis of hydrogel-ILM interface from H&E staining with heat map. 200 µm length interfaces were analyzed for all three samples. Heat map ranges from 0 with no attachment at the interface to 1 with attachment seen on all different slides.

all samples which implied a difficult imaging of the section of the retina at that time point. Indeed, islands of gels were refracting the OCT light far away from the retina therefore sectioned looked cut in half. This will be mainly solved by waiting for the setting of the gel on top of the retina. These islands are characteristics of Gtn-HPA and HA-Tyr in-situ crosslinking hydrogel formation [207] and suggest a successful injection. While the back of the eye was still blackened by the gel, its islands were observed to be sitting on top of the retina around 2-3 days for all samples. White regions of gels attached to the retina suggest 3 days to be the optimal time for setting and start of degradation. We observed a drop-in gel presence starting at 4, 5 and 6 days respectively for IPN75, Gtn-HPA and IPN50. This finding was reinforced by the total absence of gel for all samples after specific time marked on Figure 6.10 (8-9 days for IPN50, 6-7 days for Gtn-HPA and 4-5 days for IPN75). One crucial finding is that morphology of the retina and the back of the before injection and after total degradation of gel are similar, showing no sign of retinal injury nor detachment. These findings suggest successful injection of gel that is enabled to sit on top of the retina and degrades at a moderately fast rate without provoking retinal detachment.

To quantify these findings, we analyzed SD-OCT data with an image processing algorithm based on Otsu's thresholding method (see previous methods). An extraction of background and foreground was performed on n=10 images for each group. This enabled us to partially quantify the presence of hydrogel in the eye in vivo throughout time (see Figure 6.11). We then compared this quantification with a long-term in vitro degradation assay by using degrading enzymes (hyaluronidase and collagenase) with their actual concentrations found in vivo in the vitreous [85], [86]. Both in vitro and in vivo data show similar trends with a high correlation coefficient (R2=0.97) which suggest a correct analysis and measurement of gel presence in vivo with SD-OCT. A curious trend is shown for IPN75 degrading faster than Gtn-HPA besides being stiffer. This can be explained by the presence of both hyaluronidase and collagenase in the vitreous. IPN75, comprising 75% Gtn-HPA and 25% HA-Tyr, will be affected by both collagenase and hyaluronidase while the homopolymeric hydrogel, Gtn-HPA, will just be degraded by collagenase only (as we proved previously with in vitro degradation).

Being able to attach our in situ-crosslinking hydrogel to the back of the eye (ILM) is one of the core results of our study underscoring its ability to enhance not only cell therapies but also vitreal drug injections [61].

6.4.3 Vitreous transplantation of hRGCs encapsulated in gel

Confocal imaging of retina section with hRGCs

The core result of our work is the in vivo experimental demonstration that IPN made of Gtn-HPA and HA-Tyr enhance engraftment and extension of processes from encapsulated hRGC. We injected 5x104 hRGC incorporated in 3 µm of Gtn-HPA, IPN75, IPN50 or PBS into the vitreous of immunosuppressed Long Evans rats. A

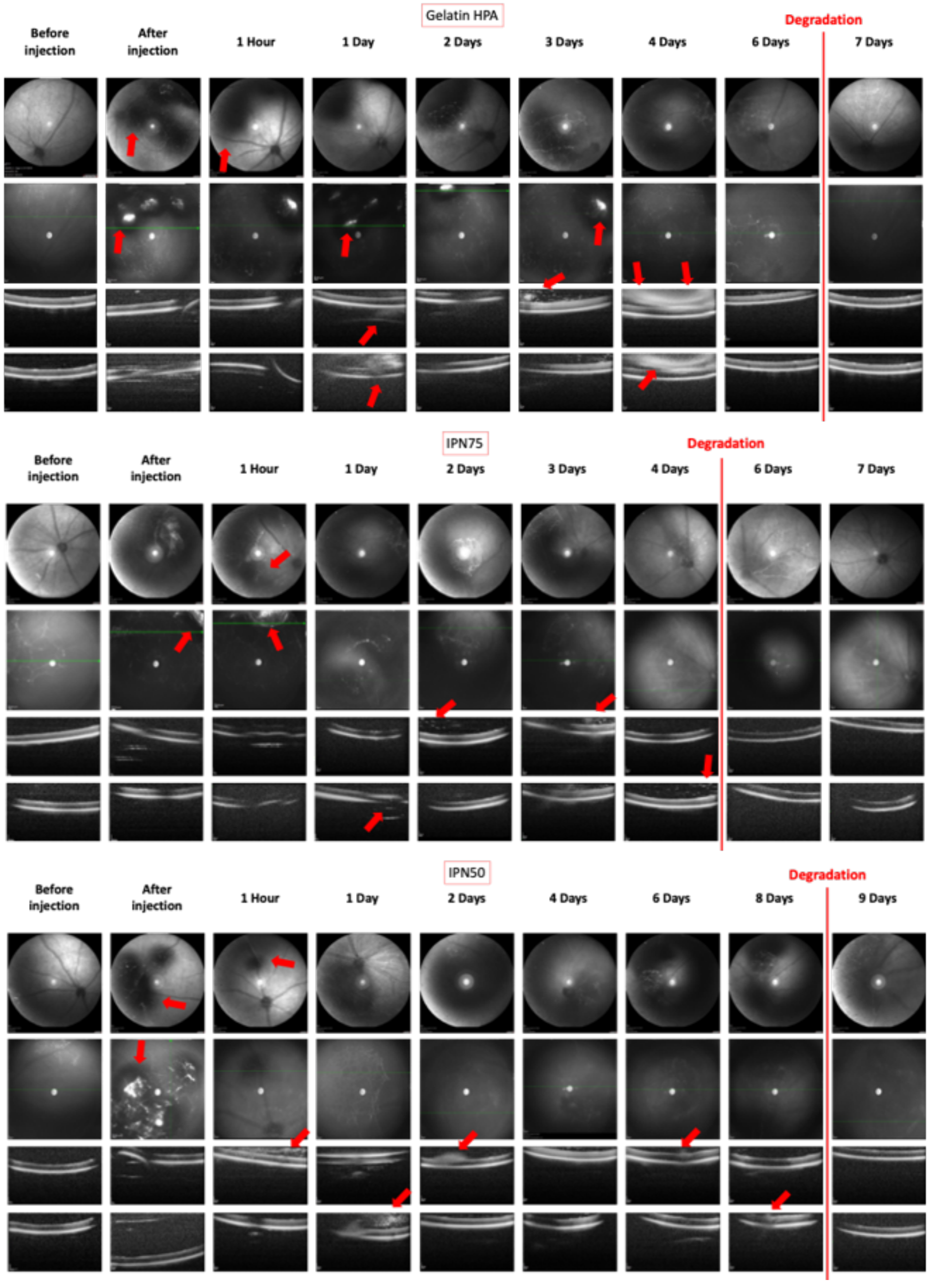

Figure 6.10: Optical coherence tomography and back of the eye imaging of Long Evans rat's post-injection.
First row: back of the eye imaging of rats injected with hydrogels (Gtn-HPA, IPN75 and IPN50) 3-days post injection. **Second row:** SD-OCT view of the section imaged. **Third and fourth rows:** SD-OCT sections imaging of live retina in rats injected with hydrogels showing retinal layers and presence of gels. Approximate degradation time is marked as a red line between two data points. Red arrows point towards islands and presence of gel on the retina and in the vitreous.

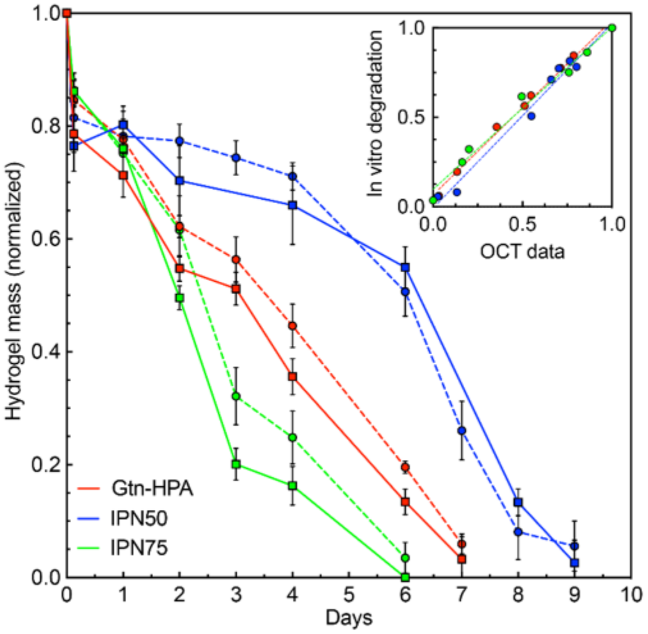

Figure 6.11: In vitro and in vivo degradation of IPNs.
Gtn-HPA, IPN75 and IPN50 hydrogels mass degraded through time during in vivo injection compared with in vitro degradation. In vitro degradation **(plain lines)** was performed using concentrations of collagenase and hyaluronidase found in the eye, while in vivo degradation **(dashed line)** was measured using SD-OCT and image processing. Normalized hydrogel mass was measured for N=15 replicates every 1-2 days. Correlation coefficient between in vitro and in vivo were measured and are shown in inset. R^2=0.97 was found for all samples with no statistical difference found between in vivo and in vitro data.

1-month study was performed to measure the impact of the gels on cell engraftment, using STEM121 (human marker; green) to identify the hRGC which were injected. To prove broad presence of human cells 1 month after injection, tiling of the whole retina were captured for all samples. As seen in Figure 6.12a, STEM121 positive cells were observed next to the optic nerve for IPN50 and IPN75 while being in the center of the retina for Gtn-HPA and sparsely distributed everywhere for the PBS sample. Due to its low intensity and the size of tiling, intrinsic TdTomato-Brn3b was observed to be really dimmed in all tiling. These tiling suggest the success of our xenotransplantation but also of engraftment due to the long-term experiment. Indeed, due to the fast degradation of hydrogels injected cells had to attach and integrate to living tissue to thrive for 1 month in vivo. These tiling also enabled us to measure the size of the retina and by using an image processing algorithm (explained in the next section) to calculate the exact fraction of injected cells ($5x10^4$ per eye) engrafted after 1 month for each whole eye.

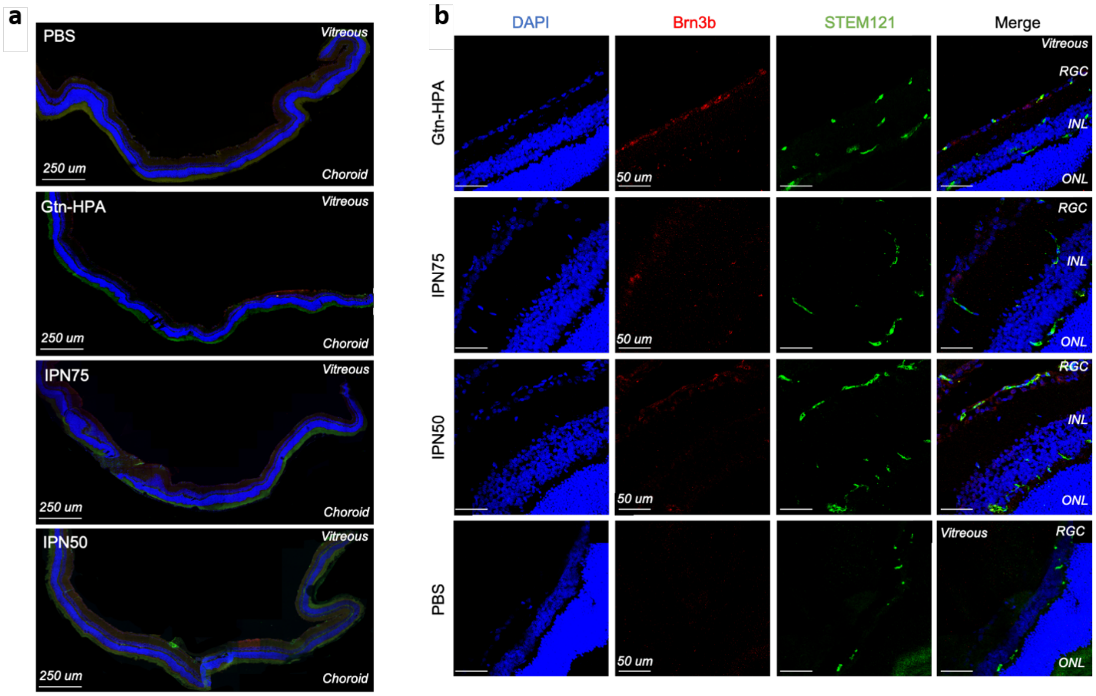

Figure 6.12: Imaging of hRGC 1-month post transplantation in Long Evans rats.
Fluorescence microscopy images of retina 1-month post transplantation. Slides were stained with DAPI-VioBlue, STEM121-FITC and Brn3b-TdTomato. **(a)** Tiling of the retina for the 4 injected groups. Images were taken at 63X magnification with confocal microscopy (scale bar – 250 µm). **(b)** Single channel fluorescence images, taken at 20X magnification, of hRGC injected in all groups (Gtn-HPA, IPN75, IPN50 and PBS). Last column shows merge image with retinal layers labelled. Scale bar is 50 µm for all images.

To further analyze location and engraftment of injected human retinal ganglion cells, we imaged sectioned at 20x magnification for all samples (Figure 6.12b). Cells were found to be mainly in the retinal ganglion cell (RGC), which is the targeted layer, and the inner nuclear layer (INL) some migrated towards the choroid, stopping in the outer nuclear layer (ONL). On first sight, we observed that cells in stiffer hydrogels (IPN5) and IPN75) were larger and more abundant than the one in Gtn-HPA. Overall cells injected in PBS were found to have the smallest size and were low in number throughout all sections analyzed. Compared to tiling, intrinsic TdTomato-Brn3b was observable in these images and shows coherent location with injected cells (co-localization of both markers being analyzed in the next section). A major difference was observed (Figure 6.13) in cell morphology among groups. Cells which had been delivered in gels were found to have processes extended toward the optic nerve (long axons).

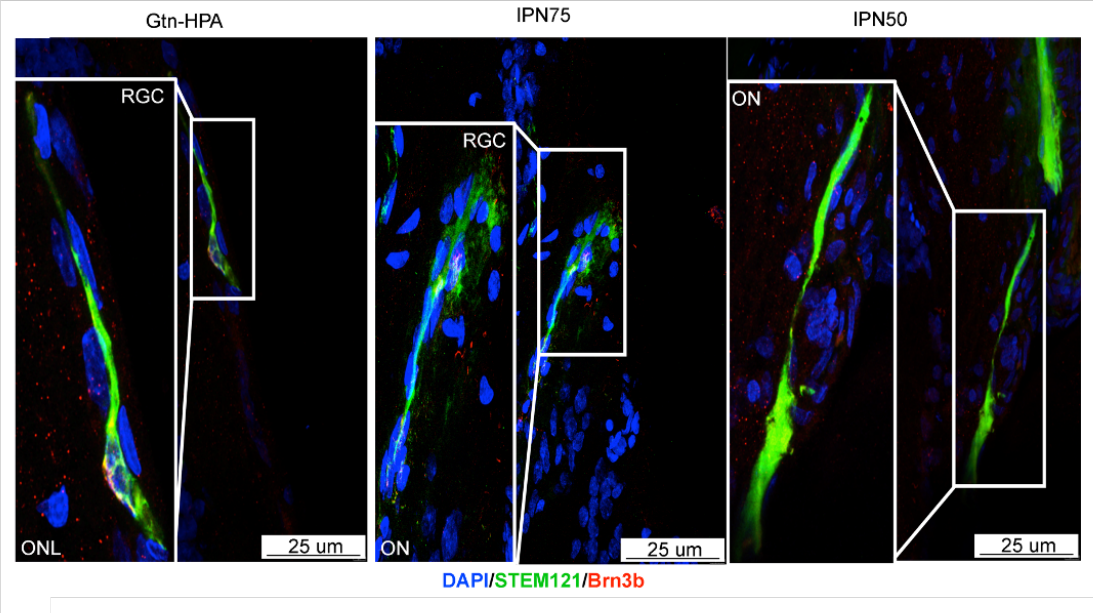

Figure 6.13: Engrafted hRGC cell morphology 1-month post-injection. Fluorescence microscopy images of retina sections 1-month post transplantation. All images were taken at 63X magnification (scale bar – 25 µm). Slides were stained with DAPI-VioBlue (nuclei staining), STEM121-FITC (human marker) and Brn3b-TdTomato (RGC marker present in all injected cells and some host RGC).

To understand and explain why injected hRGC, in the vitreous, migrate towards another layer of the retina, one needs to look at the difference in size and morphology due to the experiment being a xenotransplantation. As a fact, human RGC are 2-3 times bigger than rats RGC [208], therefore, even being attracted to stay and engraft on the RGC layer, those cells try to find the right place to thrive by migrating into other layer with bigger cells (as in INL or ONL). Of note is the location of most cells being in the targeted layer (RGC) for hydrogels groups suggesting a better release of cells throughout time onto the retina compared to cells injected in PBS only.

In vivo hRGCs migration, orientation and co-localization

Most stem cells in vivo transplantations are usually analyzed qualitatively by observing stained sections and cell morphology without applying quantification processes. To enhance this analysis, we created an image processing algorithm capable of localizing cells in their respective layer of the retina, calculating their relative orientation compared to the tissue and measuring the amount of both markers (STEM121 and Brn3b) co-localization in the cell body (Figure 6.14). We created a data set consisting of n=60 pictures in the center of the retina (usually the injected site), taken at 63x magnification, for all samples.

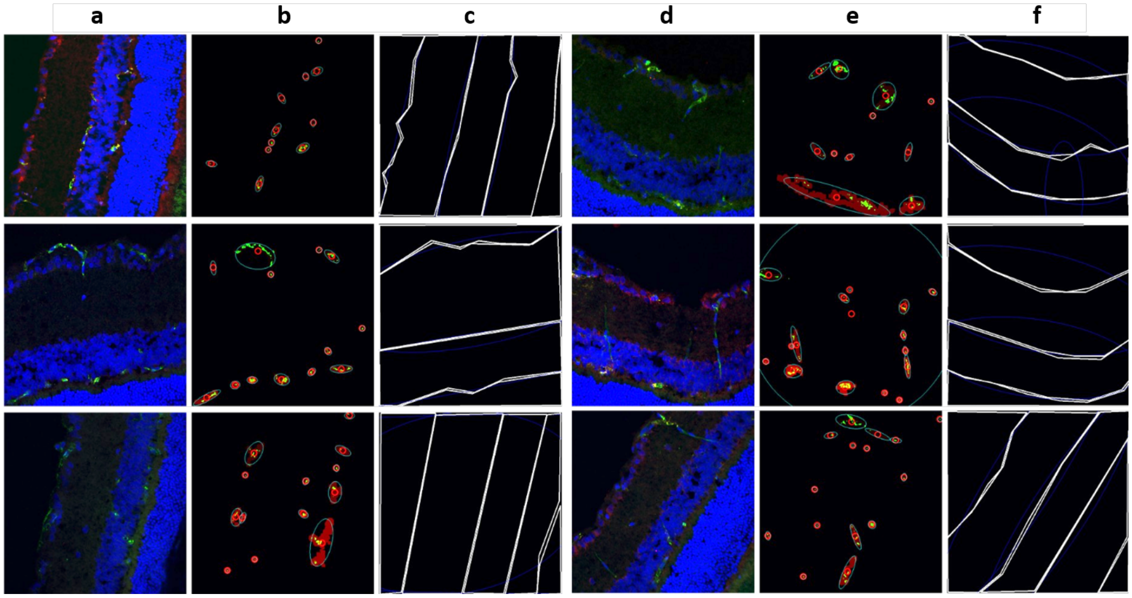

Figure 6.14: Image processing algorithm for measuring in vivo cell migration, orientation and co-localization.
(a, d) Learning data set of fluorescence microscopy images of retina. Over saturation is used for image analysis. **(b, e)** 2 steps thresholding process images to capture cell center, cell bodies and cell orientation. **(c, f)** Images annotated and separated into the different retinal layers.

As explained in previous methods, the algorithm consisted in a 2-step thresholding process which separated the cell center (possessing a high intensity) from their surrounding (dimmer intensity). To use a simple non-realistic analogy, we first segmented whole cells, then segmented nuclei, and finally removed cells not containing any nucleus. This extraction worked with most cells however, precision suffered: some pixels - especially around the border of the image - were above the threshold, leading to segmentation towards unwanted parts of the image. To solve this issue, we decided to delete the 5px border of each image (which corresponded to <1% of the image) usually just removing 1-2 cells per picture. To set a constant and relatable quantification we perform an intensity normalization for all images and were able to localize almost all cells in each image. Nonetheless, being able to extract cell location on each image was not sufficient to significantly quantify our xenotransplantation, therefore we decided to annotate each image with the retinal layers as seen with DAPI staining (third column). This annotation was done by hand using a simple online tool (Makesense.ai) which enabled us to divide each image into retinal regions (Choroid, ONL, INL, RGC and Vitreous). By merging the coordinates of cell extraction with the retinal layer we were finally able to localize each cell engraftment in the retina (as seen in Figure 6.15).

Most engrafted injected cells (40%), for all groups, were found in the RGC layer (Figure 6.15) while the rest were mainly in the inner nuclear layer (INL). No significant number of cells was found in the outer nuclear layer or in the vitreous (<4%). Of the initial 5x104 injected cells, following are the percentages of the viable engrafted cells found 1 month after injection: 52% for Gtn-HPA; 53% for IPN75; 56% for IPN50; and 38% for PBS. A noteworthy finding was that in the target RGC layer of the retina, there was a 2-fold greater number of cells delivered by the IPN50 gel compared to the saline injection group. Moreover, the IPN50 group displayed the narrowest distribution of cells in the target layer.

The ability of injected cells to extend processes is critical to induce retinal regeneration in diseases affecting the retinal ganglion cells [209]. To demonstrate the enhancement offered by the IPN gels we analyzed injected cells, found in the target RGC layer, for their cell body size (including processes) and their orientation in the retina: native RGC extending parallel to the retina cross-section [210]. The actual

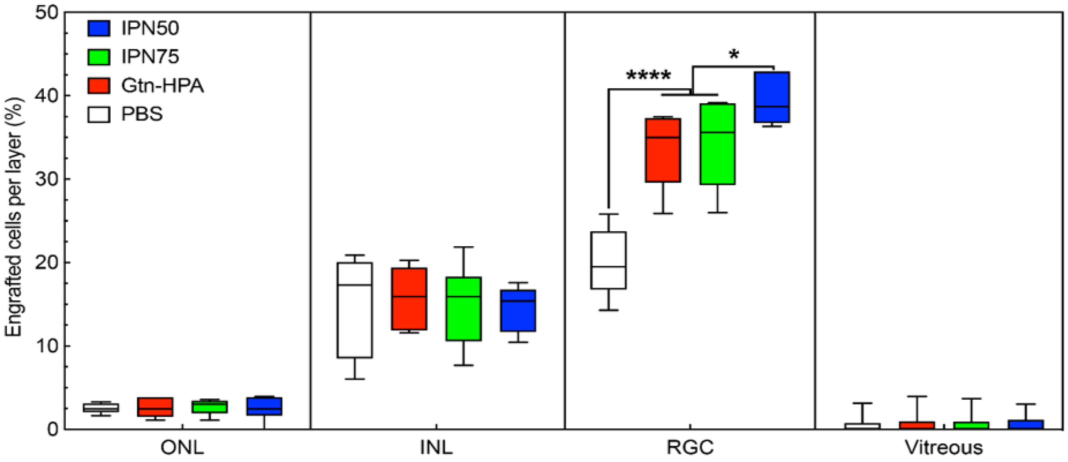

Figure 6.15: Distribution of engrafted hRGC in retinal layers.
Statistical analysis, using one-way ANOVA followed by Tukey's test, of the percentage of engrafted hRGC per layer after 1-month. N=60 field of views were analyzed. hRGC engraftment percentage was significantly higher in hydrogels groups compared to PBS (****$p<0.0001$) in the target layer (RGC): IPN50 showing a higher engraftment and narrower distribution compared to other hydrogels (*$p=0.01$).

orientation of each cell corresponds to the angle difference between its body and the layer it is located in. Both angles were measured by fitting the largest possible ellipse in both the extracted cell body and annotated layers (cell ellipses shown in second column of Figure 6.14) and using their long axes angle.

Figure 6.16a presents, in polar coordinates, the size of these cells (r) in function of their relative orientation to the retina (θ). Most elongated cells were found in the IPN50 and Gtn-HPA groups and have their orientation close to 0 degrees, while none were found in the PBS group. The distribution of medium-size cells is centered around 0 degrees for all groups with significantly more medium-size cells found in IPN50 compared to all other groups. Finally, the number of round and undifferentiated cells was uniformly distributed through size and orientation for all groups. Most human markers (including STEM121 or STEM101) are usually also staining some blood vessels, especially in the retina. Therefore, to guarantee that our in vivo quantification was performed on human injected cells and not host blood vessels (artifacts) we used a co-localization algorithm, previously described [203], which measures the presence of both STEM121 marker and human intrinsic Brn3b for each extracted cell. This code finds the M1 and M2 coefficients which correspond to the amount of respectively green and red pixels in each image while measuring the correlation coefficient of these pixels. This enabled us to demonstrate the fact that events found during staining were injected cells and not artifacts. All events were found to have a co-localization correlation coefficient higher than 70% which corresponds to the grey area in Figure 6.16b.

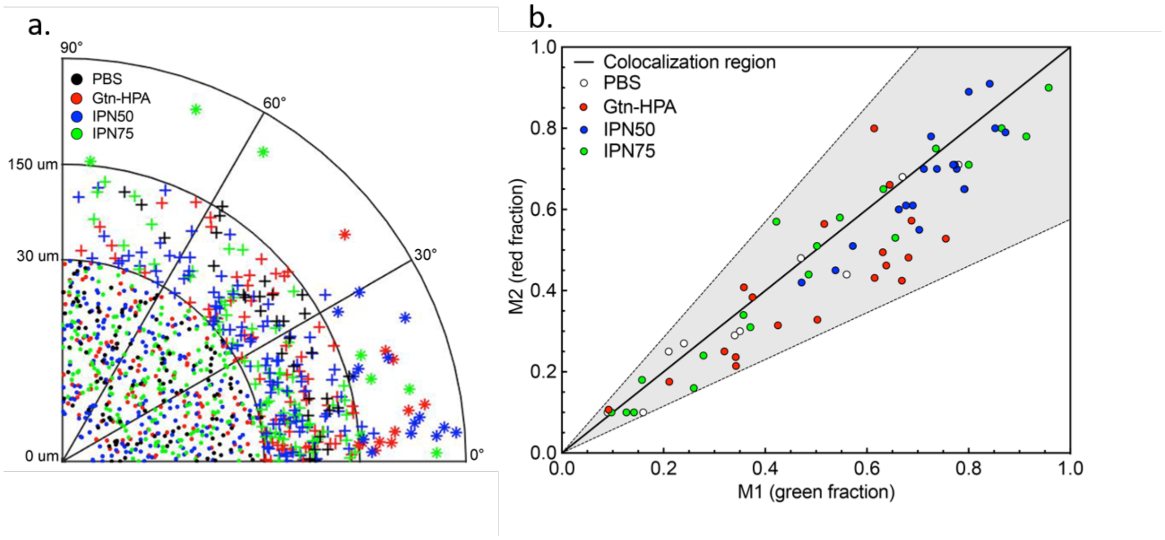

Figure 6.16: Processes extension and co-localization analysis of engrafted hRGC in the target layer.
Cell size and orientation were measured for more than 1x10^3 cells and is shown as a polar plot for all groups in **(a)**. Cells were divided into three categories: undifferentiated round cells (r< 30 µm), medium-size processes extension (30<r<150 µm) and long processes extension (r>150 µm). **(b)** Co-localization analysis of cells extended processes.

Muller and immune cells expression

While in vivo xenotransplantation was performed on immunosuppressed Long Evans rats, analyzing and measuring the core immune response to injected cells and biomaterials is critical to any transplantation. To do so, we stained eyes sections with IBA1, CD45, CD11b and CD68 markers (mainly expressed in microglia and immune cells response to injection in the retina [211]). By imaging with fluorescent confocal microscopy 15 random fields of views, we were able to observe the presence of both markers in all samples, as it can be seen in Figure 6.17. Most AB1 expression was found in the inner nuclear layer while CD45 was localized next to the injection site in the retinal ganglion cells layer. To create a significant quantification of the immune response due to the injections we used a simple image processing algorithm which consisted in calculating the surface coverage of each marker: calculating the number of positive pixels for each marker (green for IBA1 and red for CD45) and normalizing by the total number of pixel in the image. As seen in Figure 6.17, both immune markers expression was significantly higher in PBS than all other samples. In order to extract the effect of the gels from the injection itself we compared this data to the SHAM experiment (consisting in only stabbing the eye with the needle without injecting cells or buffers). All hydrogel samples possess a similar expression of immune cell markers compared to SHAM but higher than the control eye.

Specific immunolabeling of activated microglial cells was analyzed with anti-CD11b, anti-CD68 antibodies revealed high expression in group with PBS injected cells and significantly lower in the group that received cells with gels for CD68 while no significant difference was found for CD11b, as seen in Figure 6.18. Innate immune response usually mounts early in response to stress, infection, and injury and since cells with gel have shown to cause less stress during transplantation the significant lower activated microglial response was noted in group that received cells with gels. These findings suggest that the main cause of immune response when injecting cells encapsulated in our IPN is the needle injection itself, while injecting cells in PBS provokes a higher immune response. The immune reaction analysis showed the injury due to the injection could trigger a reaction from the host as seen with CD45 staining. In the PBS group, hRGC suspension are exposed to the invading leukocytes especially as xenograft in non-immunosuppressed animals. Gtn-HPA and HA-Tyr, being GMP-like approved biocompatible and biodegradable polymers, can form a protective barrier for hRGC, protecting them from the migrating immune cells.

Muller cells form the entrance path inside the retina, extending their processes through all the layers partly forming the barrier between the retinal ganglion cell layer and the vitreous: the inner limiting membrane. When activated, due to entrance of

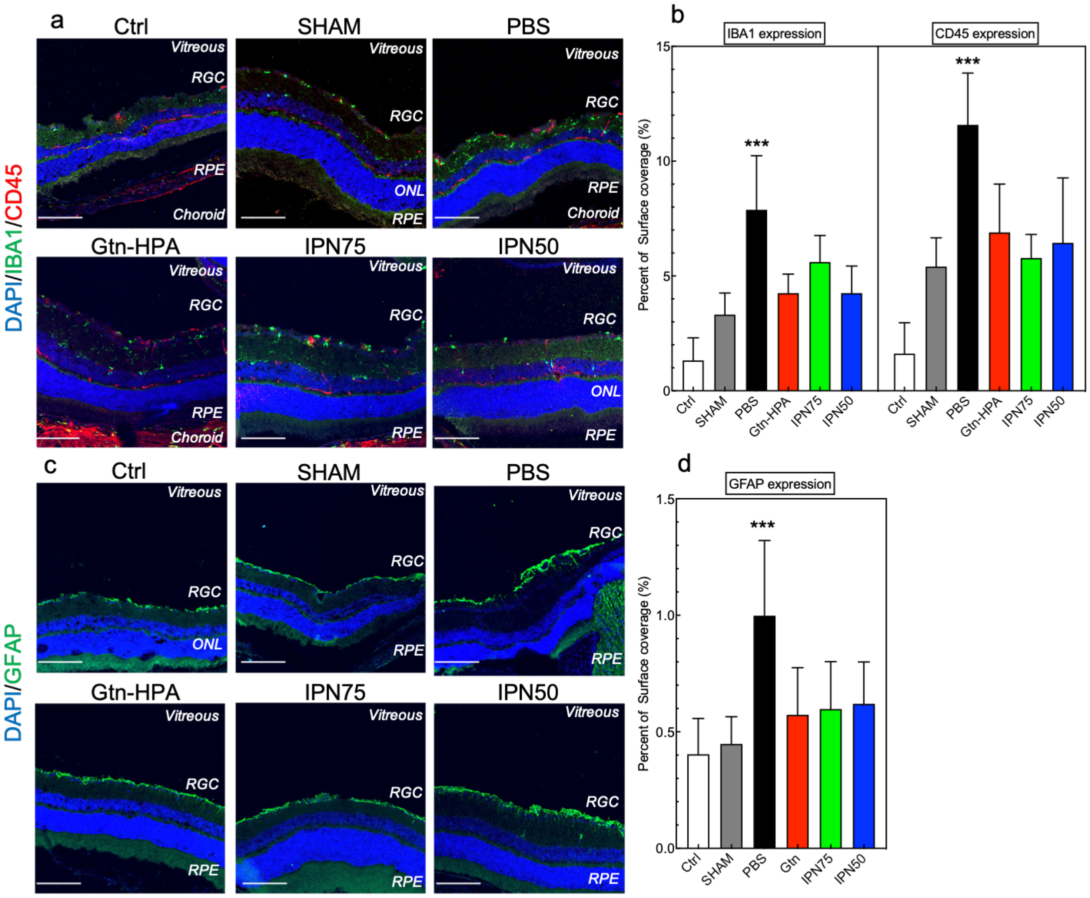

Figure 6.17: Immune response staining of xenografts, 1-month post transplantation.
Images taken under fluorescence microscopy to identify leukocytes, immune cells and Muller cells expression. All images were taken at 63X magnification. Immunohistochemistry staining of all groups for **(a)** CD45 and IBA1 or **(c)** GFAP. Scale bar is 100 µm. **(b, d)** IBA1, CD45 and GFAP expression, obtained from number of colored pixels, analyzed using one-way ANOVA (***p=0.001).

pathogens, migrating immune cells or exogenous ed human cells, Muller cells express largely Glial fibrillary acidic protein (GFAP). To measure Muller cells activation, we stained eyes sections with GFAP and imaged them with fluorescent confocal microscopy, as seen in Figure 6.17c. By using the same image processing algorithm as for the immune response, we were able to quantify GFAP expression for all samples (Figure 6.17d). An identical trend, as for immune reaction, was found in Muller cell activation with a significantly higher expression in PBS samples compared to all other groups. No differences were found between all gels and SHAM samples. These findings corroborate the immune response expression previously explained. While being a delivery vehicle and protecting cells from the intrinsic immune response, hydrogels (and especially these IPN) also facilitate the entry of exogenous cells inside the layers of the retina with less Muller cell activation observed.

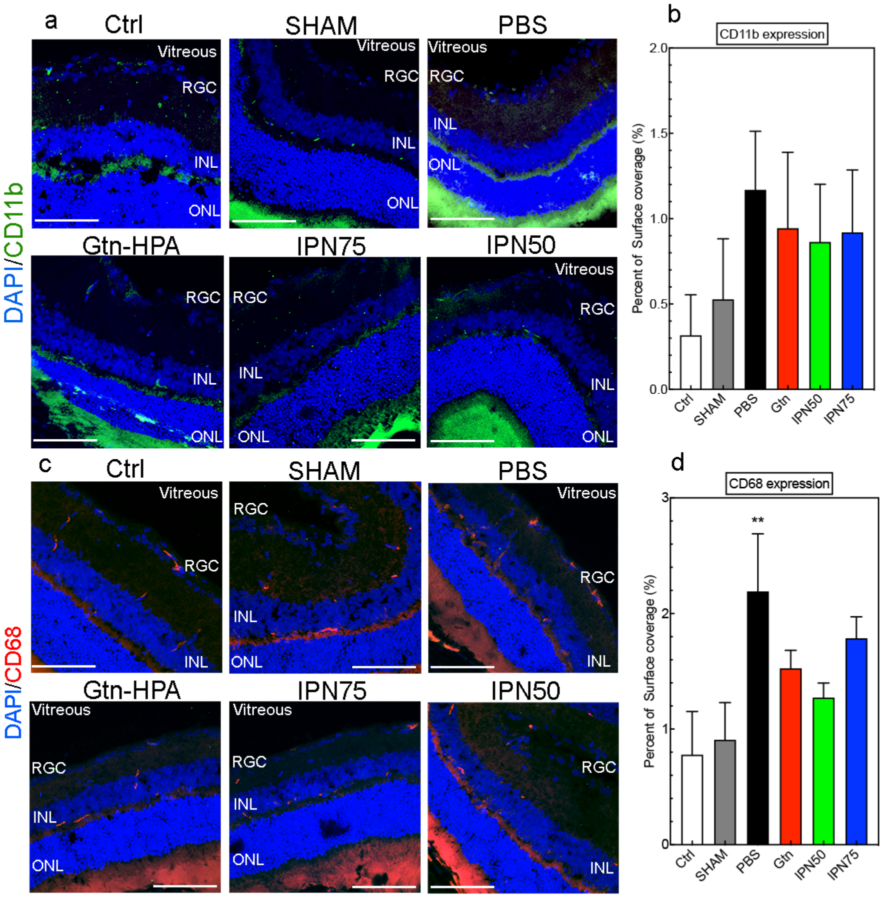

Figure 6.18: Activated microglia response staining of xenografts, 1-month post transplantation.
Images taken under fluorescence microscopy to identify activated microglia, expression. All images were taken at 63X magnification. Immunohistochemistry staining of all groups for **(a)** CD11b or **(c)** CD68. Scale bar is 100 µm. **(b, d)** CD11b and CD68 expression, obtained from number of colored pixels, analyzed using one-way ANOVA (**p=0.005).

6.5 Discussion

Prior studies addressed the advantages of Gtn-HPA as a carrier for subretinal injection of photoreceptor progenitor cells [77], [116], [168]: enzyme-mediated covalent crosslinking; independently tunable gelation rate and crosslink density; protection of cells from shear stress imparted by injection through a small-bore needle; and immune-isolation to-protect incorporated xenogeneic cells against immune cell attack. The current work demonstrates the benefits of admixing HA-Tyr with Gtn-HPA for intravitreal injection of hRGC to potentially regenerate vision lost during diseases such as Glaucoma: extending the range of the moduli of the gel; improving the attachment to the ILM; enhancement of engraftment of hRGC to the target layer; and facilitating the adoption of a natural RGC morphology of delivered cells [212] . Vitreous is one of several tissues in the body—including the hyaline cartilages—that comprises an IPN of collagen (principally type II) and HA. The IPN structure of the collagen and HA in these tissues imparts special mechanical behavior (viz., modulus of elasticity) which, in the case of the vitreous, is critical to support the surrounding ocular structures including the retina. A unique feature of the collagen-HA network in these tissues, enabled by the IPN structure, is the dynamic control of modulus offered by the HA uptake of water: the swelling of the vitreous which is due to a high fixed charge density. Therefore, stiffening the tissue by extending the collagen fibrils of the network [213]. The formation of an IPN from the mixing of Gtn-HPA and HA-Tyr was unexpected as both side groups can theoretically chemically react and bind to each other, which was not observed in our experiment. It is still unclear why the mixing of Gtn-HPA and HA-Tyr formed an IPN, as opposed to a random copolymer network, as both side groups can theoretically chemically react and bind to each other, which was not observed in our experiment. While collagen-HA IPN have previously been prepared for several applications using various methods [214], [215], none have offered the degree of in vivo tunable gelation rate and cross-link density for an injectable gel [216], [217], as provide by the gelatin-HA formulation described in the current work. In a prior study in which 5x10^4 labeled rat RGC suspended in

2 µl of PBS were injected intravitreally into adult rats [218], cells from a wide range of donor ages, but not from adults, were only occasionally found to have migrated into the ganglion cell layer . In other work, in which 40,000 or 60,000 rat RGCs in 3-4 ml of serum-free medium were injected intravitreally in rats, the exogenous cells migrated into, and established themselves in, the ganglion cell layer. They appeared to "extend axons toward the optic nerve head of the host retina and dendrites growing into the inner plexiform layer." [219] Electrophysiological recordings demonstrated the electrical excitability and light responses of the transplanted cells.

Our supposition is that incorporation and delivery of RGCs into the gelatin-HA gel primes them for their migration to and establishment and function in the retinal ganglion layer of the host, by exposing them to certain chemical and mechanical cues that effect their expression of cell adhesion molecules and other receptors, including those that control extension of afferent and efferent cell processes.

Overall, we expect this work to provide design principles for drug and stem cell therapies in the eye and other organs which depend critically on viability and stability of cells during injection and development.

Chapter 7

Isolation of rare human cone progenitor (hCPs) to restore sight

7.1 Introduction

Retinal degenerations cause visual impairment and it occurs due to progressive loss of photoreceptors which are responsible for scotopic and color vision (photopic). Patients with photoreceptor degeneration currently have no treatment available. There are approximately more than 10 million patients worldwide affected by a retinal degenerative disease affecting primarily photoreceptors (as retinitis pigmentosa, cone dystrophy and dry AMD which accounts for more than 200k patients per year in US alone). Present treatments such gene therapy still requires healthy photoreceptors to be able to achieve functional recovery. Thus far there is no treatment that has been able to restore the functionality of the retina. To find a possible treatment using stem cell therapy we have isolated pure human cone progenitor cells from a fetal source which can integrate with host retina resulting in replacement of diseased cells and return of vision. These are committed cells that are destined to mature into cone photoreceptor hence not prone to tumor formation like ESCs or IPSCs. We have successfully cultured and tested these cells and are able to make "cell banks" that can be injected subretinally in clinical setting.

7.2 Experimental design

7.2.1 Experimental groups

Table 7.1: Animal experimental groups for subretinal injection of hCPs.

Long Evans 2 weeks	**Total no of injected rats**	**Successful injections**	**No of rats with presence of cells**
16 weeks-hCP	11	10	10
14 weeks-hCP	9	9	8
SHAM	5	5	N/A
RCS rats 90 days	**Total no of injected rats**	**Successful injections**	**No of rats with presence of cells**
High dose-150k	8	7	6
Medium dose-100k	8	7	5
Low dose-50k	8	7	7
SHAM	8	8	N/A
Control	8	8	N/A
RD1 mice 1 week	**Total no of injected rats**	**Successful injections**	**No of mice with presence of cells**
High dose-100k	4	4	3
Low dose-50k	4	3	2
SHAM	4	4	N/A
Control	3	3	N/A

7.2.2 Overview of animal experiments

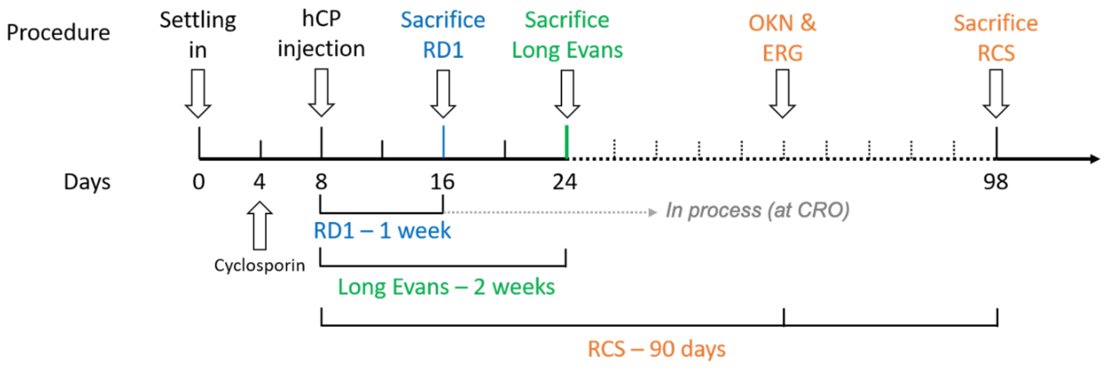

Figure 7.1: Experimental design of hCP injection in different animal models.
Rats and mice are left to settle down for 4 days after arrival, which is followed by the start of cyclosporin treatment. hCP injection is performed at day 8 post-arrival for all groups. RD1 are sacrificed 1 week later, Long Evans 2 weeks later and RCS 90 days later. OKN and ERG are measured for RCS rats 60- and 90-days post-injection.

7.2.3 Control and measured outcomes

The control group consisted of rats/mice which had no surgery. The SHAM group consisted in rats/mice which had only a minimal surgery consisting in poking the eyeball with a 31-gauge needle without injecting anything. This is performed to replicate the trauma of needle injection itself. These rats/mice were sacrificed at the same time points as the experimental groups. Outcomes for this study were based on direct examination, image processing and machine learning analysis of retinal sections or whole mount of injected rats/mice eyes. The measured outcomes were:

- % of cells engrafted expressing STEM121 (human)
- % of cells engrafted expressing Cone Arrestin (Cones)
- % of cells engrafted expressing DAPI (Nuclei)
- Number of nuclei in ONL (function of distance from injection location)

- Spatial frequency (OKN measurement of functional assay)
- Response to light stimulus (ERG)
- % area of IBA1 (immune cells)
- % area of CD45 (macrophages)

7.3 Materials and methods

7.3.1 Source and culture of hCP

Fetal eyes are received from Advanced Bioscience Resources (ABR). Tissues are collected in compliance with FDA's Donor Eligibility guidelines (21 CFR part 1271). The donors are assessed and considered free of risk factors and clinical evidence for communicable diseases. Donors are tested within 2 days of tissue harvest for human pathogens. Tests are performed at a CLIA certified lab using FDA approved test kits. Process and chain of custody for the tissue is performed with Quality oversight. Human eyes from ABR/Cambrex in California arrive 12-24 hours after sacrifice. The tissue samples, obtained overnight, is allowed to settle down for 2 hours. Then carefully, the media is aspirated and a fresh HBSS containing 1% anti-anti solution buffer is added to the tube containing the sample. Eyes are removed in a petri dish and the retina is carefully teased out by removing lens and vitreous fluid, along with RPE (retinal pigment epithelial cells) and ciliary body. Using a fine forceps retina is dissected out and suspended in 10 ml of activated papain solution (1.1mM EDTA, 0.3mM β-mercaptoethanol (bME) and 5.5mM cysteine-HCl) with 0.1 mg/ml of papain. Processed retina is incubated with papain at 37^{o}C for 30 minutes. The tissue is dissociated into single cell suspension. Finally, 40 ml of HBSS is added to the tube and centrifuges at 2000 rpm for 5 minutes. Post-centrifuge, supernatant is removed, and single cell pellet is resuspended in media and plated into a fibronectin-coated T75 flask. Defined media is shown in Table 7.2.

Table 7.2: Media components for hCP culture.

Media 1		Media 2	
Ultra media (Lonza)	500 ml	**DMEM/F12**	500 ml
L-Glutamax (Gibco)	5 ml	**L-Glutamax (Gibco)**	5.5 ml
rhEGF (Peprotech)	1 ml	**100x NEAA**	5.5 ml
rhFGF (Peprotech)	500 µl	**Sodium Pyruvate**	5 ml
Primocin (Invivogen)	1 ml	**B-mercaptoethanol**	4 µl
KOSR (Gibco)	65 ml	**bFGF**	1 ml

Culture of fetal retina cells is performed by feeding defined media (defined previously) every 3 days. When T75 flask appears to be >70% confluent, three T75 are coated with fibronectin to split the population and expand cells. At each step of the process, cell viability is measured, and cell count is analyzed with trypan blue. Media is aspirated and 10 ml of HBSS with 10% TrypZean is added to the flask to detach cells. Flask is then incubated for 5 minutes at 37ºC. Cells are collected and centrifuge at 2000 RPM for 5 minutes. Supernatant is removed and cells are re-seeded into the three coated T75 flask. 5 to 7 days post-plating, cell viability and count is measured with trypan blue and cells are prepared for first isolation.

After the first or second sort, respectively CD73$^+$ cells or hCP are culture and passaged with the same protocol as for fetal retina cells. Finally, cells are used for different experiment or cryopreserved. Cells from all flasks are detached with TrypZean (as previously described) and centrifuge at 2000 RPM after which supernatant is discarded and cell pellet is resuspended in 1ml of HBSS while trypan blue viability and cell count is performed. Cell pellet is resuspended in synth-a-freeze cryopreservation media at a concentration of 4x10^6 cells per ml. Cell suspension is pipette into cryovials at a volume of 1 ml. Vials are placed in 1 ºC container which is placed at -80ºC for 5 hours. Following which cryovials are removed and placed in liquid nitrogen until further use.

7.3.2 hCP sorting strategy

Sorting fetal retina into hCP is a 2-step process (patented) with two different sorts using the Miltenyi Tyto cell sorter [220]. For the first sort, fibronectin coated T75 flasks containing dissociated fetal retina cells are processed with 10% TrypZean to detach and collect fetal retina cells. All cells are centrifuge at 2000 RPM for 5 minutes, supernatant is discarded, and cells are collected in a 50 ml tube as a pellet. Cells are incubated with CD73-APC and CD73-PE (25 µl of each antibody in 150 µl of Tyto Buffer, Miltenyi Biotech) at 4 °C for 30 minutes. Post-incubation, 50 ml of HBSS is added and cells are centrifuge at 2000 RPM for 5 minutes to wash excess of antibodies. Cells are resuspended in 1 ml of Tyto buffer and counted using trypan blue. Depending on the cell number, more tyto buffer is added to reach a concentration of 1x10^6 cells per ml. Cell solution is filtered through 30 µm pre-separation filter. 10 ml of filtered cells solution is finally loaded into the Tyto cartridge (previously primed as per Miltenyi protocol, using only tyto buffer). 100 µl of cell suspension is taking into an Eppendorf tubes and analyzed with MACSQuant to observe and find the positive cell population before running the Tyto.

Tyto cartridge is loaded into the Tyto cell sorter for sorting cells of interest. For the machine to know the cell velocity, a cell must be stained in at least two different fluorochrome, this way the machine can calculate the time it takes the cell to go from the first laser to the second one. As soon as both these variables are stable, lasers can be started, and fluorescent data starts to appear showing an approximate of 5000-7000 cells that flows in front of the lasers. Each cell passes in front of the three lasers and its fluorescent intensity is measured and reported on the graph. The same gating strategy that was used on the control on the MACSQuant is used on the live tyto sorting machine before starting sorts. However, to capture each positive cell, the valve speed and delay of action needs to be set up. The arrival window tab allows to capture the exact population of cells flowing through the microfluidic device by adjusting the window width and making it a tight fit for fine sorts (this depends on cell size, shape, granularity, intensity, stiffness, concentration).

Tyto voltages are modified to observe the positive cell population to be in the 10^2 order of magnitude. Threshold on CD73-PE (blue laser) is applied at V=10, to delete any negative and debris population. Cell speed-threshold (red laser) is applied at V=10, to correctly measure the speed of positive cells. Gate is drawn around the high double positive cell population and window arrival is tuned to captured more than >85% of gated positive cells with less than <10% event on window edge. Sort is started when population is clear, and monitor shows perfect alignment of lasers. Sorting time is 2:30 hours for 10 ml. Average pressure applied to cells is 150-200 mPa. Post-sorting, the cartridge is taken into sterile hood compartment and positive population is collected from the positive chamber (negative population being collected too). 1% of the final population is collected into an Eppendorf tube and analyzed with MACSQuant to analyze the success of sorting CD73 positive cells. Rest of the positive cells are re-plated into a fibronectin coated T75 flask and with defined media. Finally, flask is incubated at 37 °C in hypoxia conditions. For the second sort, $CD73^+$ sorted cells are processed with TrypZean (as explained previously). The protocol of detachment, dissociation and loading in the Tyto cartridge are similar as for the first sort. This time, cells are stained with CD73-PE, Thrb-APC and CD11b-VioBlue (25 µl of each antibody in 150 µl of Tyto Buffer, Miltenyi Biotech) at 4 °C for 30 minutes. Post-incubation, 50 ml of HBSS is added and cells are centrifuge at 2000 RPM for 5 minutes to wash excess of antibodies. With the same protocol, cells are analyzed for positive population and loaded into the primed Tyto cartridge.

Tyto voltages are modified to observe the positive cell population to be in the 10^2 order of magnitude. First negative gating is performed on CD11b positive cells (usually less than <5%), then all tuning is performed on CD11b negative population. Threshold on CD73-PE (blue laser) is applied at V=50, to delete any negative and debris population. Cell speed-threshold (Thrb-APC, red laser) is applied at V=50, to correctly measure the speed of positive cells. Gate is drawn around the high double positive cell population and window arrival is tuned to captured more than >75% of gated positive cells. Sorting starts when population is clear, and monitor shows perfect alignment of lasers. Sorting time is 2:30 hours for 10 ml. Average pressure applied to cells is 250-350 mPa. Post-sorting, the same protocol is applied to collect the positive cell population and re-plate it into T75 flasks. This final subpopulation of hCP is cultured with defined media and culture appropriately for future experiments.

7.3.3 Phenotype assay with flow cytometry and immunohistochemistry

hCPs (5 x 10^5/ml in media) were trypsinized and cell pellet was collected and processed for phenotype analysis a Flow Cytometry assay. Flow Cytometry was performed using MACSQuant flow cytometer (Miltenyi, San Diego). Cells were collected and fixed with Perm/Fix buffer (BD Biosciences) at 4 °C for 15 min. Cells were then washed in wash buffer (BD Biosciences) and incubated, at room temperature, in block buffer (Pharmingen staining buffer with 2% goat serum) for 30 min. Blocked cells were seeded onto a flat bottom 96-well plate (treated, sterile, polystyrene, Thomas Scientific) and stained with conjugated primary antibodies (DAPI-VioBlue, Cone Arrestin-FITC, S-opsin-FITC, R/G opsin-FITC, Blue opsin-FITC, Rhodopsin-FITC, Recoverin-APC, Calbindin- FITC, RBPMS-APC, PKCa-FITC and Brn3a-FITC, KI67-APC) overnight at room temperature. Primary antibodies were diluted in 200 µl of antibody buffer (TBS, 0.3% Triton X-100 and 1% goat serum). After cells were washed three times for 15 min, secondary antibodies were goat-derived anti-rabbit and anti-mouse and diluted 1:200 in antibody buffer (Jackson Immunoresearch Laboratory). Secondary antibodies were applied and left at room temperature for 3 h. light scatter and fluorescence signals from each well were measured using the MACSQuant flow cytometer (2 x 10^5 events were recorded). The results were analyzed using the MACSQuantify software (https://www.miltenyibiotec.com). For each primary antibody DAPI-positive single cell population was gated. The ratio of positive cells in the gated population was estimated in comparison with blank and species-specific isotype control.

Live hCPs grown in chamber slides and cryosection from Long Evans left eye were fixed with 4% paraformaldehyde in 0.1 M PBS (Irvine Scientific) at room temperature for 20 min. These fixed cells and sections were blocked and permeabilized with a blocking solution [(Tris-buffered saline (TBS), 0.3% Triton X-100 and 3% goat serum (Jackson Immunoresearch Laboratories, West Grove, PA,] for 15 min. Samples were then rinsed twice with 0.1 M TBS buffer for 15 min each time, mounted on polysine microscope slides and incubated with primary antibodies overnight at 4 °C (DAPI-VioBlue, Cone Arrestin-APC, R/G opsin-APC, TRA-1-85- FITC, STEM121-FITC) at concentrations determined in laboratory (Table 7.3). The next day, samples were rinsed three times with TBS for 15 min. Secondary antibodies (goat-derived anti-mouse and anti-rabbit) were applied for 1h at room temperature. Samples were then washed one last time with TBS before being mounted on polysine microscope slide with lox viscosity slide mounting medium. Digital images were obtained with an Epifluroscent microscope using 20x objective. Electronic image files were managed using MATLAB software.

7.3.4 Micro-electrode array assay

Using a 1 ml pipette tip, a 2ml cell suspension containing around 500,000 hCP was placed on the MaxWell MaxOne Multielectrode Array and aligned to the electrode. 16,000 electrodes on 4 sq.mm was used. A 5-mm coverslip was placed between the microscope objective and the cell suspension to maintain an optically aberration-free transition zone from the air to the liquid. The HD-MEA chip was plugged into the interfacing circuit board. The cells were allowed to acclimate to the MEA under a 50% contrast background for 20 min. The data recorded on the MEA was sampled at 20 kHz, and filtered on-chip, approximately between 0.5 Hz and 12 kHz. Data was then filtered with a 280 Hz high-pass filter and 7 kHz low-pass filter to reduce offset effect and high frequency noises. Light stimuli were programmed and sent to a LED projector. The projected image was centered on the selected electrode region, and light stimuli were run sequentially. Prior to each stimulus, a 50% contrast background was projected onto the cell suspension for 5 min so that the cells could adapt to the mean projected photopic level.

Table 7.3: **Primary antibodies used for testing of injected hCP.**

Antibody	**Isotype**	**Dilution**	**Source**	**Target**
DAPI-VioBlue	IgG2a	1:1000	BD Biosciences	Nuclei
Cone arrestin-FITC	IgG1	1:200	BD Biosciences	Cones
S-opsin-FITC	IgG1	1:200	BD Biosciences	Cones
Blue opsin-FITC	IgG1	1:100	BD Biosciences	Cones
RG-opsin-FITC	IgG1	1:100	BD Biosciences	Cones
Recoverin-FITC	IgG1	1:100	Abcam	Photoreceptors
Calbindin-FITC	IgG1	1:50	Abcam	Horizontal
Caspase9-FITC	IgG1	1:50	Santa Cruz	Apoptosis
Rhodopsin-FITC	IgG1	1:20	Abcam	Rods
Oct4-APC	IgG2a	1:200	BD Biosciences	Stemness
PAX6-APC	IgG2a	1:100	Santa Cruz	Retinal cells
C-myc-APC	IgG2a	1:200	BD Biosciences	Stemness
Ki67-APC	IgG2a	1:50	Santa Cruz	Proliferation
RBPMS-APC	IgG2a	1:100	EMD Millipore	RGC
PkCa-FITC	IgG2a	1:50	Santa Cruz	Bipolar cells
Brn3a-FITC	IgG1	1:100	ThermoFisher	RGC
STEM121-FITC	IgG1	1:200	Abcam	Human cells
TRA-1-85-FITC	IgG1	1:100	Abcam	Human cells
Isotype Rabbit	IgG1	1:100	Abcam	Control
Isotype Mouse	IgG2a	1:100	Abcam	Control
Anti-Rabbit		1:200	BD Biosciences	Secondary
Anti-Mouse		1:200	BD Biosciences	Secondary

7.3.5 In vivo transplantation of hCPs

Animals were anesthetized with 2%-3% isoflurane (Abbott, Solna, Sweden) in combination with oxygen. Transplantations were performed on Cyclosporine (Atopica, oral solution 100 mg/ml, Novartis, USA) immunosuppressed animals. Rats/mice sedated were given intraperitoneal injection of ketamine (40-80mg/kg) and xylazine (10mg/kg) for anesthesia. Eyes were first anesthetized using topical ophthalmic proparacaine (0.5%) followed by Genteal to keep the lens moist during the surgery. Recipient were injected in sub-retinal space with hCP single-cells injections. A conjunctival incision and a small sclerotomy were performed using a fine disposal scalpel. Cells were injected into the subretinal space using a glass pipette (internal diameter, 150 µm) attached to a 50-µl Hamilton syringe via a polyethylene tubing. The hCPs were injected into the retina bleb as a single-cell suspension in PBS. The injection volume was 2 µl for all replicates. Using a glass coverslip applied on the eye checked bleb presence. Subretinal space injection was considered successful is a shining bleb was seen under the dissection surgical microscope. Triple antibiotic (Bac/Neo/Poly) was given locally at the end of the surgery to prevent further infection. The animals were then placed in their cages for a 14-day study.

The research protocol was reviewed and approved by the Schepens Eye Research Institute Animal Facility and was in accordance with the Association for Research in Vision Ophthalmology Statement for the Use of Animals in Ophthalmic and Vision Research. One, two, or thirteen (depending on the experimental design, see previous section) weeks post transplantation, immunosuppressed animals were sacrificed by CO_2 inhalation for 5 min. Cervical dislocation was performed to certify death. Eyes were enucleated and placed in 4% paraformaldehyde for 24 hours. Tissues were subsequently saturated with increased concentrations of sucrose (5%, 10%, 20%) containing Sorensen phosphate buffer. Eyes were immersed in 30% sucrose overnight or until dissection. The tissues were embedded in cryosection gelatin medium overnight.

During the sectioning process, every 4th section was stained and examined by epifluorescence for hCP presenting with STEM121-FITC (human cell marker), DAPI-VioBlue (cell nucleus), Cone Arrestin-APC (cone marker). Every 5th section was stained with TRA-1-85-FITC (human cell marker), DAPI-VioBlue and Cone Arrestin-APC. Every 6th section was stained with Human Nuclear Antigen (human nuclei), DAPI-VioBlue and Cone Arrestin-APC. After overnight incubation, samples were rinsed three times with TBS for 15 min. Secondary antibodies (goat-derived anti-mouse and anti-rabbit, DAPI-VioBlue) staining was performed for 1h at room temperature. Samples were then washed a final time with TBS before being mounted on poly-l-lysine microscope slides with low viscosity slide mounting medium. Digital images were obtained with an epifluorescence confocal microscope (Leica SP8) using 63x-oil objective.

Long Evans rats

Twenty-five male domestic rats of the Long Evans breed (age 12 weeks, approximate weight 200g) were used as recipients in the experiment. Cryosections from Long Evans rats left eyes (sectioned at 15 µm thickness on a cryostat), were fixed with 4% paraformaldehyde in 0.1 M PBS (Irvine Scientific) at room temperature for 20 min. These fixed sections were blocked and permeabilized with a blocking solution (Tris-buffered saline (TBS), 0.3% Triton X-100 and 3% goat serum (Jackson Immunoresearch Laboratories, West Grove, PA) for 15 min. Samples were then rinsed twice with 0.1 M TBS buffer for 15 min each time, mounted on polysine microscope slides.

RCS rats

Forty male Royal College of Surgeon rats (RCS) (age 2-4 weeks, approximate weight 100g) were used as recipients in the experiment [221]. The same protocol as for Long Evans sections was applied to RCS retinas. This study was performed by an outside contractor: OHSU Casey Eye Institute (Portland, Oregon), under our supervision.

RD1 mice

Fifteen female RD1 mice [222] (age 1-week, approximate weight 50g) were used as recipients in the experiment. RD1 eyes were either sectioned using the same protocol as for Long Evans retinas, or were analyzed with whole mount. Retina was dissected from the vitreous and the RPE layer of the eye. Following dissection, 4 incisions were applied onto the retina, which was then flattened on a poly-l-lysin coated microscope slide. Whole mounts were stained with STEM121-FITC (human cell marker), DAPI-VioBlue (cell nucleus), Cone Arrestin-APC (cone marker).

7.3.6 H&E and nuclei count in ONL

After sectioning, every other section was stained and analyzed with Hematoxylin and Eosin (H&E) to measure the number of nuclei in the ONL of the retina. Thermoscientific Rapid-Chrome H&E staining kit was used. This consists in an 18-steps process which permanently stains cytology specimens. Slides are dipped into a series of solutions containing 95% alcohol, distilled water, Hematoxylin, Bluing reagent, and Eosin-Y stain followed by a series of washings before the final fixing step. Slides were then mounted and observed under an upright microscope (Leica DM2500) at different magnifications. The thickness of the ONL was measured by blindly counting the number of nuclei in thickness at random distance from the injection location, every 100 µm on each side of the retina. Overall average was measured and reported for each animal.

7.3.7 ERG and OKN assays

Electroretinography (ERG) sums up all the retinal activity. Following overnight dark adaptation of 12hrs, the animals were prepared for ERG recording under dim red light. Rats were sedated using isoflurane inhalation followed by Ketamine/Xylazine injection and for mice intraperitoneal injection of ketamine/xylazine solution without isoflurane inhalation. While under anesthesia, the animal body temperature is maintained at 38° C, using a warm heating blanket, and their pupils is dilated using a drop of 1% Tropicamide followed by a drop of 1% proparacaine applied on the corneal surface. One drop of Genteal (corneal lubricant) is applied to the cornea of the untreated eye to prevent dehydration. A drop of 0.9% sterile saline is applied on the cornea of the treated eye to prevent dehydration and to allow electrical contact with the recording electrode (gold wire loop). A 25-gauge platinum needle, inserted subcutaneously in the forehead, serves as reference electrode, while a needle inserted subcutaneously near the tail serves as the ground electrode. A series of flash intensities is produced by a Ganzfeld controlled by the Diagnosys Espion3 to test both scotopic and photopic response. Using acquisition software set a 2KHz sampling rate is set with collection time ranging from 100-1000msec.

Optokinetic (OKN) response is testing with original head tracking apparatus that is further modified to suit the animals. Apparatus consisting of rotation drum with stripes with three different spatial frequencies is used for testing. Rotating drum is illuminated with 3 flood lights and turns around 170°. The intensity of light can be altered with a dimmer and rotation drum is moved to be behind a black wall to ensure only one eye at a time is exposed to the rotating stripes. The animal is placed inside a tube attached to the top of the apparatus this restricts the movement of the animal body and ensures only the head movement. To prevent the animal from escaping low shock plate is placed in front of the tube. A video camera is used to record the head movement. The tube can be rotated 190° to expose second eyes. The analysis and scoring are performed post recording.

7.3.8 Image processing for analysis of hCP distribution in RD-1 mice

The engraftment of hCPs was quantified by measuring the cell distribution pattern. After using Leica SP8 confocal microscope to image the test groups (10 fields of view per group), as explained earlier, colored images (VioBlue for DAPI, FITC for STEM121 and PE for cone arrestin) were analyzed. Segmenting and obtaining cells centroids and position was performed using the algorithm previously described (Appendix A.2). Then a density map was created by approximating each cells by a circle centered on its centroid with a radius equal to its long ellipse length. This density map enabled the measurement of the cell density anywhere on the whole mount (Appendix A.4). The distance recovery profile was then calculated by measuring the variable density away from each specific cells and was averaged for all cells. Nearest neighbor distance and index were calculated by searching for the closest cell away from each reference cell. This was performed for all cells of correct sizer throughout the entire whole mount and averaged. Finally, circles, centroids, density, NNI were plotted on the original confocal image to check for specific distribution.

7.4 Results

7.4.1 Novel microfluidic process of isolation of hCP

Sorting process, cell number and viability testing

The isolation of hCP includes an 8 steps process starting from the receipt of fetal tissue from ABR (Figure 7.2a). Isolated single cells are cultured in hypoxia conditions to obtain the appropriate number of cells for sorting (Figure 7.2b). Before seeding cells, viability is checked along with cell count that allows the estimation of the cell doubling time (Figure 7.2c). As explained in the previous methods, fetal cells are cultured and passaged upon reaching confluence and 10 million cells. Upon reaching this number cells are then sorted with the Miltenyi Tyto cell sorter using CD73 in both PE and APC fluorophores (Figure 7.2d), which is a novel antigen characterization photoreceptor precursor [223]. The sorted cell population (positive population) is analyzed with MACSQuant for purity and is then played in T25/T75 (depending on final cell number) to be cultured to reach again 10 million cells (Figure 7.2e). A second sort is performed (Figure 7.2f) by sorting the $CD73^{+}/Thrb^{+}/CD11b^{-}$ cell population. The thyroid hormone receptor beta (Thrb) is a necessary protein for the formation of cones and is only present in specific cones in the retina [224]. CD11b is an extracellular marker which binds to immune cells, specifically microglia in the fetal retina [225]. This final sort enables the isolation of pure cone progenitors (hCP). Finally (Figure 7.2g) hCPs are cultured upon reaching the desired number of cells for either animal experiments or creating a frozen cell bank (to be used for future experiments, Figure 7.2h).

The Miltenyi Tyto cell sorter is a novel microfluidic process to gently isolated specific cell population in a sterile environment. The stained cell population is loaded inside the Miltenyi cartridge in the input chamber (Figure 7.3A) which contains a mixing propeller. This cartridge is placed inside the cell sorter and upon reaching constant flow the sorting is started with a low pressure (150 mPa) which enable a high viability post-sorting. As seen in the bottom part of Figure 7.3A, cells are pushed from

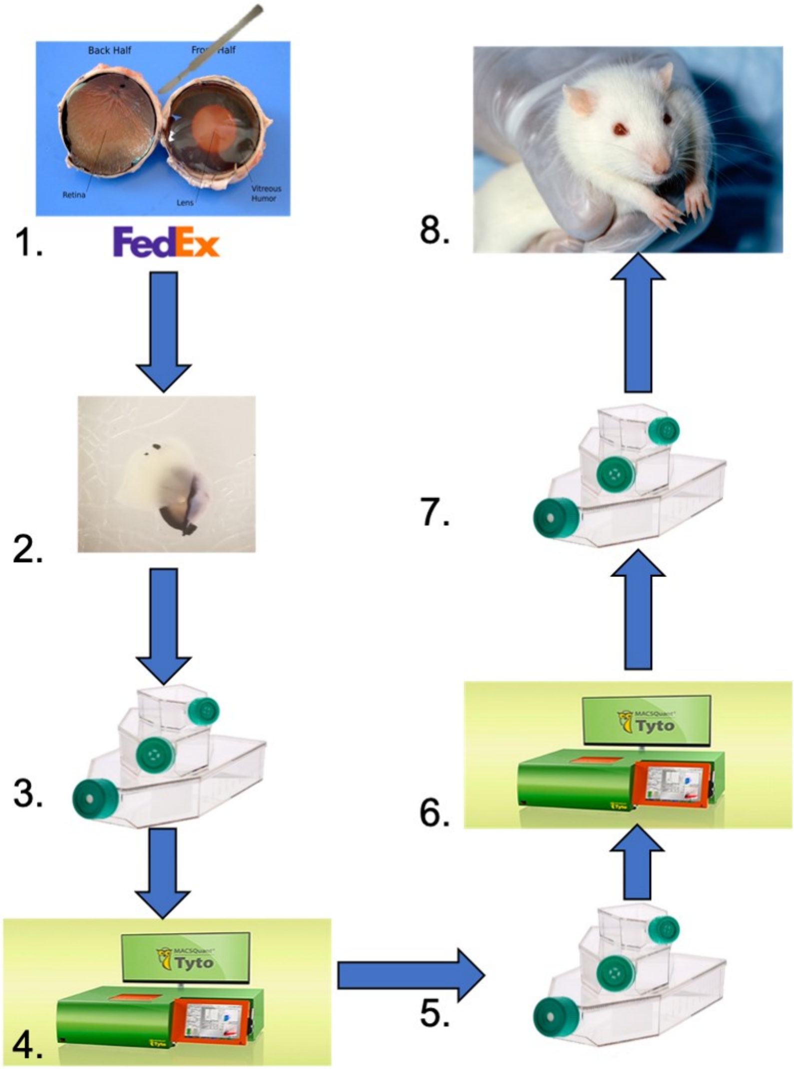

Figure 7.2: Complete isolation and banking process of hCP.
(a) Tissue is received via FedEx in 1-day delivery. **(b)** Retina is dissected out of the eyeball and dissociated with papain. **(c)** Dissociated cell suspension is cultured with defined media to obtain 10 million cells. **(d)** Cells are sorted with CD73-PE-APC. **(e)** Positive population is cultured again for 2-4 weeks. **(f)** Upon reaching 10 million cells, CD73$^+$ cells are sorted with CD73$^+$/Thrb$^+$/CD11b$^-$. **(g)** Cells are cultured for long time to create banks or be used for experiment **(h)**.

the input chamber and pass in front of 3 lasers (red, blue, and violet) which measure the fluorescence of the stained cells and their speed (measured between two lasers with positive fluorescence). Upon measuring a positive cell, the valve is electronically open, and this cell is pushed inside the positive collection chamber. The rest of the cells are pushed towards the negative collection chamber. This system allows for a precise sorting with the possibility to collect both the desired population (which usually contains a low cell number) and the negative fraction (which could be used for further analysis or another sorting).

Cell viability and attachment was observed 24h and 3 days post sorting for both 1st and 2nd sort, Figure 7.3B. T75 confluence was reached by day 7 with a viability greater than 90%. As soon as 24h post-sorting cells were found to be highly viable (seen in the live/dead assay performed) and to attach to the fibronectin coated plates. 3 days post-sorting, cells were found to be expanding, keeping a high viability. These results confirm the great capacity of the Tyto cell sorter which enable a gentle and sterile sort of specific cell subpopulations.

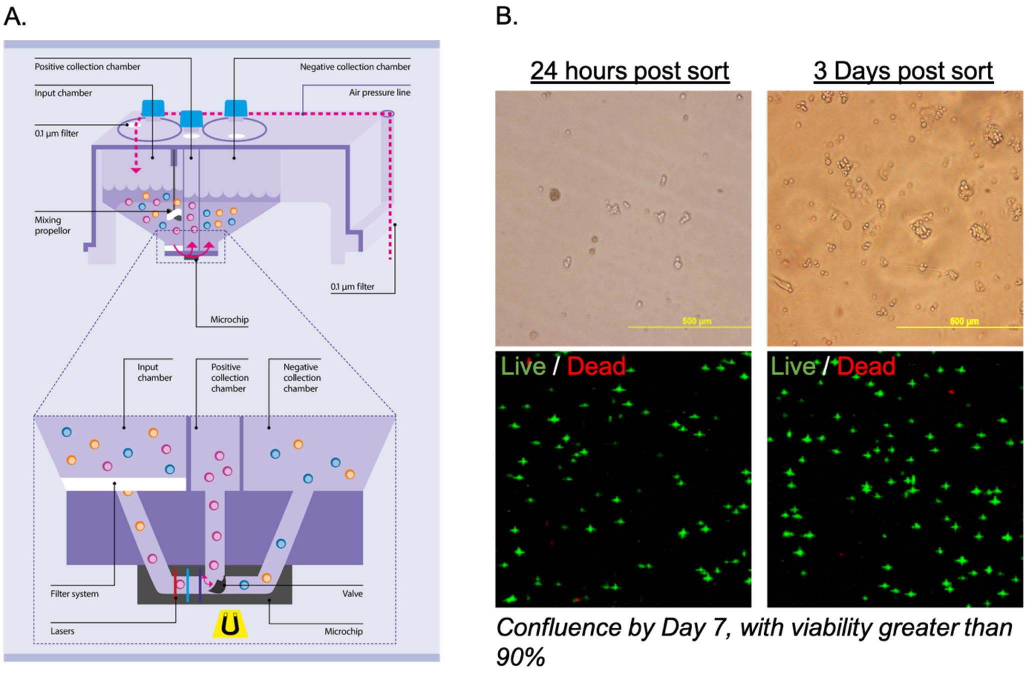

Confluence by Day 7, with viability greater than 90%

Figure 7.3: Sorting mechanics and viability testing with Miltenyi Tyto. **A.** Schematic of Miltenyi Tyto cartridge. Cell are placed in the input chamber which contains a mixing propeller and a filter. Cells go through the flow in front of 3 lasers (red, blue and violet) and are ejected with the valve opening in either the positive collection chamber (positive cells) or in the negative collection chamber. The entire process is closed and sterile. **B.** Viability and culture of hCP was tested 24h and 3 days post-sort with Live/Dead assay. Confluence was reached by day 7 and viability was greater than 90%.

Measurement of cell number is critical during the process of isolation of hCP from the fetal tissue until the final pure cone progenitor population. Figure 7.4, shows the evolution of the cell population during the sorting process for different tissue (ranging from 10 weeks to 16 weeks). As expected, a similar number of cells was obtained from the dissociated retinas independent of their age (around 1-2 million). Cell proliferation and expansion was similar for all tissues before the 1st sort and between both sorts. However, significant difference was observed in the expansion of the final hCP population depending on the tissue age. Earlier tissues were observed to be more proliferative, and their expansion was faster than older tissue: reaching more than 60 million cells after 60 days for a 10-week tissue compared to 45 million for a 16-week tissue and 40 million for a 14-week tissue). These results are coherent with the development of the fetal retina showing that earlier than 14 weeks cone progenitors are formed while rods and other types of retinal cells are forming in later stages [226]. We concluded, from this result, that using earlier tissues was beneficial to be able to reach high hCP number after 60 days, therefore only tissues 14 weeks and younger were used for all characterization and in vivo transplantations.

Staining and cell population gating

To obtain a significant purity in the hCP population, staining and gating the correct cell subpopulation is critical during the sorting process. As explained previously, cells are stained with either CD73-PE-APC (for the 1st sort) or CD73-PE, Thrb-APC and CD11b-VioBlue (for the 2nd sort). Post-staining cells are loaded inside the Tyto cartridge and sorting is performed by gating the correct population showing high positive cells in both PE and APC channel, while discarding the positive cells in the VioBlue channel. Figure 7.5 shows the gating strategy and cell population for both sorts for the input, negative and positive cell populations.

The 1st sort (shown in Figure 7.5A) targets cells stained with CD73-PE-APC. As seen in the 2 scatter plots on the left (for the input population), a distinct linear staining can be observed with a positive cell population located higher than 10^1 in both channels. The gating strategy (shown with the green gate) enables us to capture

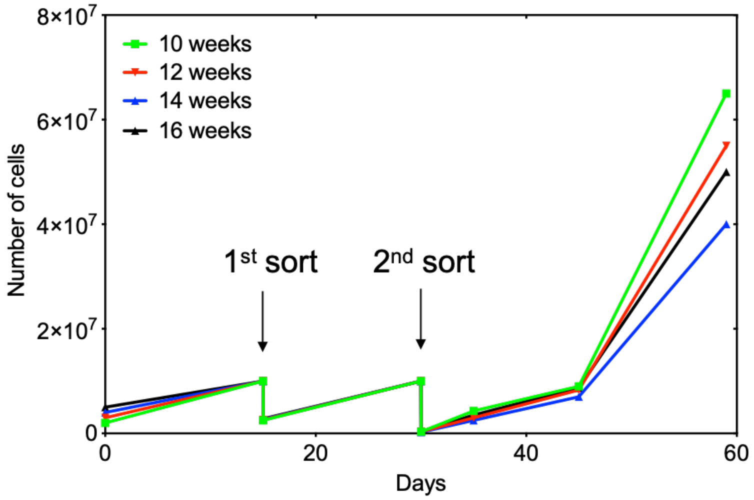

Figure 7.4: Evolution of hCP cell number during the isolation process. Starting cell number depends on the tissue age. Cells are culture for 2 weeks and upon reaching 10 million cells they are sorted, obtaining a positive population of <1M cells. These CD73$^+$ cells are cultured again for two weeks and during the 2nd sort only <400,000 cells are obtained and purified. Cells are then cultured for long-time, reaching 60 million cells depending on tissue age.

highly positive cell subpopulation, which corresponds to around 50% of the total events. Of note is that the total number of events includes both cells and debris as no DAPI or nuclei staining is performed during sorting. The negative fractions (middle column) show a lower number of positive cells (around 35%). Of note is that the yield of this sort is not optimal as many positive cells are still discarded in the negative fraction, as seen by the relatively high number of positive cells remaining. However, we have decided to focus on purity and not yield, as the final hCP population has shown to be able to expand to 60 million cells with just one tissue (as explained previously). Finally, the positive fraction (output column on the right) shows a significantly higher number of positive cells with a high purity in the cell population (around 95%). This result suggests that the 1st sort enable the isolation of a highly pure population of photoreceptor progenitor, due to their CD73 expression.

The 2nd sort (shown in Figure 7.5B) targets cells stained with CD73-PE (previous population from the 1st sort), Thrb-APC and deletes the positive CD11b cells. On the top row is shown the sorting strategy and final analysis of CD73-PE and Thrb-APC staining. As seen on the first column the starting population of CD73$^+$/Thrb$^+$ cells are lower than for the previous sort (around 20%) which is coherent with the fact that cone progenitors are a rare population in photoreceptor which mainly differentiate into rods. The negative fraction shows a significantly lower number of positive cells (around 8%) while the final positive fraction shows a high purity with more than 91% of cells expressing both a photoreceptor marker (CD73) and a cone progenitor marker (Thrb). The second row of scatter plots show the deletion of CD11b positive cells. To correctly remove the CD11b population inverse gating is performed. As seen in comparison to input, 99% of Cd11b cells were depleted during the 2nd sort. Overall, these figures suggest that this 2-step sorting strategy enables us to isolate pure cone progenitors expressing both CD73 and Thrb while removing a possible problematic population of microglia with the use of negative CD11b marker.

To understand and analyze properly the initial and final population of hCP, cells were examined with the MACSQuant flow cytometer for their relative expression of sort markers (CD73, Thrb and CD11b), as seen in Figure 7.6. The left panel (Figure 7.6A) shows the normalized count histogram for the expression of CD73-PE cells, during the 1st sort, for the input (blue), the negative fraction (red) and the output (green). As seen in this histogram, a high peak is shown around 10^1 for the input population which was the target population as seen in the output population. Of note is that the rest of the cells (with lower expression) are not seen in the output but can be measured in the negative fraction. The gating strategy is placed on top of this peak and shows a final purity of 79% for all n=40 sorts performed. The right panel (Figure 7.6B) shows the normalized count histogram for the expression of double CD73/Thrb cells, during the 2nd sort, for all three fractions. In this 2nd sort a different trend is observed with a high peak around 10^0 for the input suggesting that most cells do not express Thrb. Of note is that a small number of cells, which expresses both CD73/Thrb can be seen in the input fraction with a small peak around 10^1: this corresponds to the targeted hCP cells. After sorting, the output fraction shows a significant peak at 10^1 while most of the negative cells remain only in the negative fraction.

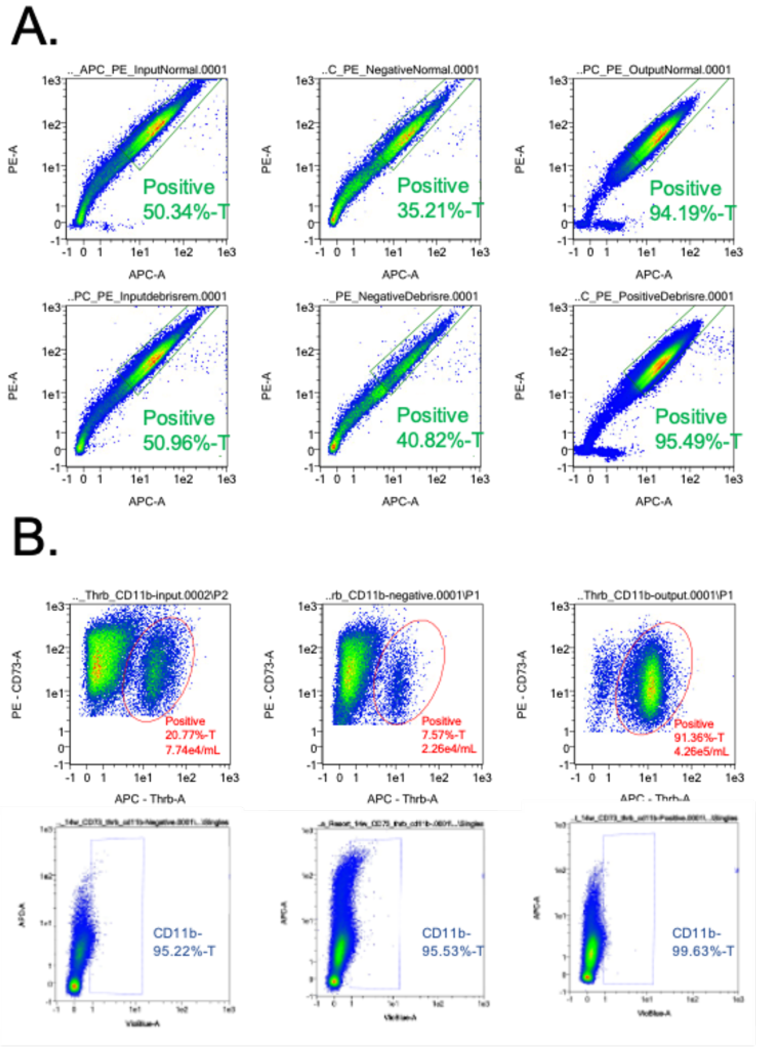

Figure 7.5: Sorting strategy to isolate pure hCP.
A. 1st sort strategy with hCP stained for CD73-PE-APC. Gate is placed on the high positive population for both fluorophores. Initial population is 50% and increases to 94% post-sorting. **B.** 2nd sort strategy with hCP stained for CD73-PE, Thrb-APC and CD11b-VioBlue. Initial population of $CD73^{+}/Thrb^{+}/CD11b^{-}$ is 20% and increases to 91% post-sorting.

These results confirm that we were able to isolate pure cone progenitors expressing both CD73 and Thrb while removing the CD11b positive cells from the final product. Of note is that the 1st sort is a broad sort that capture most of the $CD73^{+}$ positive cells with high cell number both seen in both the input and output; while the 2nd sort is a really precise sort with a smaller gate to capture the unique specific population expressing both CD73 and Thrb. After sorting and culturing hCP for 60 days (as explained before) we were able to characterize them, with different techniques to prove their identity and find their precise phenotype.

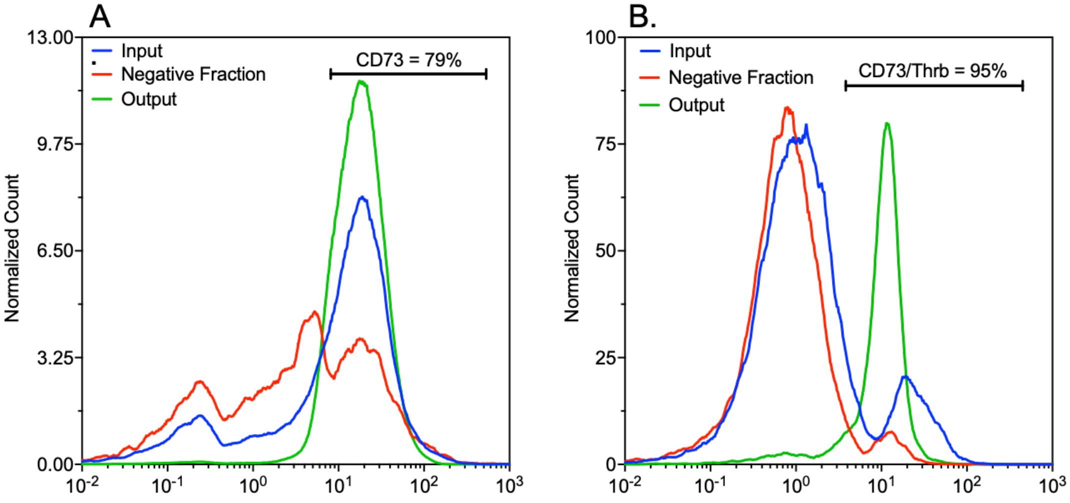

Figure 7.6: Histogram of phenotype assay during the sorting process. **A.** 1st sort phenotypic assay of different cell population (input in blue, output in green and negative in red). **B.** 2nd sort phenotypic assay of the three cell populations.

7.4.2 Characterization of final hCP population

Phenotype assay

To ensure the purity and phenotype of the final hCP population we performed multiple immunostainings and analyzed them with either flow cytometry or confluence microscopy imaging (fluorescence microscopy). These testing enabled us to precisely characterize the phenotype expressed by hCP both qualitatively and quantitatively.

We performed flow cytometry analysis over n=15 samples of hCP with different fetal tissue provenance. As seen in Figure 7.7, specific cone markers (Cone arresting, blue opsin, R/G opsin, S-opsin), photoreceptor marker (recoverin), rod marker (rhodopsin), horizontal cell marker (calbindin), retinal ganglion cell markers (Brn3a, RBPMS), bipolar cell marker (PKCa) and proliferation marker (Ki67) were analyzed. Results are shown as a normalized histogram of the cell fluorescence after staining (Figure 7.7A-C) and all results are summarized as percentage of expression in the total hCP population (Figure 7.7D). For each experiment blank sample is shown in grey and isotype control (which is placed at 2% expression) in black. Purity is shown in Figure 7.7A with cone Arrestin, blue opsin and recoverin. These three markers show a significant expression with peaks above the isotype control (higher than 10^1). This result is confirmed in the summary bar graph with more than 95% expression of cone arrestin (red), blue opsin (blue) and R/G opsin (grey). Recoverin (which also stains for rods and is present in more mature cones) was found to be on average around 70% expressed by hCP. S-opsin was found to be variable in different samples (usually dependent on the fetal tissue age) and was expressed at less than 15% in younger tissues. Of note is that a double peak can be observed for both cone arrestin and blue opsin which suggest the presence of two different population expressing higher quantity of these markers. Impurities is shown in Figure 7.7B with calbindin, Brn3a, PKCa, RBPMS and rhodopsin. The rod population was found to be near zero for all samples with rhodopsin being similar to isotype control. Retinal ganglion cells (stained with RBPMS and Brn3a) were not found in our samples with makers similar to isotype control. Calbindin, which stains for both horizontal cells and early cones progenitors, was found to be expressed around 25% which is due to some of the cones being at the early lineage or the presence of immature cones. Finally, bipolar cell marker (PKCa) was found to be expressed around 18% in all different samples. This finding suggests that the only impurity found in hCP is potentially the presence of a low population of bipolar cells. Of note is that, in the retina, cone forms their synaptic connection directly with bipolar cells [226]. Therefore, this small impurity fraction could help and enable higher engraftment and hCP in vivo by helping them forming the synaptic connection with the neural retina. Finally, proliferation was analyzed with Ki67 which shows an expression of about 25-30% (depending on tissue age) which shows the potential of hCP expansion and culture to reach higher cell number and create a cell bank for future use.

To further understand and analyze the final hCP population and the different part of the sorting process we stained for specific markers at different steps of the sorting process: fetal retina cells, 1st sorted cells, 2nd sorted cells (or hCP). We

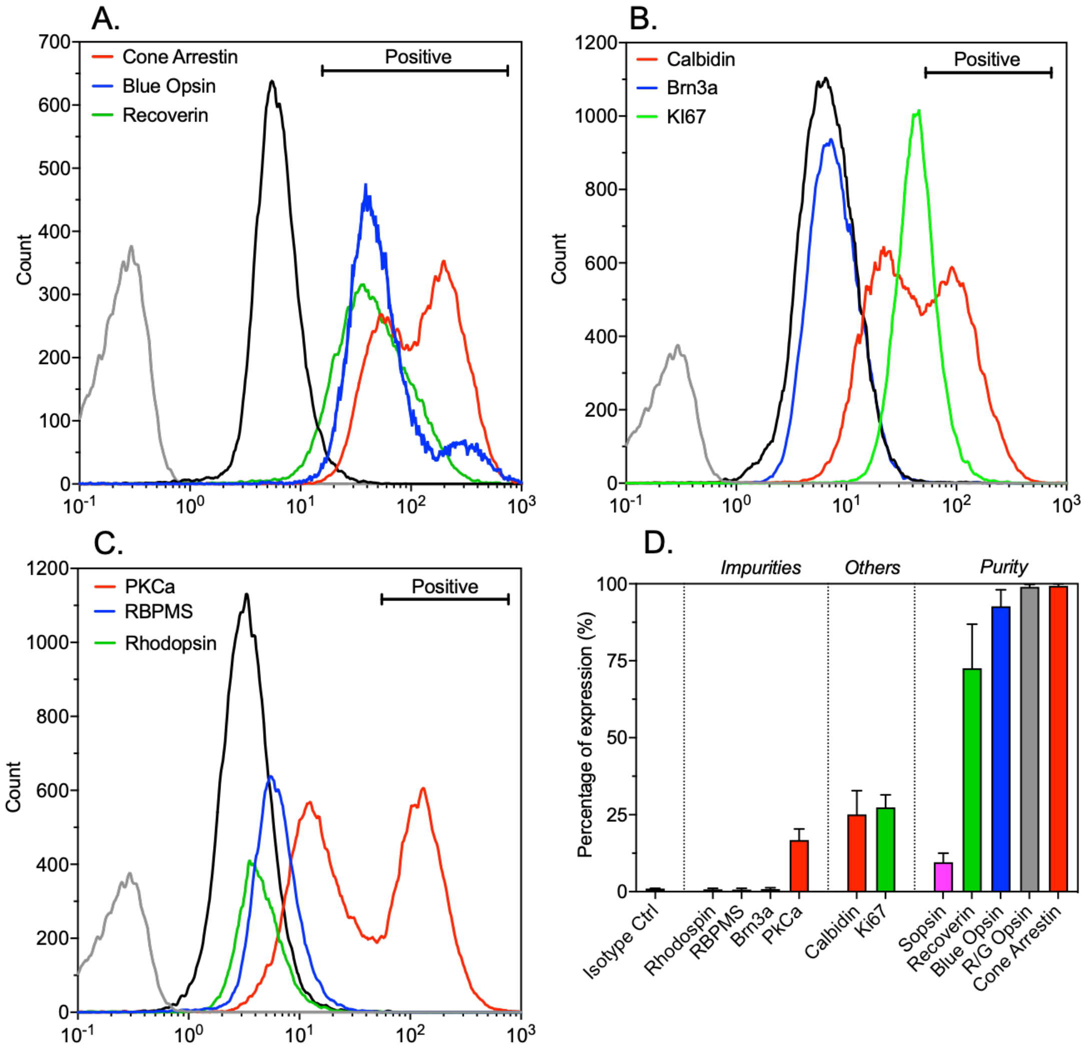

Figure 7.7: Phenotype analysis of hCPs using flow cytometry.
A-C. Histogram of cell expression for different retinal markers. **D.** Average of flow cytometry for different runs on hCPs.

analyzed our main cone marker (cone Arrestin) but also calbindin (present in early cone progenitor) and SHANK1; DAPI staining was added to be able to locate cells and differentiate them from debris. SHANK1 is a protein that is found in the pre- and post-synaptic terminal of cone photoreceptors. It is known to be involved in the scaffolding of cones in the architecture of the retina [227]. As seen in Figure 7.8 and 7.9 an increasing number of cells express cone Arrestin and SHANK1 during the isolation process: low amount is found in fetal retina cells, while high expression is observed for CD73^{+} cells; finally, almost all cells express cone Arrestin and SHANK1 in the hCP population. Calbindin (Figure 7.10) is found to be conservatively constant throughout the sorting process which is due to its function of staining both early cone progenitors and horizontal cells. These results confirm the fact that we were able to isolate cone progenitors which express specific cone markers which are present in the adult retina.

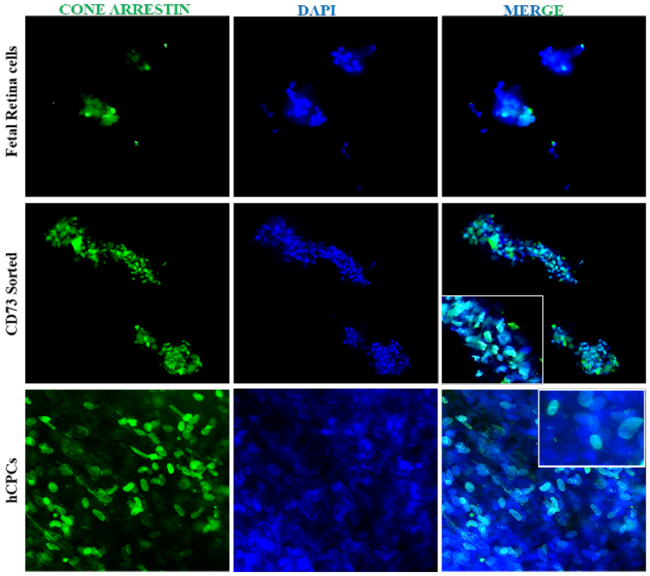

Figure 7.8: Immunohistochemistry fluorescence of cone arrestin expression in cells.
Cone arrestin expression is shown for the starting population (fetal retina cells), after 1st sort (CD73 sorted) and the final hCP population (hCPCs).

Finally, we also analyzed, with immunostaining, similar markers which were measured with flow cytometry: recoverin, R/G opsin, rhodopsin and Ki67. As seen in Figure 7.11, a similar trend as found with flow cytometry can be seen for cone specific markers with recoverin and R/G opsin being expressed by almost all cells. Rhodopsin was not found in any cells, with only specs from the antibody shown which don't align properly with DAPI and cell nuclei. Ki67 was found to be relatively present in some cells.

All these results enable a more comprehensive understanding of hCP phenotype but also of the different subpopulations present during the sorting process and in the final hCP population. We were able to prove that by using a 2-steps sorting process

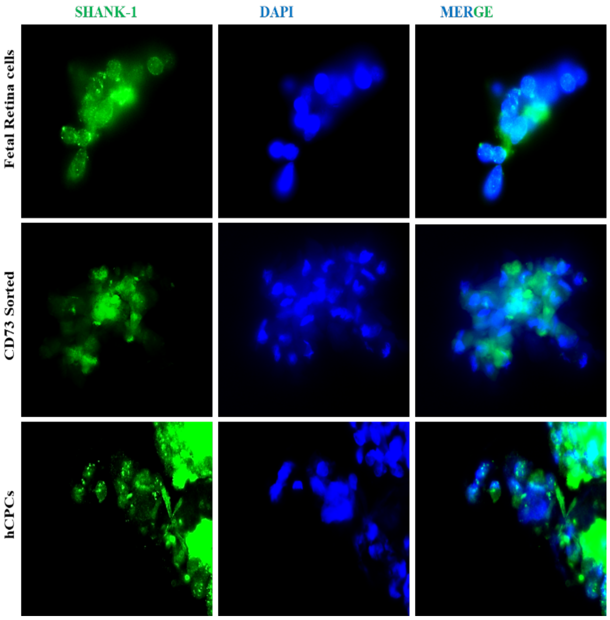

Figure 7.9: Immunohistochemistry fluorescence of SHANK-1 expression in cells.
SHANK-1 expression is shown for the starting population (fetal retina cells), after 1^{st} sort (CD73 sorted) and the final hCP population (hCPCs).

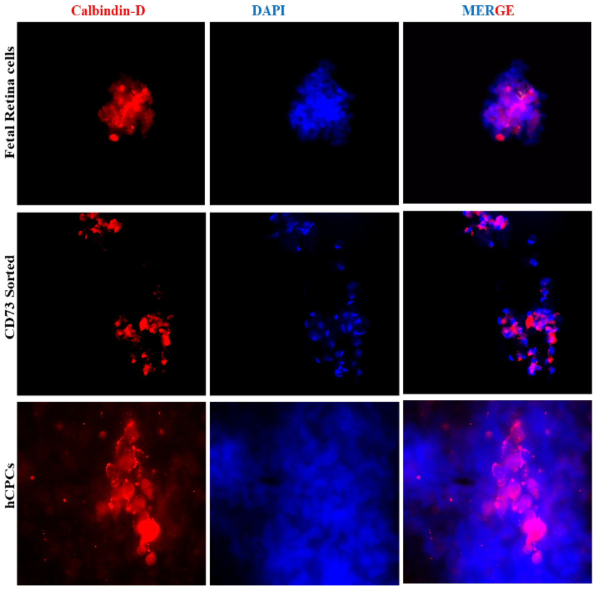

Figure 7.10: Immunohistochemistry fluorescence of calbindin expression in cells.
Calbindin expression is shown for the starting population (fetal retina cells), after 1^{st} sort (CD73 sorted) and the final hCP population (hCPCs).

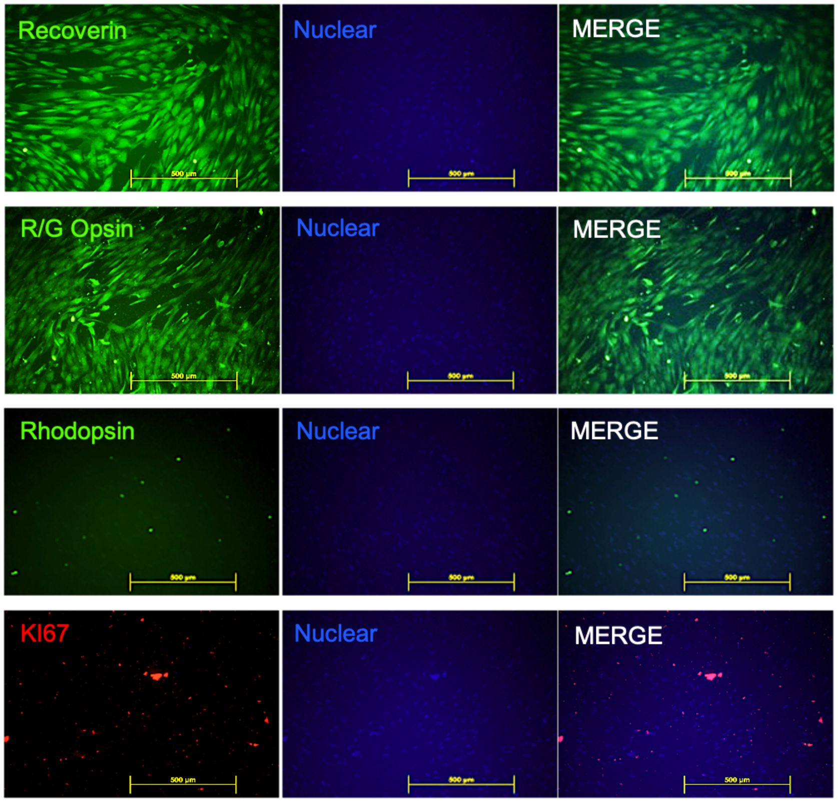

Figure 7.11: Immunohistochemistry fluorescence of other markers expression in hCP.
Photoreceptor marker (recoverin), cone marker (R/G-opsin), rod marker (rhodopsin) and proliferation marker (Ki67) are shown for the final hCP population.

with Miltenyi Tyto we can isolate pure human cone progenitor which express only the most common cone markers, have a potential for expansion and possess a relatively small impurity which is comprised of bipolar cells.

Electrophysiological testing

To finalize the characterization of hCP and prove that we were able to isolate and expand pure and functional cone progenitor cells we performed a microelectrode array (MEA) assay to prove that our hCPs were electrophysiological active. This MEA assay was performed with two different arrays (MaxWell MaxOne and Axion Biosystems) to capture different output: the MaxWell array (Figure 7.12A) enables to measure the mean spike amplitude of a region of plated hCP while the Axion array

(Figure 7.12B) can measure the spike intensity and spike rate at a specific location, showing the actual trace of the membrane potential. Therefore, we measured the base activity of our plated hCP (into a coated 24-well plate) by recording the output in both arrays with no light input, as seen in the first row of Figure 7.12A. Both arrays show little to no baseline activity in hCP when no light input is added. This result confirms that hCP are not self-firing neurons or other types of neural cells which can exert an action potential without light input. During both experiments we added a light input by shining different wavelength at different frequency onto hCP sample. The MaxWell array shows a high mean spike amplitude and an increase mean firing rate for each region of interest after light stimulation. After applying white light (using a combination of blue, red and green wavelength at the frequency of 10ms per second) the Axion array showed a membrane potential activity in hCP which is shown by the presence of spikes at different electrodes. Those spikes are then analyzed, and the spike intensity is recorded (right panel in Figure 7.12B) which shows a typical membrane potential activation with a low voltage discharge which is quickly neutralized [228].

This critical result indicates that the pure cone progenitor population which make hCP is also electrophysiologically active by having a membrane potential activity due to light input. This is an important result as it suggests that hCP could potentially replace dead photoreceptor in the degenerating retina and serves as new active photoreceptors which can respond to light. Overall, this complete characterization indicates that hCP are pure cone progenitor cells, expressing common cone markers which respond to light. To analyze their regeneration possibilities, we injected hCP into the subretinal space of different species and measured different outcomes.

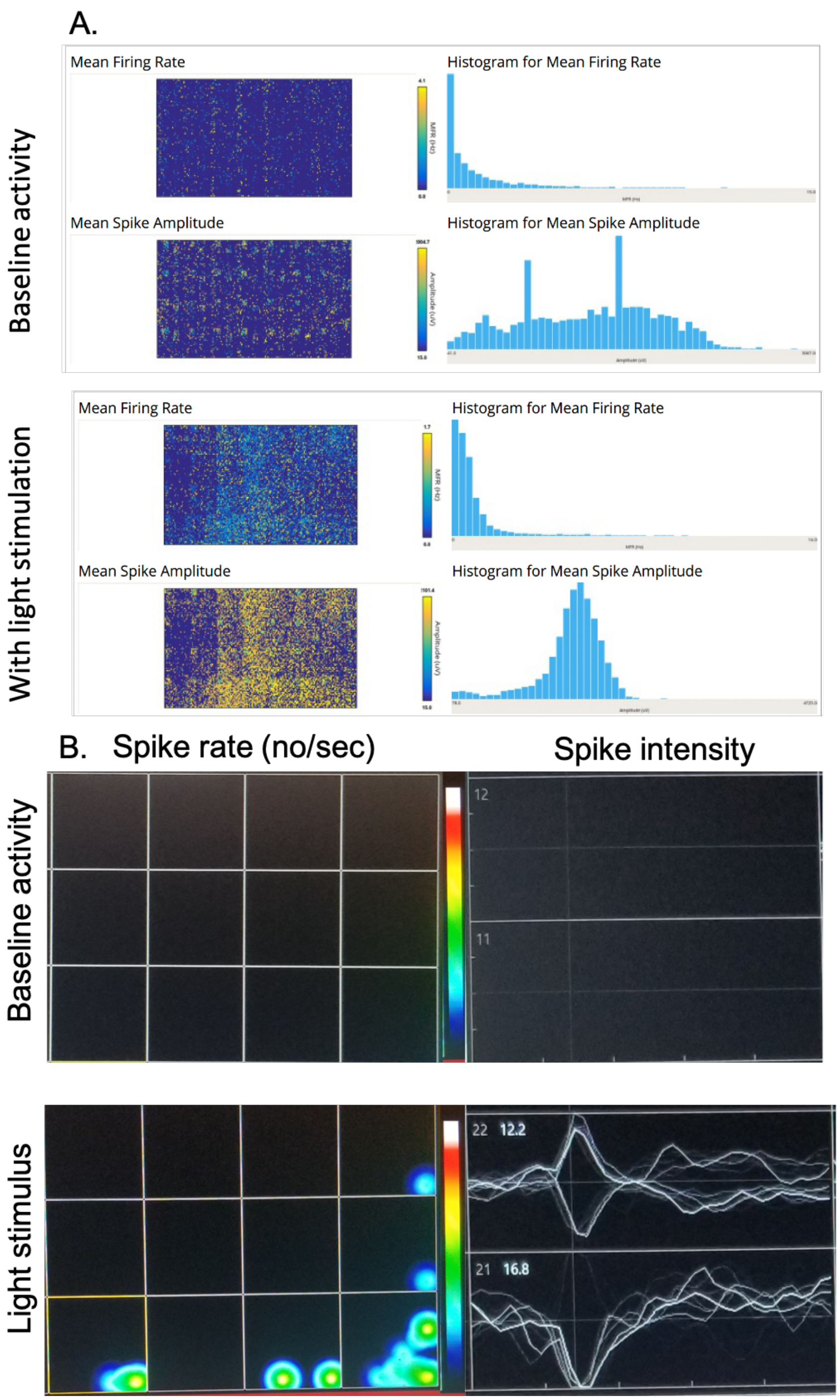

Figure 7.12: In vitro functionality testing of hCP with MEA.
A. MEA recording using the MaxWell MaxOne array. **B.** MEA recording using the Axion array with light input from the Lumos component. **First row** shows the baseline activity of cells without input while the **second row** shows their response to a light stimulus.

7.4.3 In vivo transplantation of hCP in animals

To analyze the possible engraftment and regeneration capabilities of hCP we injected them unto the subretinal space of 3 species, each one with a specific rationale and final goal, as seen in Table 7.4.

Table 7.4: Animal models used for hCP subretinal injections with rationale and goal.

Animal model	**Cell presence**	**% Cell attached**	Rationale	Findings
Long Evans	n=16/18	85%	- Experimental retinal detachment (RD) model in rodents [229] - Human features of RD	High engraftment
RCS rats	n=10/10	87%	- Model of autosomal recessive retinitis pigmentosa (RP) [221] - Critical POC for neuroprotection	Neuroprotection and increased visual acuity
RD-1 mice	n=5/7	87%	- Identified with retinal degeneration [222] - Critical POC for cell replacement	Mozaic pattern

Long Evans rats

The goal of hCP injection into the subretinal space of Long Evans -a wild type rat- was to prove the ability of exogeneous hCP to engraft during a xenotransplantation. As previously mentioned, Long Evans don't possess any innate degeneration however, by performing a subretinal injection and creating a bled in the central retina (as explained in the introduction chapter) it enables to perform an in vivo study on an experimental retinal detachment model. This short-term model (tested for 2 weeks) also provides pathologic features of human retinal detachment (RD) which happens in a lot of different retinal diseases. Therefore, we injected n=18 Long Evans rats with 50,000-100,000 hCP in their subretinal space and analyzed sections of their retina with immunofluorescence and histology 2 weeks post-transplantation. To prove the presence and short-term engraftment of hCP with stained retinas section with a human marker (either TRA-1-85 or STEM121) which only stains human cells with no cross-reactivity with the host rat cells; and a cone marker (Cone Arrestin) which can either stain most of our cones (due to their purity) and some host cones.

The first round of sections is shown in Figure 7.13 with TRA-1-85 (FITC; green), Cone Arrestin (APC; red) and DAPI (VioBlue; blue). As seen on the first row of images, most cells (here presented with green staining are in the outer nuclear layer of the retina (ONL) which hosts all the photoreceptors. The cone arrestin staining shows a high expression for the injected hCP along with some host cells. The second row shows a zoomed in image centered on the ONL (of note is that the blue channel DAPI was deleted on this picture to make it easier to see the engrafted cells). The most important feature of these confocal fluorescence microscopy is the presence of a large number of hCP engrafted in the ONL 2 weeks post-transplantation which express both a human and cone marker. In this case it is essential to observe the yellow color of all hCP integrated which represent their expression for both markers, enabling us to differentiate them from the host cones or other retinal cells.

We have also performed is second round of sections, which is shown in Figure 7.14, by staining with STEM121 (FITC; green), cone Arrestin (APC; red) and DAPI (VioBlue; blue). The first two rows show the presence of hCP integrated in the retina and expressing both human and cone marker (having a yellow color in the merge image). Of note is that this section shows the subretinal space injection with the presence of the bleb on the left side of the section (first row). The last row represents a zoomed in image of a cluster of hCP engrafted in the ONL layer of Long Evans rats. This shows the perfect co-localization of both human and cone markers.

These results suggest that injected hCP in the subretinal space of Long Evans rats engraft in the ONL layer in a large number even only 2-weeks post-transplantation. However, to further prove the efficacy of hCP we have injected them into specific strain of rats and mice possessing an innate retinal degeneration (RCS and RD1).

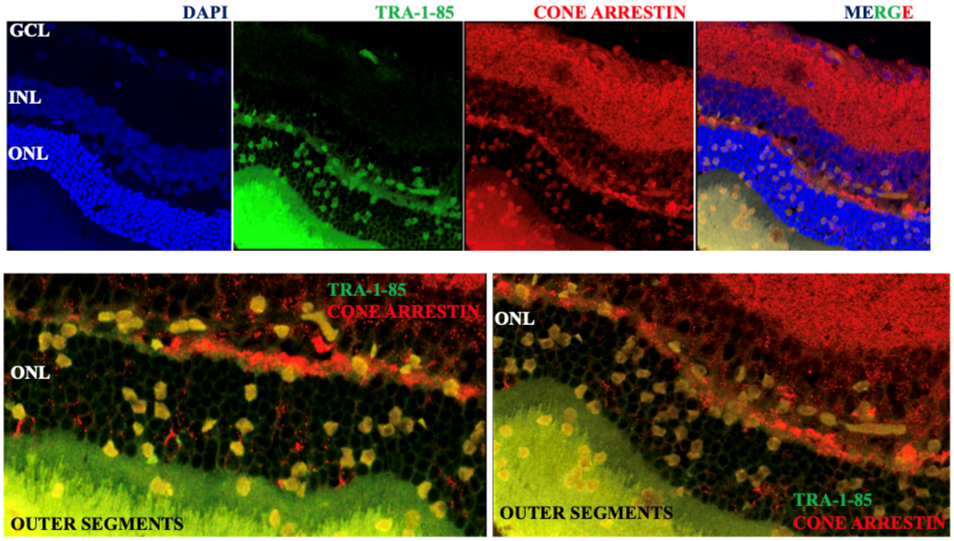

Figure 7.13: Immuno-staining 2 weeks post implant in Long Evans rats showing co-localization.
Staining is performed with TRA-1-85 (PE for human marker), Cone Arrestin (APC for cone) and DAPI (VioBlue for nuclei and structure staining). It shows high engraftment of human-cone arrestin positive cells in ONL.

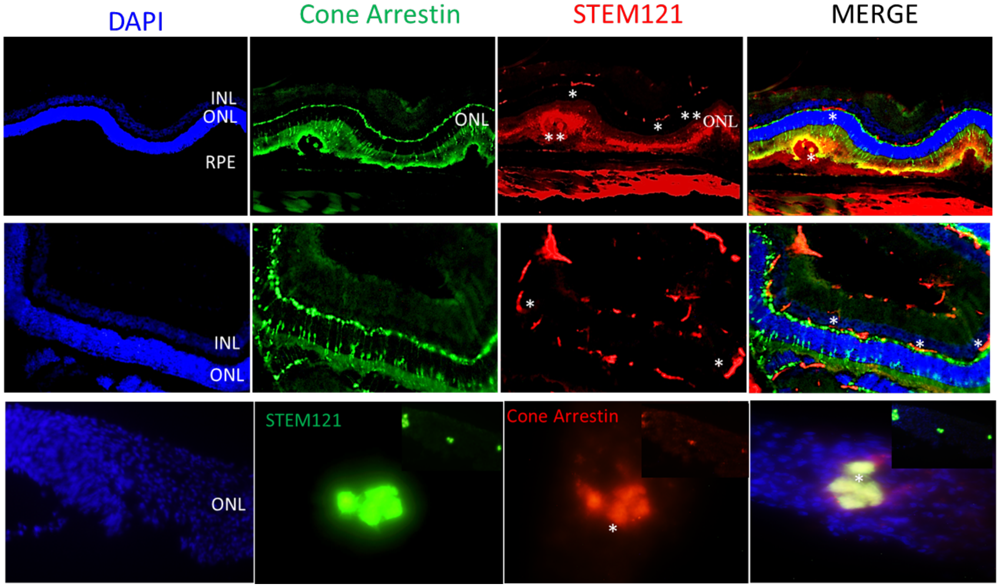

Figure 7.14: Immuno-staining with STEM121 showing co-localization.
Staining is performed with STEM121 (APC for human marker), Cone Arrestin (PE for cone) and DAPI (VioBlue for nuclei and structure staining). It shows colocalization of human and cone marker in transplanted cells.

RCS rats

Pilot efficacy studies were performed in the Royal College of Surgeon (RCS) rat model, a naturally occurring model of retinal degeneration. In these animals, there is a primary defect in RPE cells that leads to photoreceptor death. This parallels the early RPE dysfunction that is thought to occur in human dry AMD. Thus, this dysfunction mimics the photoreceptor degeneration found in atrophic AMD which is characterized by extensive loss of retinal pigment epithelium (RPE), followed by loss of photoreceptors (PRs) as is seen in the intended target cone-rod dystrophy patient population for hCP. This model has been used extensively in similar preclinical studies [230]. For this study, animals are implanted at post-natal days 21-25 (P21-25). At this time, approximately 20% of the photoreceptors have been destroyed.

This study had 4 groups: 1) high dose (100k cells), 2) low dose (50k cells), 3) vehicle (2uL of PBS), 4) control (no injection). Animals (age P21) were assessed 60 to 90 days post transplantation. hCPCs were manufactured and cell viability was measured before the initiation of injections and after completion of all procedures. The viability was 90% for all samples at the start of the injections and 81% after 4 hours on ice. The first assessment in this type of procedure is to determine the success of the subretinal injections. A shining bleb is indicative of successful placements of the injections.

In all animals tested (including control, sham, and low/high dose), hematoxylin and eosin staining (H&E) was performed on histological sections of the retina to analyze the anatomy of the rat's retina 60-90 days post-surgery. The specific region of high immune response or inflammatory regions were analyzed. The RCS rat model is a retinal degenerative model with an extreme hostile environment for cell transplantation, where ongoing inflammation often leads to poor graft survival. In this experiment, to rule out the effect of surgery on the photoreceptors we transplanted vehicle or sham injection and made direct comparison with groups that received hCP. In this model, as disease progresses the outer nuclear layer starts to degenerate quickly and by end of 3 months only 2 to 4 layers of ONL remain of the normal 10-12 in most of the animals, hence any rescue effect can be clearly monitored by counting the number of remaining ONL in the animal. H&E staining of all groups, with the ONL layer being the darkest layer can be seen in Figure 7.15.

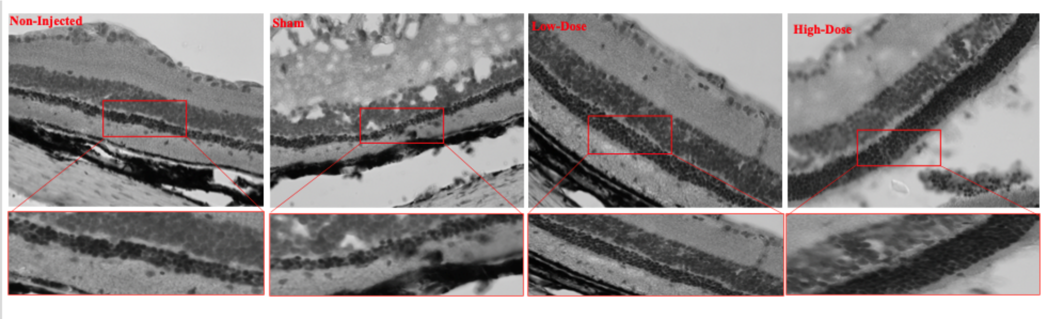

Figure 7.15: H&E staining of RCS rats-stained slides at 60 days post-injection.
Histology staining shows difference in terms of number of nuclei in the ONL layer for different groups (control, SHAM, low and high dose). Measurements were performed on n=20 field of views taken randomly in each animal.

Neuroprotection was assessed and the number of nuclei for each group was measured in histological sections with n=21 fields of view for each animal. The following results (Figure 7.16) suggest that a high dose injection of hCP enable significantly higher neuroprotection of the degenerating retina (an average of 8 nuclei compared to 2.5 and 3 respectively for control and sham). This trend is similar for injections analyzed at 60- and 72-days post-injection. Furthermore, higher neuroprotection was observed with high dose animals compared to low dose animals. Figure 7.16A shows the number of nuclei counted in a 100 μm^2 surface of the retina while Figure 7.16B shows the average thickness of ONL (measuring the number of nuclei).

Finally, neuroprotection analysis was performed by measuring and counting (blinded analysis) the number of nuclei in the ONL layer relative to distance from the injection site (Figure 7.17). To prove neuroprotection, a high number is found near the injection site while decreasing when reaching the edge of the retina. The following graphs shows a highly significant neuroprotection which is evenly distributed throughout 1400 µm of the retina for the high dose samples. Low dose is not represented here as it shows similar results.

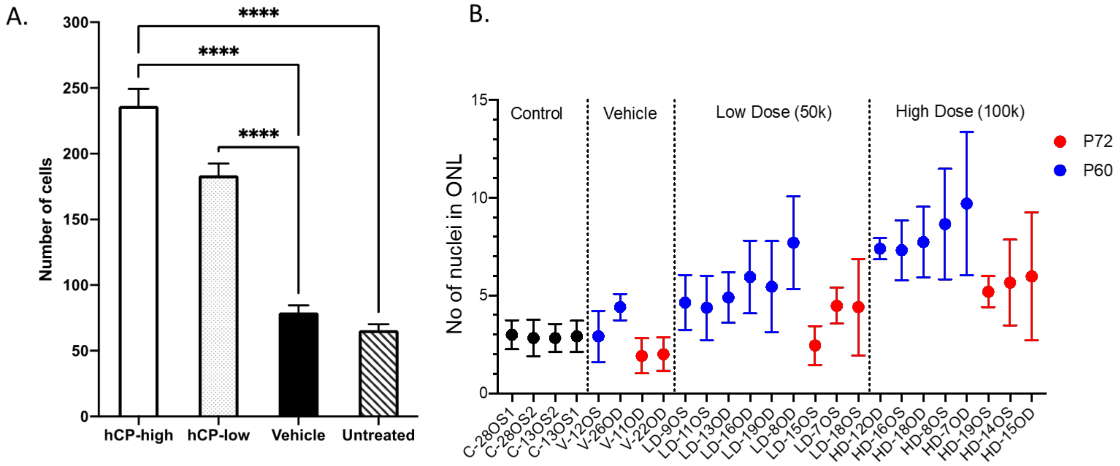

Figure 7.16: Photoreceptor rescue in each RCS rats.
A. Number of nuclei in ONL layer of each injected rats was counted for control, vehicle and low and high dose in a 100 μm^2 surface of the retina. **B.** Each rat ID is represented with its ONL count, showing higher neuroprotection from 72 days post-injection compared to 60 days for both low and high doses.

RCS rats receiving hCP injection shows better preserved grafted area and high number of ONL in comparison to the sham and control. When compared with sham the hCP injected animal showed an orderly array of ONL and INL lamination. There were 3 to 5 extra layers of ONL found in high dose animals and 2 to 5 in the low dose animals indicating the rescued effect of hCPCs even at 60-days post-injection. These result suggest a strong neuroprotection effect offered by the injection and possible engraftment of hCP even 60- to 90-days post-transplantation.

We also analyzed the integration and engraftment of hCP in retina sections with immunofluorescence (staining for STEM121-FITC as a human marker, cone arrestin-APC as cone marker and DAPI-VioBlue for retinal structure). Figure 7.18 shows the presence of many engrafted cells in the ONL layer of RCS rats. For the High dose group, all 8 injections were successful with the presence of a shining bleb and an injection in the subretinal space. Cells were found in all samples and showed high amount of engraftment, and neuroprotection (87%). For the Low dose group, all 9 injections were successful with the presence of a shining bleb and an injection in the subretinal space. Cells were found in all injected samples, but most showed less

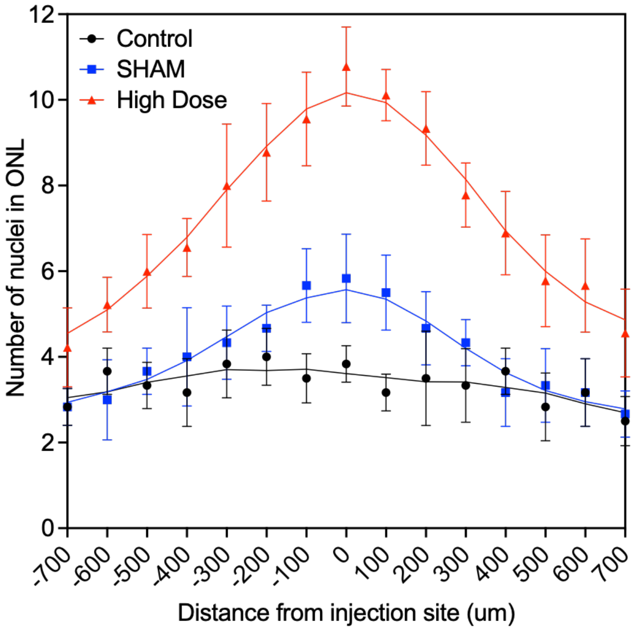

Figure 7.17: Distance from injection site photoreceptor rescue in RCS rats.
Number of nuclei in ONL layer was counted each 100-µm started at the injection site for control, vehicle and high dose. High neuroprotection was found in high dose showing high statistical difference in number of nuclei at near the injection site until 700 µm away from it.

engraftment (55%).

This experiment and its result suggest the ability of hCP to not only engraft in a hostile animal model but also preserve the retina from degenerating acting as a neuroprotectant. To confirm and further analyze these possible regenerating abilities, we also performed visual acuity testing (with OKN measurement) and functionality testing (with ERG measurement) of RCS rats. As explained in the method section OKN measurement enables for an accurate quantification of rats' visual acuity. As seen in Figure 7.19A, OKN measurements were performed on live animals at 60- and 90-days post-transplantation. For both time points a significant increase in visual acuity was observe for rats which received hCP at low or high dose. Of note is that a higher visual acuity was observed for the high dose group. We also performed OCT imaging of rats' retina, seen in Figure 7.19B, to analyze the anatomy of RCS rat's retina pre- and post-transplantation. The result suggest that no trauma or retinal

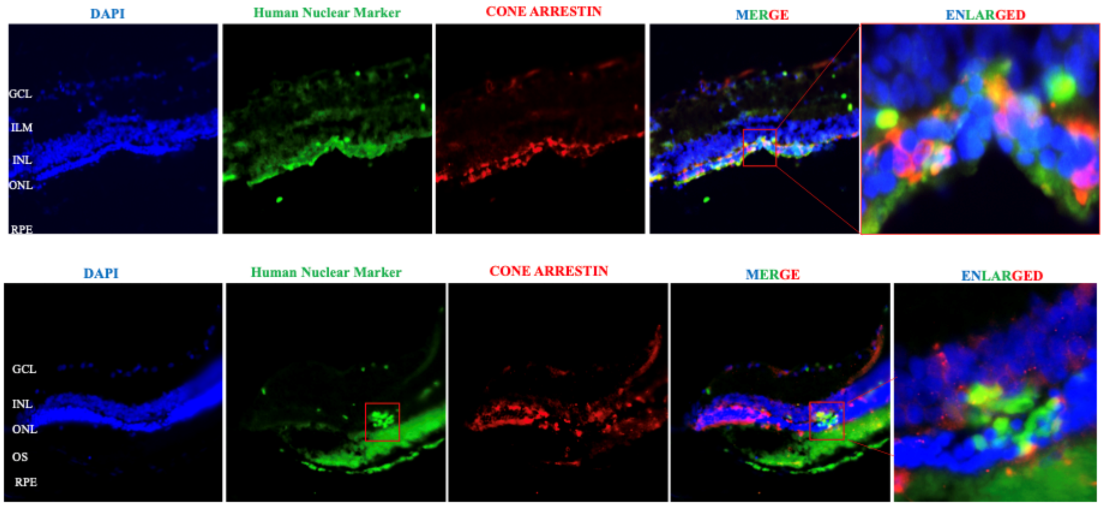

Figure 7.18: Immuno-staining of 60 days post-injection RCS retina injected with hCP.
Staining was performed with STEM121-PE as human marker, Cone Arrestin-APC for cone marker and DAPI-VioBlue for nuclei and structure marker. Double stained cells were observed in the ONL layer of the retina, engrafted and expressing both human and cone markers.

detachment was found due to the injection of hCP.

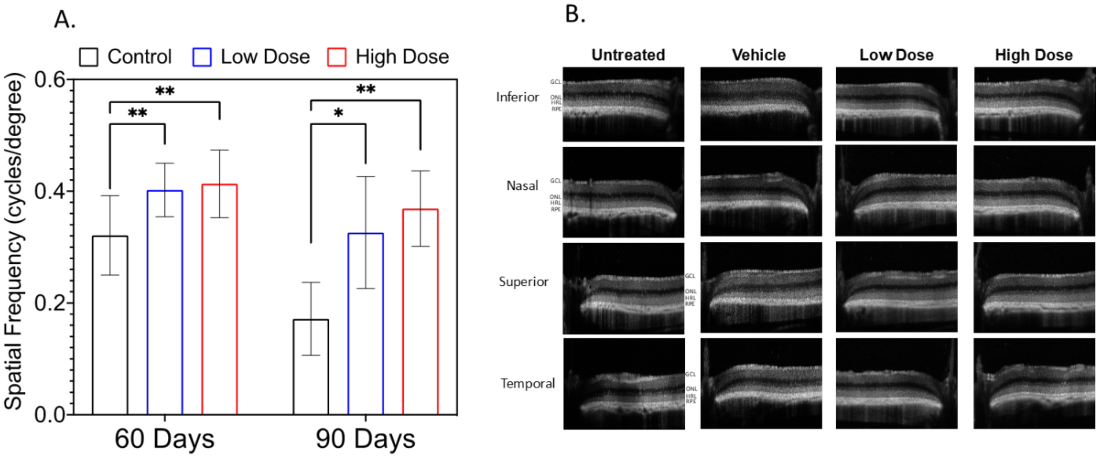

Figure 7.19: Visual acuity and retinal imaging of RCS rats receiving hCPs.
A. OKN measurement shows the improved visual acuity (spatial frequency) for rats which received low or high dose of hCPs. **B.** SC-OCT imaging of rats' retina show no trauma or retinal detachment post-transplantation in the inferior, nasal, superior, and temporal part of the retina.

Finally, functionality of RCS rats' retina was measured quantitatively with ERG measurement for both A-wave (Figure 7.20A) and B-wave (Figure 7.20B). These measurements are performed at different intensities to show the functionality of the retina in response to light. As observed in Figure 7.20, for low intensity of light all different groups and a negligible to zero response which is coherent with the absence of stimulus. However, as the intensity ramped up rats which received hCP in both low and high dose had a higher average response amplitude compared to control RCS rats.

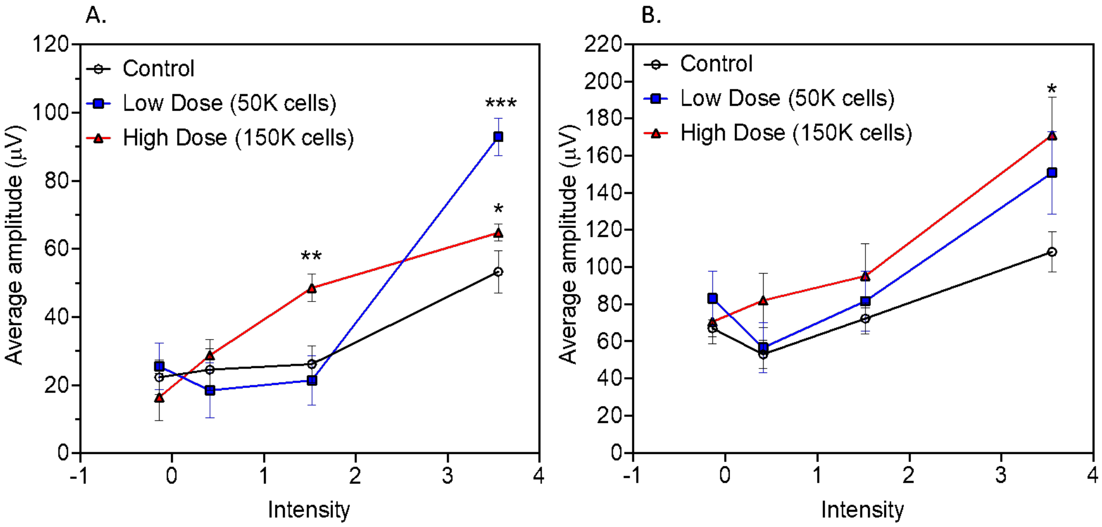

Figure 7.20: Retina functionality testing with ERG.
A. A-wave measurement with ERG of control, low dose and high dose RCS rats. **B.** B-wave measurement with ERG of control, low dose and high dose RCS rats. An improvement on retinal functionality was observed for rats which received hCPs.

These critical results demonstrate the ability of hCP to function in-vivo, that in turn results in a significant increase in retinas functionality and rat's visual acuity for both low and high doses.

RD1 mice

We have chosen RD1 mice as a model to test cell replacement as all rod and cone photoreceptors are lost rapidly, with rod death occurring first at 3 weeks of age. C3H-RD1 mice, male/female have been used with n=8 mice. This study consisted in a proof of concept by injecting 50k or 100k cells/eye in immunosuppressed RD1 mice (using cyclosporin treatment in water) at P27. One-week post-transplantation, animals were sacrificed, and retinas were sectioned and stained with human and cone marker to show the presence of cones and their engraftment pattern. As explained in previous studies, at P35 more than 90% of cones are dead in RD1, therefore the presence of any cones remaining can only be due to the engraftment of hCP or to their neuroprotective aspect as seen with RCS rats.

First, retinal section of injected RD1 were analyzed and stained with TRA-1-85-FITC, Cone Arrestin-APC, and DAPI-VioBlue to prove the presence and location of injected hCP. As seen in Figure 7.21 (rows 1 and 2), cells were found to be attached and integrated in the ONL layer (which in the case of the degenerating RD1 is comprised of only one layer of nuclei) of RD1 mice. The last row shows a control retina with no expression of TRA-1-85 (marker only for human cells) and a small amount of photoreceptor remaining (Cone Arrestin staining). This first result suggest that we were able to successfully inject hCP in the subretinal space of RD1 which then engrafted in the ONL layer.

To change the orientation of our observation and to be able to observe bigger surface area we also perform immunofluorescence staining and microscopy on whole mounted retina (see methods) which enable the visualization of a large surface of the retina. As see in Figure 7.22, we imaged both the injected (first row) and control group (second row) after staining the retinas with STEM121-FITC, Cone Arrestin-APC and DAPI-VioBlue. Of note is that many engrafted cells were found in the injected group (expressing both human and cone marker) while little to no host cones were found in the control group. This result suggests the potential of covering the retina (and in the case of human patient their fovea) with integrating and regenerating hCP.

We analyzed in more depths the pattern of engrafted hCP in RD1 by analyzing their localization on the whole mounted retinas. Figure 7.23A, show a quarter of the whole mounted retina stained with STEM121 and cone arrestin while Figure 7.23C shows a confocal microscopy fluorescence zoom of a specific ROIs of the retina. As

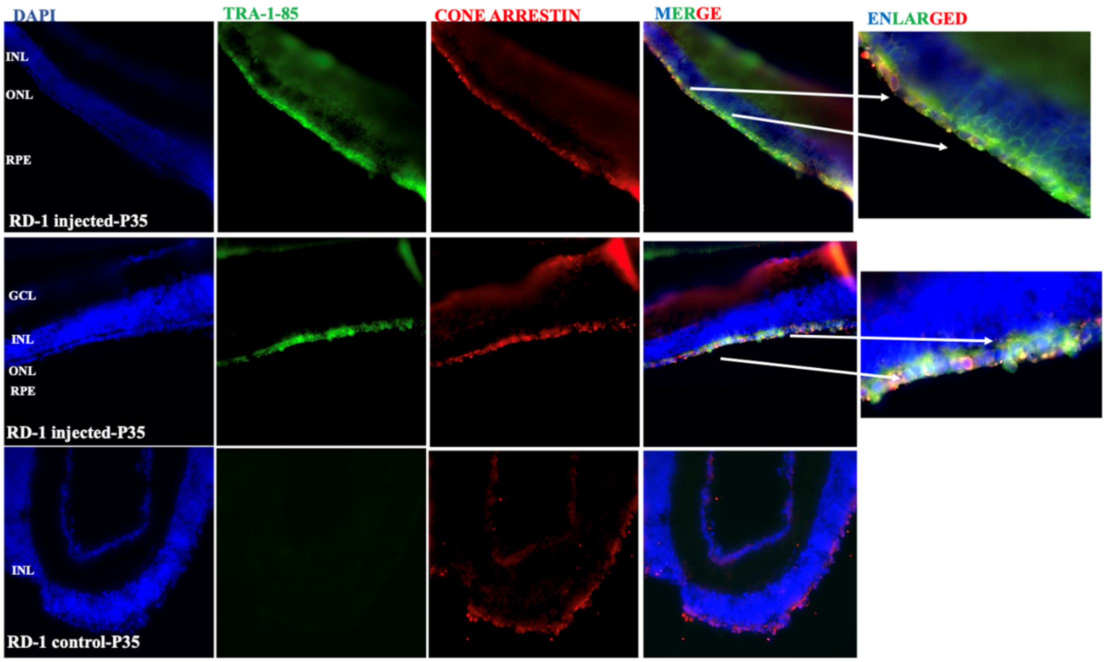

Figure 7.21: Immuno-staining of 1-week post-injection RD-1 retina injected with hCP.
Staining was performed with TRA-1-85-PE as human marker, Cone Arrestin-APC for cone marker and DAPI-VioBlue for nuclei and structure marker. Double stained cells were observed in the ONL layer of the retina, engrafted and expressing both human and cone markers.

seen in Figure 7.23A, cells were found to cover most of the retina, which is mainly due to the high number of injected cells compared to the initial number of photoreceptor present in RD1 mice. To analyze the position of injected hCP we used different image processing algorithms to compute the average local cell density (Figure 7.23B) and the nearest neighbor distance (Figure 7.23D). Both these variables enabled us to qualitatively image and analyze the presence of engrafted cells onto the retina of RD1 mice.

To perform a quantitative analysis of the presence and location of hCP in the retina we use the different image processing algorithms along with the result of both local cell density and nearest neighbor distance to compute more variables. As seen in Figure 7.24A, this first enables us to calculate the average cell density which was found to be around 1000 cells/mm^2 for the low dose (50k) and 6000 cells/mm^2 in high dose. This was compared with cultured cells in a 2D flask which have a higher

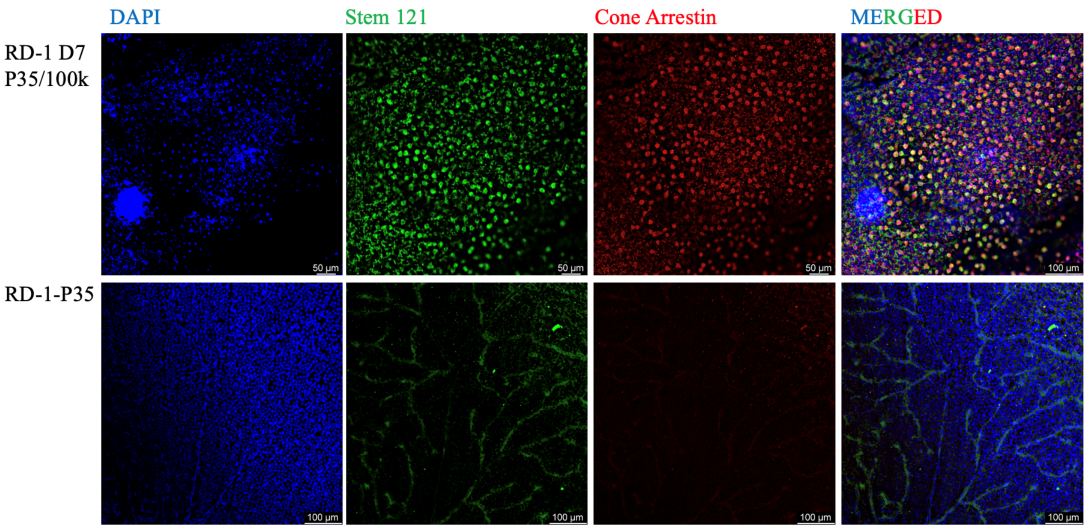

Figure 7.22: Immuno-staining of 1-week post-injection RD-1 retina injected with hCP.
Staining was performed with TRA-1-85-PE as human marker, Cone Arrestin-APC for cone marker and DAPI-VioBlue for nuclei and structure marker. Double stained cells were observed in the ONL layer of the retina, engrafted and expressing both human and cone markers.

density when confluent (around 10000 cells/mm^2). By using the data measured with the nearest neighbor distance we were able to compute the frequency of each cell nearest neighbor as seen in Figure 7.24B. The result suggests that for the high dose most cells are spaced by 15-20 µm while for the low dose 5-10 µm. Of note is that non-confluent cells in culture don't have the high peak, having most cells spaced between 5-40 µm.

To further analyze the distribution of engrafted hCP we calculated the nearest neighbor index (Figure 7.24C). The nearest neighbor index (NNI) is expressed as the ratio of the observed mean distance to the expected mean distance. The expected distance is the average distance between neighbors in a hypothetical random distribution.

$$R_n = \frac{D(obs)}{0.5 * \sqrt{\frac{a}{n}}} \tag{7.1}$$

Where Rn is the NNI, a is the area sampled and n is the number of points (cells in our case). The distribution can therefore be measured as if the index is less than

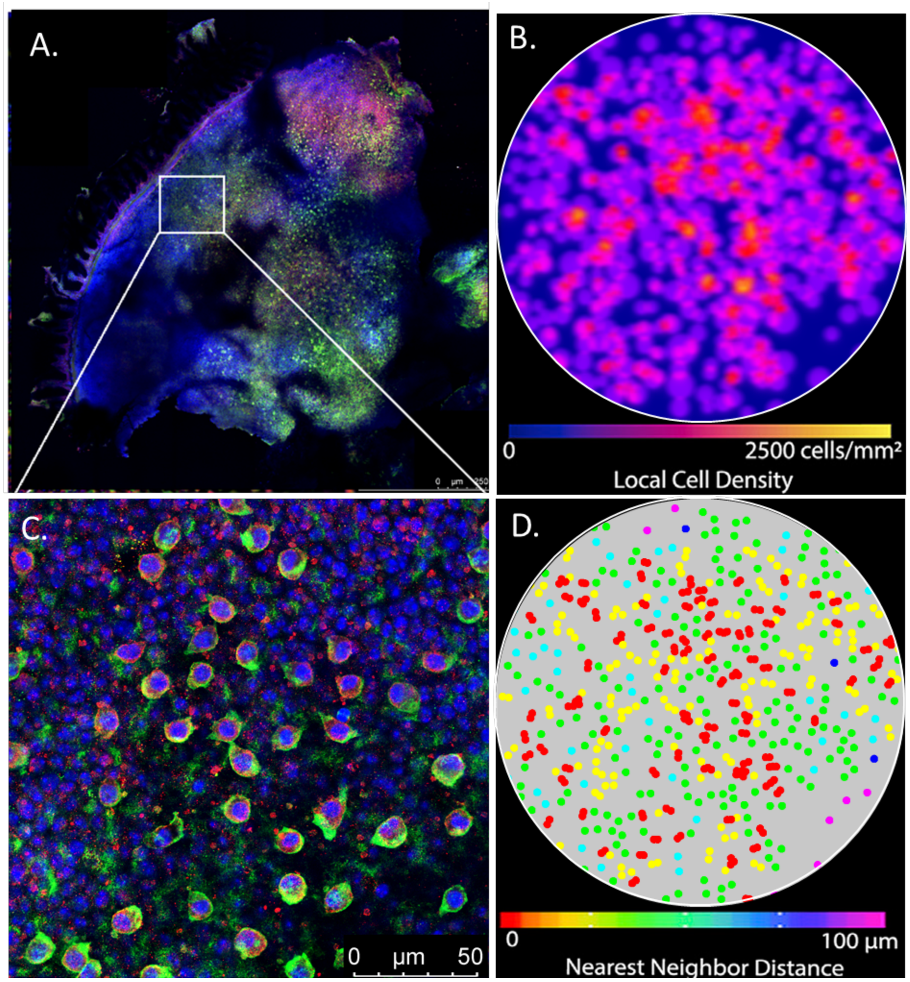

Figure 7.23: Analysis of hCP engraftment in Rd-1 mice.
A. C. Immunofluorescence of RD-1 whole mount retina stained with STEM121-PE, cone arrestin-APC, and DAPI-VioBlue. **B.** Local cell density measurement of engrafted hCPs ranging from 0 to 2500 cells/mm^2. **D.** Nearest neighbor distance measurement of engrafted hCPs ranging from 0 to 100 µm in the ROI.

1, the pattern exhibits clustering; if the index is greater than 1, the trend is toward dispersion or uniform distribution. As seen in Figure 7.24C this suggests that the low dose group exhibit a clustering pattern while the high dose exhibit a more uniformly distributed pattern (also called mosaic pattern). Of note is that cells in culture have an NNI around1 which suggest a more random distribution (coherent with cells in a 2D flask). Finally, the analyzes of the distance from a referent cell (Figure 7.24D) enables to see if the distribution pattern of each group is conserved throughout the entire retina. As expected for the low dose the density seems to fall drastically when measured away from the injection site while it stays constant for both the high dose (confirming the mosaic pattern on a large surface) and for cells in culture.

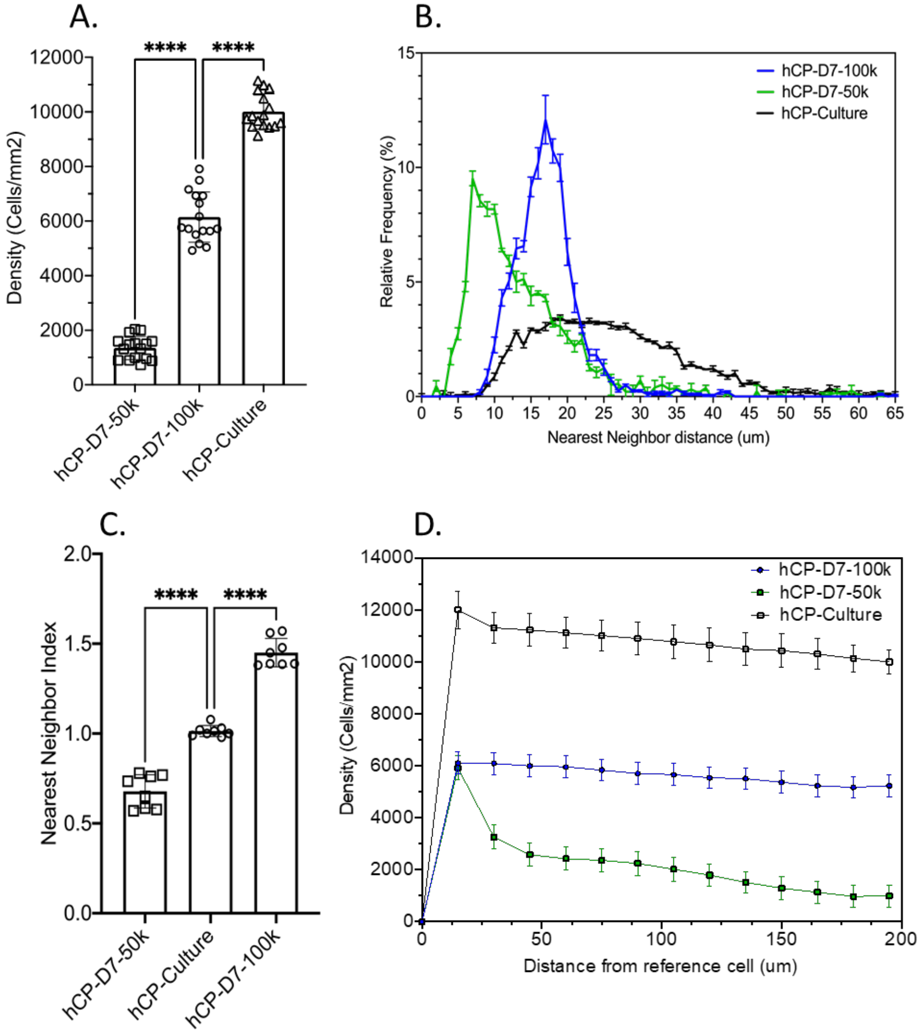

Figure 7.24: Analysis of engrafted hCPs distribution in RD-1 mice.
A. Cell density measurement compared for low dose, high dose, and cells confluent in culture. **B.** Nearest neighbor distance measurement of cells engrafted in low and high dose, compared with seeded cells in culture. **C.** Nearest neighbor index calculation for the 3 groups showing a random distribution for cells in culture, clustered distribution for low dose and mosaic pattern for high dose. **D.** Density in function of the distance from a reference cell for the 3 groups, showing the conservation of the mosaic pattern for the high dose group.

Overall, the result of this proof-of-concept in vivo study in RD1 mice suggest that hCP can integrate in a hostile environment by engrafting in a mosaic pattern (for the high dose group). This study helped us establish the most effective age for transplanting cells that can give maximum functional recovery of the animal.

7.5 Discussion

In most forms of retinal degeneration there is a primary pathological event that leads the cascade of degeneration process and most of the time the event is death of rod photoreceptor which is followed by cones [174]. The reason is unknown so far, but cones can't survive indefinitely in the absence of normal microenvironment. Even though the rods are dominant, dead cells found in the retina are cones which causes loss of visual acuity and blindness. There is no treatment to replace dying cone photoreceptor cells so far since these are a rare population of cells and culturing cells in lab conditions has been a challenge. We have succeeded in isolating pure cone progenitor cells with a 2-steps isolation process. The final product was characterized and analyzed showing a high purity of $CD73^{+}/Thrb^{+}/CD11b^{-}$ cells. The fetal retina was first dissociated and cultured to obtain desired cell number of 10M cells. The first sorting step involved tagging the cells with CD73 surface antigen which is exclusively expressed in the photoreceptor precursor population [223]. The positive cells were further cultured in hypoxia conditions (10% oxygen) and sorted with $CD73^{+}/Thrb^{+}/CD11b^{-}$ cells using Miltenyi Tyto cell sorter. Double positive staining of cells ensured higher purity with $CD11b^{-}$ acting as negative channel that allowed us to delete specific cell population. We demonstrated these cells could be cultured and expanded in hypoxia conditions. We have confirmed the phenotypical expression of these cells using MACSQuant and identified these cells as human cone progenitor cells after testing for cone Arrestin, s-opsin, m-opsin, blue-opsin expression (95%). These cells were found to have low PkCa expression (4%), and no rhodopsin, Brn3a, NeuN, RBPMS indicating the purity of these cells with few contaminating cells of non-cone lineage [231].

This strategy to isolate, enrich and culture was used to obtain large number of hCPs which were transplanted into rat eyes showing extremely high capacity to survive and engraftment into the host inner retina. hCPs were also found to have a significant neuroprotective aspect and were able to engraft in a mosaic pattern in the retina of degenerating RD1 mice. RD-1 mice have secondary degeneration of cone cells. At post-natal day 8 the degeneration of rod starts due to mutation in rod-specific phosphodiesterase gene that lead to massive loss of rod photoreceptors quickly followed by loss of cone, bipolar and horizontal cells [232]. To rescue vision, the transplantation is ideally performed at P21 to P28 as most of the native photoreceptors are completely lost hence any photoreceptor cells found in the animal can be directly attributed to the transplantation. The mosaic pattern confirms the successful engraftment of hCP and is primordial as the distribution of cones in human retina follow the same pattern in both the fovea and outer retina. In the fovea cones are predominant with some rods being in a mosaic pattern while in the rest of the retina all cones are distributed in a uniform way [9]. The engrafted hCP retains substantial fraction of its normal phenotype. Most of the engrafted cones were found in the outer nuclear layer where cones are predominantly found and where continuously expressing Arrestin or opsins like normal cone photoreceptors. We found that hCPs were stable state and persist for many weeks in RCS rats and RD1 mice without showing sign of progressive degeneration. The ability for hCP to engraft in this specific pattern suggest potentially great and conclusive result in a transplantation into human patients in a clinical trial. Even though presently gene therapy approach is gaining traction for treating retinal degeneration the biggest drawback of the technique is that it still requires few healthy cells in the host however, in the retinal degeneration disease such as AMD and RP there is cascading events that starts with either RPE malfunctioning or rod photoreceptor degeneration that continuous to destroy other associated cells such as cone and bipolar retinal cells.

The novel hCPs have shown ability to survive in the hostile environment and recuse vision in both RCS and RD1 animal model and we believe it can be either be as used a standalone cell therapy for rescuing vision by replacing diseases photoreceptors or as a complimentary system along with gene therapy to completely restore vision by replenishing retina with functional cells while gene therapy repairs the mutation.

Chapter 8

Conclusions and implications

8.1 Conclusions

The principal objective (Aim 1) of this thesis was to evaluate the ability of an injectable, gelatin and hyaluronic acid-based biomaterial (gelatin-hydroxyphenyl propionic acid, Gtn-HPA, hyaluronic acid-tyramine, HA-Tyr, or the mix of both) incorporating different growth factor (epidermal growth factor, EGF, fibroblast derived growth factor, FGF) to enhance the viability, attachment, release and engraftment of encapsulated and injected stem cells (human retinal progenitor cells (hRPCs), human retinal ganglion cells (hRGC) in order to enable retinal regeneration in the case of different retinal diseases such as Retinitis pigmentosa (RP), cone-rod dystrophy, or neurofibromatosis type 1 optic pathway glioma (NF1-OPG). The enhancement of stem cell fate would be significant because most retinal therapies and injections fail due to the hostile environment cells are subjected to. Furthermore, prior work [10], [184] has demonstrated an additional benefit to add a structural component to stem cell injections in retinal regeneration in order to match the architecture of the tissue.

To analyze this possible enhancement both human photoreceptor progenitors (hRPC) and human retinal ganglion cells (hRGC) were encapsulated in Gtn-HPA and HA-Tyr polymeric gels and injected in either the subretinal space (hRPC) or in the vitreous (hRGC) of Long Evans wild rats. This strain of rats doesn't possess any degeneration mechanism, however, due to the trauma and bleb creation during injection, it serves as a well-defined model for retinal detachment (which happens in most previously cited diseases). The Gtn-HPA/HA-Tyr gel-based therapy was evaluated for the presence of human cells engrafted in the precise location of the retina (Outer nuclear layer for hRPC or ganglion cell layer for hRGC) 2 to 4 weeks post-transplantation and compared to non-injected (controls), vehicle injected (SHAM) or PBS injected (cells injected in PBS) retinas. At both time points there was a significant increase in engrafted cells injected in our biomaterials compared to cells injected in saline. Cells were found to express either a photoreceptor or ganglion cell phenotype 1-month post transplantation and engrafted in their corresponding layer of the retina.

Moreover, the effect of different biomaterials and growth factors were tested in additional injection groups: including EGF and mixing different fractions of Gtn-HPA and HA-Tyr. For hRGC replacement, stiffer hydrogels (made of 50% Gtn-HPA and 50% HA-Tyr) were found to not only be able to attach to the inner limiting membrane (ILM) of the retina but also increase the number of engrafted cells in the RGC layer and improving their processes extension towards the optic nerve. Forming a neuronal connection suggests the ability of improving functional regeneration which can be achieved by using our biomaterials in the therapy. Our hydrogels were also tuned to enhance the stiffness, injectability and controlled attachment for future retinal therapies.

In a second objective (Aim 2), the mechanical and chemical effect of our biomaterials in vitro on different retinal cells was analyzed and measured. We, first, showed that different sensitive retinal stem cell line is resistant to the covalent crosslinking of our hydrogels, possessing a higher viability than cells deprived from nutrients in a 2D culture setting. We also proved the possibility to control the phenotypic expression of hRPC by changing the stiffness and gelatin/HA fraction in our hydrogels. Higher stiffness was shown to induce cells to express stemness marker, while softer hydrogels enabled either rods or cones photoreceptor to mature and thrive in vitro. Towards clinical translation, we analyzed the diffusion mechanics and control of growth factors and cells though our biomaterials. This study enabled a deeper comprehension of the forces in place which induce the release and thriving of stem cells when encapsulated in hydrogels and injected in the retina. A last study showed an additional benefit of our biomaterials which protect injected retinal stem cells from the shear stress which is applied during small bore needle injection.

Enhancing retinal regeneration by the addition of a biomaterials is necessary but not sufficient. One also needs to optimize the culture conditions and create animal models for testing which was performed (Aim 3). hRPC were shown to thrive and express different stemness marker when cultured in hypoxia conditions and different knockout serum (compared to fetal bovine serum usually used in cell culture). The NF1-OPG rat model was created by injecting C6 cancer cells in their optic nerve and monitoring the creation and size of tumors. A successful short-term animal model was created which could potentially enable a higher comprehension of the different mechanics of NF1-OPG.

Finally, towards clinical translation and novel therapies, our fourth objective (Aim 4) was to isolate and purify a novel cone progenitor population (hCP) which could replace dead photoreceptors in specific retinal diseases (cone-rod dystrophy). The hCP population was found to possess a high purity and a cone progenitor phenotype, being also functionally active in vitro. By injecting hCP into 3 different animal models (Long Evans rats, RCS rats and RD1 mice) we were able to prove their high engraftment possibilities, their neuroprotection abilities and their mosaic pattern cell replacement distribution. These result inform in the possibility of novel treatment for orphan retinal diseases.

8.2 Implications

The results of this thesis motivate and guide further study in a large animal model to validate not only the use of Gtn-HPA/HA-Tyr biomaterials for enhancing engraftment of retinal stem cells but also the possibility of novel regeneration process with a novel cell line (hCP). The large animal model will address key questions on the difficulties of injection of our biomaterials and will permit the calculation of a correct dosage of hCP which could be used clinically. Furthermore, the engineered biomaterials have shown significant effect on cell viability which is critical for improving the success of cell therapies. Most of the cell during clinical setting failed not due to its inability to engraft in patients but due to lack of viable cells that can be delivered into the host tissue [120]. We have addressed two major impediments and found a solution that can improve the odds of cell therapy success especially for retinal regeneration. These results also motivate the use of hCP to treat inherited retinal diseases in clinic by offering a total replacement of dead photoreceptors. This implies a GMP production of hCP with a controlled manufacturing process.

Chapter 9

Limitations and future directions

9.1 Limitations of the work

9.1.1 Engineering a bio-inspired matrix for retinal regeneration

- The immunostaining results should be validated with another methods outlined in the following section on future work
- The in-situ crosslinking of Gtn-HPA alone happens at a relatively fast pace (around 330 seconds). This short-time significantly impacted the success rate of in vivo injections in rats (from 75% to 50%). This gelation time could be modified with different chemistry to offer a longer time of animal manipulation and injection.
- ERG and OKN response were not measured in Long Evans rats for hRPC and hRGC injections, since they don't have an inherited mutation it is assumed that no differences would be seen in this animal model.
- Only short- and medium-term in vivo experiments were performed which could suggest a different outcomes a longer time points (>6 months).

9.1.2 Analyzing and measuring the effect of gels on retinal stem cells

- The use of FGF and EGF as main chemical cues was decided by the components already present in hRPC media. However, many other growth factor and neuroprotective factors (such as anti-VEGF) could be beneficial to enhance the viability and ability to engraft of injected cells.
- The control of hRPC differentiation in vivo with different biomaterial was based solely on gel stiffness. Many studies [124] have shown that not only mechanical cues but also oxygen content, chemical content and cell-biomaterial interaction have a strong impact on stem cell differentiation.
- The pore size and ligands concentrations were not studied in details, which could lead to new findings on the effect of our biomaterials on retinal stem cells.

9.1.3 Optimizing retinal cell culture and animal model (NF1-OPG)

- Our NF1-OPG animal model can only be used for short-term studies. A longer-term animal model could be useful to analyze in more depth the impact of stem cell injection to RGC replacement and tumor regression in the optic nerve.

9.1.4 Creating new clinical therapies for treating retinal diseases

- The potential for hCP engraftment and regeneration must be performed in RD1 mice by measuring ERG and OKN responses at longer time points.
- The functionality of hCP in vitro was performed on bright light and could be analyzed for different wavelength, giving rise to specific data on the type of cones present in hCP (S-cones, M-cones or L-cones).

9.2 Future directions

9.2.1 Retinal degeneration animal model for hydrogels injections

- Test Gtn-HPA/HA-Tyr cell encapsulation injections in a degenerating model with OKN and ERG measurement at different time points.
- Longer experiment (>6 months) to test for long-term effect of gels on cell engraftment and immune response.
- Modifying concentrations of the different chemicals in the gelation process (polymer weight percent, catalyzer, crosslinker) leading to an increase in gelation time thereby improving its injectability.
- Explore the effects of comorbidities (e.g., diabetes) on cell engraftment and regeneration.
- Validate the immunostaining with an additional method such as gene expression (quantitative polymerase chain reaction) in retinal tissue from the region of the injection.
- Determine the dose response of EGF and other growth factor for the differentiation, viability and proliferation of encapsulated cells.

9.2.2 Large animal model (such as rhesus monkey)

- Test Gtn-HPA/HA-Tyr in a larger animal retina and perform OCT, back of the eye imaging, behavioral testing, and imaging of the biomaterial over time.
- Cell dosage testing, towards clinical trial, which could be used for human injections.
- Biomaterials volumes dosage testing, towards clinical trial.

9.2.3 In vitro testing of injected cells onto explanted retina

- Test Gtn-HPA/HA-Tyr cell encapsulation injections on explanted retina with multi-electrode array for functionality.
- Digest retinas and sort human injected cells to test for their phenotype post-injection by flow cytometry.
- Digest the portion of retina surrounding the Gtn-HPA/HA-Tyr with cells injections site and the remaining hydrogels to measure the amount of EGF found in each with ELISA.

9.2.4 hCP clinical translation

- Optimize the formulation of hCP from frozen to direct human injection (towards clinical application).
- Perform additional analysis and testing of hCP functionality in vitro (MEA)
- Longer RD1 and RCS studies to be performed for long-term effect of hCP injections.

9.2.5 In vitro testing and miscellaneous

- Research and perform testing on novel growth factor encapsulated in hydrogels (anti-VEGF) [233]., and analyze the oxygen content in hydrogels.
- Repeat the rheology experiments with cells encapsulated in hydrogels.
- Use a compression testing apparatus on standardized geometries (formed from molds) to determine the effect of cells addition on Gtn-HPA/HA-Tyr mechanical properties after a pre-specified time delay between the initiation of covalent crosslinking and cell addition.
- Try to identify the primary degradation products of Gtn-HPA with mass spectroscopy after in vitro digestion of the preformed scaffold.

Bibliography

[1] K. Kaarniranta, A. Salminen, A. Haapasalo, H. Soininen, and M. Hiltunen, “Age-related macular degeneration (amd): Alzheimer’s disease in the eye?” *Journal of Alzheimer’s Disease*, vol. 24, no. 4, pp. 615–631, 2011, ISSN: 1387-2877.

[2] J. H. Kempen, B. J. O’Colmain, M. C. Leske, S. M. Haffner, R. Klein, S. E. Moss, H. R. Taylor, and R. F. Hamman, “The prevalence of diabetic retinopathy among adults in the united states,” *Archives of ophthalmology (Chicago, Ill.: 1960)*, vol. 122, no. 4, pp. 552–563, 2004, ISSN: 0003-9950.

[3] M. Hanany, C. Rivolta, and D. Sharon, “Worldwide carrier frequency and genetic prevalence of autosomal recessive inherited retinal diseases,” *Proceedings of the National Academy of Sciences*, vol. 117, no. 5, pp. 2710–2716, 2020, ISSN: 0027-8424.

[4] Y. Murakami, S. Notomi, T. Hisatomi, T. Nakazawa, T. Ishibashi, J. W. Miller, and D. G. Vavvas, “Photoreceptor cell death and rescue in retinal detachment and degenerations,” *Progress in retinal and eye research*, vol. 37, pp. 114–140, 2013, ISSN: 1350-9462.

[5] P. J. Mackenzie, M. Russell, P. E. Ma, C. M. Isbister, and D. A. Maberley, “Sensitivity and specificity of the optos optomap for detecting peripheral retinal lesions,” *Retina*, vol. 27, no. 8, pp. 1119–1124, 2007, ISSN: 0275-004X.

[6] A. Atkinson and C. Mazo, “Imaged area of the retina,” *Data on file, Optos*, 2015.

[7] P. A. CIBIS, B. BECKER, E. OKUN, and S. CANAAN, "The use of liquid silicone in retinal detachment surgery," *Archives of ophthalmology*, vol. 68, no. 5, pp. 590–599, 1962, ISSN: 0003-9950.

[8] M. T. Pardue and R. S. Allen, "Neuroprotective strategies for retinal disease," *Progress in retinal and eye research*, vol. 65, pp. 50–76, 2018, ISSN: 1873-1635 1350-9462. DOI: `10.1016/j.preteyeres.2018.02.002`. [Online]. Available: `https://www.ncbi.nlm.nih.gov/pmc/articles/PMC6081194/`.

[9] H. Wassle and B. B. Boycott, "Functional architecture of the mammalian retina," *Physiological reviews*, vol. 71, no. 2, pp. 447–480, 1991, ISSN: 0031-9333.

[10] N. C. Hunt, D. Hallam, V. Chichagova, D. H. Steel, and M. Lako, "The application of biomaterials to tissue engineering neural retina and retinal pigment epithelium," *Advanced Healthcare Materials*, vol. 7, no. 23, p. 1 800 226, 2018, ISSN: 2192-2640. DOI: `https://doi.org/10.1002/adhm.201800226`. [Online]. Available: `https://onlinelibrary.wiley.com/doi/abs/10.1002/adhm.201800226`.

[11] H. Kolb, "Simple anatomy of the retina," 2012.

[12] J. Z. Nowak, "Age-related macular degeneration (amd): Pathogenesis and therapy," *Pharmacological reports*, vol. 58, no. 3, p. 353, 2006, ISSN: 1734-1140.

[13] N. M. Bressler, S. B. Bressler, and S. L. Fine, "Age-related macular degeneration," *Survey of ophthalmology*, vol. 32, no. 6, pp. 375–413, 1988, ISSN: 0039-6257.

[14] C. A. Curcio, N. E. Medeiros, and C. L. Millican, "Photoreceptor loss in age-related macular degeneration," *Investigative ophthalmology & visual science*, vol. 37, no. 7, pp. 1236–1249, 1996, ISSN: 1552-5783.

[15] P. J. Francis, "Genetics of inherited retinal disease," *Journal of the Royal Society of Medicine*, vol. 99, no. 4, pp. 189–191, 2006, ISSN: 0141-0768.

[16] D. T. Hartong, E. L. Berson, and T. P. Dryja, "Retinitis pigmentosa," *The Lancet*, vol. 368, no. 9549, pp. 1795–1809, 2006, ISSN: 0140-6736.

[17] R. Allikmets, N. F. Shroyer, N. Singh, J. M. Seddon, R. A. Lewis, P. S. Bernstein, A. Peiffer, N. A. Zabriskie, Y. Li, and A. Hutchinson, "Mutation of the stargardt disease gene (abcr) in age-related macular degeneration," *Science*, vol. 277, no. 5333, pp. 1805–1807, 1997, ISSN: 0036-8075.

[18] A. A. Thiadens, T. M. L. Phan, R. C. Zekveld-Vroon, B. P. Leroy, L. I. van Den Born, C. B. Hoyng, C. C. Klaver, S. Roosing, J.-W. R. Pott, and M. J. van Schooneveld, "Clinical course, genetic etiology, and visual outcome in cone and cone–rod dystrophy," *Ophthalmology*, vol. 119, no. 4, pp. 819–826, 2012, ISSN: 0161-6420.

[19] C. J. Campen and D. H. Gutmann, "Optic pathway gliomas in neurofibromatosis type 1," *Journal of Child Neurology*, vol. 33, no. 1, pp. 73–81, 2017, ISSN: 0883-0738. DOI: `10.1177/0883073817739509`. [Online]. Available: `https://doi.org/10.1177/0883073817739509`.

[20] M. Endo, H. Yamamoto, N. Setsu, K. Kohashi, Y. Takahashi, T. Ishii, K.-i. Iida, Y. Matsumoto, M. Hakozaki, and M. Aoki, "Prognostic significance of akt/mtor and mapk pathways and antitumor effect of mtor inhibitor in nf1-related and sporadic malignant peripheral nerve sheath tumors," *Clinical Cancer Research*, vol. 19, no. 2, pp. 450–461, 2013, ISSN: 1078-0432.

[21] R. S. Apte, "Gene therapy for retinal degeneration," *Cell*, vol. 173, no. 1, p. 5, 2018, ISSN: 0092-8674.

[22] A. Kimura, K. Namekata, X. Guo, C. Harada, and T. Harada, "Neuroprotection, growth factors and bdnf-trkb signalling in retinal degeneration," *International journal of molecular sciences*, vol. 17, no. 9, p. 1584, 2016.

[23] B. Y. Chow and E. S. Boyden, "Optogenetics and translational medicine," *Science translational medicine*, vol. 5, no. 177, 177ps5–177ps5, 2013, ISSN: 1946-6234.

[24] H. P. Scholl, R. W. Strauss, M. S. Singh, D. Dalkara, B. Roska, S. Picaud, and J.-A. Sahel, "Emerging therapies for inherited retinal degeneration," *Science translational medicine*, vol. 8, no. 368, 368rv6–368rv6, 2016, ISSN: 1946-6234.

[25] J. W. B. Bainbridge, A. J. Smith, S. S. Barker, S. Robbie, R. Henderson, K. Balaggan, A. Viswanathan, G. E. Holder, A. Stockman, N. Tyler, S. Petersen-Jones, S. S. Bhattacharya, A. J. Thrasher, F. W. Fitzke, B. J. Carter, G. S. Rubin, A. T. Moore, and R. R. Ali, "Effect of gene therapy on visual function in leber's congenital amaurosis," *New England Journal of Medicine*, vol. 358, no. 21, pp. 2231–2239, 2008, ISSN: 0028-4793. DOI: `10.1056/NEJMoa0802268`. [Online]. Available: `https://doi.org/10.1056/NEJMoa0802268`.

[26] M. U. I. Ltd, *Clinical trial of gene therapy for the treatment of leber congenital amaurosis (lca)*, Generic, 2016.

[27] A. Möglich and K. Moffat, "Engineered photoreceptors as novel optogenetic tools," *Photochemical & photobiological sciences*, vol. 9, no. 10, pp. 1286–1300, 2010.

[28] *Dose-escalation study to evaluate the safety and tolerability of gs030 in subjects with retinitis pigmentosa*, Generic.

[29] *Efficacy of ubiquinone and combined antioxidant therapy in non-proliferative diabetic retinopathy*, Generic.

[30] C. Ramsden, M. Powner, A. Carr, M. Smart, L. da Cruz, and P. Coffey, "Stem cells in retinal regeneration: Past, present and future," *Development*, vol. 140, no. 12, pp. 2576–2585, 2013, ISSN: 0950-1991. DOI: `10.1242/dev.092270`.

[31] M. Young, "Stem cells in the mammalian eye: A tool for retinal repair," *Apmis*, vol. 113, no. 11-12, pp. 845–857, 2005, ISSN: 0903-4641. DOI: `10.1111/j.1600-0463.2005.apm\_334.x`.

[32] S. U. Kim and J. De Vellis, "Stem cell-based cell therapy in neurological diseases: A review," *Journal of neuroscience research*, vol. 87, no. 10, pp. 2183–2200, 2009, ISSN: 0360-4012.

[33] S. D. Schwartz, J.-P. Hubschman, G. Heilwell, V. Franco-Cardenas, C. K. Pan, R. M. Ostrick, E. Mickunas, R. Gay, I. Klimanskaya, and R. Lanza, "Embryonic stem cell trials for macular degeneration: A preliminary report," *The Lancet*, vol. 379, no. 9817, pp. 713–720, 2012, ISSN: 0140-6736. DOI: `https://doi.org/10.1016/S0140-6736(12)60028-2`. [Online]. Available: `http://www.sciencedirect.com/science/article/pii/S0140673612600282`.

[34] M. Ejtehadifar, K. Shamsasenjan, A. Movassaghpour, P. Akbarzadehlaleh, N. Dehdilani, P. Abbasi, Z. Molaeipour, and M. Saleh, "The effect of hypoxia on mesenchymal stem cell biology," *Advanced pharmaceutical bulletin*, vol. 5, no. 2, pp. 141–149, 2015, ISSN: 2228-5881 2251-7308. DOI: `10.15171/apb.2015.021`. [Online]. Available: `https://www.ncbi.nlm.nih.gov/pmc/articles/PMC4517092/`.

[35] J. S. Meyer, R. L. Shearer, E. E. Capowski, L. S. Wright, K. A. Wallace, E. L. McMillan, S. C. Zhang, and D. M. Gamm, "Modeling early retinal development with human embryonic and induced pluripotent stem cells," *Proc Natl Acad Sci U S A*, vol. 106, no. 39, pp. 16 698–703, 2009, ISSN: 1091-6490. DOI: `10.1073/pnas.0905245106`. [Online]. Available: `https://www.ncbi.nlm.nih.gov/pubmed/19706890`.

[36] S. Yamanaka, "Induction of pluripotent stem cells from mouse fibroblasts by four transcription factors," *Cell proliferation*, vol. 41, pp. 51–56, 2008, ISSN: 0960-7722.

[37] J. Luo, P. Baranov, S. Patel, H. Ouyang, J. Quach, F. Wu, A. Qiu, H. Luo, C. Hicks, J. Zeng, J. Zhu, J. Lu, N. Sfeir, C. Wen, M. Zhang, V. Reade, J. Sinden, X. Sun, P. Shaw, M. Young, and K. Zhang, "Human retinal progenitor cell transplantation preserves vision," *Journal of Biological Chemistry*, vol. 289, no. 10, pp. 6362–6371, 2014, ISSN: 0021-9258. DOI: `10.1074/jbc.M113.513713`.

[38] L. Mazzini, M. Gelati, D. C. Profico, G. Sgaravizzi, M. Projetti Pensi, G. Muzi, C. Ricciolini, L. Rota Nodari, S. Carletti, C. Giorgi, C. Spera, F. Domenico,

E. Bersano, F. Petruzzelli, C. Cisari, A. Maglione, M. F. Sarnelli, A. Stecco, G. Querin, S. Masiero, R. Cantello, D. Ferrari, C. Zalfa, E. Binda, A. Visioli, D. Trombetta, A. Novelli, B. Torres, L. Bernardini, A. Carriero, P. Prandi, S. Servo, A. Cerino, V. Cima, A. Gaiani, N. Nasuelli, M. Massara, J. Glass, G. Soraruù, N. M. Boulis, and A. L. Vescovi, "Human neural stem cell transplantation in als: Initial results from a phase i trial," *Journal of translational medicine*, vol. 13, pp. 17–17, 2015, ISSN: 1479-5876. DOI: `10.1186/s12967-014-0371-2`. [Online]. Available: `https://www.ncbi.nlm.nih.gov/pmc/articles/PMC4359401/`.

[39] R. Aramant and M. Seiler, "Transplanted sheets of human retina and retinal pigment epithelium develop normally in nude rats," *Experimental Eye Research*, vol. 75, no. 2, pp. 115–125, 2002, ISSN: 0014-4835. DOI: `10.1006/exer.2002.2001`.

[40] E. Lee and R. E. MacLaren, "Sources of retinal pigment epithelium (rpe) for replacement therapy," *British journal of ophthalmology*, vol. 95, no. 4, pp. 445–449, 2011, ISSN: 0007-1161.

[41] *Intravitreal mesenchymal stem cell transplantation in advanced glaucoma*, Generic.

[42] *Safety and tolerability of sub-retinal transplantation of hesc derived rpe (ma09-hrpe) cells in patients with advanced dry age related macular degeneration*, Generic.

[43] *Retinal pigment epithelium safety study for patients in b4711001*, Generic.

[44] *Production of ipsc derived rpe cells for transplantation in amd*, Generic.

[45] *Clinical study of subretinal transplantation of human embryo stem cell derived retinal pigment epitheliums in treatment of macular degeneration diseases*, Generic.

[46] *Stem cell therapy for outer retinal degenerations*, Generic.

[47] *Sub-retinal transplantation of hesc derived rpe(ma09-hrpe)cells in patients with stargardt's macular dystrophy*, Generic.

[48] *Treatment of dry age related macular degeneration disease with retinal pigment epithelium derived from human embryonic stem cells*, Generic.

[49] *Subretinal transplantation of retinal pigment epitheliums in treatment of age-related macular degeneration diseases*, Generic.

[50] *Study of subretinal implantation of human embryonic stem cell-derived rpe cells in advanced dry amd*, Generic.

[51] *Safety and efficacy of intravitreal injection of human retinal progenitor cells in adults with retinitis pigmentosa*, Generic.

[52] *Safety of a single, intravitreal injection of human retinal progenitor cells (jcell) in retinitis pigmentosa*, Generic.

[53] *Safety and tolerability of hrpc in retinitis pigmentosa*, Generic.

[54] B. Xian and B. Huang, "The immune response of stem cells in subretinal transplantation," *Stem cell research & therapy*, vol. 6, pp. 161–161, 2015, ISSN: 1757-6512. DOI: `10.1186/s13287-015-0167-1`. [Online]. Available: `https://www.ncbi.nlm.nih.gov/pmc/articles/PMC4568575/`.

[55] J. E. DiCarlo, V. B. Mahajan, and S. H. Tsang, "Gene therapy and genome surgery in the retina," *The Journal of Clinical Investigation*, vol. 128, no. 6, pp. 2177–2188, 2018, ISSN: 0021-9738. DOI: `10.1172/JCI120429`. [Online]. Available: `https://doi.org/10.1172/JCI120429`.

[56] P. C. Dromel and D. Singh, "9 - biomanufacturing," in *3D Printing in Medicine and Surgery*, D. J. Thomas and D. Singh, Eds. Woodhead Publishing, 2021, pp. 137–170, ISBN: 978-0-08-102542-0. DOI: `https://doi.org/10.1016/B978-0-08-102542-0.00009-9`. [Online]. Available: `https://www.sciencedirect.com/science/article/pii/B9780081025420000099`.

[57] D. Singh, P. C. Dromel, S.-b. Wang, and A. Tripathi, "Nanosystems for repairing retinal degeneration," in *Immobilization Strategies*. Springer, 2021, pp. 195–217.

[58] T. V. Johnson, N. D. Bull, and K. R. Martin, "Identification of barriers to retinal engraftment of transplanted stem cells," *Investigative Ophthalmology & Visual Science*, vol. 51, no. 2, pp. 960–970, 2010, ISSN: 1552-5783. DOI: `10.1167/iovs.09-3884`. [Online]. Available: `https://doi.org/10.1167/iovs.09-3884`.

[59] N. A. Hotaling, V. Khristov, Q. Wan, R. Sharma, B. S. Jha, M. Lotfi, A. Maminishkis, J. Simon Carl G., and K. Bharti, "Nanofiber scaffold-based tissue-engineered retinal pigment epithelium to treat degenerative eye diseases," *Journal of ocular pharmacology and therapeutics : the official journal of the Association for Ocular Pharmacology and Therapeutics*, vol. 32, no. 5, pp. 272–285, 2016, ISSN: 1557-7732 1080-7683. DOI: `10.1089/jop.2015.0157`. [Online]. Available: `https://www.ncbi.nlm.nih.gov/pmc/articles/PMC4904235/`.

[60] B. G. Ballios, M. J. Cooke, D. van der Kooy, and M. S. Shoichet, "A hydrogel-based stem cell delivery system to treat retinal degenerative diseases," *Biomaterials*, vol. 31, no. 9, pp. 2555–2564, 2010, ISSN: 0142-9612. DOI: `https://doi.org/10.1016/j.biomaterials.2009.12.004`. [Online]. Available: `http://www.sciencedirect.com/science/article/pii/S0142961209013635`.

[61] P. Dromel, D. Singh, T. Christoff-Tempesta, T. Martheswaran, A. Alexander-Katz, M. Spector, and M. Young, "Controlling growth factor diffusion by modulating water content in injectable hydrogels," *Tissue Engineering*, no. ja, 2020, ISSN: 1937-3341.

[62] R. C. Cooper and H. Yang, "Hydrogel-based ocular drug delivery systems: Emerging fabrication strategies, applications, and bench-to-bedside manufacturing considerations," *Journal of Controlled Release*, vol. 306, pp. 29–39, 2019, ISSN: 0168-3659.

[63] M. Lutolf and J. Hubbell, "Synthetic biomaterials as instructive extracellular microenvironments for morphogenesis in tissue engineering," *Nature biotechnology*, vol. 23, no. 1, p. 47, 2005, ISSN: 1546-1696.

[64] J. Yao, C. W. Ko, P. Y. Baranov, C. V. Regatieri, S. Redenti, B. A. Tucker, J. Mighty, S. L. Tao, and M. J. Young, "Enhanced differentiation and delivery of mouse retinal progenitor cells using a micropatterned biodegradable thin-film polycaprolactone scaffold," *Tissue Eng Part A*, vol. 21, no. 7-8, pp. 1247–60, 2015, ISSN: 1937-335X. DOI: `10.1089/ten.TEA.2013.0720`. [Online]. Available: `https://www.ncbi.nlm.nih.gov/pubmed/25517296`.

[65] M. Tomita, E. Lavik, H. Klassen, T. Zahir, R. Langer, and M. Young, "Biodegradable polymer composite grafts promote the survival and differentiation of retinal progenitor cells," *Stem Cells*, vol. 23, no. 10, pp. 1579–1588, 2005, ISSN: 1066-5099. DOI: `10.1634/stemcells.2005-0111`.

[66] P. Xiang, K.-C. Wu, Y. Zhu, L. Xiang, C. Li, D.-L. Chen, F. Chen, G. Xu, A. Wang, and M. Li, "A novel bruch's membrane-mimetic electrospun substrate scaffold for human retinal pigment epithelium cells," *Biomaterials*, vol. 35, no. 37, pp. 9777–9788, 2014, ISSN: 0142-9612.

[67] J. Park, P. Baranov, A. Aydin, H. Abdelgawad, D. Singh, W. Niu, M. Kurisawa, M. Spector, and M. Young, "In situ cross-linking hydrogel as a vehicle for retinal progenitor cell transplantation," 2019.

[68] A. M. Shadforth, K. A. George, A. S. Kwan, T. V. Chirila, and D. G. Harkin, "The cultivation of human retinal pigment epithelial cells on bombyx mori silk fibroin," *Biomaterials*, vol. 33, no. 16, pp. 4110–4117, 2012, ISSN: 0142-9612.

[69] J. Yao, B. A. Tucker, X. Zhang, P. Checa-Casalengua, R. Herrero-Vanrell, and M. J. Young, "Robust cell integration from co-transplantation of biodegradable mmp2-plga microspheres with retinal progenitor cells," *Biomaterials*, vol. 32, no. 4, pp. 1041–1050, 2011, ISSN: 0142-9612.

[70] M. J. Mazumder, S. D. Fitzpatrick, B. Muirhead, and H. Sheardown, "Cell-adhesive thermogelling pnipaam/hyaluronic acid cell delivery hydrogels for potential application as minimally invasive retinal therapeutics," *Journal of biomedical materials research Part A*, vol. 100, no. 7, pp. 1877–1887, 2012, ISSN: 1549-3296.

[71] J. Kundu, A. Michaelson, K. Talbot, P. Baranov, M. J. Young, and R. L. Carrier, "Decellularized retinal matrix: Natural platforms for human retinal progenitor cell culture," *Acta biomaterialia*, vol. 31, pp. 61–70, 2016, ISSN: 1742-7061.

[72] L.-S. Wang, F. Lee, J. Lim, C. Du, A. C. A. Wan, S. S. Lee, and M. Kurisawa, "Enzymatic conjugation of a bioactive peptide into an injectable hyaluronic acid–tyramine hydrogel system to promote the formation of functional vasculature," *Acta Biomaterialia*, vol. 10, no. 6, pp. 2539–2550, 2014, ISSN: 1742-7061. DOI: `https://doi.org/10.1016/j.actbio.2014.02.022`. [Online]. Available: `https://www.sciencedirect.com/science/article/pii/S1742706114000749`.

[73] L. Wang, C. Du, J. Chung, and M. Kurisawa, "Enzymatically cross-linked gelatin-phenol hydrogels with a broader stiffness range for osteogenic differentiation of human mesenchymal stem cells," *Acta Biomaterialia*, vol. 8, no. 5, pp. 1826–1837, 2012, ISSN: 1742-7061. DOI: `10.1016/j.actbio.2012.02.002`.

[74] M. Kurisawa, J. E. Chung, Y. Y. Yang, S. J. Gao, and H. Uyama, "Injectable biodegradable hydrogels composed of hyaluronic acid–tyramine conjugates for drug delivery and tissue engineering," *Chemical communications*, no. 34, pp. 4312–4314, 2005.

[75] P. C. Dromel, D. Singh, A. Alexander-Katz, M. Kurisawa, M. Spector, and M. Young, "Injectable gelatin hydroxyphenyl propionic acid hydrogel protects human retinal progenitor cells (hrpcs) from shear stress applied during small-bore needle injection," *Applied Materials Today*, vol. 19, p. 100 602, 2020, ISSN: 2352-9407.

[76] F. P. Melchels, A. M. Barradas, C. A. van Blitterswijk, J. de Boer, J. Feijen, and D. W. Grijpma, "Effects of the architecture of tissue engineering scaffolds on cell seeding and culturing," *Acta Biomater*, vol. 6, no. 11, pp. 4208–17, 2010, ISSN: 1878-7568. DOI: `10.1016/j.actbio.2010.06.012`. [Online]. Available: `https://www.ncbi.nlm.nih.gov/pubmed/20561602`.

[77] J. W. Bae, J. H. Choi, Y. Lee, and K. D. Park, "Horseradish peroxidase-catalysed in situ-forming hydrogels for tissue-engineering applications," *Journal of Tissue Engineering and Regenerative Medicine*, vol. 9, no. 11, pp. 1225–1232, 2015, ISSN: 1932-6254. DOI: `10.1002/term.1917`. [Online]. Available: `https://onlinelibrary.wiley.com/doi/abs/10.1002/term.1917`.

[78] N. K. Nema, N. Maity, B. K. Sarkar, and P. K. Mukherjee, "Matrix metalloproteinase, hyaluronidase and elastase inhibitory potential of standardized extract of centella asiatica," *Pharmaceutical Biology*, vol. 51, no. 9, pp. 1182–1187, 2013, ISSN: 1388-0209.

[79] J. Oswald and P. Baranov, "Regenerative medicine in the retina: From stem cells to cell replacement therapy," *Ther Adv Ophthalmol*, vol. 10, p. 2 515 841 418 774 433, 2018, ISSN: 2515-8414. DOI: `10.1177/2515841418774433`. [Online]. Available: `https://www.ncbi.nlm.nih.gov/pubmed/29998222`.

[80] V. M. Sluch, C.-h. O. Davis, V. Ranganathan, J. M. Kerr, K. Krick, R. Martin, C. A. Berlinicke, N. Marsh-Armstrong, J. S. Diamond, H.-Q. Mao, and D. J. Zack, "Differentiation of human escs to retinal ganglion cells using a crispr engineered reporter cell line," *Scientific Reports*, vol. 5, no. 1, p. 16 595, 2015, ISSN: 2045-2322. DOI: `10.1038/srep16595`. [Online]. Available: `https://doi.org/10.1038/srep16595`.

[81] G. Ai, X. Shao, M. Meng, L. Song, J. Qiu, Y. Wu, J. Zhou, J. Cheng, and X. Tong, "Epidermal growth factor promotes proliferation and maintains multipotency of continuous cultured adipose stem cells via activating stat signal pathway in vitro," *Medicine*, vol. 96, no. 30, e7607–e7607, 2017, ISSN: 1536-5964 0025-7974. DOI: `10.1097/MD.0000000000007607`. [Online]. Available: `https://www.ncbi.nlm.nih.gov/pmc/articles/PMC5627837/`.

[82] J. L. Close, J. Liu, B. Gumuscu, and T. A. Reh, "Epidermal growth factor receptor expression regulates proliferation in the postnatal rat retina," *Glia*, vol. 54, no. 2, pp. 94–104, 2006, ISSN: 0894-1491.

[83] G. Choe, J. Park, H. Park, and J. Lee, "Hydrogel biomaterials for stem cell microencapsulation," *Polymers*, vol. 10, no. 9, 2018, ISSN: 2073-4360. DOI: `10.3390/polym10090997`.

[84] A. Grignolo, "Fibrous components of the vitreous body," *AMA archives of ophthalmology*, vol. 47, no. 6, pp. 760–774, 1952, ISSN: 0096-6339.

[85] D. M. Schwartz, S. Shuster, M. D. Jumper, A. Chang, and R. Stern, "Human vitreous hyaluronidase: Isolation and characterization," *Current Eye Research*, vol. 15, no. 12, pp. 1156–1162, 1996, ISSN: 0271-3683. DOI: `10.3109/02713689608995150`. [Online]. Available: `https://doi.org/10.3109/02713689608995150`.

[86] M. van Deemter, H. H. Pas, R. Kuijer, R. J. van der Worp, J. M. Hooymans, and L. I. Los, "Enzymatic breakdown of type ii collagen in the human vitreous," *Invest Ophthalmol Vis Sci*, vol. 50, no. 10, pp. 4552–60, 2009, ISSN: 1552-5783. DOI: `10.1167/iovs.08-3125`. [Online]. Available: `https://www.ncbi.nlm.nih.gov/pubmed/19420340`.

[87] T. Lim, W. Toh, L. Wang, M. Kurisawa, and M. Spector, "The effect of injectable gelatin-hydroxyphenylpropionic acid hydrogel matrices on the proliferation, migration, differentiation and oxidative stress resistance of adult neural stem cells," *Biomaterials*, vol. 33, no. 12, pp. 3446–3455, 2012, ISSN: 0142-9612. DOI: `10.1016/j.biomaterials.2012.01.037`.

[88] J. Bystroňová, I. Ščigalková, L. Wolfová, M. Pravda, N. E. Vrana, and V. Velebný, "Creating a 3d microenvironment for monocyte cultivation: Ecm-mimicking hydrogels based on gelatine and hyaluronic acid derivatives," *RSC Advances*, vol. 8, no. 14, pp. 7606–7614, 2018. DOI: `10.1039/C7RA13739G`. [Online]. Available: `http://dx.doi.org/10.1039/C7RA13739G`.

[89] M. Shivashankar and B. K. Mandal, "A review on interpenetrating polymer network," *Int. J. Phram. Phram. Sci*, vol. 4, no. 5, pp. 1–7, 2012.

[90] G. Ahn, Y. Kim, S.-W. Lee, Y. Jeong, H. Son, and D. Lee, "Effect of heterogeneous multi-layered gelatin scaffolds on the diffusion characteristics and

cellular activities of preosteoblasts," *Macromolecular Research*, vol. 22, 2014. DOI: `10.1007/s13233-014-2024-y`.

[91] T. Riaz, R. Zeeshan, F. Zarif, K. Ilyas, N. Muhammad, S. Safi, A. Rahim, S. Rizvi, and I. Rehman, "Ftir analysis of natural and synthetic collagen," *Applied Spectroscopy Reviews*, vol. 53, pp. 703–746, 2018. DOI: `10.1080/05704928.2018.1426595`.

[92] S. Oliveira, B. C. da Silva, I. Riegel-Vidotti, A. Urbano, P. Faria Tischer, and C. Tischer, "Production and characterization of bacterial cellulose membranes with hyaluronic acid from chicken comb," *International Journal of Biological Macromolecules*, vol. 97, 2017. DOI: `10.1016/j.ijbiomac.2017.01.077`.

[93] M. Amer, F. Rose, L. White, and K. Shakesheff, "A detailed assessment of varying ejection rate on delivery efficiency of mesenchymal stem cells using narrow-bore needles," *Stem Cells Translational Medicine*, vol. 5, no. 3, pp. 366–378, 2016, ISSN: 2157-6564. DOI: `10.5966/sctm.2015-0208`.

[94] B. Wahlberg, H. Ghuman, J. Liu, and M. Modo, "Ex vivo biomechanical characterization of syringe-needle ejections for intracerebral cell delivery," *Scientific Reports*, vol. 8, 2018, ISSN: 2045-2322. DOI: `10.1038/s41598-018-27568-x`.

[95] B. Angenieux, D. F. Schorderet, and Y. Arsenijevic, "Epidermal growth factor is a neuronal differentiation factor for retinal stem cells in vitro," *Stem Cells*, vol. 24, no. 3, pp. 696–706, 2006, ISSN: 1066-5099.

[96] Q. Chai, Y. Jiao, and X. Yu, "Hydrogels for biomedical applications: Their characteristics and the mechanisms behind them," *Gels*, vol. 3, no. 1, p. 6, 2017.

[97] W. Pan, B. Caswell, and G. Karniadakis, "A low-dimensional model for the red blood cell," *Soft Matter*, vol. 6, no. 18, pp. 4366–4376, 2010, ISSN: 1744-683X. DOI: `10.1039/c0sm00183j`.

[98] S. P. Sutera and R. Skalak, "The history of poiseuille's law," *Annual Review of Fluid Mechanics*, vol. 25, no. 1, pp. 1–20, 1993.

[99] K. B. Chandran, S. E. Rittgers, and A. P. Yoganathan, *Biofluid mechanics : the human circulation*, 2nd. Boca Raton: CRC Press, Taylor& Francis Group, 2012, xx, 431 pages, ISBN: 9781439845165. [Online]. Available: `https://www.taylorfrancis.com/books/9781439845189`.

[100] K. Hutter and K. Jöhnk, *Continuum methods of physical modeling: continuum mechanics, dimensional analysis, turbulence*. Springer Science& Business Media, 2013, ISBN: 3662064022.

[101] N. Guz, M. Dokukin, V. Kalaparthi, and I. Sokolov, "If cell mechanics can be described by elastic modulus: Study of different models and probes used in indentation experiments," *Biophysical Journal*, vol. 107, no. 3, pp. 564–575, 2014, ISSN: 0006-3495. DOI: `10.1016/j.bpj.2014.06.033`.

[102] M. H. Cohen and D. Turnbull, "Molecular transport in liquids and glasses," *The Journal of Chemical Physics*, vol. 31, no. 5, pp. 1164–1169, 1959, ISSN: 0021-9606.

[103] H. Yasuda, A. Peterlin, C. Colton, K. Smith, and E. Merrill, "Permeability of solutes through hydrated polymer membranes. part iii. theoretical background for the selectivity of dialysis membranes," *Die Makromolekulare Chemie: Macromolecular Chemistry and Physics*, vol. 126, no. 1, pp. 177–186, 1969, ISSN: 0025-116X.

[104] N. A. Peppas and C. T. Reinhart, "Solute diffusion in swollen membranes. part i. a new theory," *Journal of membrane science*, vol. 15, no. 3, pp. 275–287, 1983, ISSN: 0376-7388.

[105] J. T. Edward, "Molecular volumes and the stokes-einstein equation," *Journal of Chemical Education*, vol. 47, no. 4, p. 261, 1970, ISSN: 0021-9584.

[106] R. Cukier, "Diffusion of brownian spheres in semidilute polymer solutions," *Macromolecules*, vol. 17, no. 2, pp. 252–255, 1984, ISSN: 0024-9297.

[107] A. R. Altenberger, M. Tirrell, and J. S. Dahler, "Hydrodynamic screening and particle dynamics in porous media, semidilute polymer solutions and polymer gels," *The Journal of chemical physics*, vol. 84, no. 9, pp. 5122–5130, 1986, ISSN: 0021-9606.

[108] L. Johansson, U. Skantze, and J. E. Loefroth, "Diffusion and interaction in gels and solutions. 2. experimental results on the obstruction effect," *Macromolecules*, vol. 24, no. 22, pp. 6019–6023, 1991, ISSN: 0024-9297.

[109] A. Ogston, "The spaces in a uniform random suspension of fibres," *Transactions of the Faraday Society*, vol. 54, pp. 1754–1757, 1958.

[110] L. Johansson and J.-E. Löfroth, "Diffusion and interaction in gels and solutions. 4. hard sphere brownian dynamics simulations," *The Journal of chemical physics*, vol. 98, no. 9, pp. 7471–7479, 1993, ISSN: 0021-9606.

[111] U. Aftab, C. Jiang, B. Tucker, J. Kim, H. Klassen, E. Miljan, J. Sinden, and M. Young, "Growth kinetics and transplantation of human retinal progenitor cells," *Experimental Eye Research*, vol. 89, no. 3, pp. 301–310, 2009, ISSN: 0014-4835. DOI: `10.1016/j.exer.2009.03.025`.

[112] L. Wang, J. Chung, P. Chan, and M. Kurisawa, "Injectable biodegradable hydrogels with tunable mechanical properties for the stimulation of neurogenesic differentiation of human mesenchymal stem cells in 3d culture," *Biomaterials*, vol. 31, no. 6, pp. 1148–1157, 2010, ISSN: 0142-9612. DOI: `10.1016/j.biomaterials.2009.10.042`.

[113] L. Pham, L. H. Dang, M. D. Truong, T. H. Nguyen, L. Le, V. T. Le, N. D. Nam, L. G. Bach, V. T. Nguyen, and N. Q. Tran, "A dual synergistic of curcumin and gelatin on thermal-responsive hydrogel based on chitosan-p123 in wound healing application," *Biomedicine& Pharmacotherapy*, vol. 117, p. 109 183, 2019, ISSN: 0753-3322. DOI: `https://doi.org/10.1016/j.biopha.2019.109183`. [Online]. Available: `http://www.sciencedirect.com/science/article/pii/S0753332219319171`.

[114] P. Yang, M. J. Seiler, R. B. Aramant, and S. R. Whittemore, “In vitro isolation and expansion of human retinal progenitor cells,” *Experimental Neurology*, vol. 177, no. 1, pp. 326–331, 2002, ISSN: 0014-4886. DOI: `https://doi.org/10.1006/exnr.2002.7955`. [Online]. Available: `http://www.sciencedirect.com/science/article/pii/S0014488602979550`.

[115] C. Yongming, K. Biddell, S. Aiying, P. A. Relue, and J. D. Johnson, “An automatic cell counting method for optical images,” in *Proceedings of the First Joint BMES/EMBS Conference. 1999 IEEE Engineering in Medicine and Biology 21st Annual Conference and the 1999 Annual Fall Meeting of the Biomedical Engineering Society (Cat. N*, vol. 2, 819 vol.2. DOI: `10.1109/IEMBS.1999.803974`.

[116] F. Lee, K. H. Bae, and M. Kurisawa, “Injectable hydrogel systems crosslinked by horseradish peroxidase,” *Biomedical Materials*, vol. 11, no. 1, p. 014 101, 2015, ISSN: 1748-605X. DOI: `10.1088/1748-6041/11/1/014101`. [Online]. Available: `http://dx.doi.org/10.1088/1748-6041/11/1/014101`.

[117] W. L. Grayson, F. Zhao, B. Bunnell, and T. Ma, “Hypoxia enhances proliferation and tissue formation of human mesenchymal stem cells,” *Biochem Biophys Res Commun*, vol. 358, no. 3, pp. 948–53, 2007, ISSN: 0006-291X (Print) 0006-291X (Linking). DOI: `10.1016/j.bbrc.2007.05.054`. [Online]. Available: `https://www.ncbi.nlm.nih.gov/pubmed/17521616`.

[118] M. Semo, N. Haamedi, L. Stevanato, D. Carter, G. Brooke, M. Young, P. Coffey, J. Sinden, S. Patel, and A. Vugler, “Efficacy and safety of human retinal progenitor cells,” *Transl Vis Sci Technol*, vol. 5, no. 4, p. 6, 2016, ISSN: 2164-2591. DOI: `10.1167/tvst.5.4.6`. [Online]. Available: `https://www.ncbi.nlm.nih.gov/pubmed/27486556`.

[119] X. Deng, D. Zhu, C. Spee, and D. R. Hinton, “A 3d co-culture system facilitates photoreceptor-like differentiation of human retinal progenitor cells,” *Investigative Ophthalmology & Visual Science*, vol. 51, no. 13, pp. 5950–5950, 2010, ISSN: 1552-5783.

[120] N. C. Hunt, D. Hallam, A. Karimi, C. B. Mellough, J. Chen, D. H. W. Steel, and M. Lako, "3d culture of human pluripotent stem cells in rgd-alginate hydrogel improves retinal tissue development," *Acta Biomaterialia*, vol. 49, pp. 329–343, 2017, ISSN: 1742-7061. DOI: `https://doi.org/10.1016/j.actbio.2016.11.016`. [Online]. Available: `http://www.sciencedirect.com/science/article/pii/S1742706116306031`.

[121] M. Missaire and R. Hindges, "The role of cell adhesion molecules in visual circuit formation: From neurite outgrowth to maps and synaptic specificity," *Developmental neurobiology*, vol. 75, no. 6, pp. 569–583, 2015, ISSN: 1932-846X 1932-8451. DOI: `10.1002/dneu.22267`. [Online]. Available: `https://www.ncbi.nlm.nih.gov/pmc/articles/PMC4855686/`.

[122] E. Vecino, J. P. Heller, P. Veiga-Crespo, K. R. Martin, and J. W. Fawcett, "Influence of extracellular matrix components on the expression of integrins and regeneration of adult retinal ganglion cells," *PloS one*, vol. 10, no. 5, e0125250–e0125250, 2015, ISSN: 1932-6203. DOI: `10.1371/journal.pone.0125250`. [Online]. Available: `https://www.ncbi.nlm.nih.gov/pmc/articles/PMC4446304/`.

[123] Y. Cai, X. Dai, Q. Zhang, and Z. Dai, "Gene expression of oct4, sox2, klf4 and myc (oskm) induced pluripotent stem cells: Identification for potential mechanisms," *Diagnostic pathology*, vol. 10, pp. 35–35, 2015, ISSN: 1746-1596. DOI: `10.1186/s13000-015-0263-7`. [Online]. Available: `https://www.ncbi.nlm.nih.gov/pmc/articles/PMC4414430/`.

[124] N. D. Leipzig and M. S. Shoichet, "The effect of substrate stiffness on adult neural stem cell behavior," *Biomaterials*, vol. 30, no. 36, pp. 6867–6878, 2009, ISSN: 0142-9612.

[125] T. Marquardt, R. Ashery-Padan, N. Andrejewski, R. Scardigli, F. Guillemot, and P. Gruss, "Pax6 is required for the multipotent state of retinal progenitor cells," *Cell*, vol. 105, no. 1, pp. 43–55, 2001, ISSN: 0092-8674.

[126] T. Instruments, *Thermal analysis to determine various forms of water present in hydrogels*, Generic, 2020.

[127] X. N. Zhang, Y. J. Wang, S. Sun, L. Hou, P. Wu, Z. L. Wu, and Q. Zheng, "A tough and stiff hydrogel with tunable water content and mechanical properties based on the synergistic effect of hydrogen bonding and hydrophobic interaction," *Macromolecules*, vol. 51, no. 20, pp. 8136–8146, 2018, ISSN: 0024-9297.

[128] B. Amsden, "Solute diffusion within hydrogels. mechanisms and models," *Macromolecules*, vol. 31, no. 23, pp. 8382–8395, 1998, ISSN: 0024-9297.

[129] J. Zhu and R. E. Marchant, "Design properties of hydrogel tissue-engineering scaffolds," *Expert review of medical devices*, vol. 8, no. 5, pp. 607–626, 2011, ISSN: 1743-4440.

[130] F. Cilurzo, F. Selmin, P. Minghetti, M. Adami, E. Bertoni, S. Lauria, and L. Montanari, "Injectability evaluation: An open issue," *AAPS PharmSciTech*, vol. 12, no. 2, pp. 604–609, 2011, ISSN: 1530-9932. DOI: `10.1208/s12249-011-9625-y`. [Online]. Available: `https://www.ncbi.nlm.nih.gov/pmc/articles/PMC3134656/`.

[131] D. W. Thompson, "Fluid mechanics and transfer processes, j. m. kay and r. m. nedderman, 1985, 602 pages. published by cambridge university press, 69.50 us (hardcover), 29.95 us (paperback)," *The Canadian Journal of Chemical Engineering*, vol. 65, no. 3, pp. 526–527, 1987, ISSN: 0008-4034. DOI: `10.1002/cjce.5450650328`. [Online]. Available: `https://onlinelibrary.wiley.com/doi/abs/10.1002/cjce.5450650328`.

[132] B. Patrick H., B. Andrea, Z. Huaying, E. Christine, and S. Peter, *Density and viscosity values measured for PBS solutions containing different fractions of H₂¹⁸O*. 2013. DOI: `10.1371/journal.pone.0026221.t001`. [Online]. Available: `https://plos.figshare.com/articles/%5C_Density%5C_and%5C_viscosity%5C_values%5C_measured%5C_for%5C_PBS%5C_solutions%5C_containing%5C_different%5C_fractions%5C_of%5C_H%5C_2%5C_18%5C_O%5C_/392982`.

[133] J. Chao, "Chapter 624 - mouse kallikrein 9, epidermal growth factor-binding protein," in *Handbook of Proteolytic Enzymes (Third Edition)*, N. D. Rawlings and G. Salvesen, Eds. Academic Press, 2013, pp. 2830–2831, ISBN: 978-0-12-382219-2. DOI: `https://doi.org/10.1016/B978-0-12-382219-2.00624-4`. [Online]. Available: `http://www.sciencedirect.com/science/article/pii/B9780123822192006244`.

[134] C. R. White and J. A. Frangos, "The shear stress of it all: The cell membrane and mechanochemical transduction," *Philosophical transactions of the Royal Society of London. Series B, Biological sciences*, vol. 362, no. 1484, pp. 1459–1467, 2007, ISSN: 0962-8436 1471-2970. DOI: `10.1098/rstb.2007.2128`. [Online]. Available: `https://www.ncbi.nlm.nih.gov/pmc/articles/PMC2440408/`.

[135] D. M. Schonk, H. J. Kuijpers, E. van Drunen, C. H. van Dalen, A. H. Geurts van Kessel, R. Verheijen, and F. C. Ramaekers, "Assignment of the gene(s) involved in the expression of the proliferation-related ki-67 antigen to human chromosome 10," *Hum Genet*, vol. 83, no. 3, pp. 297–9, 1989, ISSN: 0340-6717. DOI: `10.1007/bf00285178`. [Online]. Available: `https://www.ncbi.nlm.nih.gov/pubmed/2571566`.

[136] S. Elmore, "Apoptosis: A review of programmed cell death," *Toxicologic pathology*, vol. 35, no. 4, pp. 495–516, 2007, ISSN: 0192-6233 1533-1601. DOI: `10.1080/01926230701320337`. [Online]. Available: `https://www.ncbi.nlm.nih.gov/pmc/articles/PMC2117903/`.

[137] P. Li, D. Nijhawan, I. Budihardjo, S. M. Srinivasula, M. Ahmad, E. S. Alnemri, and X. Wang, "Cytochrome c and datp-dependent formation of apaf-1/caspase-9 complex initiates an apoptotic protease cascade," *Cell*, vol. 91, no. 4, pp. 479–489, 1997, ISSN: 0092-8674. DOI: `10.1016/S0092-8674(00)80434-1`. [Online]. Available: `https://doi.org/10.1016/S0092-8674(00)80434-1`.

[138] X. Zhu, B. Brown, A. Li, A. J. Mears, A. Swaroop, and C. M. Craft, "Grk1-dependent phosphorylation of s and m opsins and their binding to cone arrestin

during cone phototransduction in the mouse retina," *Journal of Neuroscience*, vol. 23, no. 14, pp. 6152–6160, 2003, ISSN: 0270-6474.

[139] M. Al-Ubaidi, M. Naash, and S. Conley, "A perspective on the role of the extracellular matrix in progressive retinal degenerative disorders," *Investigative Ophthalmology & Visual Science*, vol. 54, no. 13, pp. 8119–8124, 2013, ISSN: 0146-0404. DOI: `10.1167/iovs.13-13536`.

[140] N. Davidenko, C. Schuster, D. Bax, R. Farndale, S. Hamaia, S. Best, and R. Cameron, "Evaluation of cell binding to collagen and gelatin: A study of the effect of 2d and 3d architecture and surface chemistry (vol 27, 148, 2016)," *Journal of Materials Science-Materials in Medicine*, vol. 29, no. 4, 2018, ISSN: 0957-4530. DOI: `10.1007/s10856-018-6047-3`.

[141] K. E. Kador and J. L. Goldberg, "Scaffolds and stem cells: Delivery of cell transplants for retinal degenerations," *Expert Review of Ophthalmology*, vol. 7, no. 5, pp. 459–470, 2012. [Online]. Available: `https://doi.org/10.1586/eop.12.56`.

[142] S. Levenberg, N. Huang, E. Lavik, A. Rogers, J. Itskovitz-Eldor, and R. Langer, "Differentiation of human embryonic stem cells on three-dimensional polymer scaffolds," *Proceedings of the National Academy of Sciences of the United States of America*, vol. 100, no. 22, pp. 12 741–12 746, 2003, ISSN: 0027-8424. DOI: `10.1073/pnas.1735463100`.

[143] H. Kurazumi, M. Kubo, M. Ohshima, Y. Yamamoto, Y. Takemoto, R. Suzuki, S. Ikenaga, A. Mikamo, K. Udo, K. Hamano, and T. Li, "The effects of mechanical stress on the growth, differentiation, and paracrine factor production of cardiac stem cells," *Plos One*, vol. 6, no. 12, 2011, ISSN: 1932-6203. DOI: `10.1371/journal.pone.0028890`.

[144] K. Boochoon, J. Manarang, J. Davis, A. McDermott, and W. Foster, "The influence of substrate elastic modulus on retinal pigment epithelial cell phagocytosis," *Journal of Biomechanics*, vol. 47, no. 12, pp. 3237–3240, 2014, ISSN: 0021-9290. DOI: `10.1016/j.jbiomech.2014.06.021`.

[145] S. R. Hynes and E. B. Lavik, "A tissue-engineered approach towards retinal repair: Scaffolds for cell transplantation to the subretinal space," *Graefe's Archive for Clinical and Experimental Ophthalmology*, vol. 248, no. 6, pp. 763–778, 2010, ISSN: 0721-832X.

[146] A. R. Khare and N. A. Peppas, "Investigation of hydrogel water in polyelectrolyte gels using differential scanning calorimetry," *Polymer*, vol. 34, no. 22, pp. 4736–4739, 1993, ISSN: 0032-3861.

[147] S. Nakagawa, S. Takada, R. Takada, and M. Takeichi, "Identification of the laminar-inducing factor: Wnt-signal from the anterior rim induces correct laminar formation of the neural retina in vitro," *Dev Biol*, vol. 260, no. 2, pp. 414–25, 2003, ISSN: 0012-1606 (Print) 0012-1606 (Linking). [Online]. Available: `https://www.ncbi.nlm.nih.gov/pubmed/12921742`.

[148] P. Baranov, B. Tucker, and M. Young, "Low-oxygen culture conditions extend the multipotent properties of human retinal progenitor cells," *Tissue Engineering Part a*, vol. 20, no. 9-10, pp. 1465–1475, 2014, ISSN: 1937-3341. DOI: `10.1089/ten.tea.2013.0361`.

[149] K. Pramanik, "Biomaterials for tissue engineered scaffolds," *2010 Advanced Technologies For Enhancing Quality of Life (At-Equal)*, pp. 93–99, 2010. DOI: `10.1109/ATEQUAL.2010.7`.

[150] H. Klassen, B. Ziaeian, I. I. Kirov, M. J. Young, and P. H. Schwartz, "Isolation of retinal progenitor cells from post-mortem human tissue and comparison with autologous brain progenitors," *Journal of Neuroscience Research*, vol. 77, no. 3, pp. 334–343, 2004, ISSN: 0360-4012. DOI: `10.1002/jnr.20183`. [Online]. Available: `https://onlinelibrary.wiley.com/doi/abs/10.1002/jnr.20183`.

[151] S. Schmitt, U. Aftab, C. Jiang, S. Redenti, H. Klassen, E. Miljan, J. Sinden, and M. Young, "Molecular characterization of human retinal progenitor cells," *Investigative Ophthalmology & Visual Science*, vol. 50, no. 12, pp. 5901–5908,

2009, ISSN: 1552-5783. DOI: `10.1167/iovs.08-3067`. [Online]. Available: `https://doi.org/10.1167/iovs.08-3067`.

[152] A. Vugler, A. J. Carr, J. Lawrence, L. L. Chen, K. Burrell, A. Wright, P. Lundh, M. Semo, A. Ahmado, C. Gias, L. da Cruz, H. Moore, P. Andrews, J. Walsh, and P. Coffey, "Elucidating the phenomenon of hesc-derived rpe: Anatomy of cell genesis, expansion and retinal transplantation," *Exp Neurol*, vol. 214, no. 2, pp. 347–61, 2008, ISSN: 1090-2430 (Electronic) 0014-4886 (Linking). DOI: `10.1016/j.expneurol.2008.09.007`. [Online]. Available: `https://www.ncbi.nlm.nih.gov/pubmed/18926821`.

[153] C. Mas-Bargues, J. Sanz-Ros, A. Román-Domínguez, M. Inglés, L. Gimeno-Mallench, M. El Alami, J. Viña-Almunia, J. Gambini, J. Viña, and C. Borrás, "Relevance of oxygen concentration in stem cell culture for regenerative medicine," *International journal of molecular sciences*, vol. 20, no. 5, p. 1195, 2019, ISSN: 1422-0067. DOI: `10.3390/ijms20051195`. [Online]. Available: `https://www.ncbi.nlm.nih.gov/pmc/articles/PMC6429522/`.

[154] R. E. Ferner, "Neurofibromatosis 1 and neurofibromatosis 2: A twenty first century perspective," *The Lancet Neurology*, vol. 6, no. 4, pp. 340–351, 2007, ISSN: 1474-4422.

[155] D. B. Zimmer and L. J. Van Eldik, "Analysis of the calcium-modulated proteins, s100 and calmodulin, and their target proteins during c6 glioma cell differentiation," *The Journal of cell biology*, vol. 108, no. 1, pp. 141–151, 1989, ISSN: 0021-9525.

[156] D. Giakoumettis, A. Kritis, and N. Foroglou, "C6 cell line: The gold standard in glioma research," *Hippokratia*, vol. 22, no. 3, pp. 105–112, 2018, ISSN: 1108-4189 1790-8019. [Online]. Available: `https://www.ncbi.nlm.nih.gov/pmc/articles/PMC6801124/`.

[157] D. Liu and J. Yu, "Otsu method and k-means," in *2009 Ninth International Conference on Hybrid Intelligent Systems*, vol. 1, IEEE, pp. 344–349, ISBN: 0769537456.

[158] D. Singh, P. C. Dromel, and M. Young, “Low-oxygen and knock-out serum maintain stemness in human retinal progenitor cells,” *Molecular Biology Reports*, 2020, ISSN: 1573-4978. DOI: `10.1007/s11033-020-05248-2`. [Online]. Available: `https://doi.org/10.1007/s11033-020-05248-2`.

[159] D. Singh, P. C. Dromel, T. Perepelkina, P. Baranov, and M. Young, “C6 cell injection into the optic nerve of long-evans rats: A short-term model of optic pathway gliomas,” *Cell Transplantation*, vol. 29, p. 0 963 689 720 964 383, 2020, ISSN: 0963-6897.

[160] I. S. Trowbridge and M. L. Thomas, “Cd45: An emerging role as a protein tyrosine phosphatase required for lymphocyte activation and development,” *Annual review of immunology*, vol. 12, no. 1, pp. 85–116, 1994, ISSN: 0732-0582.

[161] Q. T. Ostrom, H. Gittleman, P. Liao, T. Vecchione-Koval, Y. Wolinsky, C. Kruchko, and J. S. Barnholtz-Sloan, “Cbtrus statistical report: Primary brain and other central nervous system tumors diagnosed in the united states in 2010–2014,” *Neuro-Oncology*, vol. 19, no. suppl_5, pp. v1–v88, 2017, ISSN: 1522-8517. DOI: `10.1093/neuonc/nox158`. [Online]. Available: `https://doi.org/10.1093/neuonc/nox158`.

[162] N. Nagano, H. Sasaki, M. Aoyagi, and K. Hirakawa, “Invasion of experimental rat brain tumor: Early morphological changes following microinjection of c6 glioma cells,” *Acta neuropathologica*, vol. 86, no. 2, pp. 117–125, 1993, ISSN: 0001-6322.

[163] M. Peoc’h, G. D. Le, A. Trayaud, R. Farion, J. B. Le, B. Pasquier, and C. Remy, “Quantification and distribution of neovascularization following microinjection of c6 glioma cells in rat brain,” *Anticancer research*, vol. 19, no. 4B, pp. 3025–3030, 1999, ISSN: 0250-7005.

[164] C. L. Shields, J. A. Shields, K. Baez, J. R. Cater, and P. de Potter, “Optic nerve invasion of retinoblastoma. metastatic potential and clinical risk factors,” *Cancer*, vol. 73, no. 3, pp. 692–698, 1994, ISSN: 0008-543X.

[165] S. Ekmark-Lewén, A. Lewén, C. Israelsson, G. L. Li, M. Farooque, Y. Olsson, T. Ebendal, and L. Hillered, "Vimentin and gfap responses in astrocytes after contusion trauma to the murine brain," *Restorative neurology and neuroscience*, vol. 28, no. 3, pp. 311–321, 2010, ISSN: 0922-6028.

[166] J. Campisi, "Aging, cellular senescence, and cancer," *Annu Rev Physiol*, vol. 75, pp. 685–705, 2013, ISSN: 1545-1585 (Electronic) 0066-4278 (Linking). DOI: `10.1146/annurev-physiol-030212-183653`. [Online]. Available: `https://www.ncbi.nlm.nih.gov/pubmed/23140366`.

[167] H. Rubin, "Intracellular free mg(2+) and mgatp(2-) in coordinate control of protein synthesis and cell proliferation," in *Magnesium in the Central Nervous System*, R. Vink and M. Nechifor, Eds. Adelaide (AU), 2011, ISBN: 9780987073051. [Online]. Available: `https://www.ncbi.nlm.nih.gov/pubmed/29920017`.

[168] F. Wang, V. Zachar, C. P. Pennisi, T. Fink, Y. Maeda, and J. Emmersen, "Hypoxia enhances differentiation of adipose tissue-derived stem cells toward the smooth muscle phenotype," *Int J Mol Sci*, vol. 19, no. 2, 2018, ISSN: 1422-0067 (Electronic) 1422-0067 (Linking). DOI: `10.3390/ijms19020517`. [Online]. Available: `https://www.ncbi.nlm.nih.gov/pubmed/29419805`.

[169] C. Hadjimichael, K. Chanoumidou, N. Papadopoulou, P. Arampatzi, J. Papamatheakis, and A. Kretsovali, "Common stemness regulators of embryonic and cancer stem cells," *World journal of stem cells*, vol. 7, no. 9, pp. 1150–1184, 2015, ISSN: 1948-0210. DOI: `10.4252/wjsc.v7.i9.1150`. [Online]. Available: `https://www.ncbi.nlm.nih.gov/pmc/articles/PMC4620423/`.

[170] H. Abdollahi, L. J. Harris, P. Zhang, S. McIlhenny, V. Srinivas, T. Tulenko, and P. J. DiMuzio, "The role of hypoxia in stem cell differentiation and therapeutics," *J Surg Res*, vol. 165, no. 1, pp. 112–7, 2011, ISSN: 1095-8673 (Electronic) 0022-4804 (Linking). DOI: `10.1016/j.jss.2009.09.057`. [Online]. Available: `https://www.ncbi.nlm.nih.gov/pubmed/20080246`.

[171] M. V. Gustafsson, X. Zheng, T. Pereira, K. Gradin, S. Jin, J. Lundkvist, J. L. Ruas, L. Poellinger, U. Lendahl, and M. Bondesson, “Hypoxia requires notch signaling to maintain the undifferentiated cell state,” *Developmental cell*, vol. 9, no. 5, pp. 617–628, 2005, ISSN: 1534-5807.

[172] R. P. Hill, D. T. Marie-Egyptienne, and D. W. Hedley, “Cancer stem cells, hypoxia and metastasis,” in *Seminars in radiation oncology*, vol. 19, Elsevier, pp. 106–111.

[173] J. Wanek, P. Y. Teng, N. P. Blair, and M. Shahidi, “Inner retinal oxygen delivery and metabolism under normoxia and hypoxia in rat,” *Invest Ophthalmol Vis Sci*, vol. 54, no. 7, pp. 5012–9, 2013, ISSN: 1552-5783 (Electronic) 0146-0404 (Linking). DOI: `10.1167/iovs.13-11887`. [Online]. Available: `https://www.ncbi.nlm.nih.gov/pubmed/23821203`.

[174] G. B. Arden, R. L. Sidman, W. Arap, and R. O. Schlingemann, “Spare the rod and spoil the eye,” *Br J Ophthalmol*, vol. 89, no. 6, pp. 764–9, 2005, ISSN: 0007-1161 (Print) 0007-1161 (Linking). DOI: `10.1136/bjo.2004.062547`. [Online]. Available: `https://www.ncbi.nlm.nih.gov/pubmed/15923516`.

[175] T. S. Kern and B. A. Berkowitz, “Photoreceptors in diabetic retinopathy,” *J Diabetes Investig*, vol. 6, no. 4, pp. 371–80, 2015, ISSN: 2040-1116 (Print) 2040-1116 (Linking). DOI: `10.1111/jdi.12312`. [Online]. Available: `https://www.ncbi.nlm.nih.gov/pubmed/26221514`.

[176] R. D. Braun, R. A. Linsenmeier, and T. K. Goldstick, “Oxygen consumption in the inner and outer retina of the cat,” *Invest Ophthalmol Vis Sci*, vol. 36, no. 3, pp. 542–54, 1995, ISSN: 0146-0404 (Print) 0146-0404 (Linking). [Online]. Available: `https://www.ncbi.nlm.nih.gov/pubmed/7890485`.

[177] M. K. Lin, S. H. Kim, L. Zhang, Y. T. Tsai, and S. H. Tsang, “Rod metabolic demand drives progression in retinopathies,” *Taiwan J Ophthalmol*, vol. 5, no. 3, pp. 105–108, 2015, ISSN: 2211-5056 (Print) 2211-5056 (Linking). DOI: `10.1016/j.tjo.2015.06.002`. [Online]. Available: `https://www.ncbi.nlm.nih.gov/pubmed/29018679`.

[178] B. S. Winkler, M. E. Boulton, J. D. Gottsch, and P. Sternberg, "Oxidative damage and age-related macular degeneration," *Molecular vision*, vol. 5, p. 32, 1999.

[179] P. Baranov, G. Brooke, S. Patel, M. Young, and J. Sinden, "Human retinal progenitor cells as a tool for retinal repair: Establishing cell lines for clinical study," *Investigative Ophthalmology & Visual Science*, vol. 54, no. 15, 2013, ISSN: 0146-0404.

[180] P. Tsonis and K. Del Rio-Tsonis, "Lens and retina regeneration: Transdifferentiation, stem cells and clinical applications," *Experimental Eye Research*, vol. 78, no. 2, pp. 161–172, 2004, ISSN: 0014-4835. DOI: `10.1016/j.exer.2003.10.022`.

[181] K. Warfvinge, J. Kiilgaard, E. Lavik, E. Scherfig, R. Langer, H. Klassen, and M. Young, "Retinal progenitor cell xenografts to the pig retina - morphologic integration and cytochemical differentiation," *Archives of Ophthalmology*, vol. 123, no. 10, pp. 1385–1393, 2005, ISSN: 0003-9950. DOI: `10.1001/archopht.123.10.1385`.

[182] C. W. Little, B. Castillo, D. A. DiLoreto, C. Cox, J. Wyatt, C. Del Cerro, and M. Del Cerro, "Transplantation of human fetal retinal pigment epithelium rescues photoreceptor cells from degeneration in the royal college of surgeons rat retina," *Investigative ophthalmology & visual science*, vol. 37, no. 1, pp. 204–211, 1996, ISSN: 1552-5783.

[183] M. Spector and T. Lim, "Injectable biomaterials: A perspective on the next wave of injectable therapeutics," *Biomedical Materials*, vol. 11, no. 1, 2016, ISSN: 1748-6041. DOI: `10.1088/1748-6041/11/1/014110`.

[184] Y. Liu, R. Wang, T. Zarembinski, N. Doty, C. Jiang, C. Regatieri, X. Zhang, and M. Young, "The application of hyaluronic acid hydrogels to retinal progenitor cell transplantation," *Tissue Engineering Part a*, vol. 19, no. 1-2, pp. 135–142, 2013, ISSN: 1937-3341. DOI: `10.1089/ten.tea.2012.0209`.

[185] C. Behl, J. Davis, R. Lesley, and D. Schubert, “Hydrogen peroxide mediates amyloid beta protein toxicity,” *Cell*, vol. 77, no. 6, pp. 817–827, 1994, ISSN: 0092-8674.

[186] R. DESIKAN, A. REYNOLDS, T. J. HANCOCK, and J. S. NEILL, “Harpin and hydrogen peroxide both initiate programmed cell death but have differential effects on defence gene expression in arabidopsis suspension cultures,” *Biochemical Journal*, vol. 330, no. 1, pp. 115–120, 1998, ISSN: 0264-6021.

[187] T. Xia, W. Liu, and L. Yang, “A review of gradient stiffness hydrogels used in tissue engineering and regenerative medicine,” *Journal of Biomedical Materials Research Part A*, vol. 105, no. 6, pp. 1799–1812, 2017, ISSN: 1549-3296.

[188] F. Giordano, A. De Marzo, F. Vetrini, and V. Marigo, “Fgf and egf differently affect differentiation of murine retinal stem cells in vitro,” 2007.

[189] K. Gregory-Evans, F. Chang, M. D. Hodges, and C. Y. Gregory-Evans, “Ex vivo gene therapy using intravitreal injection of gdnf-secreting mouse embryonic stem cells in a rat model of retinal degeneration,” *Molecular vision*, vol. 15, p. 962, 2009.

[190] G. Q. Daley and D. T. Scadden, “Prospects for stem cell-based therapy,” *Cell*, vol. 132, no. 4, pp. 544–548, 2008, ISSN: 0092-8674.

[191] R. Singh, O. Cuzzani, F. Binette, H. Sternberg, M. D. West, and I. O. Nasonkin, “Pluripotent stem cells for retinal tissue engineering: Current status and future prospects,” *Stem cell reviews and reports*, vol. 14, no. 4, pp. 463–483, 2018, ISSN: 2629-3277 1550-8943. DOI: `10.1007/s12015-018-9802-4`. [Online]. Available: `https://www.ncbi.nlm.nih.gov/pmc/articles/PMC6013538/`.

[192] S. Murikipudi, H. Methe, and E. R. Edelman, “The effect of substrate modulus on the growth and function of matrix-embedded endothelial cells,” *Biomaterials*, vol. 34, no. 3, pp. 677–684, 2013, ISSN: 1878-5905 0142-9612. DOI: `10.1016/j.biomaterials.2012.09.079`. [Online]. Available: `https://www.ncbi.nlm.nih.gov/pmc/articles/PMC3505450/`.

[193] R. R. Bourne, H. R. Taylor, S. R. Flaxman, J. Keeffe, J. Leasher, K. Naidoo, K. Pesudovs, R. A. White, T. Y. Wong, S. Resnikoff, J. B. Jonas, and S. Vision Loss Expert Group of the Global Burden of Disease, "Number of people blind or visually impaired by glaucoma worldwide and in world regions 1990 - 2010: A meta-analysis," *PLoS One*, vol. 11, no. 10, e0162229, 2016, ISSN: 1932-6203 (Electronic) 1932-6203 (Linking). DOI: `10.1371/journal.pone.0162229`. [Online]. Available: `https://www.ncbi.nlm.nih.gov/pubmed/27764086`.

[194] S. Becker, K. Eastlake, H. Jayaram, M. F. Jones, R. A. Brown, G. J. McLellan, D. G. Charteris, P. T. Khaw, and G. A. Limb, "Allogeneic transplantation of muller-derived retinal ganglion cells improves retinal function in a feline model of ganglion cell depletion," *Stem Cells Transl Med*, vol. 5, no. 2, pp. 192–205, 2016, ISSN: 2157-6564 (Print) 2157-6564 (Linking). DOI: `10.5966/sctm.2015-0125`. [Online]. Available: `https://www.ncbi.nlm.nih.gov/pubmed/26718648`.

[195] A. M. Miltner and A. La Torre, "Retinal ganglion cell replacement: Current status and challenges ahead," *Dev Dyn*, vol. 248, no. 1, pp. 118–128, 2019, ISSN: 1097-0177 (Electronic) 1058-8388 (Linking). DOI: `10.1002/dvdy.24672`. [Online]. Available: `https://www.ncbi.nlm.nih.gov/pubmed/30242792`.

[196] O. Rabesandratana, A. Chaffiol, A. Mialot, A. Slembrouck-Brec, C. Joffrois, C. Nanteau, A. Rodrigues, G. Gagliardi, S. Reichman, J.-A. Sahel, A. Chédotal, J. Duebel, O. Goureau, and G. Orieux, "Generation of a transplantable population of human ipsc-derived retinal ganglion cells," *Frontiers in Cell and Developmental Biology*, vol. 8, no. 1129, 2020, ISSN: 2296-634X. DOI: `10.3389/fcell.2020.585675`. [Online]. Available: `https://www.frontiersin.org/article/10.3389/fcell.2020.585675`.

[197] Y. Liu and R. K. Lee, "Cell transplantation to replace retinal ganglion cells faces challenges - the switchboard dilemma," *Neural Regen Res*, vol. 16, no. 6, pp. 1138–1143, 2021, ISSN: 1673-5374 (Print) 1673-5374 (Linking). DOI: `10.`

4103/1673-5374.300329. [Online]. Available: https://www.ncbi.nlm.nih.gov/pubmed/33269762.

[198] F. Lee, J. E. Chung, and M. Kurisawa, "An injectable hyaluronic acid–tyramine hydrogel system for protein delivery," *Journal of Controlled Release*, vol. 134, no. 3, pp. 186–193, 2009, ISSN: 0168-3659. DOI: https://doi.org/10.1016/j.jconrel.2008.11.028. [Online]. Available: http://www.sciencedirect.com/science/article/pii/S0168365908007773.

[199] J. P. Steimel, J. L. Aragones, H. Hu, N. Qureshi, and A. Alexander-Katz, "Emergent ultra–long-range interactions between active particles in hybrid active–inactive systems," *Proceedings of the National Academy of Sciences*, vol. 113, no. 17, p. 4652, 2016. DOI: 10.1073/pnas.1520481113. [Online]. Available: http://www.pnas.org/content/113/17/4652.abstract.

[200] M. L. Gardel, M. T. Valentine, and D. A. Weitz, "Microrheology," in *Microscale Diagnostic Techniques*, K. S. Breuer, Ed. Berlin, Heidelberg: Springer Berlin Heidelberg, 2005, pp. 1–49, ISBN: 978-3-540-26449-1. DOI: 10.1007/3-540-26449-3_1. [Online]. Available: https://doi.org/10.1007/3-540-26449-3%5C_1.

[201] V. M. Sluch, X. Chamling, M. M. Liu, C. A. Berlinicke, J. Cheng, K. L. Mitchell, D. S. Welsbie, and D. J. Zack, "Enhanced stem cell differentiation and immunopurification of genome engineered human retinal ganglion cells," *Stem cells translational medicine*, vol. 6, no. 11, pp. 1972–1986, 2017, ISSN: 2157-6564 2157-6580. DOI: 10.1002/sctm.17-0059. [Online]. Available: https://www.ncbi.nlm.nih.gov/pmc/articles/PMC6430043/.

[202] N. Otsu, "A threshold selection method from gray-level histograms," *IEEE Transactions on Systems, Man, and Cybernetics*, vol. 9, no. 1, pp. 62–66, 1979, ISSN: 2168-2909. DOI: 10.1109/TSMC.1979.4310076.

[203] M. Kreft, I. Milisav, M. Potokar, and R. Zorec, "Automated high through-put colocalization analysis of multichannel confocal images," *Computer Methods and Programs in Biomedicine*, vol. 74, no. 1, pp. 63–67, 2004, ISSN: 0169-

2607. DOI: `https://doi.org/10.1016/S0169-2607(03)00071-3`. [Online]. Available: `https://www.sciencedirect.com/science/article/pii/S0169260703000713`.

[204] I. Charles, A. Khalyfa, D. M. Kumar, R. R. Krishnamoorthy, R. S. Roque, N. Cooper, and N. Agarwal, "Serum deprivation induces apoptotic cell death of transformed rat retinal ganglion cells via mitochondrial signaling pathways," *Investigative ophthalmology & visual science*, vol. 46, no. 4, pp. 1330–1338, 2005, ISSN: 1552-5783.

[205] J. L. Goldberg, J. S. Espinosa, Y. Xu, N. Davidson, G. T. Kovacs, and B. A. Barres, "Retinal ganglion cells do not extend axons by default: Promotion by neurotrophic signaling and electrical activity," *Neuron*, vol. 33, no. 5, pp. 689–702, 2002, ISSN: 0896-6273.

[206] S. Heegaard, O. Jensen, and J. Prause, "Structure and composition of the inner limiting membrane of the retina," *Graefe's archive for clinical and experimental ophthalmology*, vol. 224, no. 4, pp. 355–360, 1986, ISSN: 1435-702X.

[207] T. C. Lim, E. Mandeville, D. Weng, L.-S. Wang, M. Kurisawa, K. Leite-Morris, M. H. Selim, E. H. Lo, and M. Spector, "Hydrogel-based therapy for brain repair after intracerebral hemorrhage," *Translational Stroke Research*, vol. 11, no. 3, pp. 412–417, 2020, ISSN: 1868-601X. DOI: `10.1007/s12975-019-00721-y`. [Online]. Available: `https://doi.org/10.1007/s12975-019-00721-y`.

[208] J. Danias, F. Shen, D. Goldblum, B. Chen, J. Ramos-Esteban, S. M. Podos, and T. Mittag, "Cytoarchitecture of the retinal ganglion cells in the rat," *Investigative Ophthalmology & Visual Science*, vol. 43, no. 3, pp. 587–594, 2002, ISSN: 1552-5783.

[209] H. A. Quigley, R. W. Nickells, L. A. Kerrigan, M. E. Pease, D. J. Thibault, and D. J. Zack, "Retinal ganglion cell death in experimental glaucoma and after axotomy occurs by apoptosis," *Investigative ophthalmology & visual science*, vol. 36, no. 5, pp. 774–786, 1995, ISSN: 1552-5783.

[210] R. L. Rockhill, F. J. Daly, M. A. MacNeil, S. P. Brown, and R. H. Masland, "The diversity of ganglion cells in a mammalian retina," *Journal of Neuroscience*, vol. 22, no. 9, pp. 3831–3843, 2002, ISSN: 0270-6474.

[211] H. Xu, M. Chen, E. J. Mayer, J. V. Forrester, and A. D. Dick, "Turnover of resident retinal microglia in the normal adult mouse," *Glia*, vol. 55, no. 11, pp. 1189–1198, 2007, ISSN: 0894-1491. DOI: `https://doi.org/10.1002/glia.20535`. [Online]. Available: `https://doi.org/10.1002/glia.20535`.

[212] S. Becker, K. Eastlake, H. Jayaram, M. F. Jones, R. A. Brown, G. J. McLellan, D. G. Charteris, P. T. Khaw, and G. A. Limb, "Allogeneic transplantation of müller-derived retinal ganglion cells improves retinal function in a feline model of ganglion cell depletion," *STEM CELLS Translational Medicine*, vol. 5, no. 2, pp. 192–205, 2016, ISSN: 2157-6564. DOI: `https://doi.org/10.5966/sctm.2015-0125`. [Online]. Available: `https://doi.org/10.5966/sctm.2015-0125`.

[213] C. S. Nickerson, J. Park, J. A. Kornfield, and H. Karageozian, "Rheological properties of the vitreous and the role of hyaluronic acid," *Journal of biomechanics*, vol. 41, no. 9, pp. 1840–1846, 2008, ISSN: 0021-9290.

[214] S. Suri and C. E. Schmidt, "Photopatterned collagen–hyaluronic acid interpenetrating polymer network hydrogels," *Acta biomaterialia*, vol. 5, no. 7, pp. 2385–2397, 2009, ISSN: 1742-7061.

[215] T. Walimbe, S. Calve, A. Panitch, and M. P. Sivasankar, "Incorporation of types i and iii collagen in tunable hyaluronan hydrogels for vocal fold tissue engineering," *Acta biomaterialia*, vol. 87, pp. 97–107, 2019, ISSN: 1742-7061.

[216] F. Chen, P. Le, K. Lai, G. M. Fernandes-Cunha, and D. Myung, "Simultaneous interpenetrating polymer network of collagen and hyaluronic acid as an in situ-forming corneal defect filler," *Chemistry of Materials*, vol. 32, no. 12, pp. 5208–5216, 2020, ISSN: 0897-4756.

[217] F. Li, M. Ducker, B. Sun, F. G. Szele, and J. T. Czernuszka, "Interpenetrating polymer networks of collagen, hyaluronic acid, and chondroitin sulfate as scaffolds for brain tissue engineering," *Acta Biomaterialia*, vol. 112, pp. 122–135, 2020, ISSN: 1742-7061.

[218] J. Hertz, B. Qu, Y. Hu, R. D. Patel, D. A. Valenzuela, and J. L. Goldberg, "Survival and integration of developing and progenitor-derived retinal ganglion cells following transplantation," *Cell Transplant*, vol. 23, no. 7, pp. 855–72, 2014, ISSN: 1555-3892 (Electronic) 0963-6897 (Linking). DOI: `10.3727/096368913X667024`. [Online]. Available: `https://www.ncbi.nlm.nih.gov/pubmed/23636049`.

[219] P. Venugopalan, Y. Wang, T. Nguyen, A. Huang, K. J. Muller, and J. L. Goldberg, "Transplanted neurons integrate into adult retinas and respond to light," *Nature communications*, vol. 7, no. 1, pp. 1–9, 2016, ISSN: 2041-1723.

[220] J. S. Rajkumar, M. Maddison, D. Singh, P. COLOMBE, M. Spector, and M. J. Young, "Enrichment of a retinal ganglion cell population using a novel microfluidic sorting strategy," *Investigative Ophthalmology & Visual Science*, vol. 61, no. 7, pp. 2521–2521, 2020, ISSN: 1552-5783.

[221] M. Tso, C. Zhang, A. S. Abler, C.-J. Chang, F. Wong, G.-Q. Chang, and T. T. Lam, "Apoptosis leads to photoreceptor degeneration in inherited retinal dystrophy of rcs rats," *Investigative Ophthalmology & Visual Science*, vol. 35, no. 6, pp. 2693–2699, 1994, ISSN: 1552-5783.

[222] B. Leclercq, D. Hicks, and V. Laurent, "Photoperiod integration in c3h rd1 mice," *Journal of Pineal Research*, e12711, 2020, ISSN: 0742-3098.

[223] H. Koso, C. Minami, Y. Tabata, M. Inoue, E. Sasaki, S. Satoh, and S. Watanabe, "Cd73, a novel cell surface antigen that characterizes retinal photoreceptor precursor cells," *Investigative ophthalmology & visual science*, vol. 50, no. 11, pp. 5411–5418, 2009, ISSN: 1552-5783.

[224] L. Ng, J. B. Hurley, B. Dierks, M. Srinivas, C. Saltó, B. Vennström, T. A. Reh, and D. Forrest, "A thyroid hormone receptor that is required for the development of green cone photoreceptors," *Nature genetics*, vol. 27, no. 1, pp. 94–98, 2001, ISSN: 1546-1718.

[225] A. M. Santos, D. Martín-Oliva, R. M. Ferrer-Martín, M. Tassi, R. Calvente, A. Sierra, M.-C. Carrasco, J. L. Marín-Teva, J. Navascués, and M. A. Cuadros, "Microglial response to light-induced photoreceptor degeneration in the mouse retina," *Journal of Comparative Neurology*, vol. 518, no. 4, pp. 477–492, 2010, ISSN: 0021-9967.

[226] M. J. Hollenberg and A. W. Spira, "Human retinal development: Ultrastructure of the outer retina," *American Journal of Anatomy*, vol. 137, no. 4, pp. 357–385, 1973, ISSN: 0002-9106.

[227] S. L. Stella Jr, A. Vila, A. Y. Hung, M. E. Rome, U. Huynh, M. Sheng, H.-J. Kreienkamp, and N. C. Brecha, "Association of shank 1a scaffolding protein with cone photoreceptor terminals in the mammalian retina," 2012, ISSN: 1932-6203.

[228] I. Ben-Oren, G. Peleg, A. Lewis, B. Minke, and L. Loew, "Infrared nonlinear optical measurements of membrane potential in photoreceptor cells," *Biophysical journal*, vol. 71, no. 3, pp. 1616–1620, 1996, ISSN: 0006-3495.

[229] J. C. Lau and R. A. Linsenmeier, "Oxygen consumption and distribution in the long-evans rat retina," *Experimental eye research*, vol. 102, pp. 50–58, 2012, ISSN: 0014-4835.

[230] M. La Vail, R. Sidman, and C. Gerhardt, "Congenic strains of rcs rats with inherited retinal dystrophy," *Journal of Heredity*, vol. 66, no. 4, pp. 242–244, 1975, ISSN: 0022-1503.

[231] J. C. Gardner, G. Liew, Y.-H. Quan, B. Ermetal, H. Ueyama, A. E. Davidson, N. Schwarz, N. Kanuga, R. Chana, and E. R. Maher, "Three different cone opsin gene array mutational mechanisms with genotype–phenotype correlation

and functional investigation of cone opsin variants," *Human mutation*, vol. 35, no. 11, pp. 1354–1362, 2014, ISSN: 1059-7794.

[232] G. Huber, S. C. Beck, C. Grimm, A. Sahaboglu-Tekgoz, F. Paquet-Durand, A. Wenzel, P. Humphries, T. M. Redmond, M. W. Seeliger, and M. D. Fischer, "Spectral domain optical coherence tomography in mouse models of retinal degeneration," *Investigative ophthalmology & visual science*, vol. 50, no. 12, pp. 5888–5895, 2009, ISSN: 1552-5783.

[233] J. S. Heier, D. M. Brown, V. Chong, J.-F. Korobelnik, P. K. Kaiser, Q. D. Nguyen, B. Kirchhof, A. Ho, Y. Ogura, and G. D. Yancopoulos, "Intravitreal aflibercept (vegf trap-eye) in wet age-related macular degeneration," *Ophthalmology*, vol. 119, no. 12, pp. 2537–2548, 2012, ISSN: 0161-6420.

Appendix A

Algorithms for image processing and analysis

A.1 Area counting of cell fluorescence

```
%% Thresholds
I = 10; ThresholdGreen = 50; ThresholdRed = 50;

%% Image analysis
s = strcat(num2str(I),’gelegf.tif’);
A = imread(s);
Size = size(A); Totalpixels = Size(1)*Size(2);
r = A(:,:, 1); g = A(:,:, 2); b = A(:,:, 3);

%% Red/Green images
justGreen = g - r/2 - b/2; justRed = r - g/2 - b/2;

%% Image processing
Green = justGreen > ThresholdGreen;
Red = justRed > ThresholdRed;
```

```
SUMg = sum(sum(Green)); SUMr = sum(sum(Red));

%% Results
PercentGreen = 100 * SUMg / Totalpixels;
PercentRed = 100 * SUMr / Totalpixels;
```

A.2 Cell counting of Live/Dead assays

```
%% Open image & first filters
int=2; A = imread(’Cult.tif’); greenChannel = A(:,:,2);
I = greenChannel; I = adapthisteq(I);
I = imclearborder(I); I = wiener2(I, [int int]);

%% Change to binary and get cells
bw = im2bw(I, graythresh(I)); bw2 = imfill(bw,’holes’);
bw3 = imopen(bw2, strel(’disk’,2)); bw4 = bwareaopen(bw3, 1);

%% Checking grouped cells
bw4_perim = bwperim(bw4);
overlay1 = imoverlay(I, bw4_perim, [1 .3 .3]);

%% Discover putative cell centroids
maxs = imextendedmax(I, 5); maxs = imclose(maxs, strel(’disk’,3));
maxs = imfill(maxs, ’holes’); maxs = bwareaopen(maxs, 2);
overlay2 = imoverlay(I, bw4_perim | maxs, [1 .3 .3]);

%%Background and maxima pixels.
Jc = imcomplement(I); I_mod = imimposemin(Jc,  bw4 | maxs);
L = watershed(I_mod); labeledImage = label2rgb(L);
```

```
stats = regionprops(’table’,L,’Perimeter’,’Area’,’Centroid’,’MajorAxisLength’);

%% Final Count and final overlay
[LL, num] = bwlabel(L);
mask = im2bw(LL, 1);
overlay3 = imoverlay(I, mask, [.3 1 .3]);
number(int)=num;

%% Take care of too big and too small
Centroidx=stats.Centroid(:,1);Centroidy=stats.Centroid(:,2);
Good.Centroid=[Centroidx(stats.MajorAxisLength>small &
stats.MajorAxisLength<big) Centroidy(stats.MajorAxisLength>small &
stats.MajorAxisLength<big)];
Good.Radius=stats.MajorAxisLength(stats.MajorAxisLength>small
& stats.MajorAxisLength<big);

%% Number of cells
imwrite(A,’myGray.png’); figure; imshow(overlay3); hold on; for kab=1:num
size_string = sprintf(’%u’,kab);
text(stats.Centroid(kab,1)-30,stats.Centroid(kab,2)+40,size_string,’Color’,’y’,...
’FontSize’,14,’FontWeight’,’bold’); end

%% Distribution of size
RealAreaDistrib=stats.MajorAxisLength.*2000/919;
figure; imshow(overlay3); hold on; for ka=1:num
size_string = sprintf(’%2.2f’,RealAreaDistrib(ka));
text(stats.Centroid(ka,1)-30,stats.Centroid(ka,2)+40,size_string,’Color’,’w’,...
’FontSize’,14,’FontWeight’,’bold’); end

%% Granularity
```

```
figure; imshow(overlay3); hold on; for k=1:num
Metric(k)=(4*pi.*stats.Area(k))./(stats.Perimeter(k).*stats.Perimeter(k));
if Metric(k)>1; Metric(k)=1; end
metric_string = sprintf('%2.2f',Metric(k));
text(stats.Centroid(k,1)-30,stats.Centroid(k,2)+40,metric_string,'Color','r',...
'FontSize',14,'FontWeight','bold'); end
```

A.3 Cell migration, orientation and co-localization algorithm

```
%% Importing packages import cv2, import glob, import math, import matplotlib.pyplot as plt, import numpy as np, import json, from shapely.geometry import Point, from shapely.geometry.polygon import, Polygon, import os, import pandas as pd
```

```
%% Make grid
def make_frame_grid(frames, frames_info=None,
num_cols=5, size=1.5, fontsize=8, save_path=None):
num_lines = len(frames) // num_cols + 1
h, w, _ = frames[0].shape; ratio = h/w
fig = plt.figure(figsize=(num_cols*size/ratio,num_lines*size))
plt.tight_layout() for i, frame in enumerate(frames):
ax1 = fig.add_subplot(num_lines, num_cols, i+1)
ax1.set_yticklabels([]); ax1.set_xticklabels([])
if frames_info is not None: info = frames_info[i]; # ax1.set_xlabel(info)
ax1.set_title(info, fontdict='fontsize': fontsize); ax1.imshow(frame)
plt.subplots_adjust(wspace=.001, hspace=.3 if frames_info is not None else 0.001)
if save_path is not None:
plt.savefig(save_path,bbox_inches = 'tight',pad_inches = 0)
```

```
else: plt.show(), plt.close()

%% Files from confocal
json_files = [’labels_gtn copy.json’]#, ’labels_ipn75.json’, ’labels_pbs.json’,
’layers_ipn50.json’]; by_file = {}; by2_file = {}
for file in json_files: with open(file, ’r’) as f: lines = json.load(f)
for key, value in lines.items():
regions = value[’regions’]; num_regions = len(regions)
polygon_per_regions = {}; points_per_regions = {}
for _, region in regions.items():
points_x = region[’shape_attributes’][’all_points_x’]
points_y = region[’shape_attributes’][’all_points_y’]
for x, y in zip(points_x, points_y): points.append((x,y))
region_name = region[’region_attributes’][’label’]
polygon_per_regions[region_name] = Polygon(points)
points_per_regions[region_name] = points by_file[key] = polygon_per_regions

%% Define polygons and ellipses
def polygon_orientation(points, debug=False):
i=0.001; cv2_contour = []; for p in points:
cv2_contour.append([p]); while len(cv2_contour)<5: cv2_contour.append([p])
i=i+0.001; cv2_contour = np.array(cv2_contour, dtype=np.int32)
ellipse = cv2.fitEllipse(cv2_contour)
if debug: canvas = np.ones_like(img)*255
canvas = cv2.drawContours(canvas, [cv2_contour], -1, (0,255,0), 3)
cv2.ellipse(canvas, ellipse, (0,255,255))
plt.imshow(canvas); return ellipse

%% Capture only positive cells
def get_centers(green): GREEN_THRESHOLD = 55
```

```
BLUR_SIZE = 1; CLOSING_SIZE = 1; OPENING_SIZE = 2
blurred = cv2.blur(green, (BLUR_SIZE, BLUR_SIZE))
thresholded = np.array(blurred > GREEN_THRESHOLD, dtype=np.uint8)
kernel = np.ones((CLOSING_SIZE, CLOSING_SIZE), np.uint8)
imask = cv2.morphologyEx(thresholded, cv2.MORPH_CLOSE, kernel)
kernel = np.ones((OPENING_SIZE, OPENING_SIZE), np.uint8)
imask = cv2.morphologyEx(imask, cv2.MORPH_OPEN, kernel) return imask

%% Image distortion and kernels
column_names = ["layer", "file", "group", "center", "size", "center", "axes",
"angle cell","angle layer"]; result_lines = []
for file, info in by_file.items(): group = file.split(’_’)[0]
file_id = file.replace(’.png’, ”)
path = os.path.join(’data’, file_id, file_id + ’.tif’)
img = cv2.imread(path)[:,:,::-1]
green = cv2.imread(path.replace(’shot4’, ’shot2’))[:,:,1]
centers = get_centers(green)
blurred = cv2.blur(green, (BLUR_SIZE, BLUR_SIZE))
thresholded = np.array(blurred > GREEN_THRESHOLD, dtype=np.uint8)
kernel = np.ones((DILATATION_SIZE,DILATATION_SIZE),np.uint8)
eroded = cv2.dilate(thresholded,kernel,iterations = 1)
kernel = np.ones((CLOSING_SIZE, CLOSING_SIZE), np.uint8)
imask = cv2.morphologyEx(thresholded, cv2.MORPH_CLOSE, kernel)
kernel = np.ones((OPENING_SIZE, OPENING_SIZE), np.uint8)
imask = cv2.morphologyEx(imask, cv2.MORPH_OPEN, kernel)
connectivity = 4
ret, markers, stats, centroids = cv2.connectedComponentsWithStats
(eroded, connectivity , cv2.CV_32S)

%% Remove components without any center in them
```

```
clean_centroids = []; for component_id, centroid in enumerate(centroids):
component_mask = np.where(markers == component_id)
masked_centers = centers[component_mask]
masked_eroded = np.array(markers == component_id, dtype=np.uint8)
if np.sum(masked_centers) == 0:
markers[component_mask] = 0; else: area = len(component_mask[0])
contours, hierarchy = cv2.findContours
(masked_eroded, cv2.RETR_EXTERNAL,cv2.CHAIN_APPROX_NONE)
if len(contours[0]) <= 5: print("ERROR WITH CONTOUR for " + file)
else: ellipse = cv2.fitEllipse(contours[0])
clean_centroids.append((centroid, area / (img.shape[0] * img.shape[1]), ellipse))
composed = np.zeros_like(img)
Polylayers = np.zeros_like(img,dtype=np.uint8)
no_markers = markers == 0; markers = markers * 4 + 10
markers[no_markers] = 0
composed[:,:, 0] = markers; composed[:,:, 1] = centers

%% Draw the centers
for (centroid, area, ellipse) in clean_centroids:
center = (int(centroid[0]), int(centroid[1]))
cv2.circle(composed, center, 10, (255, 0, 0), 2)
cv2.ellipse(composed, ellipse,(0,255,255))
single_point = Point(center[0], center[1])
for region_id, polygon in info.items():
if polygon.contains(single_point):
center, axes, angle = ellipse
Grandaxe=axes[1]; #angle=math.fmod(angle,90)
polygon_ellipse = polygon_orientation(list(polygon.boundary.coords))
cv2.ellipse(Polylayers, polygon_ellipse,(0,0,255))
_, poly_axes, poly_angle = polygon_ellipse
```

```
result_lines.append([region_id, file, group, centroid, area, center,
Grandaxe, angle, poly_angle])
print("center {} is in polygon for region {} with {} and {}".format
(centroid, region_id, Grandaxe,poly_angle))
make_frame_grid([img, composed,Polylayers], num_cols=3, size=70,
save_path="ipn6.jpeg")
df = pd.DataFrame(result_lines, columns=column_names)
df.to_excel(’results.xls’)
```

A.4 RD1 whole mount distribution analysis

```
%% Density Maps
MAP=zeros(2048,2048,3);MAP(:,:,3)=0.3;x=0;y=0;r=0;xp(1)=-1;yp=-1;
for map=1:length(Good.Centroid); y=round(Good.Centroid(map,1));
x=round(Good.Centroid(map,2)); r=round(Good.Radius(map)*1.2);
MAP((xx-x^2+(yy-y).^2<r^2)=MAP((xx-x).^2+(yy-y^2<r^2)+0.2;
end; figure; imshow(MAP); MAP0=uint8(MAP);

%% Find Distance recovery Profile
D=zeros(Rmax,length(Good.Centroid)); for centre=1:length(Good.Centroid)
p=0; for R=1:50:Rmax; p=p+1; for search=1:2048; for search1=1:2048
if(round(abs(search-Good.Centroid(centre,2)))==R
&& round(abs(search1-Good.Centroid(centre,1)))<=R)
D(p,centre)=D(p,centre)+MAP(search1,search,1);
elseif(round(abs(search-Good.Centroid(centre,2)))<=R
&& round(abs(search1-Good.Centroid(centre,1)))==R)
D(p,centre)=D(p,centre)+MAP(search1,search,1); end; end; end; end; end

%% Find nearest neighbors and MAP
for start=1:length(Good.Centroid)
```

```
Distance(:,start)=sqrt((Good.Centroid(start,1)-Good.Centroid(:,1^ 2
+(Good.Centroid(start,2)-Good.Centroid(:,2)).^ 2);
Distance(start,start)=10^10; NND(start,:)=min(Distance(:,start)); end
MAP3=zeros(2048,2048,3); MAP2=MAP0;
for map=1:length(Good.Centroid);r=round(Good.Radius(map)); r=20;
y=round(Good.Centroid(map,1)); x=round(Good.Centroid(map,2));
if(x+r>2048 || y+r>2048 || x-r<0 || y-r<0); continue; end
if(NND(map)<30); MAP3((xx-x^2+(yy-y).^2<r^2)=0.1;
elseif(NND(map)>=30 && NND(map)<50)
MAP3((xx-x).^2+(yy-y).^2<r^2)=0.2;
elseif(NND(map)>=50 && NND(map)<70)
MAP3((xx-x).^2+(yy-y^2<r^2)=0.3;
elseif(NND(map)>=70 && NND(map)<90)
MAP3((xx-x).^2+(yy-y^2<r^2)=0.4;
elseif(NND(map)>=90 && NND(map)<110)
MAP3((xx-x).^2+(yy-y).^2<r^2)=0.5;
elseif(NND(map)>=110 && NND(map)<200)
MAP3((xx-x).^2+(yy-y).^2<r^2)=0.6; end; end
figure; imshow(MAP); MAP4=uint8(MAP3);

%% Work on Density MAP
for alpha1=1:2048; for alpha2=1:2048; if(MAP3(alpha1,alpha2,1)==0.1)
MAP4(alpha1,alpha2,1)=255;MAP4(alpha1,alpha2,2)=0;MAP4(alpha1,alpha2,3)=0;
elseif(MAP3(alpha1,alpha2,1)==0.2) MAP4(alpha1,alpha2,1)=255;
MAP4(alpha1,alpha2,2)=255;MAP4(alpha1,alpha2,3)=0;
elseif(MAP3(alpha1,alpha2,1)==0.3) MAP4(alpha1,alpha2,1)=0;
MAP4(alpha1,alpha2,2)=255;MAP4(alpha1,alpha2,3)=0;
elseif(MAP3(alpha1,alpha2,1)==0.4) MAP4(alpha1,alpha2,1)=0;
MAP4(alpha1,alpha2,2)=255;MAP4(alpha1,alpha2,3)=255;
elseif(MAP3(alpha1,alpha2,1)==0.5) MAP4(alpha1,alpha2,1)=0;
```

```
MAP4(alpha1,alpha2,2)=0;MAP4(alpha1,alpha2,3)=255;
elseif(MAP3(alpha1,alpha2,1)==0.6) MAP4(alpha1,alpha2,1)=255;
MAP4(alpha1,alpha2,2)=0;MAP4(alpha1,alpha2,3)=255; else
MAP4(alpha1,alpha2,1)=200;MAP4(alpha1,alpha2,2)=200;MAP4(alpha1,alpha2,3)=200;
end; end; end; for inttt=1:620
plot(Good.Centroid(inttt,1), Good.Centroid(inttt,2),Colors(inttt), ’MarkerSize’,69)
viscircles(Good.Centroid(inttt,:),Good.Radius(inttt),’Color’,Colors(inttt),’LineWidth’,0.1);
end; imshow(MAP4);
```